High power diamond Schottky diode

Aboulaye Traoré

UNIVERSITÉ DE GRENOBLE

THÈSE

Pour obtenir le grade de

DOCTEUR DE L'UNIVERSITÉ DE GRENOBLE

Spécialité : **Nano Electronique Nano Technologies (NENT)**

Arrêté ministériel : 7 août 2006

Présentée par

« Aboulaye TRAORE »

Thèse dirigée par **« Julien PERNOT »**,
codirigée par **« Etienne GHEERAERT »** et
co-encadré par **« David EON»**

préparée au sein du **Institut Néel – CNRS Grenoble**
dans **Electronique, Electrotechnique, Automatique et Traitement du Signal (EEATS)**

High power diamond Schottky diode

Thèse soutenue publiquement le **16 décembre 2014,**
devant le jury composé de :

M. Jocelyn, ACHARD
Professeur, Laboratoire des Sciences des Procédés et des Matériaux (France), Rapporteur

M. José ALVAREZ
Chargé de recherche, Laboratoire de Génie Electrique de Paris (France) Examinateur

M. Christian BRYLINSKI
Professeur, Laboratoires des Multimatériaux et Interfaces (France), Rapporteur

M. David EON
Maître de conférence, Université Joseph Fourier (France), Co-encadrant de thèse

M. Satoshi KOIZUMI
Docteur, National Institute for Materials Science (Japon), Examinateur

M. Christoph NEBEL
Professeur, Fraunhofer Institute for Applied Solid State Physics (Allemagne), Examinateur

M. Julien PERNOT
Maître de conférence, Université Joseph Fourier (France), Directeur de thèse

Contents

List of Figures

List of Tables

Introduction

Energy is a crucial resource in our modern societies where economic development and modernization are the main concerns. Besides its necessity in industry as well as in services in order to ensure human well-being such as transport, telecommunications, energy is essential to produce vital resources such as clean water or to guarantee healthcare. Several primary sources gas, oil, coal, uranium (nuclear) available on our planet, are basically transformed into electricity which is the energy source for industry as well as for household and office appliances (refrigeration, lighting, air conditioners, computers, fax, etc.) [1]. With the world population increasing more specifically in urban areas and furthermore due to emerging economies, world electricity demand is continuously growing [1]. For the next 20 years, the international energy agency estimates the global electricity demand growth to more than 75% expanding from 16400 TWh/year in 2007 to 28900 TWh/year in 2030 [1, 2]. Apart from the fact that the continuous and sustainable supply of electricity is jeopardized since primary energy sources are limited, the electricity-related greenhouse gas emission (CO_2 emission) contributes to the average rise of global temperature and then to the current climate change (CO_2 emission due to electricity production should increase about 40% in 2030 expanding from 28.8 Gt/year in 2007 to 40.2 Gt/year in 2030 [1, 2]).

In this respect, reducing the environmental impact of electricity production and promoting a management of fossil energy sources are more than ever required to maintain the viability of our modern societies. The sustainable development and the fight against climate change are today international issues [2]. For example, in 2014, France national assembly discussed a law project on Energy "Transition énergétique pour la croissance verte" in order to reduce the greenhouse gas emission by 40%, to increase the amount of renewable power to 32% of total energy consumption, while dividing the latter by two by 2030 [3]. In 2013, the United States administration announced a major climate action

to introduce new standards for power plants, more funding and incentives for energy efficiency and renewable, provide more global leadership to reduce carbon emission... [1]. This announcement follows a "Smart Grid" project launched in 2009. The main idea behind the "Smart Grid" concept, is to link all the elements (generators, consumers and those that do both) together for a dynamical energy management. Permanent communications between utility and its customers are expected to optimize energy efficiency and mitigate CO_2 emission [4, 5]. The "Smart Grid" concept is today well accepted since it should allow a greater utilization of renewable energy sources. The European council experts of the Taskforce for Smart Grids mentioned that Smart Grids should play an important role in implementing EU energy policy targeting a share of 75% of renewable energy in gross final consumption. Besides the smart grids favoring renewable energy utilization such as photovoltaic or wind, one can mention the electric vehicles and the hybrid electric vehicles intensively promoted today.

In response to these policies and to the new applications driven by an efficient energy management, power electronics need a "complete makeover". Power electronics represent the main technological bridges used for energy processing from source transformation (coal, fuels, gas, renewable) to the end-users (household, office, industry, etc). It is well known that the electricity processing through power conversion systems using the well-established silicon technologies, are in major part responsible for approximately 80% of the energy lost along the chain from primary sources to end-users [2]. Over the last decades, wide band gap semiconductors (GaN, SiC, Diamond), which offer better electrical properties, have been identified as the appropriate materials to overcome silicon limitations and to improve the efficiency of the energy chain by minimizing losses. The transition from silicon to gallium nitride (GaN) and silicon carbide (SiC) devices in power electronics has been already ignited.

Diamond, the ultimate semiconductor for power electronics still at the Research & Development stage, is intensively investigated by several research groups over the world. Over the last 20 years, the technological progresses achieved in diamond growth, its doping, and its surface treatment, allow today to fabricate various electronics devices (Schottky diode, field effect transistors, bipolar transistors, Metal Oxide Semiconductor capacitor, PIN, etc). Among these diamond-based devices, Schottky diode is the most advanced. Nevertheless, this unipolar device still suffers from several imperfections that must be corrected in order to fabricate a demonstrator with outstanding electrical

properties surpassing SiC-based devices (the main wide bandgap material industrialized today) and making the most of the superior electrical and thermal properties of diamond.

The present thesis attempts to contribute to this effort by investigating and enhancing the electrical performance of diamond Schottky rectifiers. In this regard, several open questions must be first considered: (i) Can we demonstrate the superiority of diamond-based rectifiers using the available electronic grade diamond substrates? (ii) Is the elevated ionization energy of dopants redhibitory? (iii) What is the best structure for diamond Schottky diodes? (iv) What kind of metal (Schottky electrode) must be used to reach high performances?. In order to propose workable answers, this report is divided as follows:

Chapter 1: The main wide bandgap (WBG) semiconductors, the share of WBG-based devices in the power electronics market and its expected evolution, will be introduced in this chapter. In a second part, the state of the art of devices based on diamond, the ultimate material for power electronics, will be described.

Chapter 2: The main transport properties (mobility, carrier density, and resistivity) will be investigated over a wide doping and compensation range, and at different temperatures. This work will highlight the influence of dopants ionization energy and of the relevant scattering mechanisms on diamond transport properties.

Chapter 3: The fabrication process of the pseudo-vertical diode structure used (motivated by the unavailability of commercial electronic grade highly conductive diamond substrates) will be introduced. The growth process together with the main characterization techniques used to investigate the epi-layers surface and the volume defects will be introduced. The geometrical considerations, the doping level, the trade-off between serial resistance and breakdown voltage will be presented.

Chapter 4: The electrical characterization of pseudo vertical diamond Schottky rectifiers based on an oxygen-terminated diamond surface covered by the easily oxidizable refractory metals like zirconium (Zr) will be discussed. Zr Schottky contact deposition process together with its interface investigation by High-Resolution Transmission Electron Microscopy (HRTEM) and Electron Energy Loss Spectroscopy (EELS) will

be analyzed. The room temperature electrical characteristics followed by their thermal stability will then be presented and discussed. Finally, the electrical characteristics of annealed Zr/oxygen terminated diamond junctions will be investigated.

References:

[1] International Energy Agency IEA, World Energy Outlook 2013, Renewable energy outlook, www.iea.org

[2] ABB, The evolving world of power opportunities and challenges, www.abb.com

[3] http://www.assemblee-nationale.fr, Energie: Transition énergétique pour la croissance verte, extrait du rendu du conseil des ministres 30/07/14

[4] Electric Power Research Institute EPRI, The Green Grid, Energy Saving and Carbon Emission Reductions Enabled by a Smart Grid, June 2008, www.epri.com

[5]: Gimelec industrie, Livre blanc des industriels au service de l'inteligence énergétique, RÉSEAUX ÉLECTRIQUE INTELLIGENTS, www.gimelec.fr

Chapter 1

Diamond power devices

Contents

1.1 Introduction

Power electronics is today involved in a mutation process to meet energy efficiency and clean energy policies launched by governments over the world and furthermore to provide answers to the power market evolution related to these policies. Silicon-based devices are today the most advanced and mature technology for power applications ranging from high-voltage direct current (HVDC) converter stations to the flexible ac transmission system (FACTS) devices used in a large number of fields such as to control and regulate ac power grids, the electric drive in transportation systems, variable-speed drivers for motors, interfaces with storage devices of several types...[Tolbert 2005] Depending on the intended field, various Si devices can be used: Thyristors that offer the highest blocking voltage ranging between 10 kV and 8 kV (maximum current about 2.2 kA) and are essentially used for very high voltage applications (grid converter stations) where high frequencies are not required (operating frequency limited at 100 Hz). They have been improved into IGCT (Integrated gate-commutated Thyristor) or GTO (Gate Turn Off) thyristors, which have a higher operating frequency between 100 Hz and 1kHz but a lower blocking voltage (below 8 kV) even maximum current (2 kA). However, IGCT or GTO are used to address a large number applications (Motor control, wind, grid, rail traction...). For power inverters, IGBT (Insulated Gate Bipolar Transistor) is preferentially used because of its best trade-off between high blocking voltage (up to 6 kV) and high operating frequency (about 100 kHz). For small converter power supply and amplifiers, less specific transistors (MOSFET, JFET, Bipolar) are used.

For all these Si-based devices, the first limitation is the low thermal conductivity of silicon limiting the maximum operating temperature to less than 150 °C. This requires a significant thermal management effort (forced air or water-cooled heat sinks for example). On the other hand, for high-voltage applications such as switching in transmission level (blocking voltage higher than 100 kV), the low critical field of silicon (0.3 MV/cm) limiting the maximum blocking capability of Si-based down to 10 kV, stacking packaged devices in series is required [Tolbert 2005]. Besides the need of series stacking with complicated triggering to maintain voltage-sharing between devices [Tolbert 2005] in the stack and the thermal management to maintain devices temperature below 150 °C, it is generally reported that the use of Si-based devices in electricity processing are in major part responsible of 80% of losses over the whole energy chain (from energy generation sources to end users) [Millán 2012].

Contrary to silicon, the enormous potentiality to save energy using WBG semiconductor-based devices is well recognized. Indeed, most of WBG materials (silicon carbide, gallium nitride, diamond) outstrip silicon in term of physical properties needed for high voltage, high frequencies, and high temperature applications. Their physical and thermal properties, superior to those of silicon may allow smaller, faster, and more efficient power devices.

This chapter will first attempt to give a general overview of main WBG materials and of the expected impact of WBG devices. In a second part, the state of the art of devices based on diamond, the ultimate material for power electronics, will be introduced.

1.2 Wide band gap semiconductors

Table 1.1 summarizes the physical properties of candidates for silicon replacement in power applications: Silicon Carbide (SiC), Gallium Nitride (GaN), and diamond. All of these materials have larger critical field and higher thermal conductivity than silicon. Diamond is outstanding among these candidates due to its high critical field 10 MV/cm (more than 30 times that of Si and 3 more times that of SiC), its higher electron mobility 1000 cm^2/Vs (comparable to SiC) and hole mobility 2000 cm^2/Vs (higher than all electron mobilities), and higher thermal conductivity 22 W/cmK (20 times that of Si and 6 times that of copper). As a result, the theoretical Figure Of Merit (FOM) of diamond are much higher than those of its challengers. Figures of merit are generally used to compare materials in view of a specific application field. These FOM are respectively:

Johnson's figure of merit (JFM): It represents the ability of a material for high frequency and high power transistor applications [Johnson 1965]. This FOM is both applicable to FET and with caution to bipolar transistor.

$$JFM = \left(\frac{F_B.v_s}{2\pi}\right)^2 \tag{1.1}$$

Keyes' figure of merit (KFM): It displays the thermal limitation to the switching behavior at high frequency [Keyes 1972].

$$KFM = \lambda \left(\frac{c.v_s}{2\pi.\epsilon_r}\right)^{1/2} \tag{1.2}$$

where c is the light velocity.

Property	[unit]	Si	4H-SiC	GaN	Diamond
Band gap	E_G [eV]	1.1 i	3.23 i	3.45 d	5.45 i
Dielectric constant	ϵ_r	11.8	9.8	9	5.5
Breakdown Field	F_B [MV/cm]	0.3	2	3 - 4	10
Thermal conductivity	λ [W/cm.K]	1.5	5	1.5	22
Sat. drift velocity e^-	v_s [10^7 cm/s]	1.0	2.0	2.2	2.7
Sat. drift velocity h^+	v_s [10^7 cm/s]	1.0			1.1
Electrons mobility	μ_e [cm^2/V.s]	1500	1000	1250	1000
Holes mobility	μ_h [cm^2/V.s]	480	100	200	2000
Johnson's FOM	JFM [10^{23} $\Omega.W/s^2$]	2	405	1103	3064
Keyes' FOM	KFM [10^7 W/K.s]	9	49	16	215
Baliga's FOM	BFM [Si=1]	1	165	635	23017

Table 1.1: Physical properties at room temperature of silicon (Si) and major wide band gap materials (SiC, GaN, diamond) used in power electronics and the related figures of merit (Johnson, Keyes and Baliga, see description in the text). In the band gap row, i and d denote respectively an indirect and direct band gap. If temperature dependent, the values are given at room temperature. The FOM were calculated at 300K for electrons except for diamond.

Baliga's figure of merit (BFM): It defines a material efficiency to minimize conduction losses in power applications [Baliga 1982, Baliga 1989].

$$BFM = \epsilon_r.\mu.F_B^3 \tag{1.3}$$

The FOM reported in Table 1.1 are room temperature values calculated for electrons except for diamond where the calculated FOM are those of holes. This was motivated by the fact that p-type diamond is preferentially used for unipolar devices such as Schottky diodes (this thesis) due to the lower ionization energy of the boron acceptor in comparison with the phosphorus donor (confer section 1.4). The FOM reported in Table 1.1 highlights the high BFM of diamond (36 times that of GaN and 139 higher that of SiC), its elevated KFM (2.8 times that of GaN and 7 times that of SiC), and the highest JFM (6 times than those GaN and 3 higher than those SiC). Because of these superior properties, diamond is well now widely considered as the ultimate semiconductor for power applications.

1.3 Wide band gap power devices market

As reported by the advanced manufacturing office of US department of energy, WBG-based devices should enhance the energy efficiency in industrial-scale power electronics

and clean energy technologies because of their superior electrical and thermal properties. Indeed, WBG materials may induce several energy-related benefits in power electronics systems, namely: (i) energy loss reduction up to 90% of those currently occurring in AC-to-DC and DC-to-AC electrical conversions [Tolbert 2005], (ii) higher voltage operation than for Si-based devices, which should greatly enhance the number of high-power applications [Ozpineci 2011], (iii) better tolerance of power systems to high operating temperatures resulting in smaller and lighter systems with reduced life cycle energy use [Ozpineci 2011], (iv) higher frequency operations opening up a range of new applications such as radio frequency (RF) amplifiers [Ozpineci 2011], (v) more reliable and consistent power electronic device operation. These features may find various applications in industrials motors (higher-efficiency, variable-speed drives in motors-pumps, fans) and in grid integration (reduction by 50% of losses upon converting DC electricity generated by renewable sources into AC electricity used for household and offices appliances, accelerate high-voltage DC power lines development more efficient than high-voltage AC transmission lines). Electrical vehicles EV and hybrids HEV (losses reduction by 66% during EV/HEV battery recharging, size reduction of automotive cooling system by 60%), as well as military applications (satellite communications, high frequency and high-power radar) among others, would also benefit from such a technological breakthrough.

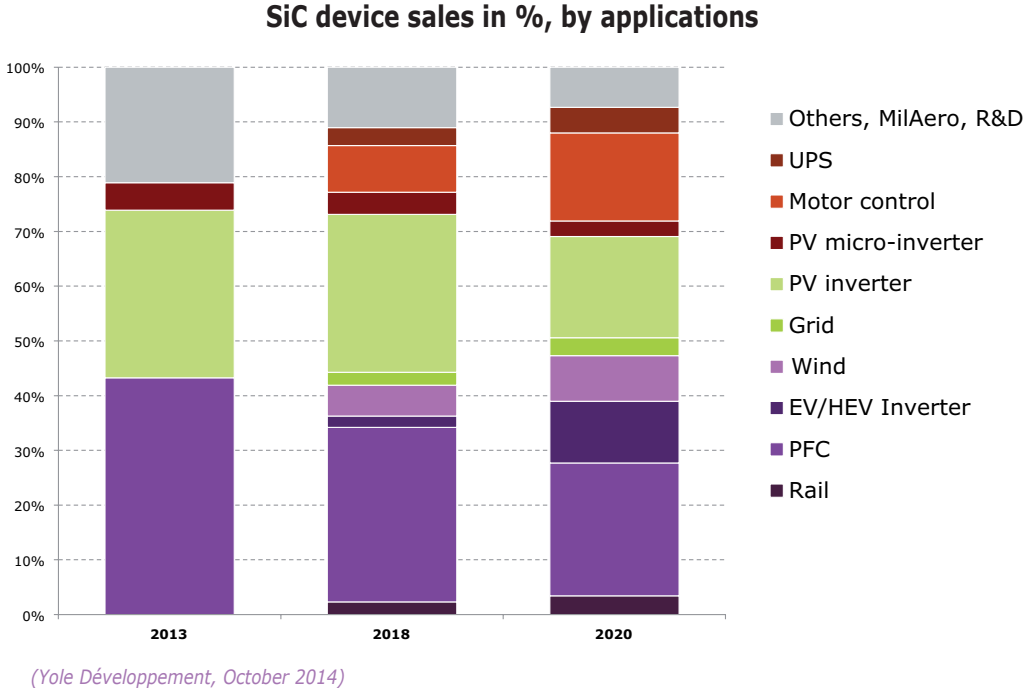

Figure 1.1: SiC devices sales by applications in 2013 its expected evolutions in 2018 and 2020 reported by Yole développement.

SiC is today the most technologically advanced WBG material available at the industrial scale. In 2013, SiC market was estimated to 100 M$ (Yole développement) and should increase with of rate of 39% per year and reach 800 M$ in 2020. SiC devices such as Schottky diodes (SD), JFET and MOSFET withstanding 1700 V blocking voltage (and working up to 300°C) are commercialized by Infineon (Europe), Rohm (Japan) or Cree (United States). Figure 1.1 reported by Yole développement shows the applications of SiC devices in 2013 together with the expected evolution in 2018 and 2020. It can be noticed that SiC technologies are mainly used in the energy sector (75% of sold devices) such as wind and solar inverters (PV inverter). In 2018 and 2020, SiC devices should be adopted in more applications such as rail tractions, grid, PFC (Power Factor Correction boost converter), Electric Vehicle (EV), and Hybrid EV converter (EV/HEV converter),... .

Most of these future applications are in energy, transportation and industry sectors where high voltages are required as shown on Figure 1.2 illustrating the power market segmentation versus bias range in 2013 (Yole développement). For the energy segment, very high voltage range (above 3.3 kV) is predominant (about 90%) and high voltage range (2kV to 3.3 kV) is furthermore used. For transportation, these two voltage ranges are equivalent and complemented by medium voltage range (1.2 kV to 1.7 kV) for less than 10%. Finally, in the industry, the medium range is predominant with more than 60% of devices sold.

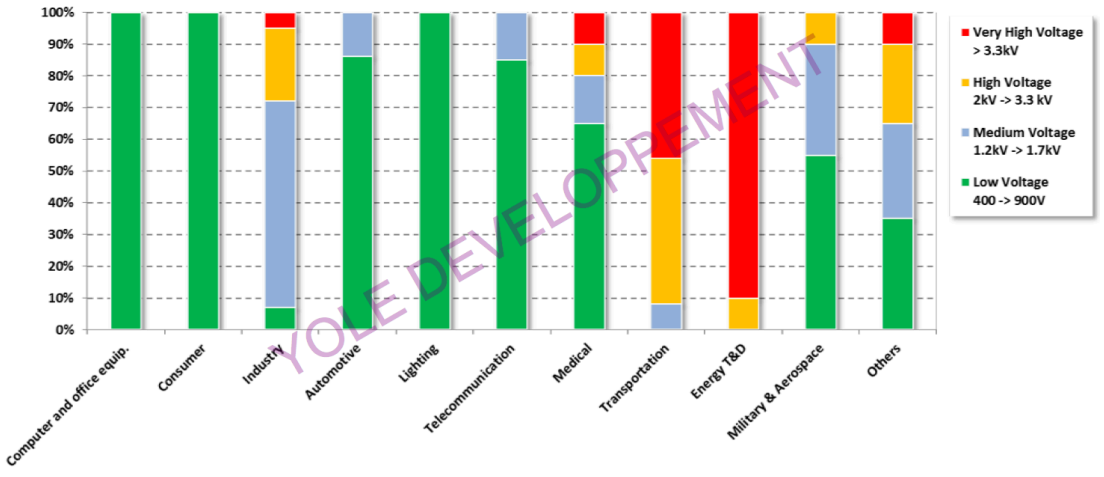

Figure 1.2: Market segmentation in power electronics reported by Yole développement illustrating device revenues distributesd by voltage range in 2013.

The total power market represented about 11.5 B$ in 2013 with 73% (8 425 M$) related to the low voltage range (400 to 900 V) using silicon technologies. For medium, high,

and very high voltages ranges about 23% of total market (3075 M$), SiC devices are less cost-driven and SiC value should be obvious (Yole développement). Yole experts identified that the most pertinent market for SiC that land in high and very high voltage applications. Even if SiC wafers are expensive (4 inch wafer price varying between 1300 and 2000 $) compared to Si (4 inch wafer price below 100 $), the energy-related benefits to this material allow to compete and even to surpass silicon in the high voltage range of applications.

Contrary to SiC technology, which propagates in high voltage applications, Yole experts predict that GaN-based devices designed for the low voltage range (0 to 1000 V) may be commercialized in 2015. The medium voltage range (1000 to 1700 V) should be in prototyping phase, and devices with higher blocking capacity (above 1.7 kV) in Research & Development step. In 2020, GaN power market will be at least 600 M$ as shown on Figure 1.3 (Yole développement) mainly due to GaN on Si technology, and reach more 7% of the power devices.

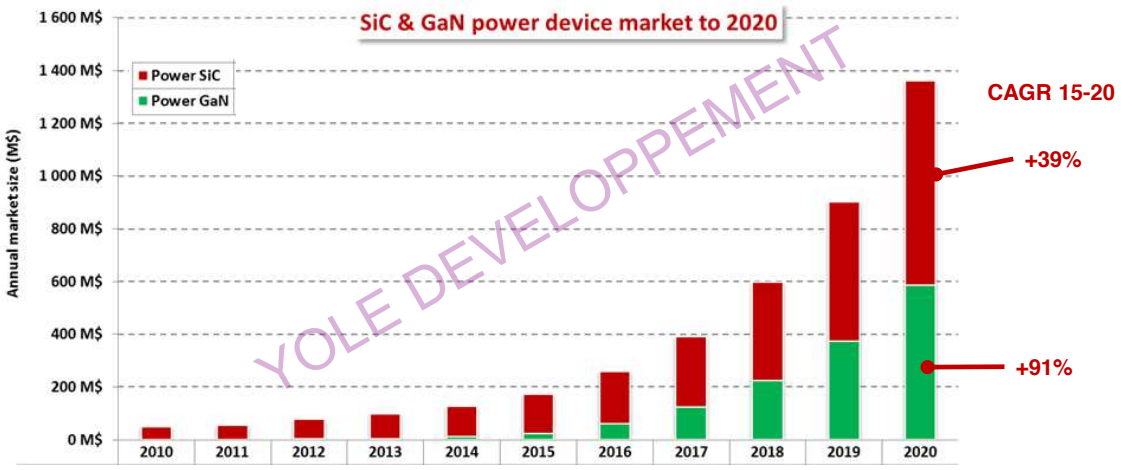

Figure 1.3: Annual SiC & GaN device market size to 2020 reported by Yole développement.

The market addressed by SiC technology can be extended to diamond since the latter is the ultimate semiconductor for high voltage range applications. Diamond-based devices are still at the prototype development step. Market & Technology analysts at Yole développement reported that diamond materials for semiconductor devices will surpass 43 M$in 2020. This market will be mainly related to diamond heat spreaders used in high-power device thermal management. Unfortunately, the main barrier to devices fabrications remains the electronic grade samples size about 3×3 mm^2. For diamond power devices, at least low defects 2-inch wafers are required as mentioned by Yole

experts. Such diamond electronic grade wafers are predicted to be available around 2016 or 2017.

1.4 State of art of diamond devices

1.4.1 Diamond substrate

Diamond is an allotrope of carbon characterized by a tetrahedral arrangement of carbon atoms bonded together by strong covalent sp^3-bonds that crystallizes in a variation of face centered cubic structure: the so-called diamond lattice. Diamond is doped with Boron (B) for *p*-type with an ionization energy about 380 meV and Phosphorous (P) for *n*-type with an ionization energy about 570 meV (Fig. 1.4). Moreover, Nitrogen incorporation in diamond leads to *n*-type diamond with an ionization energy about 1.7eV. This *n*-type dopant, too deep for conductive device applications, is commonly studied in quantum optics and spintronics applications when coupled with a nitrogen vacancy (NV) centers. This material is today mainly synthesized by the high-pressure high temperature (HPHT) process from graphite phase and furthermore by chemical synthesis (CVD process) from gaseous phases under low pressure and moderate temperatures (see chapter 3 for more information). For device fabrication, HPHT or CVD diamonds can be used as substrate for high quality epitaxial layer growth by CVD process. The two main suppliers of HPHT substrates are Sumitomo from Japan and Element 6 from United Kingdom. Typical sizes available depend on the crystalline orientation : 3×3 mm^2 for [100] oriented plates and 2×2 mm^2 for [111] oriented plates. However, larger substrate sizes up to 8×8mm^2 plates are commercially available. Finally, highly conductive substrates (boron doping) and heteroepitaxial diamond growth (on iridium substrates as example) on larger surfaces are being intensively investigated by several groups.

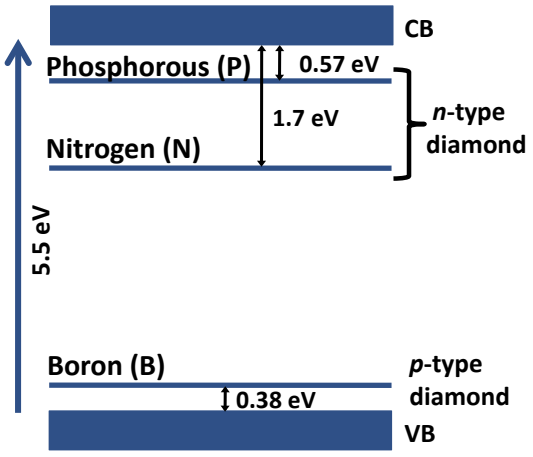

Figure 1.4: Diamond Band diagram together with the main dopants.

1.4.2 General overview

Several groups reported various innovative diamond-based power devices demonstrators using some specific methods to fabricate ever higher performance devices. Since 1997, and the subsequent report of ultraviolet light-emitting pn diodes reported by Koizumi et *al* [Koizumi 2001] in 2001, diamond has been used in a number of, both unipolar and bipolar devices, (*pn* junction [Tavares 2005], Schottky-*pn* diode [Makino 2009], emitting *pin* junction [Makino 2008], bipolar transistors [Kato 2013], field effect transistor [Kawarada 1994]...). This part will summarize the most advanced devices and the main technological breakthroughs overcome for each.

Field Effect Transistor FET: Since high operating frequencies are aimed at for such devices, boron doped diamond is preferentially used because of its higher hole mobility (2000 cm^2/Vs at RT) and lower ionization energy (better electrical conduction) than n-type diamond. However, the ionization threshold of 0.37 eV, is still very high and diamond FET architectures illustrated on Figure 1.5, are designed to benefit from boron doping and to minimize the ON resistance as much as possible.

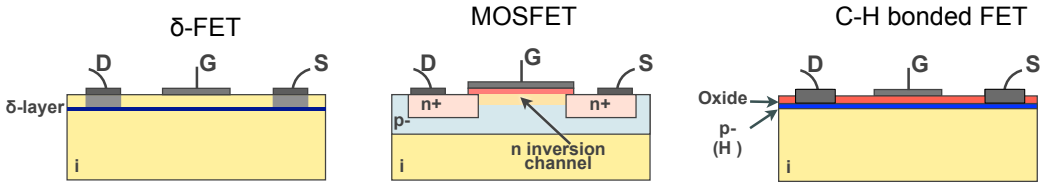

Figure 1.5: Different architectures of diamond field effect transistors (FET) investigated today: delta-FET (left), Metal Oxide Semiconductor FET (MOSFET middle), H-terminated FET (right).

Boron δ-FET (Fig. 1.5, left hand side), which consists of a thin heavily doped (metallic) layer between two intrinsic layers resulting theoretically in high mobility, has been intensively studied by several groups [Elhajj 2008, Tumilty 2009, Chicot 2012, Scharpf 2013, Balmer 2013] : Institut Néel, CEA-LIST, IEMN (France), E6, UCL (United Kingdom), Waseda University (Japan) and Ulm university (Germany). Unfortunately the measured hole mobility in δ-FET is behind expectations and typically lower than 100 cm^2/Vs at room temperature [Chicot 2012, Balmer 2013]. An alternative to δ-FET is Hydrogen-terminated diamond FET (Fig. 1.5, right hand side) using a 2D hole gas at the surface [Kawarada 1994, Hirama 2006, Hirama 2010, Kasu 2012]. Such transistors demonstrate high frequency operation up to 45 GHz. The issue of this architecture was the thermal instability of C-H bonds on diamond surface inducing 2D hole gas at

the surface. This limitation was overcome using an oxide to stabilize the hydrogenated surface [Hiraiwa 2012]. In 2014, Liu et *al* [Liu 2014] reported Ta_2O_5/Al_2O_3 bilayer gate oxide diamond H-FET and Kawarada et *al* [Kawarada 2014] Al_2O_3 gate oxide H-FET for high temperature (400 °C) and high voltage (500 V) operations. Additionally to this promising architecture, the French group where this thesis was prepared, reported a Metal Oxide Semiconductor (MOS) structure on diamond and the possibility to control the holes or electrons density in diamond with a gate voltage [Chicot 2013]. This essential breakthrough opens the door toward high power diamond MOS field effect transistor MOSFET fabrication (Fig. 1.5 center hand side).

Bipolar junction: Among the interesting features of diamond devices, PIN junctions and Schottky diodes are the most advanced and continuously improve in order to fully exploit diamond's superior electrical properties. In 2013, Suzuki et *al* [Suzuki 2013] reported PIN diodes with a sharp and repeatable avalanche breakdown at 920 V (2.3 MV/cm). A high serial resistance leading to low current limited the forward performances of these devices. In 2014, Makino et *al* [Makino 2014] used highly conducting boron doped diamond (p^+) and phosphorous doped diamond (n^-) (Fig. 1.6, left hand side) with hopping conduction to get a low on-resistance and thus enhance the forward current of diamond-based PIN diodes (expending from $\sim 10^{-2}$ A/cm^2 at 10 V to 10^3 A/cm^2). However, this new architecture induced a higher reverse current (from $\sim 10^{-7}$ A/cm^2 at 10 V to 10^{-4} A/cm^2). On the other hand, this new approach has been adopted in the so-called Schottky-*pn* diodes illustrated on Figure 1.6 (center hand side) with an active *n*-type diamond sandwiched between the heavily doped p^+-type diamond and Schottky electrode. For these devices, a forward current of 60000 A/cm^2 at 6 V (specific resistance of 0.03 mΩ.cm^2) was measured and the blocking electric field was 3.4 MV/cm (active *n*-type layer thickness about 160 nm).

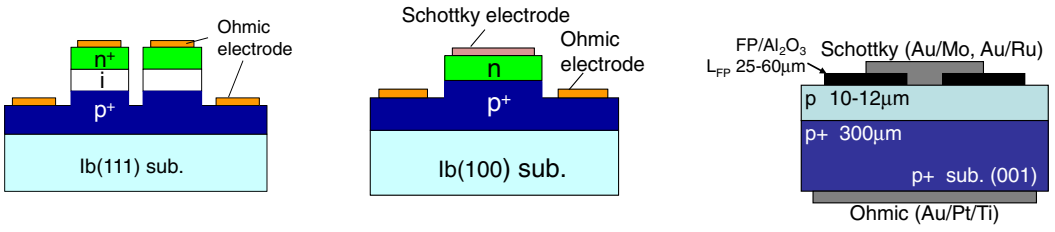

Figure 1.6: Schematic diagram of Schottky p^+-i-n^+ diodes (left) [Makino 2014], Schottky-np diodes (center), and boron doped diamond Schottky diodes (right) [Umezawa 2014].

However, Schottky diodes using boron doping are today the most promising. Their current state of art is schematically illustrated in Figure 1.6 (right hand side). High-current vertically structured diamond Schottky diodes with thick field plates have been demonstrated by Umezawa et *al* [Umezawa 2014]. An Al_2O_3 field plate was deposited (1.8 μm thick) and 1000 $\times$ 1000 μm Schottky electrodes were fabricated. A forward current of 1 A at 4 V was achieved at room temperature and at 250 °C, this current level was reached at 2 V. For large area devices, a maximum blocking voltage of 300 V was reported at 250 °C ($\sim$ 0.3 MV/cm).

1.5 Diamond Schottky diodes

A Schottky diode is a unipolar device using the non-linear current transport behavior of rectifying metal semiconductor junction under applied bias voltage (see Chapter 4). Such a device behaves like a switch triggered by the bias voltage across its terminals. Schottky diodes are used in silicon-based power conversion systems because of their fast recovery time and of their low turn-on voltage (low forward voltage drop) leading to lower power losses and faster switching than conventional PN or PIN junction diodes. Indeed, besides their lower forward voltage drop 0.15 V to 0.45 V (0.6 V - 1.7 V for PN diodes), current transport in Schottky diodes is related to majority carrier contrary to bipolar devices such as PN junction diodes where minority carrier injection in the active area was the main current transport mechanism. Schottky diode can thus switch rapidly from forward to reverse bias without minority carrier storage effects (reverse recovery effects) usually encountered for conventional bipolar silicon based technologies. Schottky diodes are characterized on one hand by their serial resistance and their blocking voltage, both related to semiconductor electrical properties. On the second hand, their forward voltage drop and the reverse leakage current will basically depends on the quality of the rectifying metal-semiconductor interface.

The vertical structure is one of the best geometrical configurations leading to a low serial resistance. This structure is characterized by a vertical electrical current transport through a stack comprising an active layer and a highly conductive substrate (metallic behavior). In "punch through" configuration, the active layer mainly supports the reverse voltage drop due to a negligible depletion region expansion into the highly conductive substrate. The breakdown voltage (BV) and the specific resistance ($R \times S$) in

this geometry are defined as follows:

$$BV = E_M W - qNW^2/(2\epsilon_r) \tag{1.4}$$

$$R \times S \approx W/\sigma + R_{sub} \times S + R_C \times S, with \quad \sigma = qp\mu \tag{1.5}$$

S, q, E_M, W, ϵ_r, N, p, $\sigma, \mu, R_{sub} \times S$, and $R_C \times S$ are the diode section, the elementary charge, the avalanche breakdown field, the drift layer thickness, the dielectric constant, the doping level, the carrier concentration, the drift layer conductivity, the carrier mobility, the specific resistance of the highly conductive substrate, and the specific resistance of the ohmic contacts respectively. In vertical diode configuration, both $R_{sub} \times S$ and $R_C \times S$ have to be negligible compared to the specific resistance of the active layer in order to minimize diode serial resistance. The use of a substrate doped above the metallic transition (degenerate semiconductor) allows generally to meet these requirements. Accordingly, besides the geometrical parameter W (active layer thickness) and S (devices area), the doping level N of diode active layer will define both specific resistance and breakdown voltage. Indeed, a low specific resistance corresponding to a high conductivity will be obtained for a highly doped active layer. Conversely, a highly doped active layer gives rise to a low breakdown voltage. In the case of Si-based devices, where the critical field is lower (0.3 MV/cm), a high blocking voltage implies a high serial resistance.

Moreover, wide band semiconductors such as SiC or diamond (Fig. 1.7), lead to an enhancement of the trade-off between $(R \times S)$ and BV because of their high critical field (3 and 10 MV/cm respectively). For example, a specific resistance of 10^{-2} $\Omega.cm^2$ involves a BV around 300 V for Si and a BV about 3000 V for SiC and diamond. For diamond devices, the specific on state resistance decreases versus temperature opposite to the case of SiC (Fig. 1.7) for a operating temperature of 250 °C. This decrease is explained by the improvement of boron (activation energy 0.38 eV) ionization rate versus temperature (see Chapter 2).

The Schottky diode, compared to other diamond power devices (Bipolar transistor [Kato 2012], junction field effect transistor [Kawarada 1994, Hiraiwa 2012], Schottky-pn diode [Makino 2014, Makino 2009], is the most promising because of the highest breakdown voltage reported (2.5 kV [Twitchen 2004], 6.7 kV [Butler 2003], 10 kV [Volpe 2010], 8-12 kV [Huang 2004]) and because of recent architectural progress to minimize its serial

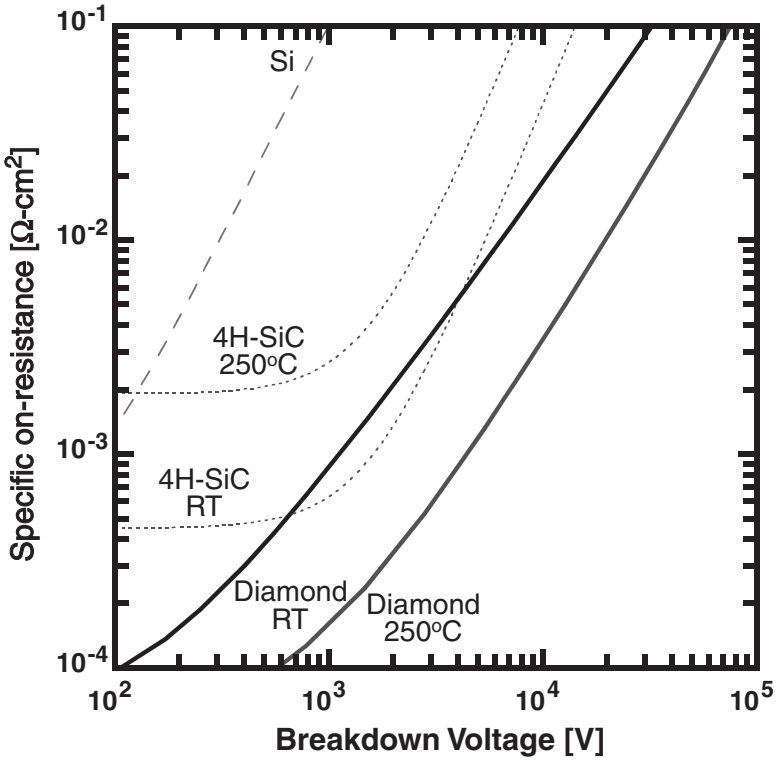

Figure 1.7: Specific on-state resistance and Breakdown voltage [Umezawa 2012] for Si,SiC and diamond vertical Schottky diodes.

resistance. Indeed, the high serial resistance of the lightly doped Schottky active layer required to get a high breakdown field is one of the main limitations of such a device. The use of pseudo vertical (with a heavily boron doped buried layer) or vertical architectures (with a heavily boron doped substrate), allowed a significant reduction of the diamond diode serial resistance. The reported forward current for these diodes architectures are higher than 100 A/cm^2. A 1 Ω serial resistance [Umezawa 2013] was recently demonstrated for a vertical diamond Schottky diode operating at 250 °C. However, the breakdown field reached in pseudo vertical and vertical Schottky diodes (2.1 MV/cm [Umezawa 2013], 2.7 MV/cm [Kumaresan 2010]) even with a field plate structure used to avoid the edge field enhancement [Ikeda 2009] are much lower compared to those found for lateral diodes (7.7 MV/cm [Volpe 2010]) and to the very first value reported for bulk diamond (higher than 10 MV/cm) [Landstrass 1993]. It is generally admitted that the main reason of such low breakdown field and high reverse current values of pseudo vertical and vertical diamond Schottky diodes lies in defects such as dislocations which propagate from the heavily boron doped diamond substrate to the active layer [Ohmagari 2011]. On the other hand, diamond Schottky diode performance is closely linked to the thermal and chemical stability of the Schottky contact and to the interface

states density. Schottky metal selection and surface pretreatment are crucial to get low enough barrier heights (low forward voltage drop), low defect density at interfaces and a thermally stable interface (low reverse current).

Aiming to fabricate high performance diamond Schottky diodes, the following chapters will be focused on: (i) the investigation of electronic properties of lightly doped diamond and their dependence on the temperature and on the compensation level, (ii) the geometrical structure adopted, the growth related issues in order to minimize surface and volume defects in diode active layers, (iii) the selection of the Schottky metal, the diamond surface treatment prior to Schottky contact deposition, the electrical characteristics of fabricated devices and their thermal stability.

Chapter 2

Electrical properties of doped diamond

Contents

2.1 Introduction

In this chapter, the transport properties of doped diamond will be introduced in order to establish a useful tool, which allows a rapid evaluation of the resistivity versus doping level and compensation for both p-type and n-type diamond. Besides geometrical considerations (shape, thickness l, area S, etc...) generally chosen to minimize the power devices serial resistance ($Rs = \rho \times l/S$) and so favor high forward currents (see Chapter 4), the most important parameter to enhance the latter is the semiconductor resistivity, which depends on the carrier concentration (p) and the carrier mobility (μ) through $\rho = 1/(qp\mu)$. The high ionization energy of the impurities used to dope diamond, namely Boron for p-type with an activation energy about 380 meV and Phosphorous for n-type with an activation energy about 570 meV, gives rise to a low ionization rate at room temperature and so to a resistive material. Moreover, according to the current situation of electronic grade diamond samples size basically (3×3 mm^2), the processing of diamond power device demonstrators, which may compete with Si or SiC based devices, requires the minimization of doped diamond resistivity as much as possible without excessively altering its outstanding electrical properties.

The common way to improve the conductivity of doped diamond and get a low resistivity is the increase of carrier concentration via a higher doping level or a high operating temperature. However, the carrier concentration enhancement solutions are counterbalanced by a limitation of carrier mobility due to scattering mechanisms as described by low field Hall transport analysis reported by Pernot et *al.* for both n-type [Pernot 2006, Pernot 2008] and p-type diamond [Pernot 2010]. The authors investigated theoretically the temperature dependence of the carrier concentration and their mobility using the charge balance neutrality equation and taking into account all relevant scattering mechanisms which limit the mobility: by phonon scattering, scattering by ionized impurities and neutral impurities. The comparison of experimental data together with theoretical calculations, allowed identifying the limiting scattering mechanisms over a wide temperature range. It was established that the room temperature (RT) carrier mobility in slightly doped diamond (with a low compensation) is related to acoustic phonon scattering thus leading to maximum mobility of 2000 cm^2/Vs for holes and 1030 cm^2/Vs for electrons. Moreover, the RT carrier mobility decreases as a function of dopant density for both n-type and p-type, due to neutral impurities scattering. On the other hand, a high compensation level reduces the mobility values as result of the scattering by ionized impurities [Pernot 2008, Pernot 2010]. At high temperature,

carrier mobility is limited by lattice scattering namely, optical phonon for p-type diamond and intervalley phonon for n-type diamond. These works provided the theoretical background and mathematical tools as well as the empirical parameters (acoustic deformation potential, effective coupling constant for optical phonon,) needed to evaluate theoretically the Hall carrier mobility in doped diamond in large range of temperature, doping level, and compensation.

This chapter is a direct follow up of previous works reported in references [Pernot 2008, Pernot 2010]. We will attempt to establish a full picture of the main transport properties (mobility, carrier density, and resistivity) versus doping and compensation level at 300 K and 500 K for both n-type and p-type diamond. This works aims at defining the best trade-off range between all for the intended field of application (high power or high frequency). The analytical Hall transport model reported by Pernot et *al*. [Pernot 2010, Pernot 2008] and its main results will be introduced first. The carrier concentration, carrier mobility, and resistivity will then be calculated using this analytical model and compared to the experimental data reported in literature. Finally, each of these main transport properties will be plotted versus doping level and compensation ranging from 10^{14} to 10^{20} cm^{-3} at 300 K and 500 K.

2.2 Boron doped diamond (p-type)

2.2.1 Theoretical background

Hole transport in diamond occurs mostly within the three uppermost valence bands namely: the light holes (lh) and heavy holes (hh) bands degenerated at the Γ point of the Brillouin zone and the spin-orbit splitter (so) band positioned at 13 meV below these latters [Willatzen 1994]. For the calculations performed here and for those reported in ref [Pernot 2010, Pernot 2006], this small energy splitting was overlooked and the three bands are considered as degenerated at the Γ point of the Brillouin zone. Moreover, the three valence bands are considered to be parabolic with representative effective masses of Ref [Willatzen 1994]: m_{hh}^{*100}=0.427 m_0, m_{hh}^{*110}=0.69 m_0 for the heavy holes, m_{lh}^{*100}=0.366 m_0, m_{lh}^{*110}=0.276 m_0 for the light holes and m_{so}^{*}=0.394 m_0 for the spin-orbit holes. The corresponding values for the density of state mass are $m_{hh}^{*} = ((m_{hh}^{*110})^2 m_{hh}^{*100})^{1/3} = 0.588\ m_0$ and $m_{lh}^{*} = ((m_{lh}^{*110})^2 m_{lh}^{*100})^{1/3} = 0.303\ m_0$. Finally, to compute the position of the Fermi level for a given free hole population, we get the total density of state mass $m^* = (m_{lh}^{*3/2} + m_{hh}^{*3/2} + m_{so}^{*3/2})^{2/3}$= 0.908 m_0. The carrier concentration (p) is then determined using the charge balance neutrality equation in the general case of Fermi distribution [Pernot 2001] and the mobility (μ) is evaluated using the classical multi-band equations:

$$\mu_H = \frac{p_{hh}\mu_{hh} + p_{hl}\mu_{hl} + p_{so}\mu_{so}}{p_{hh} + p_{hl} + p_{so}}, \tag{2.1}$$

p_i ($i = l, h, so$) in which lh, hh and so refer to the light, heavy and spin-orbit holes concentration and μ_i to their mobility respectively. Moreover, this last expression is simplified since the Hall scattering factor r_H is approximated to unity (see ref [Pernot 2010] for the general expression and the motivations for this last assumption). On the other hand, the mobility μ_i is calculated using the relaxation time approximation $\mu_i = e\overline{\tau_i}/m^*$, where $\overline{\tau_i}$ is average value of the total relaxation time evaluated using the Matthiessen rule:

$$\frac{1}{\overline{\tau_i}} = \sum_n \frac{1}{\tau_{in}}, \tag{2.2}$$

in which τ_{in} is the relaxation time assigned to scattering mechanism n for each band i. Four main hole scattering mechanisms have been considered : ionized impurity scattering (ii), neutral impurity scattering (ni), acoustic phonon scattering (ac) and non-polar optical phonon scattering (op). The expression of relaxation times corresponding to the different scattering mechanisms enumerated above are reported in reference [Pernot 2010].

2.2.2 Temperature dependence of hole density and mobility

Figure 2.1 shows the typical hole concentration and mobility temperature dependence obtained by Hall effect measurements for lightly boron doped diamond. These results were reported by Volpe et *al*. [Volpe 2009b] for diamond epitaxial layers (epi-layer) grown on Ib HPHT substrate using a similar reactor (homemade NIRIM type reactor, see Chapter 3) and quasi identical growth conditions than those of the epi-layers grown during this thesis for Schottky diodes devices fabrication.

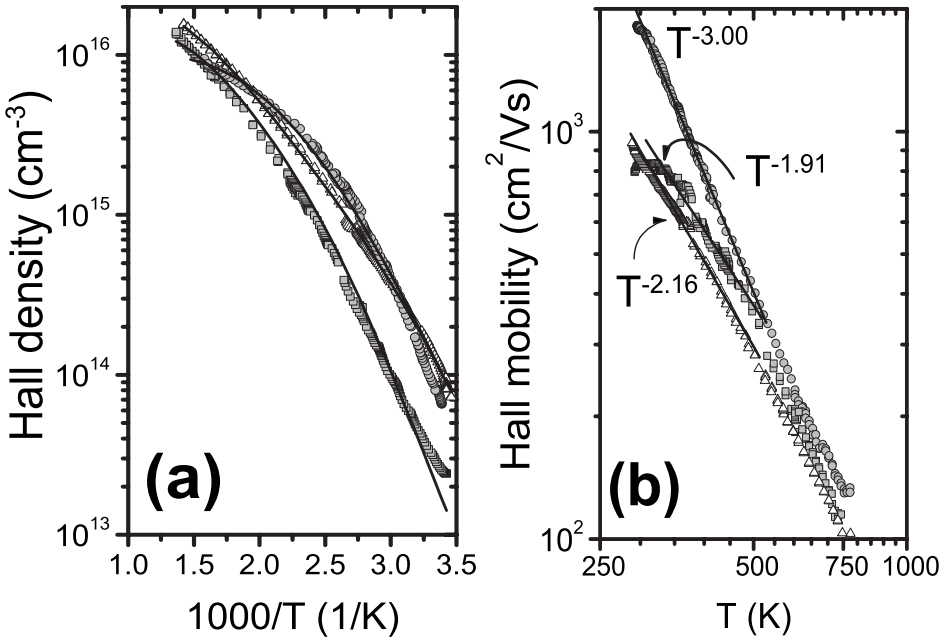

Figure 2.1: Temperature dependence of the Hall hole density (a) and mobility (b) of slightly boron doped diamond layers reported by Volpe et al [Volpe 2009b]. The doping level were ranging between 10^{16} *cm*$^{-3}$ *and* 5×10^{16} *cm*$^{-3}$ *and the compensation between* 10^{14} *cm*$^{-3}$ *and* 5×10^{15} *cm*$^{-3}$.

For these epi-layers where high RT hole mobility were measured (up to 1870 cm^2/Vs), boron concentration was ranging from 10^{16} cm^{-3} and 5×10^{16} cm^{-3}. On the other hand, the compensation varied between 10^{14} cm^{-3} and 5×10^{15} cm^{-3}. Hole concentration increases at high temperature because of the thermal ionization of boron acceptors. Even for these relatively low doping levels, only the ionization regime is observed for the selected measurement temperature range (from 300 K to 750 K). The full boron ionization regime (exhaustion regime where $p = N_A - N_D$) occurs at temperatures above 750 K due to the high ionization energy of boron (0.38 eV). Conversely, the mobility is $T^{-\alpha}$ dependent ($\alpha > 0$). This feature commonly encountered for most of semiconductors is related to the phonon scattering mechanisms. For lightly doped diamond ($N_A \leq 10^{17}$ cm^{-3})

with a low compensation level ($N_A \leq 10^{15}$ cm^{-3}) as shown on Figure 2.2 [Pernot 2010], the RT hole mobility is limited by acoustic phonon scattering. Noting that the relaxation time of this mode is proportional to $\rho_m v_{\parallel}^2/(m^{*3/2}C_a^2)$, where $C_a = 8$ eV is the acoustical deformation potential, $\rho_m = 3515$ kg.m^{-3} the crystal mass density, and $v_{\parallel} = 17536$ m.s^{-1} the velocity of longitudinal phonon. Its was then established that the RT hole mobility in boron doped diamond (2000 cm^2/Vs) is higher than the other semiconductors in column IV (for both electron and hole). Indeed, the high crystal mass density of diamond counterbalances the relatively large C_a (8 eV compared to 5 eV for silicon) and the density of states effective mass (0.908 m$_0$ compared to 0.81 m$_0$ for silicon) in case of p-type material. For phosphorous doped diamond, i.e. n-type diamond, since the RT electron mobility in slightly doped and low compensating materials is still limited by the (ac) scattering mode, the maximum electron mobility of 1000 cm^2/Vs is two times lower than the hole mobility, mainly due to the acoustic deformation potential being higher for n-type diamond ($C_a = 17.5$ eV).

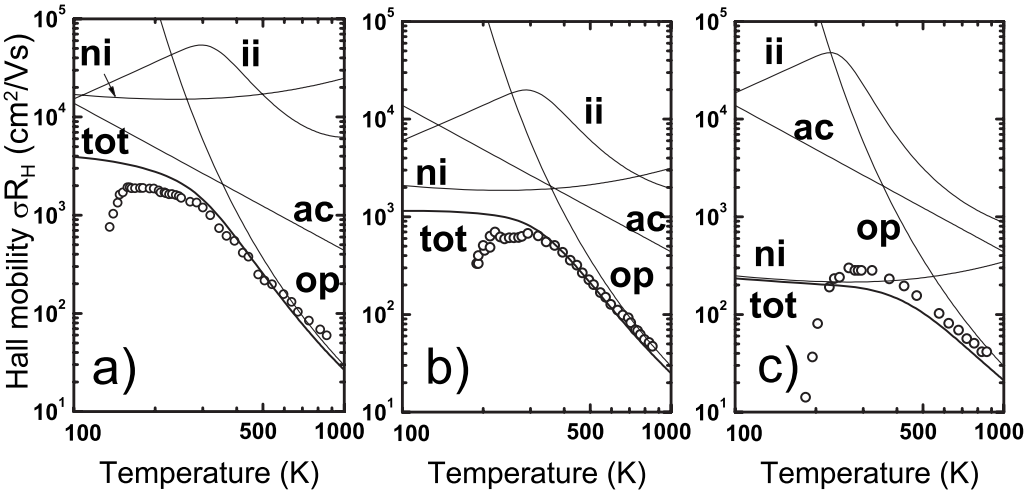

Figure 2.2: Temperature dependence of the Hall mobility in boron doped diamond together with the scattering modes (ionized impurities ii, neutral impurity ni, acoustic phonon ac, and optical phonon op) reported in reference [Pernot 2010]. The term tot denotes the theoretical moblity taking into account all the scattering processes. Experimental data are illustrated by symbols: (a) $N_A = 2.5 \times 10^{17}$ cm^{-3} and $N_D = 10^{15}$ cm^{-3}, (b) $N_A = 2 \times 10^{18}$ cm^{-3} and $N_D = 3 \times 10^{15}$ cm^{-3}, (c) $N_A = 1.7 \times 10^{19}$ cm^{-3} and $N_D = 5 \times 10^{15}$ cm^{-3}.

Moreover, at high temperature, the hole mobility in diamond is limited by optical phonon scattering. The key parameter in this scattering mode is the optical phonon energy, about 165 meV in diamond (63 meV for silicium), which explains the larger mobility of holes in diamond at high temperature (300 cm^2/Vs [Pernot 2010] at 500 K) in comparison to electrons in Si (150 cm^2/Vs [Dorkel 1981] at 500 K) and 4H-SiC (30 cm^2/Vs

[Pernot 2005] at 500 K). This is due to the lower phonon population in diamond (high phonon energy). On the other hand, the neutral impurities scattering mode starts to be the limiting mode at RT when the boron acceptor concentration increases as shown on Figure 2.2 b) for $[B] = 2\times10^{18}$ cm^{-3} and Figure 2.2 c) for $[B] = 1.7\times10^{19}$ cm^{-3}. Accordingly, the maximum RT hole mobility in case of uncompensated diamond, is governed by the lattice scattering (ac+op mode) for a doping level lower than 10^{17} cm^{-3}. Above this upper doping limit, the mobility tends to decrease because of neutral impurities scattering [Pernot 2010].

2.2.3 Hole density and mobility versus doping level (N_A) and compensation (N_D)

2.2.3.1 Experimental setup

The analytical model previously described, highlights the main mechanisms governing hole mobility over various temperatures ranges. A maximum RT hole mobility of 2000 cm^2/Vs is predicted for uncompensated slightly doped diamond layer due to lattice scattering related intrinsic diamond properties. This is well illustrated in Figure 2.3 where the theoretical hole density, hole mobility, and resistivity obtained for different doping levels N_A (10^{15} cm^{-3}, 10^{16} cm^{-3}, 10^{17} cm^{-3}, 10^{18} cm^{-3}, and 10^{19} cm^{-3}) are plotted assuming a similar compensation level ($N_D = 10^{14}$ cm^{-3}).

At room temperature (RT), the hole density rises from 10^{13} cm^{-3} to 5×10^{15} cm^{-3} when N_A varies from 10^{15} cm^{-3} to 10^{19} cm^{-3}. Moreover, the temperature dependence of hole mobility is not affected by acceptor concentration variation if N_A lower than 10^{17} cm^{-3}. As previously discussed, the mobility of holes is limited by lattice scattering (ac+op mode defined by diamond intrinsic properties) in the case of uncompensated lightly doped diamond [Pernot 2010]. At RT, a hole mobility of 1800 cm^2/Vs (related to acoustic phonon scattering [Pernot 2010]) should be achieved if the doping level is lower than 10^{17} cm^{-3} and the compensation about 10^{14} cm^{-3}. At high temperature, for example 600 K where the full ionization of boron acceptors (exhaustion regime where $p = N_A - N_D$) occurs, hole mobility is limited by optical phonon scattering [Pernot 2010] and a 130 cm^2/Vs mobility should be obtained. On the other hand, the neutral impurities scattering starts to be the limiting mode at RT when $N_A \geq 10^{17}$ cm^{-3}. For $N_A = 10^{19}$ cm^{-3} (for example), the RT hole mobility drops from 1800 cm^2/Vs ($N_A \leq 10^{17}$ cm^{-3}) to 300 cm^2/Vs. At high temperature, the optical phonon scattering is enhanced and a lower mobility is

obtained for heavily doped diamond as shown on Figure 2.3.

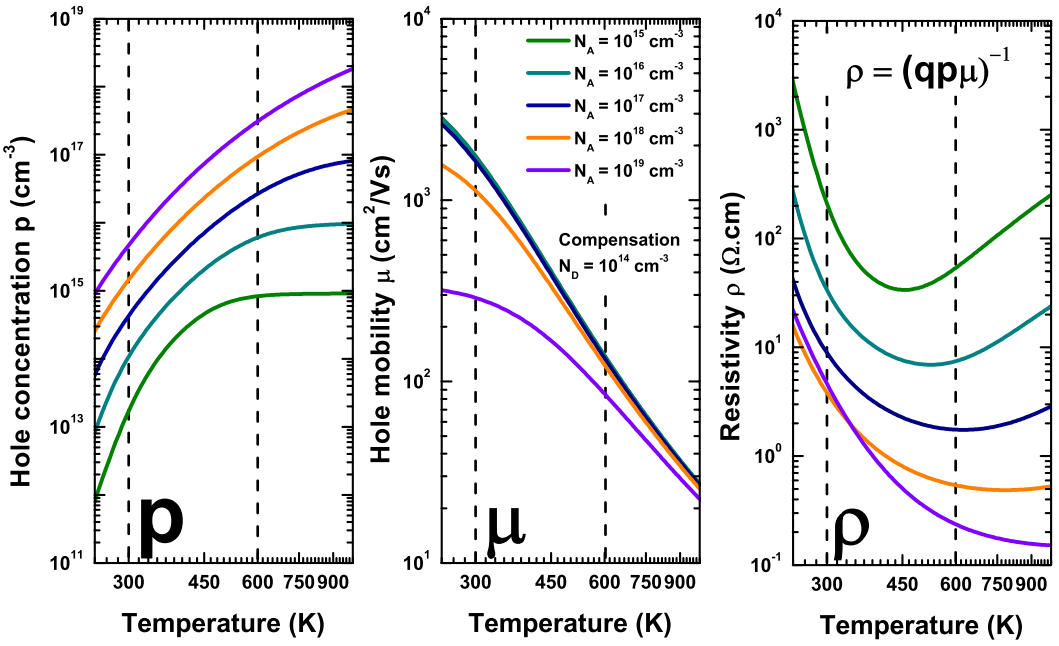

Figure 2.3: Theoretical hole density (left), hole mobility (middle), and resistivity (right) calculated for different acceptor concentration N_A and a constant compensation level N_D using the analytical model reported in reference [Pernot 2010].

Using these theoretical hole concentrations and their mobility, the temperature dependence of doped diamond resistivity ($\rho = (qp\mu)^{-1}$) has been calculated. Figure 2.3 shows the expected resistivity profile for each N_A. The temperature dependence of mobility is characterized by: (i) a decrease stage due to the thermal ionization of boron acceptors, (ii) a minimum value when the exhaustion regime is reached (full boron ionization), and (iii) an increase stage related to hole mobility diminution versus temperature (constant hole concentration in exhaustion regime). These different stages can be observed on Figure 2.3 for lightly doped diamond ($N_A \leq 10^{17}$ cm^{-3}) where the exhaustion regime arises below 700 K. Thus, a minimum resistivity should be obtained between 450 K and 600 K if $N_A \leq 10^{17}$ cm^{-3}. For heavily doped diamond ($N_A \geq 10^{17}$ cm^{-3}), the thermal ionization of boron acceptors occurs over the whole temperature range (from 300 K to 1000 K) and the resistivity decreases with temperature in all cases. However, Figure 2.3 shows that the resistivity of diamond doped at 10^{19} cm^{-3} should be higher than that obtained for $N_A = 10^{18}$ cm^{-3} when the temperature is lower than 320 K. This is a consequence of the constant boron ionization energy assumption made for these calculations. For boron doped diamond, the metallic transition happens around a doping level of 5×10^{20} cm^{-3} [Klein 2007]. The acceptor band broadening leading to a apparent lower ionization energy as shown on Figure 2.4 [Fiori 2012], can not be neglected for

$N_A > 10^{17}$ cm^{-3}.

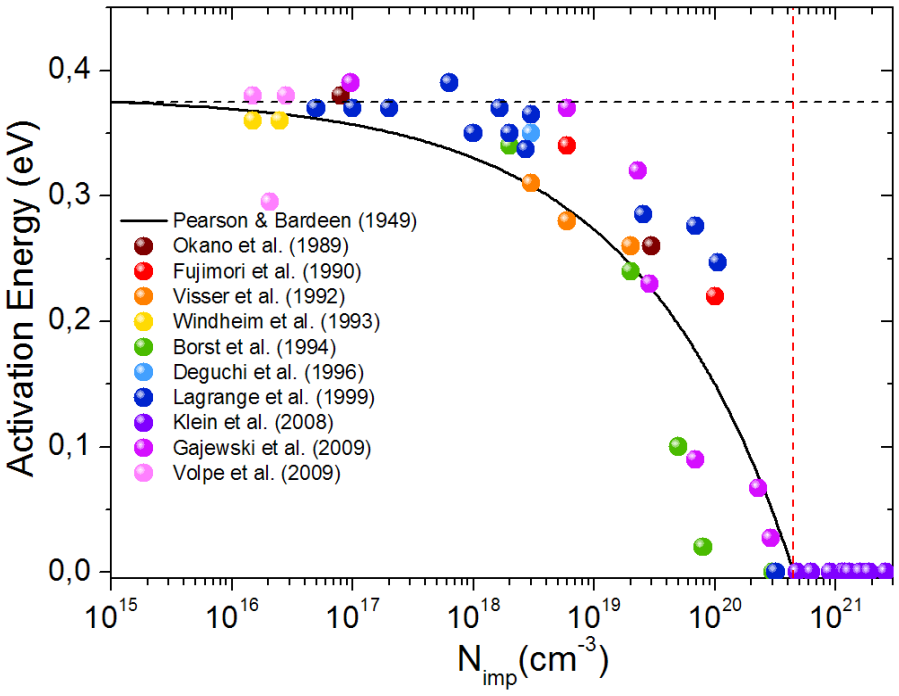

Figure 2.4: Activation energy as function of boron incorporation reported in the literature [Fiori 2012]. The solid line is the Pearson-Bardeen fitting model: $E_a = E_{a0} - a \times N_{imp}^{1/3}$, $E_{a0} = 0.38$ *eV*, $a = 4.7877 \times 10^{-8}$ *eVcm*.

Additionally to this requirement, i.e. including the ionization energy diminution versus acceptor concentration N_A, the electrical properties discussed above are affected by a high compensation level. This is illustrated on figure 2.5 where the temperature dependence of hole density, hole mobility, and the resistivity are calculated for an acceptor concentration of 10^{16} cm^{-3} with different compensation levels. For a compensation ratio k ($k = N_D/N_A$) lower than 10 %, the hole density and mobility versus temperature can be considered as unchanged. Above this compensation ratio limit, both hole density and mobility decrease. For example, for k values around 80 %, the RT hole density decreases from 10^{14} cm^{-3} ($k \leq 10\%$) down to 10^{12} cm^{-3}. The RT hole mobility drops from 1800 cm^2/Vs to a value lower than 1000 cm^2/Vs due to ionized impurities scattering. The resistivity is therefore much higher than that of the uncompensated material. The high temperature mobility is not affected by a high compensation since identical features are obtained.

Aiming to investigate the influence of the doping level and compensation over wide doping and compensation ranges, the hole density and mobility were calculated for N_A and N_D ranging from 10^{14} cm^{-3} to 10^{20} cm^{-3}. These calculations were done for room

temperature (300 K) and 500 K operation. The theoretical curves are compared to experimental data reported by several authors for epi-layers grown on (100)-oriented diamond substrates. Boron ionization energy diminution versus N_A was taken into account using the Pearson and Bardeen model established by fitting experimental ionization energies as shown on Figure 2.4 [Fiori 2012].

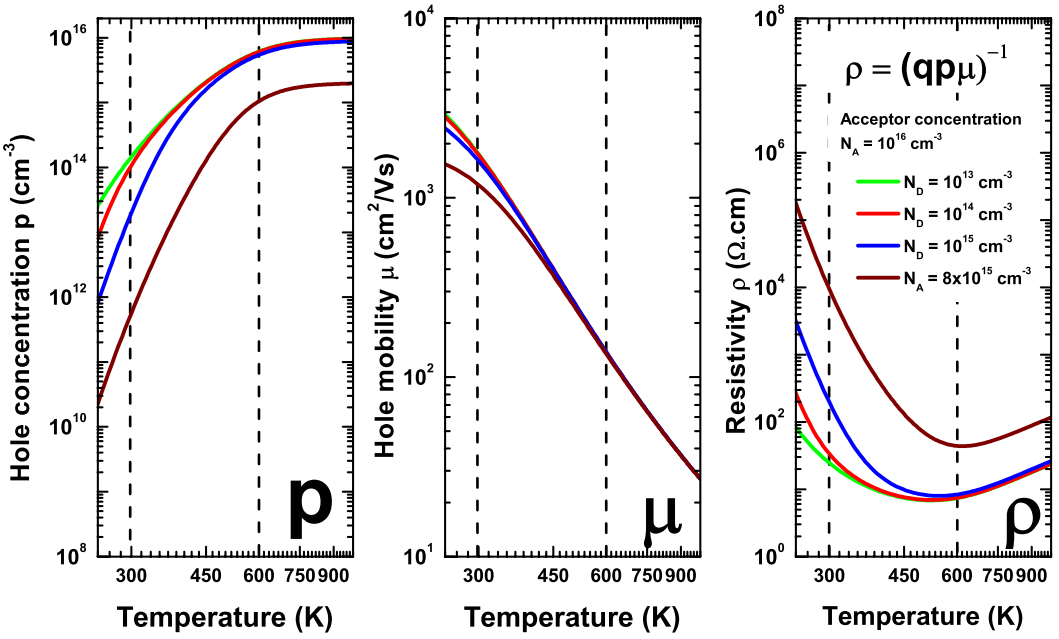

Figure 2.5: Theoretical hole density (left), mobility (center), and resistivity (right) calculated at a constant acceptor concentration N_A with various compensation levels N_D using the analytical model reported by Pernot et al [Pernot 2010].

2.2.3.2 Hole density versus N_A and N_D

Figure 2.6 shows the theoretical hole density versus N_A and N_D at 300 K and 500 K. A filled contour plot was adopted. For such a plot, an isovalue, i.e. a constant hole density regardless of doping level and compensation, is described by a given color corresponding to a value indicated on a color bar (left side). Moreover, for a given acceptor concentration N_A, the calculations are performed for compensation level N_D ranging between 10^{14} cm^{-3} and N_A. This upper limit ($N_D = N_A$ a full compensated material) similar to an undoped material, delimits an uncolored triangle area where the material may be considered as n-type ($N_D > N_A$). On the other hand, the theoretical hole density versus N_A and N_D are plotted together with symbols corresponding to experimental data reported by various authors for boron doped diamond layer. The value of each symbol is indicated by its face color according to the color bar located on the left side. Thus, a discrepancy between the theoretical calculation and the experimental data

can be rapidly depicted by a color contrast. This type of illustration will be adopted for all theoretical calculations discussed in this chapter (density, mobility, and resistivity).

The theoretical hole density profiles at 300 K and 500 K shown on Figure 2.6 are in good agreement with the experimental data reported by Volpe et *al* [Volpe 2009b], Gabrysch et *al* [Gabrysch 2008], Werner et *al* [Werner 1997], and Tsukioka et *al* [Tsukioka 2006]. For uncompensated p-type diamond ($N_D \leq 10^{14}$ cm^{-3}), the ionization rate (p/N_A) is about 1 % at RT and less than 0.1 % if the compensation ratio k ($k = N_D/N_A$) is higher than 10 %. For example, at a doping level of 10^{17} cm^{-3}, a RT hole density of 10^{15} cm^{-3} may be obtained for a compensation of 10^{14} cm^{-3} ($k = 0.1\%$) and the RT density drops to 10^{14} cm^{-3} for a compensation of 10^{16} cm^{-3} ($k = 10\%$).

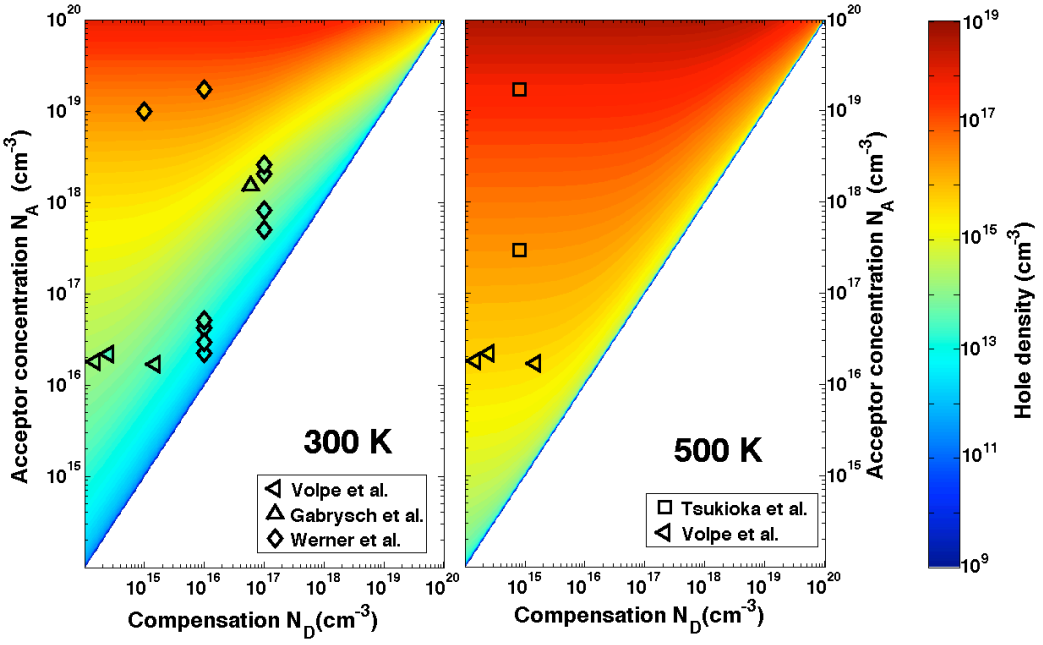

Figure 2.6: Theoretical hole density as function of acceptor concentration and compensation at 300 K and 500 K. The symbols are experimental data reported by Volpe et al [Volpe 2009b], Gabrysch et al [Gabrysch 2008], Werner et al [Werner 1997], and Tsukioka et al [Tsukioka 2006]

At high temperature (500 K), the ionization rate is enhanced. For acceptor concentrations lower than 10^{17} cm^{-3}, the exhaustion regime is reached. In this regime, where acceptors are fully ionized, the hole density p is equal to $N_A - N_D$ thus leading to ionization rate of $1 - N_D/N_A$. In case of low compensated materials ($N_D << N_A$), the ionization rate is therefore 100 % i.e. all acceptor atoms will introduce a carrier in the valence band ($p \approx N_A$). This is well illustrated on Figure 2.4 where for a doping level of 10^{16} cm^{-3}, hole density at 500 K is about 10^{16} cm^{-3} when the compensation is lower than 10^{15} cm^{-3}. Above this limit, acceptors compensation significantly reduces hole

density leading then to a lower value than previously. For a doping level higher than 10^{17} cm^{-3}, the exhaustion regime occurs at temperature higher than 500 K, and the ionization rate is approximately 10% for a compensation ratio below 10 %.

In summary, the theoretical hole density profile versus N_A and N_D established a compensation limit around 10 % of the acceptor concentration beyond which p-type diamond RT carrier density decreases due to compensation effect. For a compensation lower than this limit, p-diamond behaves like an uncompensated material at room temperature and 500 K where the exhaustion regime is reached for a doping level below 10^{17} cm^{-3}.

2.2.3.3 Hole mobility versus N_A and N_D

As for hole density reported above, the theoretical hole mobility profile versus acceptor concentration and compensation was established for 300 K and 500 K (Fig.2.7). At room temperature, the theoretical curve predicts a maximum mobility of 2000 cm^2/Vs for N_A lower than 10^{17} cm^{-3} and a compensation N_D below 10^{15} cm^{-3}. For a doping level and a compensation out of these ranges, the RT mobility tends to decrease due to neutral and ionized impurities scattering [Pernot 2010]. For instance, the mobility drops from 2000 to 250 cm^2/Vs when the doping level increases from 10^{16} cm^{-3} to 10^{19} cm^{-3} due to neutral impurities scattering in the case of uncompensated materials ($N_D \leq 10^{14}$ cm^{-3}). Conversely, for a given N_A such as 10^{17} cm^{-3}, hole mobility is two times lower for a compensation level equal to 10^{14} cm^{-3} ($\sim$ 1800 cm^2/Vs) than for 10^{16} cm^{-3} ($\sim$ 900 cm^2/Vs) because of ionized impurities limitation. Moreover, this observation can be generalized for $N_A \geq 10^{16}$ cm^{-3} as a 10% compensation induces a mobility two times lower than the maximum value expected for uncompensated material.

Moreover, the experimental RT hole mobility reported by different authors [Volpe 2009b, Gabrysch 2008, Werner 1997, Tsukioka 2006] matches well the theoretical mobility values, except for a few samples. Two kinds of discrepancies appear: a lower mobility than the theoretical calculations (for example values with $N_D = 10^{17}$ cm^{-3} also reported by Werner et *al* [Werner 1997] see Fig.2.7) and sometimes a higher experimental value than the theoretical one (as example values with $N_D = 7 \times 10^{18}$ cm^{-3} reported by Werner et *al* [Werner 1997] confer Fig.2.7). These discrepancies may result from a wrong acceptor concentration or a wrong compensation level (or both) for these experimental data. However, another hypothesis would be that the set of scattering processes considered in our calculations is not compete enough.

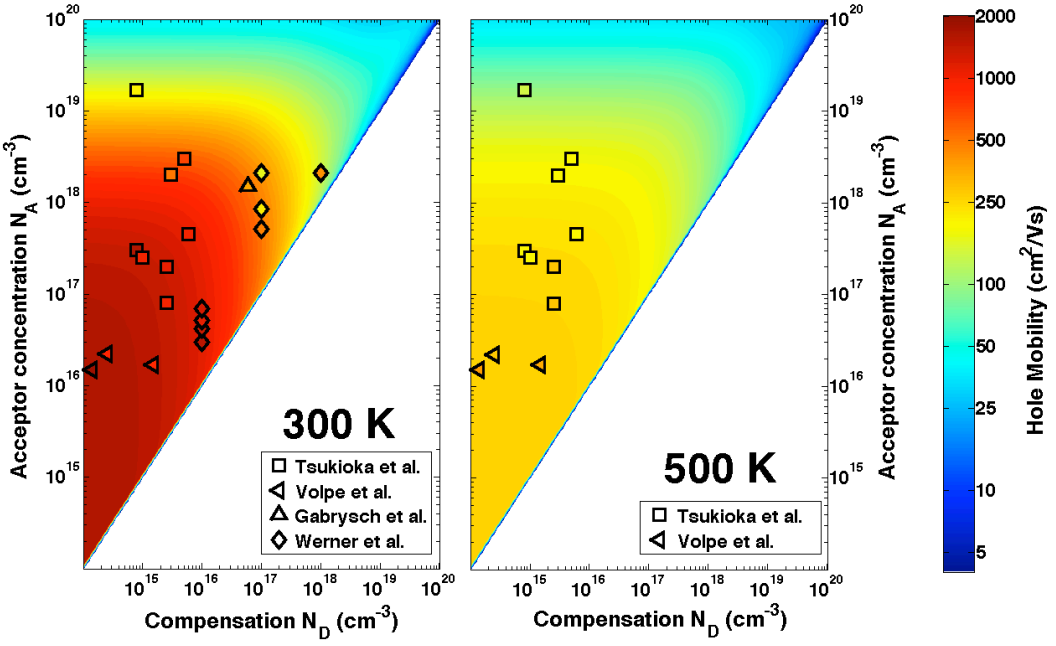

Figure 2.7: Theoretical hole mobility as function of acceptor concentration and compensation at 300 K and 500 K. The symbols are experimental data reported by Volpe et al [Volpe 2009b], Gabrysch et al [Gabrysch 2008], Werner et al [Werner 1997], and Tsukioka et al [Tsukioka 2006].

It has to be noticed that only few experimental data do not match the theoretical maps curves. For the majority of these data, a good agreement is obtained even at high temperature, as shown on Figure 2.7 where the theoretical mobility profile at 500 K is plotted together with experimental data (left hand graph). Optical phonon scattering is the limiting mechanism at high temperature for slightly doped layer. Accordingly, the mobility is about 300 cm^2/Vs for a doping level below 10^{17} cm^{-3} even for high compensation ratios (above 10%). For N_A higher than this limit, the influence of neutral impurities starts to be noticeable thus inducing a mobility degradation. This doping level situation may be considered as insensitive to the compensation if the compensation ratio is under 10 %.

2.2.4 *p*-type diamond resistivity as a function of N_A and N_D

Figure 2.8 shows the *p*-type diamond resistivity versus N_A and N_D at 300 K and 500 K. For the doping range and compensation values previously defined as leading to the highest RT mobility (2000 cm^2/Vs) i.e. when doped diamond behaves as an uncompensated material ($N_A \sim 10^{15}$ cm^{-3} to 10^{17} cm^{-3} and 10^{14} $cm^{-3} \leq N_D \leq 10^{16}$ cm^{-3}), the RT resistivity is ranging from 100 and 10 Ω.cm. At 500 K, it decreases to values

between 30 and 1 Ω.cm. Away from this ideal N_A range, the resistivity is enhanced for low compensation level because of a higher carrier density which counterbalances the low carrier mobility related to neutral impurities scattering [Pernot 2010].

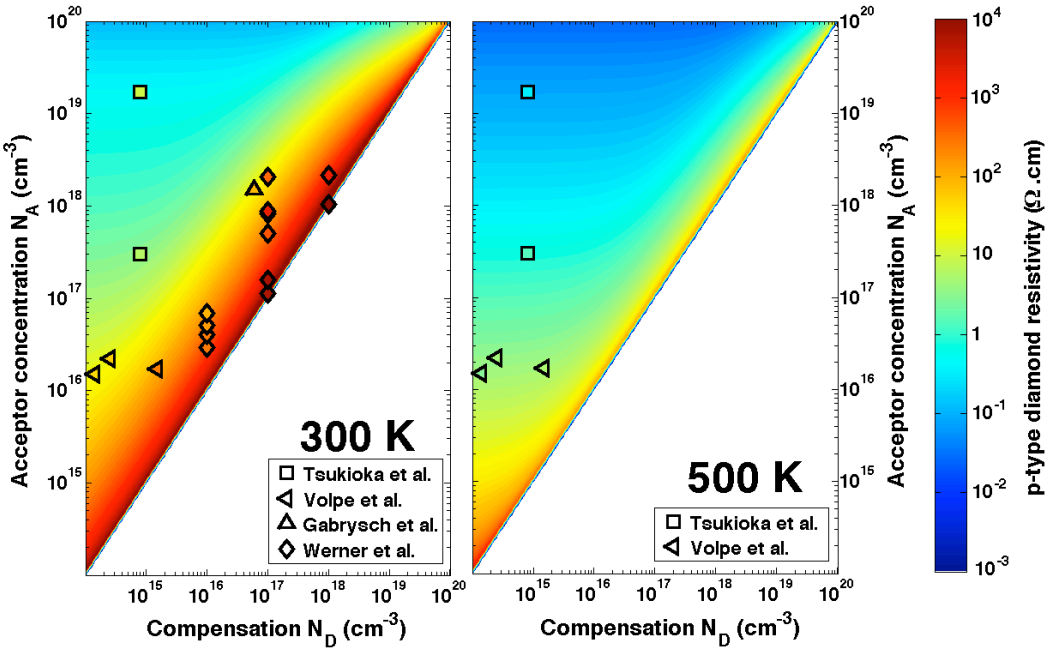

Figure 2.8: Calculated p-type diamond resistivity as function of acceptor concentration and compensation at 300 K and 500 K. The symbols are experimental data reported by Volpe et al [Volpe 2009b], Gabrysch et al [Gabrysch 2008], Werner et al [Werner 1997], and Tsukioka et al [Tsukioka 2006].

2.3 Phosphorous doped diamond (n-type)

2.3.1 Experimental setup

In this section, the electrical properties of n-type diamond will be calculated using an identical approach as discussed previously for p-type material. These calculations will be undertaken using the model [Pernot 2006, Pernot 2001] for n-type diamond. Electron densities versus donor concentration (N_D) and compensation (N_A) will be first calculated using the neutrality equation [Pernot 2001] and a constant ionization energy ($E_d = 0.58$ eV) of phosphorous over the whole doping range ($10^{14} \leq N_D \leq 10^{20}$ cm^{-3}). For highly phosphorous doped layers, the classical way to estimate E_d consisting to fit the temperature dependence of Hall carrier density, is no more appropriated due to hopping mechanism present at relatively high temperature [Matsumoto 2014, Makino 2014]. The reported phosphorous ionization energy calculated taking into account the hopping mechanism, may be considered as constant when the doping level is below 10^{20} cm^{-3} as reported in these references [Matsumoto 2014, Makino 2014]. This is commonly explained as the consequence of the small Bohr radius of phosphorous in diamond which does not favor the electrons wave functions overlapping inducing the impurities band broadening (ionization energy diminution versus doping level). The metal insulator transition has never been observed in n-type diamond.

Additionally to electron density calculation, the theoretical electron mobility versus donor concentration and compensation will be established taking into account the main relevant scattering modes described in Reference [Pernot 2006]: intravalley acoustic phonons (ac), intervalley phonons (iph), ionized impurities (ii) and neutral impurities (ni). As for p-type diamond, the room temperature electron mobility of lightly doped material is limited by acoustic phonon scattering modes. As discussed for p-type doping, this mode depends on crystal mass density ρ, the density of states effective mass m^*, and the acoustic deformation potential C_a. The high value m^* and/or C_a favors a low mobility whereas the high crystal mass density may induces a high mobility ($\mu_{ac} = e\tau_{ac}/m^*$, $\tau_{ac} \propto \rho v_{\|}^2/(m^{*3/2}C_a^2)$) [Pernot 2001, Pernot 2010].
The high RT hole mobility (2000 cm^2/Vs) in diamond is related to its crystal mass density (3515 kgm^{-3}) which counterbalances the influence of m^* and C_a [Pernot 2010]. For n-type diamond, the maximum RT electron mobility is about 1000 cm^2/Vs. This relatively low electron mobility compared to that of holes in diamond, is basically due to the higher acoustic deformation potential C_a for electrons (17.5 eV) than for holes (8

eV). It should be mentioned that electron mobility limitations due to this (ac) scattering mode occurs over a wide temperature range as shown on Figure 2.9 for phosphorous doped diamond with $N_D = 6.8 \times 10^{16}$ cm^{-3} and $N_A = 8.8 \times 10^{15}$ cm^{-3}. (ac) scattering is predominant until to 700 K. Above this temperature, the mobility is governed by inter valley (iph) scattering. On the other hand, the influence of high phosphorous incorporation (high doping level) together with compensation effects on the electron mobility has been already reported [Pernot 2008]. As discussed for p-type doping, the neutral and ionized impurities scattering modes are enhanced by doping and/or by compensation, leading to a lower mobility value than that of uncompensated and slightly doped n-type diamond [Pernot 2008]. Thus, the variations of the RT electron mobility versus N_D and N_A were established in reference [Pernot 2008].

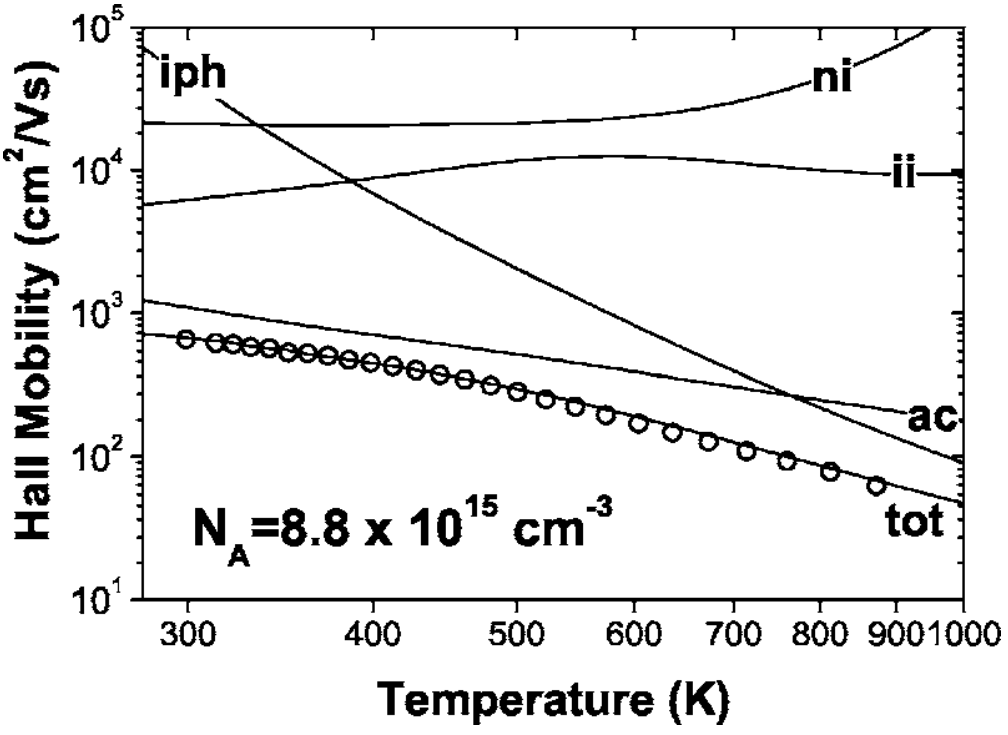

Figure 2.9: Temperature dependence of electron mobility in phosphorous doped diamond ($N_D = 6.8 \times 10^{16}$ cm^{-3}, $N_A = 8.8 \times 10^{15}$ cm^{-3}) together with the contributions of the scattering modes (ionized impurities ii, neutral impurity ni, acoustic phonon ac, and intervalley phonon iph) [Pernot 2010].

Such a mobility simulation has been performed again in this work aiming to evaluate the n-type diamond resistivity as function of donor concentration and compensation level. The theoretical electron concentration (n) and their mobility (μ_n) has been first computed for N_D and N_A ranging between 10^{14} cm^{-3} and 10^{20} cm^{-3}. The theoretical calculations have been undertaken for room temperature and 500 K and furthermore

compared to experimental data of phosphorous doped diamond films grown on synthetic diamond (111)-oriented substrates and measured by Satoshi KOIZUMI at the National Institute for Materials Science NIMS. The growth conditions of these layers are described in reference [Koizumi 2006]. The phosphorous concentration (N_D) and the compensating center density (N_A) are obtained from the fit of experimental Hall electron densities using the neutrality equation for each sample [Pernot 2008]. The theoretical and experimental values of electron concentration (n) and mobility (μ_n) are compared at 300 K and 500 K for a donor concentration (N_D) and compensation (N_A) ranging between 10^{14} and 10^{20} cm^{-3}. Finally, the resistivity maps are calculated and discussed.

2.3.2 Electron concentration

Figure 2.10 shows the theoretical electron concentration versus N_D (donor concentration) and N_A (compensation) at 300 K and 500 K together with symbols (circle) corresponding to the experimental data obtained for phosphorous doped diamond layer grown on (111)-oriented Ib substrate [Koizumi 2006, Pernot 2008].

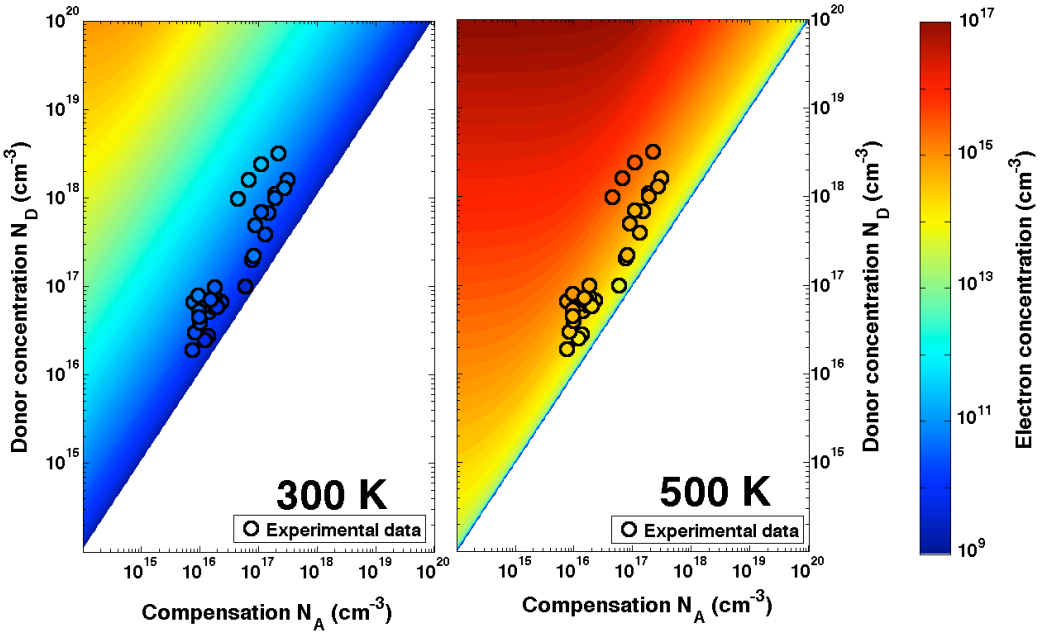

Figure 2.10: Theoretical electron densities as a function of donor concentration and compensation at 300 K and 500 K. The symbols are experimental data reported in reference [Pernot 2008].

At RT and 500 K, the theoretical electron density profiles are in good agreement with the experimental data. Moreover, the correlation between the doping level and the compensation reported in reference [Pernot 2008] was demonstrated again since n stays

relatively constant (same color means constant value) when N_D increases. For the experimental data discussed here, the donor density increase is counterbalanced by a higher compensation level in such a way that an identical carrier concentration is always obtained. For uncompensated n-type diamond ($N_A \leq 10^{14}$ cm^{-3}), the ionization rate (n/N_D) is lower than 0.1 % at RT thus indicating that less 1 atom over 1000 donors is ionized at RT. At 500 K, for acceptor concentrations lower than 10^{17} cm^{-3} and a compensation of 10^{14} cm^{-3}, the ionization rate is about 10 %. In comparison, for p-type doping, the acceptor are fully ionized in the same doping and compensation ranges and the ionization rate is approximately 100 %. This relatively low ionization rate in n-type diamond is due to the higher phosphorous ionization energy (0.57 eV). The exhaustion regime for n-type diamond occurs then at higher temperature than 500 K for N_D range discussed above. Moreover, the ionization ratio is lower than 10% at 500 K for $N_D \geq 10^{17}$ cm^{-3}. As an example, for $N_D = 10^{20}$ cm^{-3}, electron density is equal to 10^{17} cm^{-3} thus corresponding to a n/N_D ratio of 0.001. This can be ascribed to the constant activation energy assumption over the whole N_D range which was made in our calculations. This hypothesis was based on experimental results indicating a constant E_a for doping levels lower than 10^{20} cm^{-3} [Matsumoto 2014, Makino 2014]. Moreover, a high compensation level also contributed to reduce the electron density. The compensation effect can be assumed as negligible if the compensation ratio k ($k = N_A/N_D$) is below 10 %. It must noticed that the conduction through only the conduction band have been considered for building the Figure 2.10, and that hopping mechanisms were neglected.

2.3.3 Electron mobility

The theoretical electron mobility versus donor concentration and compensation was calculated at 300 K and 500 K (Fig.2.11). A maximum mobility of 1000 cm^2/Vs at RT and 250 cm^2/Vs at 500 K may be expected for a doping level lower than 10^{17} cm^{-3} and a compensation below 10^{15} cm^{-3} as shown on Figure 2.11. Out of these N_D and N_A limits, the mobility decreases as a function of N_D and N_A due to neutral and ionized impurities scattering [Pernot 2008]. Thus, the mobility drops from 1000 to 120 cm^2/Vs for doping level increases from 10^{16} cm^{-3} to 10^{19} cm^{-3} in case of uncompensated n-type material ($N_D \leq 10^{14}$ cm^{-3}).

Moreover, as for p-type diamond, it shows that a 10% of donor compensation induces a mobility twice lower than the maximum value expected for uncompensated material with $N_A \geq 10^{16}$ cm^{-3}. As an example, for N_D of 10^{18} cm^{-3}, the mobility of electrons

drops from 500 to 250 cm^2/Vs when the compensation level N_A increases from 10^{14} cm^{-3} ($k = 0.01\%$) to 10^{17} cm^{-3} ($k = 10\%$). These theoretical calculations are in good agreement with the experimental data reported in reference [Pernot 2008], expect for some data points for which a lower mobility value compared to our calculations was observed. This kind of discrepancy has been discussed previously in the case of p-type materials. It can be ascribed to additional scattering mechanisms (defects), which were not considered here (neutral impurities, ionized impurities, phonon scattering).

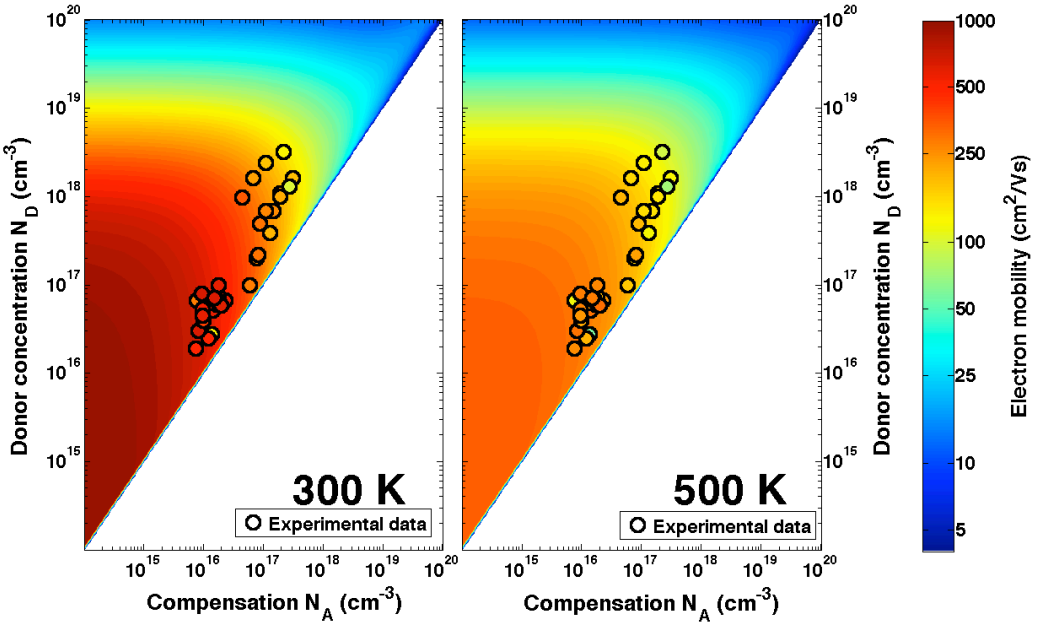

Figure 2.11: Theoretical electron mobility as a function of donor concentration and compensation at 300 K and 500 K. The symbols are experimental data reported in reference [Pernot 2008].

2.3.4 n-type diamond resistivity

Figure 2.12 shows the full picture of n-type diamond resistivity versus N_A and N_D at 300 K and 500 K. Besides a good agreement with the experimental data, the minimum resistivity at RT and 500 K is always obtained for a N_D ranging between 10^{18} cm^{-3} and 10^{19} cm^{-3} and N_A lower than 10^{15} cm^{-3}. This feature only observed for n-type diamond is a consequence of the constant ionization energy level assumption underlying our calculations. For 10^{15} cm$^{-3} \leq N_D \leq 10^{17}$ cm^{-3} and 10^{14} cm$^{-3} \leq N_D \leq 10^{15}$ cm^{-3}, it was demonstrated that a high mobility around 1000 cm^2/Vs should be obtained. Unfortunately, this high mobility is counterbalanced by the low ionization rate of phosphorous donor (high ionization energy). At RT, the n-type diamond resistivity is thus ranging between 10^5 and 10^3 Ω.cm for these doping and compensation ranges. At 500 K, the

resistivity is still relatively high (10^2 and 10 Ω.cm) compared to p-type diamond in the same doping range where the RT and 500 K resistivity are respectively more than 100 times and 10 times lower than those of n-type materials.

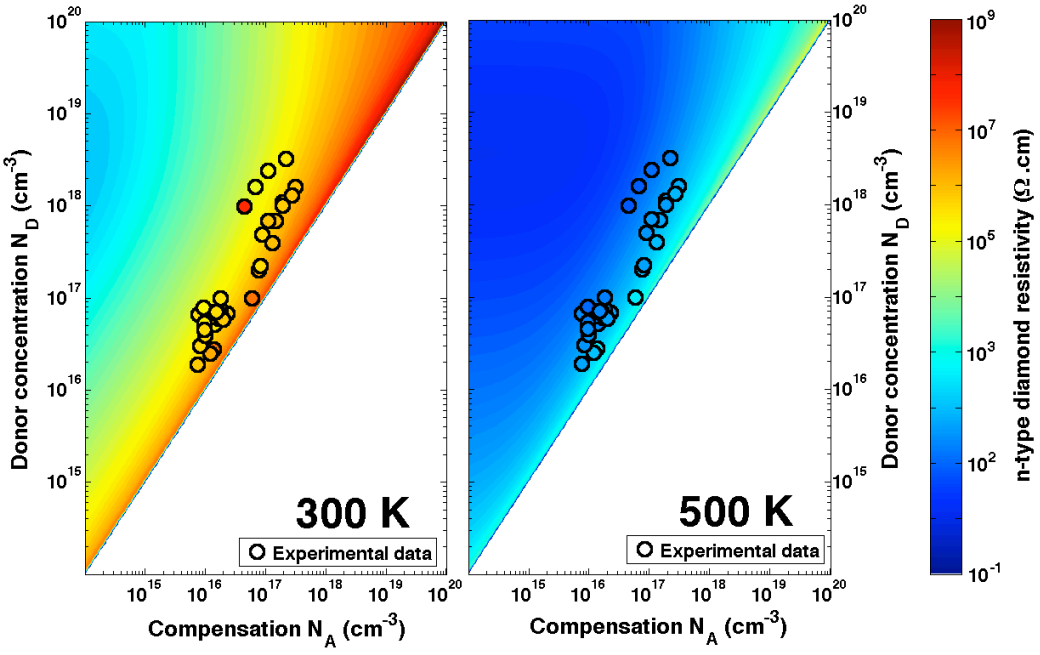

Figure 2.12: n-type diamond resistivity as a function of donor concentration and compensation at 300 K and 500 K. The symbols are experimental data reported in reference [Pernot 2008].

2.4 Conclusion

The analytical Hall transport model reported by Pernot et al.[Pernot 2010, Pernot 2008] was used to investigate the main transport properties (mobility, carrier density, and resistivity) as a function of doping level and compensation for both n-type and p-type diamond. For each type of dopant, the theoretical carrier density, carrier mobility, and resistivity profile for a doping level and a compensation ranging between 10^{14} to 10^{20} cm^{-3} was calculated for room temperature and at 500 K. These theoretical calculations, in good agreement with experimental data reported by several authors, offer the unique opportunity to estimate the electrical properties of diamond layer for a given doping level and a given compensation. The electrical features of diamond devices can be then preselected and furthermore optimized before their fabrication.

On the other hand, the calculations performed in this chapter delineated a compensation limit and doping range in which carrier density and their mobility are weakly altered as compared to uncompensated materials. For p-type diamond with less than 10% of boron acceptor compensated and a doping below 10^{17} cm^{-3}, a RT mobility close to the maximum of 2000 cm^2/Vs may be expected. This optimal compensation range and doping range are similar to those of n-type diamond where a maximum RT electron mobility of 1000 cm^2/Vs should be obtained. Unfortunately, these high mobility values are counterbalanced by the low ionization rates of diamond dopants, thus leading to a high room temperature resistivity for both p-type and n-type materials. Indeed, only 1% of boron acceptors are ionized at RT whereas less than 0.1% phosphorous donors should be ionized. Thus, the RT resistivity of p-type diamond in this low doping range varies between 100 $\Omega.cm$ (for $N_A = 10^{15}$ cm^{-3}) and 10 $\Omega.cm$ (for $N_A = 10^{17}$ cm^{-3}). Conversely, for n-type diamond, the RT resistivity is at least 100 times higher with values between 10^5 $\Omega.cm$ (for $N_A = 10^{15}$ cm^{-3}) and 10^3 $\Omega.cm$ (for $N_A = 10^{17}$ cm^{-3}).

For power unipolar devices such as Schottky diodes where slightly doped active layers are preferentially selected in order to achieve a high blocking voltage, boron-doped diamond (p-type diamond) is therefore more appropriate. At high temperature such as 500 K, the resistivity of p-type diamond is significantly reduced due to the thermal activation of boron acceptors. Such a high operating temperature will then enhance the electrical performance of diamond power devices.

Chapter 3

Diamond Schottky diodes engineering

Contents

3.1 Introduction

This chapter will describe the fabrication process of the pseudo-vertical diode structure used in this thesis. This choice was motivated by the current unavailability of commercial electrical grade highly conductive diamond substrates, probably, at the moment, the major obstacle towards vertical diamond Schottky diodes fabrication (the optimal geometrical configuration).

So far, vertical diamond Schottky diode structures suffer from the propagation of defects such as dislocations [Umezawa 2012, Ohmagari 2011] from heavily doped substrate (highly conductive substrate) in the diode active layer, as a result of epitaxial growth. In consequence, the obtained critical field (2.1 MV/cm [Umezawa 2013], 2.7 MV/cm [Kumaresan 2010] best values reported for vertical structure), even with a field plate meant to avoid the edge field enhancement [Ikeda 2009], is much lower than that achieved for the lateral diamond Schottky diodes (7.7 MV/cm [Volpe 2010]) or than the very first value reported for diamond (higher than 10 MV/cm) [Landstrass 1993]. A lateral diode is obtained by fabricating Schottky and ohmic electrodes on top of the active layer. The electrical current transport in this configuration takes place in a highly resistive active layer. An additional high resistance due to ohmic contact on lightly doped layer (about 300 $\Omega.cm^2$ [Kumaresan 2009]) also limits diodes current (below 100 A/cm^2) in forward regime. In this thesis, a pseudo-vertical diode structure was adopted.

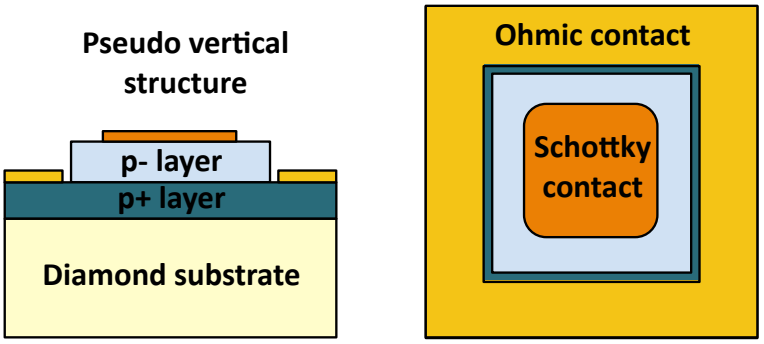

Figure 3.1: Pseudo vertical Schottky diode structure.

For the pseudo-vertical diode [Kumaresan 2009, Muret 2011], the epitaxial stack of two layers is made. The active layer (p^- layer) is grown on a highly conductive epi-layer (p^+ layer) grown on an insulating diamond substrate. This design is generally used in order to get an electrical behavior close to that of the vertical structure. The active layer is etched back in order to fabricate the ohmic contact on the top of the highly doped layer, thus delineating the pseudo-vertical structure as shown on Figure 3.1. The fabrication process of this structure involves:

1. **epitaxy of active and p^+ layer,**
2. **ohmic contact fabrication,**
3. **Schottky contact deposition.**

As for the vertical structure, the diode performance will be in part related to the crystal quality of the p^+ layer and furthermore to its doping level. A high quality p^+ layer will favor the minimization of defects inside the active layer (p^- layer). Moreover, this layer has to be sufficiently doped to get a metallic behavior to minimize its contribution to the diode serial resistance and achieve a negligible ohmic contact resistance.

In this chapter, the epi-layers growth step and the contact fabrication step will be introduced. The growth process together with the main characterization techniques used to investigate epi-layers surface and volume defects, will be described first, and the obtained results will be discussed. The final step towards pseudo-vertical diode fabrication, the Schottky metal deposition step, will be reported in the next chapter.

3.2 Diamond synthesis

Diamond is an allotrope of carbon characterized by a tetrahedral arrangement of carbon atoms bonded together by strong covalent sp^3-bonds that crystallizes in a variation of face centered cubic structure: the so-called diamond lattice. This confers to diamond its extreme hardness and furthermore its amazing properties such as a high thermal conductivity and a high melting point.
Figure 3.2 shows the Pressure-Temperature (P-T) phase diagram of elemental carbon together with the main techniques for diamond synthesis [Bundy 1980]. Under normal conditions, as shown on Figure 3.2, the thermodynamically favored carbon phase is graphite. The graphite structure is characterized by carbon atoms (sp^2 hybridization) bonded in sheets of hexagonal lattice linked to each other by weak Van der Waals forces. Contrary to diamond, graphite is soft, slippery, and metallic due to its sp^2 hybridization. Despite the low energy difference between diamond and graphite phases (less than 0.025 eV/atom at room temperature [Anthony 1990]), the diamond phase exists under normal conditions because a high activation energy is necessary to promote the structural transition from diamond to graphite, leading to extremely slow reaction kinetics. Diamond is said to be metastable under normal conditions and it may remain such for an almost indefinitely long time thanks to this kinetic stability.

The synthesis of diamond has been a long quest, dating back from the seventeenth century when the French scientist Antoine Lavoisier and co-workers proved that diamond was a form of carbon. This material is today mainly synthesized by the high-pressure high temperature (HPHT) process from graphite phase and furthermore by chemical synthesis (Chemical Vapor Deposition) from gaseous phases under low pressure and moderate temperatures (Fig. 3.2).

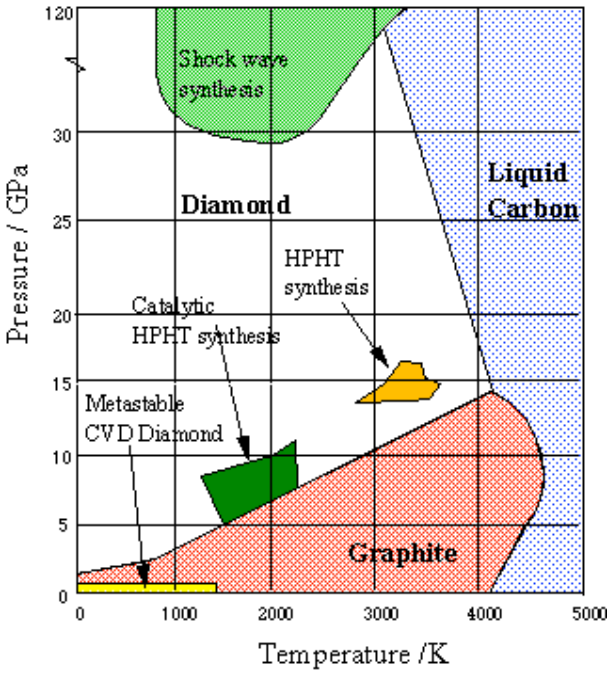

Figure 3.2: The P-T phase and reaction diagram of elemental carbon [Bundy 1980].

HPHT synthesis: this technique is similar to the natural process of carbon crystallization in diamond under the Earth mantle (depths of 140 to 190 km) under extreme conditions where diamond is the thermodynamically stable phase of carbon. General Electric in USA was the first company to achieve a reproducible and verifiable HPHT diamond growth process around 1955s using the catalytic HPHT methods. Contrary to the logic behind HPHT synthesis, consisting to apply a sufficient pressure to shorten the bonds between graphite layers to force carbon rings to conform to the diamond lattice, the catalytic HPHT method used a solvent material (the catalyst) in order to dissolve graphite layers and build from the dissolved atoms, diamond lattice (the template being provided by a seed) [Ferro 2002]. The solvent acts as a catalyst for the transformation of non-diamond phase in diamond and furthermore as a relative good solvent of non-diamond carbon, lowering the activation energy of the reaction of graphite conversion in diamond [Ferro 2002]. Accordingly, the (P-T) conditions for catalytic HPHT synthesis, shown on Figure 3.2, are much lower compared to HPHT methods. Metal catalysts such

nickel or cobalt are commonly used in catalytic HPHT synthesis consisting to compress with huge hydraulic presses at high temperature, a metal-solvated carbon (graphite) mixture in the presence of a diamond seed. HPHT diamonds are generally Ib type i.e. they contain a high nitrogen (N) concentration in single substitutional form (N>5 ppm). Diamond crystals are generally classified in types Ia, Ib, IIa, and IIb according to the concentration and clustering of Nitrogen atoms. The types IIa and IIb may often be considered as free of nitrogen because of their very small concentration of nitrogen (below 5 ppm). The main features of IIb diamonds is their small amount of uncompensated boron leading to p-type conductivity. Moreover, diamond containing nitrogen in single substitutional form are called type Ib while those containing aggregated nitrogen atoms in either platelet or tetrahedron forms, are classified as type Ia (most of natural diamonds are type Ia). Besides their Ib type, HPHT diamonds have many crystal defects and impurities (metallic contamination) not suitable for electrical application. They are mainly used in industrial applications such as cutting and drilling. However, HPHT diamonds may be used as substrate in diamond-based devices processing for high quality epitaxial diamond growth by a CVD process.

Chemical Vapor Deposition (CVD): the CVD process consists in depositing a solid material from gaseous phases at the surface of substrate. This method is widely used in diamond devices processing since it is the main technique allowing diamond synthesis at low pressure and moderate temperature (Fig. 3.2). Furthermore, CVD provides an easier control of diamond electrical properties such as its doping level (in situ doping). In 1962, Eversole's experiment was one of the first documented reports about CVD diamond. This experiment consisted to diamond growth on a heated natural diamond substrate (from 600 °C to about 1600 °C) from thermally decomposed carbon-containing gas such as carbon oxides or methyl group-containing gas [Ferro 2002].

One of the major steps forward in CVD diamond synthesis was the use of atomic hydrogen in the synthesis reaction chamber, as proposed in the early 1970's. Atomic hydrogen is known to play a number of critical roles in CVD synthesis of diamond, as illustrated on Figure 3.3 [Goodwin 1997]. Atomic hydrogen preferentially etches away non-diamond phases such as graphite and prevents their formation by saturating the dangling bonds, thus making high quality diamond growth possible. Moreover, atomic hydrogen highly contributes to hydrocarbon radicals generation in the gaseous phase. It is also allowed the abstraction of hydrogen from hydrocarbons attached to the surface, thus creates vacant sites on the growing surface [Anthony 1990]. Its concentration should be as much as possible in order to improve both the diamond growth rate and its crystal

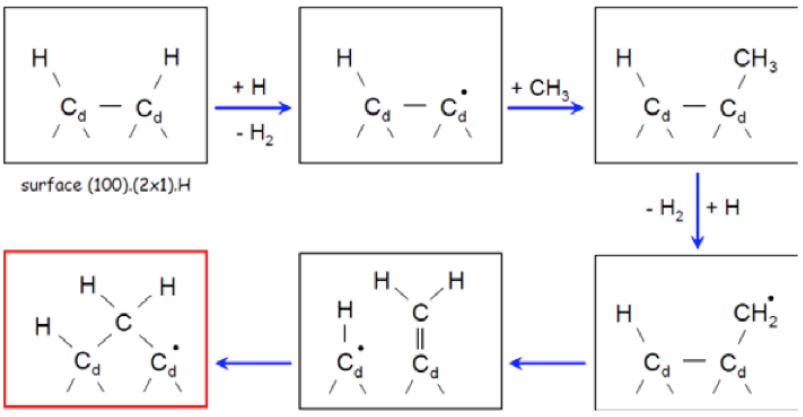

Figure 3.3: Dimer opening & Carbon insertion (Goodwin & Butler, 1998) [Goodwin 1997].

quality [Achard 2011]. Hot Filament assisted CVD (HFCVD) and Microwave Plasma enhanced CVD (MPCVD) reactors built respectively in 1982 and 1983 by Japanese researchers in National Institute for Material Sciences (NIMS) (ex National Institute of Research on Inorganic Materials NIRIM), are the main techniques used today to generate the high atomic hydrogen density necessary to CVD diamond growth. MPCVD synthesis is preferentially used to get high purity film compared to HFCVD where the film can be contaminated by metallic atoms or particles emitted by the wire. Today, CVD diamonds are commonly obtained from gaseous mixture of methane (CH_4) and hydrogen (H_2) in vacuum chambers where active species i.e. hydrocarbon radicals and atomic hydrogen are generated by microwave excitation (MPCVD reactor). Besides its use in devices and jewellery, CVD synthesis of diamond has many industrial applications such as the coating of wear parts of machine tool components. Moreover, CVD diamonds cost is relatively low compared to HPHT, due to the smaller and less expensive production equipments.

3.3 Epi-layers growth by MPCVD

This section summarizes the growth processes together with the standard conditions under which the diodes active layers (p^- layer) and the highly conductive contact layers (p^+ layer) have been fabricated in this thesis. The stack comprising the p^- layer and the p^+ layer was grown by MPCVD on Ib (100) HPHT diamond substrates (Sumitomo Electric Ltd). The set of substrates used in thesis is reported in table 3.1. These substrates were finely polished in order to minimize the consequence of scaife polishing (abrasive process) on as-received substrates. Indeed, besides the relatively high roughness ($\sim$ 1.5

nm) induced by scaife polishing method, the as-received substrates have a subsurface damaged area (subsurface hardening), which generally leads to defects (extended defects such as dislocations) in epi-grown layers.

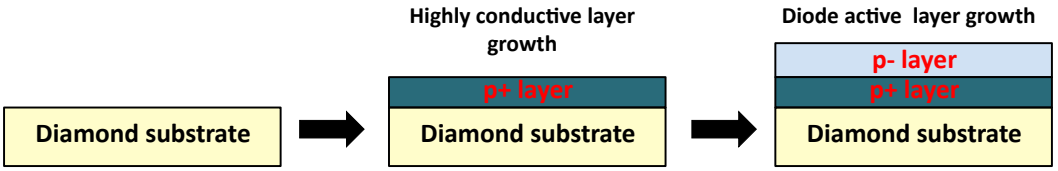

Figure 3.4: Epi-layers schematic stacking.

Diamond substrates were re-polished by Syntek Co. LtD a Japanese company. The polishing method allowed removing the subsurface hardening zone and led to a lower surface roughness (≈ 0.33 nm). Table 3.1 summarizes the specifications of samples used in this thesis.

Table 3.1: Specifications of samples reported in this thesis.

Sample	Size	Substrate	Orientation	Polishing
#1	3×3 (mm^2)	Ib HPHT	(100)	Syntek
#2	3×3 (mm^2)	Ib HPHT	(100)	Syntek
#3	4.5×4.5 (mm^2)	Ib HPHT	(100)	Syntek

For each sample, a chemical cleaning was performed prior to growth in order to remove any surface contamination. Diamond samples were cleaned in a hot acid mixture (250 °C) $HClO_4$:H_2SO_4: HNO_3 (1:3:4 Volume to Volume V/V) followed by a HF:HNO_3 (1:1 V/V) treatment. Moreover, pure hydrogen plasma pre-treatment was performed in situ prior to growth to etch away any remaining non-diamond carbon phases such as graphite and to set the diamond sample temperature to the growth temperature.

The highly conductive boron doped diamond (p^+ layer) was first grown on diamond substrates. This p^+ layer was then used as a pseudo substrate for diode active layer growth. The key point in this step is the doping level of both the p^+ and active layers. The main role of the p^+ layer is to connect the active layer backside to ohmic contact without inducing an additional resistance. Here, p^+ layer was grown with a gaseous mixture of CH_4, B_2H_6, and H_2 in a home made NIRIM type reactor (subsection 3.3.1). The growth conditions were set to achieve a doping level above the critical value for the metallic transition (5×10^{20} cm^{-3} [Klein 2007]).

The active layer (p^- layer) was then grown on the p^+ layer in either NIRIM type reactor or a commercial type reactor "PLASSYS BJ 150" (subsection 3.3.1). The p^- layers were non-intentionally doped using a gaseous mixture of CH_4, O_2, and H_2 aiming at slightly doped layers. In such growth, the boron source was the residual boron atoms (memory effect) in the growth chamber.

3.3.1 Growth reactors

In this work, both a home-made NIRIM type reactor and a bell jar commercial type reactor PLASSYS BJ 150 were used for epi-layers growth. PLASSYS BJ150 is a high-power microwave cavity plasma reactor known to promote high gas temperature (3200 K) needed for an efficient atomic hydrogen production by thermal dissociation of H_2 [Silva 2009] contrary to the NIRIM type reactor where direct electron-impact induced H_2 dissociation mainly occurs [Fiori 2012]. Moreover, the high deposition pressure available together with the strong activation of gaseous phases in the PLASSYS BJ150 lead to high growth rates (several microns per hour). This reactor was used for thick p^- layer growth. The main specifications of these reactors are described below.

Home-made NIRIM type reactor: Figure 3.5 shows the schematic diagram of this growth reactor [Fiori 2012]. This home-made reactor is a modified Japanese (NIMS lab) MPCVD reactor [Kamo 1983]), which is characterized by a plasma ball located at the intersection of a waveguide and the growth chamber. The gaseous mixture is injected from the top of growth chamber composed by an inner (25 mm diameter) and an outer (40 mm diameter) silica tubes. A microwave generator, operating at 2.45 GHz (power range 0 -2 KW), was used as plasma excitation source. The sample holder, formed by silicon substrate coated with a polycrystalline diamond layer, is located on the top of the inner tube fixed to a linear Z-axis guided UHV magnetically coupled metallic transporter. Thus, the deposition temperature can be set by vertically adjusting the sample holder position compared to the plasma ball. A single colour pyrometer (960 nm), with an emissivity set at 0.4, was used to estimate sample temperatures taking in account the contribution of the sample holder.

The growth pressure is set with a throttle valve actuated by a PID controller with five set points. The available pressures are 2.5, 4, 9, 33 and 50 Torr. The 33 and 50 Torr

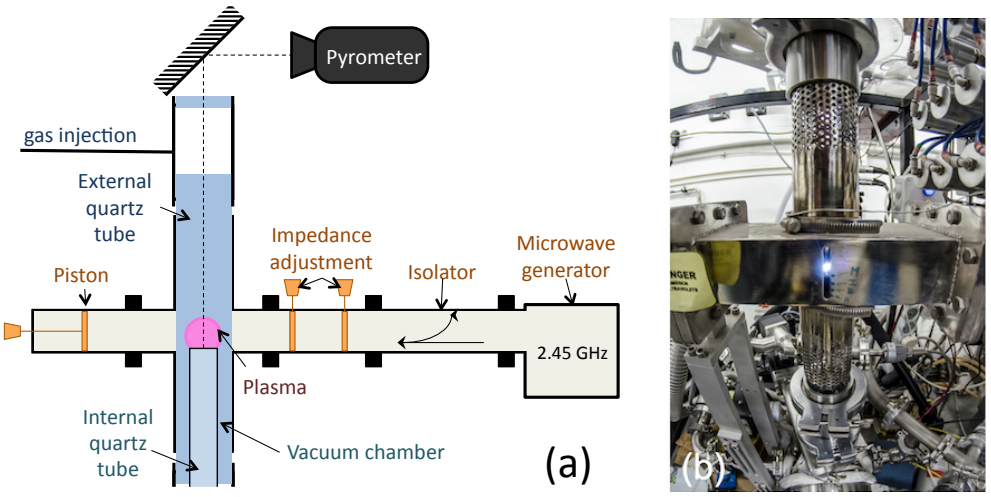

Figure 3.5: (a) Schematic diagram of NIRIM type reactor [Fiori 2012] together with its picture (b).

pressures were used for diamond deposition. Conversely, 2.5 and 4 Torr were used respectively for pure hydrogen and pure oxygen plasma ignition. The 9 Torr pressure was used for oxygen plasma etching.

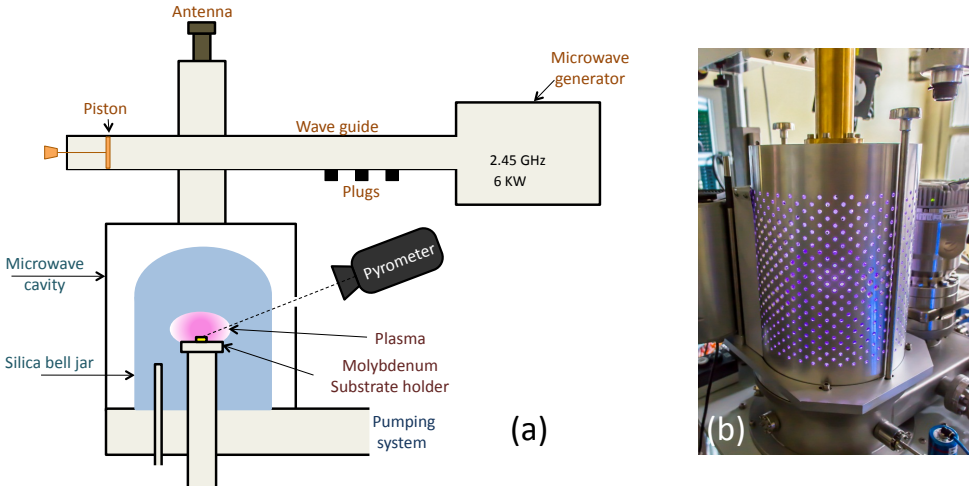

Figure 3.6: (a) Schematic diagram of PLASSYS BJ150 reactor together with its picture (b).

PLASSYS BJ150: Figure 3.6 shows the schematic diagram of PLASSYS BJ150 reactor. The growth chamber is composed by a silica bell jar fixed to a high vacuum gate valve (VAT DN 100) with a pneumatic actuator. This growth chamber is inside a cylindrical TM_{022} resonant cavity excited by an antenna through a coaxial port. A microwave generator, operating at 2.45 GHz and delivering a maximum power of 6 kW, is used as plasma excitation source to activate the gaseous mixture injected from the bottom of the growth chamber. The deposition pressure can be set (throttle valve with

a controller) over the whole range from 10 to 300 mbar (7.5 to 225 Torr). The diamond sample is bonded (carbon bond) onto a 2-inch ($\sim$ 50 mm) molybdenum substrate located on a sample holder with a water-cooling system and a linear Z-axis motion system.

3.3.2 Heavily doped layer

Heavily doping has been intensively investigated at Institut Néel. Several growth set-ups are defined to get high boron incorporation in epi-layer and therefore to reach high electrical conductivity. Figure 3.7 shows the typical incorporated boron atoms concentration versus ($[B]/[C]$) ratio and methane concentration in gaseous mixture ($[CH_4]/[H_2]$) reported by A. Fiori [Fiori 2012] for epi-layers grown using a pressure of 33 Torr and a substrate temperature of 830 °C in our home-made NIRIM-type reactor. The incorporated boron concentrations were estimated by Secondary Ion Mass Spectroscopy (SIMS). For a gas mixture with 4% of methane in hydrogen and a ($[B]/[C]$) ratio at least 10^3 ppm, a high boron incorporation above the metal transition level $\sim 5\times10^{20}$ cm^{-3} can be expected (Fig. 3.7). Apart from their relatively high growth rate (13 and 30 nm/min), these conditions were proposed as the most efficient to lower the density of defects such as dislocations.

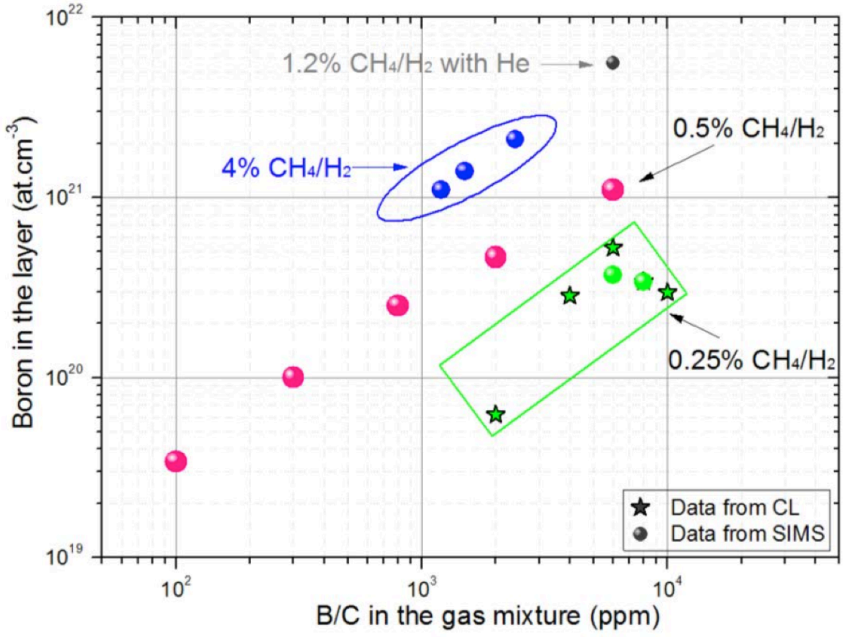

Figure 3.7: Incorporated boron vs. ([B]/[C]) in the gas mixture at different ($[CH_4]/[H_2]$) ratios [Fiori 2012] for NIRIM-type reactor.

Accordingly, the heavily doped layer p^+ layer was grown with a gas mixture of diborane ([B]/[C] =1200 ppm), methane ($[CH_4]/[H_2]$ =4%) and hydrogen, using a pressure of

33 Torr and a temperature of 830 °C. An hydrogen plasma treatment (one hour) was performed prior to the growth using 200 sccm (standard cubic centimeter per minute) H_2 gas flow, a pressure of 33 Torr and a temperature of 880 °C. The total gas flow and the growth duration were respectively 300 sccm and 15 min. The typical thickness of p^+ layer was ranging between 200 nm and 500 nm.

It might be noted that this thin p^+ layer was grown in order to minimize defects generation and thus improve the quality of the active layer (p^- layer) by reducing defects propagation from p^+ layer in p^- layer. On the other hand, the range of p^+ layer thickness should ensure the electrical transparency of the latter i.e., its contribution in diode serial resistance should be negligible compared to that of the slightly doped p^- layer with a thickness higher than 1 μm. Indeed, the theoretical calculations performed in chapter 2, predict a RT resistivity between 10^2 Ω.cm and 10^3 Ω.cm for low compensated (less than 10% of acceptor atoms) boron doped layer with [B] ranging between 10^{15} cm^{-3} and 10^{16} cm^{-3}. For samples #1 and #2, where 1.3 μm thick p^- layers were grown (see Table 3.2), the specific resistance of diodes active layer should be ranging from 0.013Ω.cm^2 to 0.13 Ω.cm^2. Since 100 μm diameter circular electrodes were fabricated (see Chapter 4), the serial resistance related to the active layer is expected to range between 160 and 1700 Ω. Conversely, the resistance induced by the p^+ layer is roughly 20 Ω and can be considered as negligible compared to that of the p− layer. However, this assumption may be inappropriate for the large area devices (500 × 500 μm^2) fabricated on sample #3 (see Chapter 4) for which the resistance related to p^- layer lies between 10 and 100 Ω.

3.3.2.1 Epi-layer surface morphology

The surface morphology of the epi-grown layers was investigated by optical profilometry in order to identify their main topological defects and moreover to estimate their average roughness. Optical profilometry is extremely versatile for carrying out accurate measurements of the shape and texture of all types of surfaces on the micrometric down to nanometric scales. Here, a Veeco 3D optical profiler Contour GT was used to investigate the surface topography of epi-layers. This optical profiler is characterized by fair lateral resolution (0.5 μm) and a very high vertical resolution, below 0.1 nm. Such an optical profiler is a high-speed system (maximum scan speed 92 μm/sec) that allows us to easily investigate a large area. This is one of the main advantages of this system compared to other surface techniques such as Atomic Force Microscopy (vertical resolution about 0.1

nm, lateral resolution below 10 nm) not practical for areas greater than 100 μm because of its limited scanning speed (several minutes for a typical image).

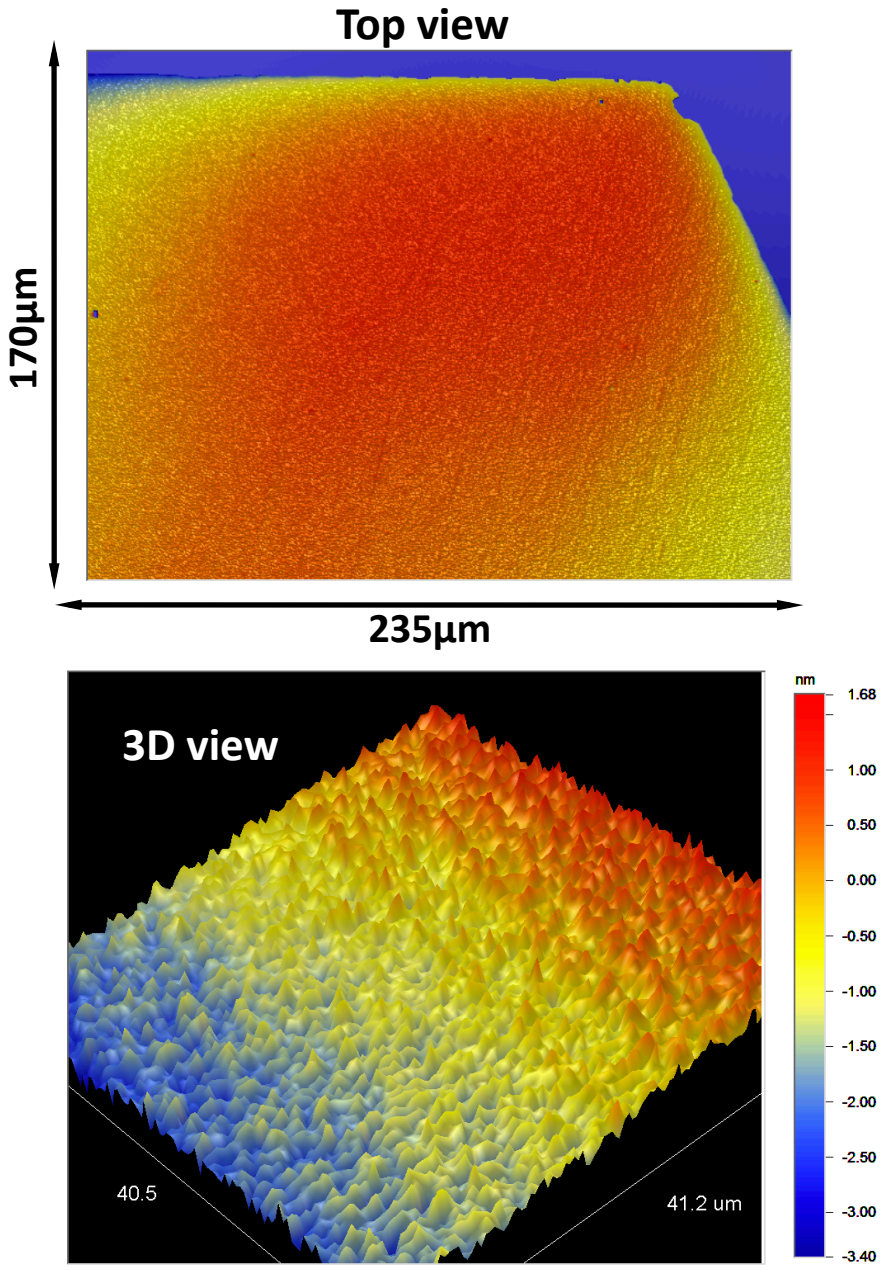

Figure 3.8: Typical surface morphology (Top view and 3D view) of p^+ layer obtained by optical profiler.

Figure 3.8 shows the typical surface topography of p^+ epi-layers and furthermore their typical texture (3D view). P^+ layers are generally free of surface defects. Moreover, one can estimate over a complete 3D surface, the mean roughness Sa and the Root Mean Square (RMS) roughness of these epi-layers using such a surface image. The typical values of Sa and RMS obtained for p^+ layers are around 0.26 nm and 0.35 nm

respectively.

3.3.2.2 Epi-layer thickness

The thickness of epi-grown layers were estimated by ellipsometry measurements. Spectroscopic ellipsometry is a powerful optical technique based on measurement of the change of polarization state of light over a wide spectral range after reflection on the material of interest. This technique is generally used to investigate the characteristics of thin films: their composition, thickness, doping level, electrical conductivity,....
Spectroscopic ellipsometry was demonstrated at Institut Néel [Bousquet 2014] as a powerful non-destructive tool to probe the thickness, the optical parameters and electronic properties of semiconducting and metallic single crystal diamond epi-layers and multilayers. Such a characterization can be performed during sample growth (in situ ellipsometry). Spectroscopic Ellipsometry were performed using a J.A Woollam M-2000 ellipsometer. Ex-situ (after growth) and in-situ (during growth) ellipsometry measurements were therefore performed to estimate epi-layer thickness and furthermore to set hydrogen treatment conditions for growth using PLASSYS BJ 150 reactor. The estimated typical p^+ layer thickness for all 3 samples using spectroscopic ellipsometry, was about 400 nm corresponding to a growth rate of 26 nm/min.

3.3.2.3 Summary

A 400 nm-thick heavily boron doped layer was grown on Ib (100) sumitomo HPHT substrates (Table 3.2) with a gaseous mixture of diborane ([B]/[C] =1200 ppm), methane ($[CH_4]/[H_2]$ =4%) and hydrogen using a pressure of 33 Torr and a temperature of 830 °C in a home made NIRIM-type reactor. The growth rate was about 26 nm/min. The obtained epi-layers are free of surfaces defects and characterized by a typical mean roughness of 0.26 nm and Root Mean Square of 0.35 nm. The next step towards pseudo-vertical structure fabrication is the slightly doped active layer growth, which will be discussed in the next section.

3.3.3 Slightly doped layer

This step is important since electrical performance of the fabricated devices will be closely linked to the crystalline quality of the slightly doped epi-layer. The epi-layers were mainly grown from a gaseous mixture of CH_4, O_2, and H_2. The boron atoms source

is related to memory effect i.e. to the residual boron atoms contamination in growth chamber. Oxygen was added in the gaseous mixture to reduce boron incorporation and to improve the quality of the epi-grown layer [Volpe 2009a]. Indeed, oxygen gas is known to give rise to hydroxyl OH species, which reduce boron incorporation rate in epi-grown layer by oxydizing chemically active BH_x species originated from B_2H_6 decomposition [Omnès 2011]. Moreover, oxygen is supposed to contribute to the reduction of the graphitic phases formation on the growing surface and furthermore to increase their etching rate [Frenklach 1991, Harris 1989]. Both NIRIM type and PLASSYS BJ150 reactors were used for diodes active layers growth. The p^- layers growth on sample #1 and #2 was performed with NIRIM type reactor. For sample #3, the PLASSYS BJ150 reactor was used to get a thicker film. The growth conditions set-up together with the surface morphology (roughness, unepitaxial defects) of epi-grown layers, will be discussed in this part.

3.3.3.1 Main surface defects

The main surface defects usually encountered on epi-grown diamond surfaces, as shown on Figure 3.9, are Unepitaxial Crystals (UC), Pyramidal Hillocks (PH), Flat-top Hillocks (FH), and Round Hillocks (RH). FH defects are truncated PH characterized by a quadrilateral basis and (111) lateral facets. PH hillocks are sometimes topped by UC defects. Conversely, RH hillocks have a conical shape with an elliptical basis. RH defects are commonly difficult to observe due to their small size. Tallaire et *al*. [Tallaire 2008] carried out some investigations about the relationship between such surface defects and extended crystallographic defects. The hillocks type defects (PH, FH, RH) were found to result from extended crystallographic defects: a bunch of dislocations formed at the interface between the substrate and the layer. Conversely, UC defects were found to be embedded in CVD layer without any relationship with neither extended defects nor substrate imperfections. The nucleation of these defects in CVD epi-layers depends on growth conditions and their inhibition requires an efficient suppression of non-diamond phases [Tallaire 2008].

3.3.3.2 Growth in the NIRIM type reactor (samples #1 and #2)

The growth conditions used in the NIRIM type reactor were based on those defined in reference [Volpe 2010] to get high crystal quality using that same reactor. Volpe et *al*.

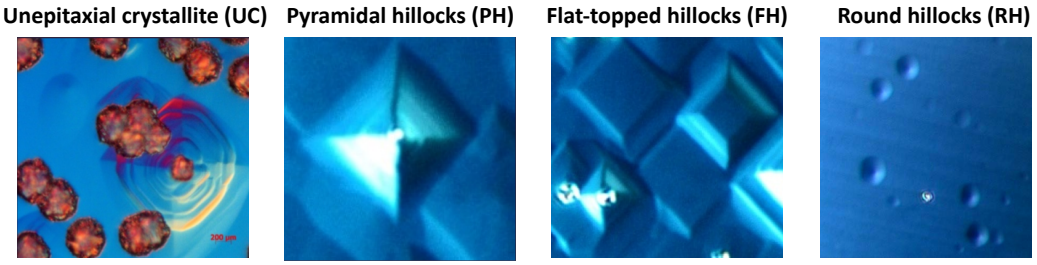

Figure 3.9: Differential Interference Contrast images (DIC) of main surfaces defects encountered on epi-growth layers [Fiori 2012]. From left to right : Unepitaxial Crystallites (UC), Pyramidal Hillocks (PH), Flat-topped Hillocks (FH), and Round Hillocks (RH).

[Volpe 2010] demonstrated a high breakdown voltage about 10 kV (corresponding to 7.7 MV/cm) with p^- layer grown with a gaseous mixture of 1% of CH_4 and 0.25% of O_2 in hydrogen gas, under a 33 Torr pressure and a substrate temperature of 910 °C. Unfortunately, these conditions led to a high density of surface defects such as UC defects, which are not suitable for large area device fabrication. Consequently, the growth conditions were adjusted in order to minimize surface contamination.

The p^- layer was therefore grown with 0.75% of CH_4 and 0.25% of O_2 in hydrogen gas, using a 33 Torr pressure and a temperature of 910 °C. Pure hydrogen plasma treatment was performed prior to the growth using 33 Torr pressure and a temperature of 880 °C. The influence of residual boron in growth chamber was minimized by using non-boron contaminated inner and outer fused silica tube. The growth duration was 140 min. An ex-situ ellipsometry measurement was performed to determine the layer thickness. The estimated thickness was about 1.3 μm corresponding to a growth rate of 9.3 nm/sec. The typical surface morphology of p^- epi-layer obtained using these conditions was shown on Figure 3.10. These layers were contaminated by UC, PH, and RH defects. The UC defects are most predominant defect type. These defects are generally randomly dispersed and form sometimes clusters as shown Figure 3.11.

Such surface defects are not related to extended crystallographic defects or substrate imperfections as reported by Tallaire et *al* [Tallaire 2008]. Moreover, the authors reported the possibility to remove UC defects by performing hydrogen or oxygen plasma etching treatment. This kind of etching treatment was not performed in order to preserve the epi-layers smooth surface.

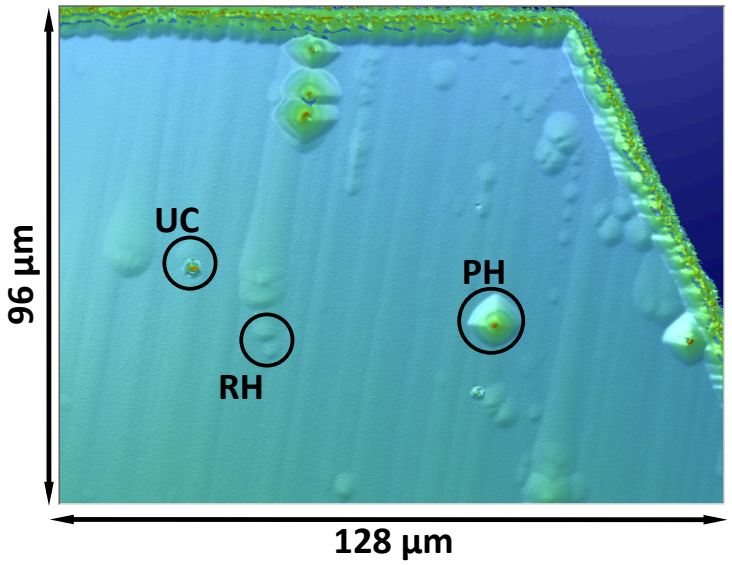

Figure 3.10: Typical surface topography obtained by optical profilometry. The main defects such as Unepitaxial Crystallites (UC), Pyramidal Hillocks (PH), and Round Hillocks (RH) are illustrated.

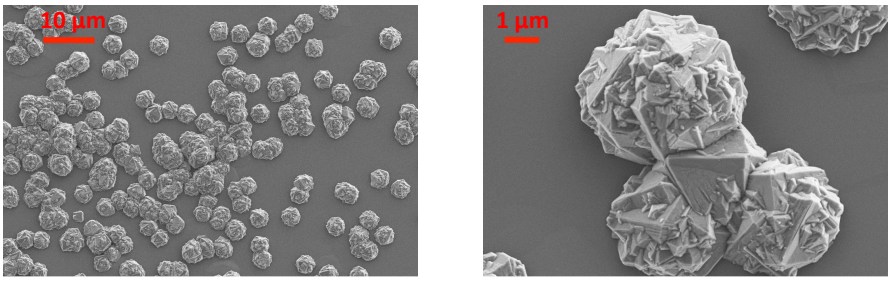

Figure 3.11: SEM image of unepitaxial crystals contamination on epi-layer surface.

On the other hand, it is well admitted that high power density plasma leading to a high atomic hydrogen density, allows getting a defect free surface [Achard 2011]. Thus, aiming at fabricating large area devices on defect free surface, the PLASSYS BJ 150 reactor was used to grow the p^- layer in the case of sample #3. The growth conditions together with the obtained results will be discussed in the next part.

3.3.3.3 Growth in PLASSYS BJ 150 (sample #3)

The main documented reports about CVD diamond grown in PLASSYS BJ 150 were published by the French group from "Laboratoire des Sciences des Procédés et des Matériaux" (LSPM). The influence of various process parameters such as the deposition pressure, substrate temperature, and methane concentration were intensively investigated by this group in order to get both a large growth rate (several microns per hour)

and a high quality diamond thick film (several hundreds of microns). The most optimal growth conditions which preferentially favored the (100) direction growth were CH_4/H_2 ratio of 4 %, a deposition pressure of 200 mbar, and a temperature of 850 °C [Achard 2005, Silva 2009]. The growth rate under such conditions was about 6 μm/h. Starting from these conditions, we investigated growth conditions using a gaseous mixture of methane, oxygen, and hydrogen in order to identify the best set leading to the lowest number of defects on the epi-layer surface.

The first optimization step before p^- layer growth was the definition of hydrogen plasma treatment conditions. Apart from the fact that it etches non-diamond phases prior to the growth, hydrogen plasma treatment allows rising up the diamond sample temperature to the target value. According to the conditions used (pressure, power, duration), the etching phenomenon occurring during hydrogen plasma treatment can be enough to completely remove the p^+ layer previously deposited onto diamond sample, leading therefore to a strong residual boron level in growth chamber. In situ ellipsometry measurements were then performed to identify less aggressive hydrogen plasma treatment conditions. For a treatment temperature about 890 °C and a gas flow of 500 sccm, the etching rate was 2 nm/min using a pressure of 150 mbar and 6 nm/min for a pressure of 200 mbar. The etching rate was found to be lower than 1.5 nm/min for a pressure of 110 mbar. Thus, hydrogen treatment step was performed using a 500 sccm gas flow, a 110 mbar pressure, and a temperature of 900 °C. The microwave power was 1800 W and the treatment duration was 20 min. Moreover, the influence of the methane concentration in the gaseous mixture on the epi-layer surface state was investigated. Non-intentionally diamond doped layers were grown on substrate with 7 %, 5%, and 4% of methane in gaseous mixture. These growths were performed using a pressure of 150 mbar, a deposition temperature of 900 °C, and a fixed O_2/H_2 ratio of 0.75%. The total gas flow was 500 sccm. Figure 3.12 shows the typical surface morphology of epi-layers obtained for these different CH_4 concentrations.

The surface texture of the epi-layer obtained with 7% of CH_4 was non-uniform. It seems to be a consequence of an inhomogeneous growth occurring under these conditions. Moreover, the round hillocks (RH) defects mainly appeared for a lower methane concentration as shown on Figure 3.12 (case B and C). The RH defects density onto the layer surface was significantly reduced for 4% of CH_4 in total gas flow. The number of defects is reduced when a deposition pressure of 200 mbar was used (Fig. 3.13).

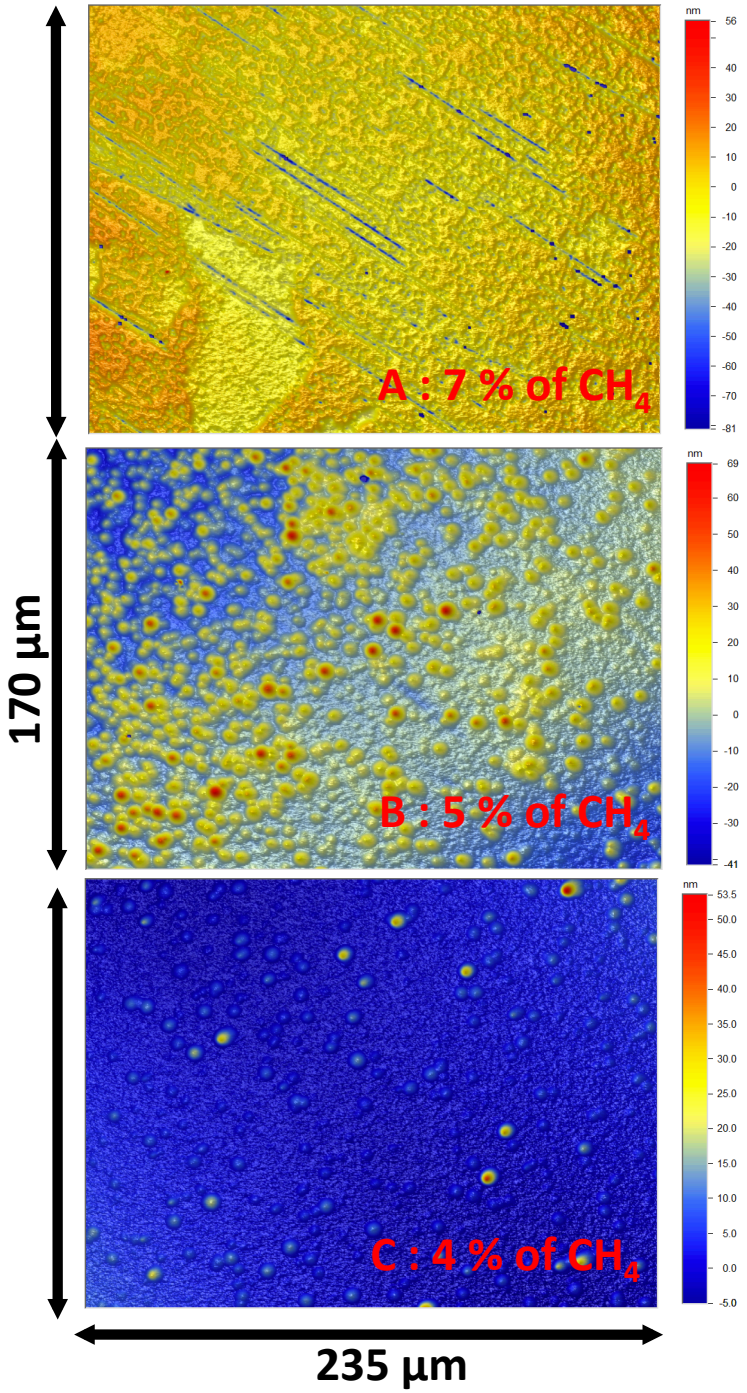

Figure 3.12: Typical surface morphology obtained using a deposition temperature around 900 °C, a 150 mbar pressure, various methane concentration. The gas flow was 500 sccm and oxygen molar ratio was set to 0.75%. A : 7% of CH_4 under 150 mbar, B : 5% of CH_4 under 150 mbar, C : 4% of CH_4 under 150 mbar

Accordingly, a 2.5 μm thick non-intentionally boron doped layer was then grown on sample #3 with 4% of CH_4 and 0.75% of O_2 in hydrogen gas, using a 200 mbar (150 Torr) pressure and a temperature of 940 °C. The microwave power was 1450 W and the total gas flow 500 sccm. The resulting growth rate was about 1.8 μm/h.

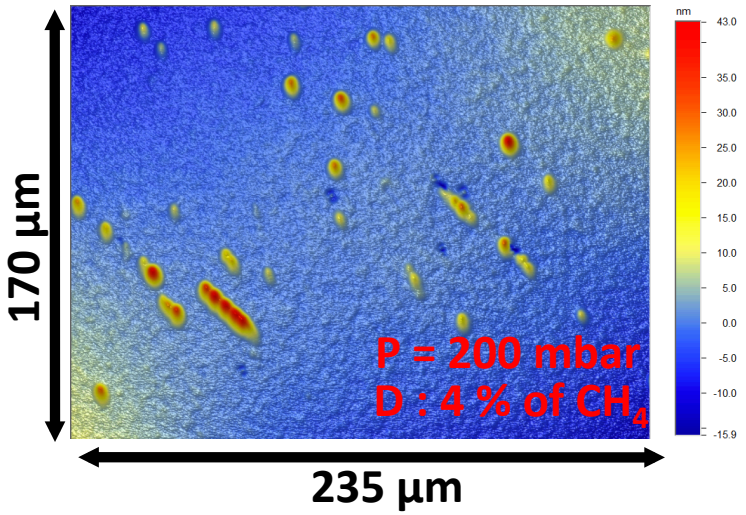

Figure 3.13: Typical surface morphology obtained using a deposition temperature about 900 °C*, a 200 mbar (150 Torr) pressure, 4% of* CH_4 *in gaseous mixture.*

3.3.3.4 Summary

1.3 μm-thick p^- layers were grown on sample #1 and #2 with 0.75% methane and 0.25% of oxygen in hydrogen gas using a pressure of 50 Torr and a temperature of 910 °C. These growths were performed in the NIRIM type reactor. Moreover, the PLASSYS reactor was used to grow a 2.5 μm on the sample #3 with 4% of CH_4 and 0.75% of O_2 in hydrogen gas, at a pressure of 200 mbar (150 Torr), and a temperature of 940 °C. Table 3.2 summarizes for each samples, the growth conditions and the thickness of epi-layers p^- and p^+. The epi-layers grown on samples #1 and #2 were mainly contaminated by unepitaxial crystals known to be embedded in CVD layer without any relationship with neither extended neither defects nor substrate imperfections [Tallaire 2008]. Conversely, round hillocks were the predominant defects on the surface of sample #3. These defects were found to be correlated to the growth conditions. In order to investigate the crystal quality of these epi-layers i.e. the extended defects such as dislocations and furthermore point defects such as silicon impurities, a 5 K cathodoluminescence (CL) spectroscopy was performed. Moreover, CL spectroscopy is known to be a non-destructive tool well suited to estimate the doping level. The measurement set-up together with the obtained results will be discussed in the next subsection.

Table 3.2: Growth conditions and thickness of epi-layers grown on samples described in this thesis. (1) *growth performed with NIRIM type reactor,* (2) *growth performed with PLASSYS BJ150 reactor*

Layer	Sample	Growth conditions					Thickness
		CH_4/H_2	O_2/H_2	[B]/[C]	T	P	
p^+	#1 #2 #3	4%	-	1200 ppm	830 °C	33 Torr	400 nm
p^-	#1 (1)	0.75%	0.25%	-	910 °C	50 Torr	1.3 μm
	#2 (1)	0.75%	0.25%	-	910 °C	50 Torr	1.3 μm
	#3 (2)	4%	0.75%	-	940 °C	150Torr	2.5 μm

3.3.4 Cathodoluminescence spectroscopy

Cathodoluminescence (CL) spectroscopy is an optical characterization technique generally used to investigate defects and among which dopants in a semiconducting material. CL spectroscopy allows the analysis of light emitted by a material under electron beam excitation. Such a light emission is due to radiative intrinsic or extrinsic (assisted by gap states) electron-hole pair or exciton recombinations. An exciton is an electron - hole pair linked by electrostatic attraction that can diffuse in crystal (free exciton). In doped semiconductors, a part of the so-called Free Exciton (FE) will be bound to neutral impurities (dopants or carrier traps) via Van der Waals interactions (Bound Exciton BE). BE formation is more efficient at low temperature since most of the impurities are neutral and furthermore because of their lower energy compared to free exciton. Accordingly, CL measurements are generally performed at low temperature to favor such BE exciton radiative transition in order to investigate the natures of impurities on which they are localized. For indirect gap semiconductors such as diamond, FE and BE recombinations are assisted by phonon (conservation of crystal momentum). Indeed, the minimum of diamond conduction band is shifted by 0.76 π/a in the (100) direction of the first Brillouin zone (Fig. 4.13). Transverse Acoustic TA ($\sim$ 87 meV [Warren 1966]), Transverse Optic TO ($\sim$ 141 meV[Warren 1966]), and Longitudinal Optic LO ($\sim$ 162 meV [Warren 1966]), are the main phonon involved in the excitonic transitions in diamond[Dean 1965]. The transition energy was then defined by $\hbar\nu = E_g - E_x - \hbar\omega_{ph}$ for FE transition and $\hbar\nu = E_g - E_x - E_b - \hbar\omega_{ph}$

Table 3.3: Main excitonic trasition in boron doped diamond.

Symbol	Phonon involved in excitonic recombination	Energy (eV)
FE^{TO}	Transerve Optic phonon (TO)	5.268
FE^{TA}	Transerve Acoustic phonon (TA)	5.322
FE^{LO}	Longitudinal Optic phonon (TO)	5.246
BE^{TO}	Transerve Optic phonon (TO)	5.215
BE^{NP}	Non Phonon assited transition (NP)	5.356
BE^{LO}	Longitudinal Optic phonon (TO)	5.193

for BE transition. E_g, E_x, E_b, and $\hbar\omega_{ph}$ are respectively the band gap, exciton binding energy (80 meV [Dean 1965]), exciton localization energy, and the phonon energy.

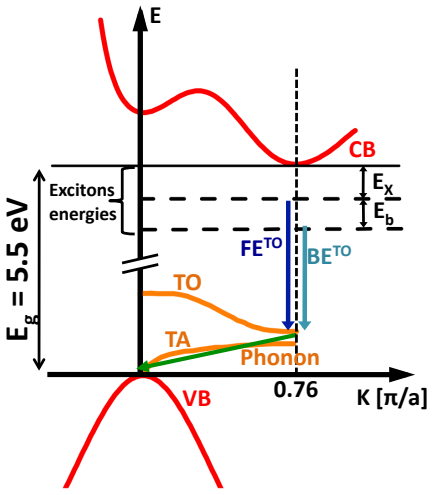

Figure 3.14: Diamond band diagram with main intrinsic and extrinsic transitions.

For boron-doped diamond, low temperature CL spectroscopy has been reported as a non-destructive tool to estimate the doping level [Omnès 2011]. Table 3.3 summarizes the main FE and BE excitonic transition linked to boron. A linear relationship between boron concentration [B] and CL intensity ratio $I_{BE^{TO}}/I_{FE^{TO}}$ was demonstrated in reference [Omnès 2011] for doping level ranging between 10^{16} cm^{-3} and 10^{18} cm^{-3}:

$$[B](cm^{-3}) = 3.5 \times 10^{16} \times \frac{I_{BE^{TO}}}{I_{FE^{TO}}}(cm^{-3}) \quad (3.1)$$

Besides providing an estimate of the doping and furthermore allowing the investigation of points defects linked to silicon or nitrogen incorporation, for example, CL spectroscopy is one of the main non-destructive techniques to investigate extended defects such as dislocations in diamond. Indeed, the radiative extended defects are commonly associated to broad bands in CL spectrum of diamond. For example, the extended defects such as dislocations are related to the so-called band A emission (Green band 2.3, 2.5 eV, blue band around 2.9 eV [Zaitsev 2010]). Aiming at estimating boron concentration, and in order to investigate silicon or nitrogen incorporation, and furthermore to reveal extended defects such as dislocations in epi-layers growth, cathodoluminescence spectroscopy was performed at 5 K.

3.3.4.1 Experimental setup

Figure 3.15 shows the schematic diagram of CL system used in this work. (1) Electron beam generated by a FEI Quanta 200 Scanning Electron Microscope (SEM) gun was focused on the sample (0.2 - 30 kV range acceleration voltage) in order to generate holes-electrons pairs. The sample was located on a cold stage GATAN using liquid helium to set the temperature (5 to 300 K range). A parabolic mirror (2) was used to collect and to reflect in a collimated beam towards a planar-convex lens, the light resulting from radiative hole-electron pair recombination. The emitted light was then focalized on the entrance slit of a monochromator. A HR460 Jobin Yvon monochromator (3) with near UV 600gr/mm or 1800gr/mm gratings, and associated to a photomultiplier (PM) or CCD (256 × 1024 matrix pixels) was used to analyse the emitted light and generate a spectrum. In this work, samples were cooled down to 5 K. The acceleration voltage was fixed to 10 kV or 15 kV for respectively 1.3 μm thick p^- layer (samples #1 *and* #2) or 2.5 μm (sample # 3) p^- layers. These accelerations voltages were selected in order to limit the probe volume to these epi-layers and avoid a possible contribution of p^+ layer and HPHT substrate.

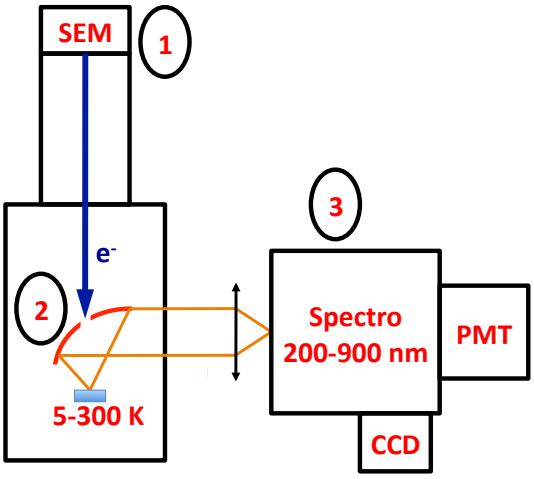

Figure 3.15: Schematic diagram of CL system used

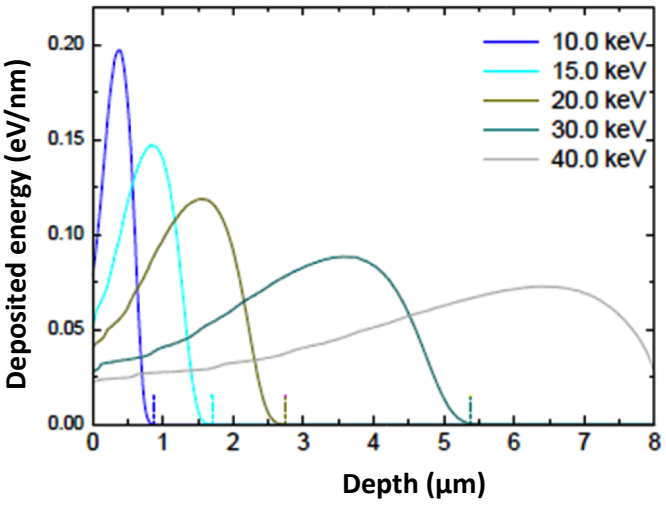

Figure 3.16: Deposited energy versus depth in diamond calculated by Monte-Carlo [Volpe 2009a]

Indeed, there is a relationship between the probe depth Z (μm) and electron (electron beam) energy E (keV) defined by the acceleration voltage: $Z = \alpha \times E^{\beta}$ ($\alpha = 0.02$, $\beta = 1.67$ [Kanaya 1972]). Probe depths of ~ 0.94 μm and ~ 1.84 μm are thus obtained for 10 keV and 15 keV respectively. The radiative electron-hole pair recombination (CL signal) will take place in the volume delimited by these probing depths, as shown in Figure 3.16 where the deposited energy is plotted versus probe depth for a given electron beam energy, as calculated by Monte-Carlo simulations [Volpe 2009a].

3.3.4.2 Results analysis

Figure 3.17 shows the 5K CL signal (normalized with respect to the FE peak intensity) obtained for both sample #1 and sample#3.

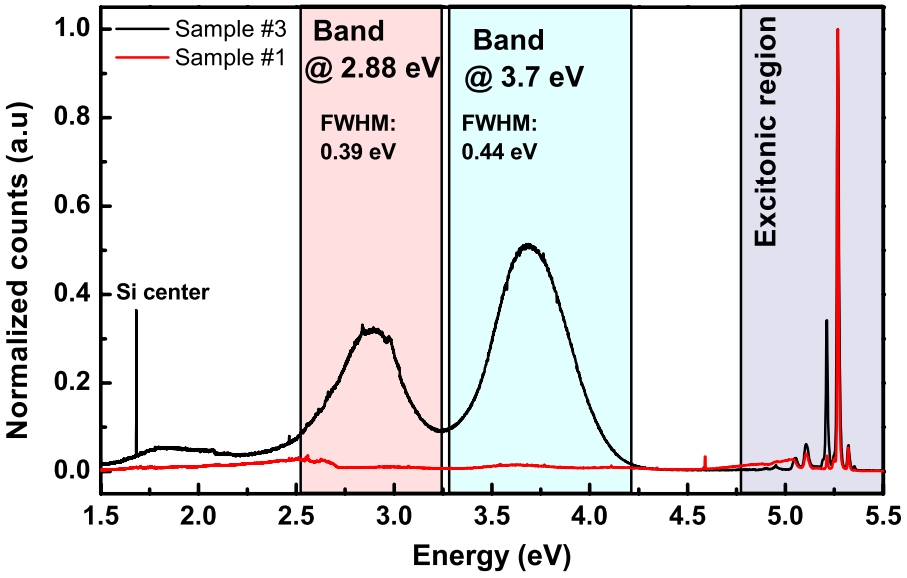

Figure 3.17: 5K cathodoluminescence spectrum for epi-layers growth in NIRIM type (sample #1) and PLASSYS BJ150 (sample #3) reactors.

Besides the excitonic region, The CL spectrum mainly exhibited broad bands around 2.88 eV (FWHM of 0.39 eV) and 3.7 eV (FWHM of 0.44 eV). The SiV center (interstitial Si, carbon vacancy complex) was also observed at 1.681, 1.682 eV [Zaitsev 2010]. The broad band around 2.88 eV is the blue band-A generally encountered for both single crystal and polycrystalline diamond, is well known as a feature of extended defects such as dislocations. Takeuchi et *al* [Takeuchi 2001] attributed such a band emission to sp^2 defects in diamond structures at incoherent grain boundaries and/or dislocations. Conversely, the band around 3.7 eV can be related to several origins. The main plausible origins are oxygen-related defects and boron related defects. Indeed, Mori et *al*

[Mori 1992] reported a broad band 3.75 eV (FWHM of 0.7 eV) as a feature of oxygen-related defects. In Mori's experiment, this band is supposed to appear due to oxygen diffusion in superficial diamond layer after treatment in $CrO_3 + H_2SO_4$ solution at 200 °C by H_2 treatment [Zaitsev 2010]. On the other hand, Lawson et *al* [Lawson 1995] reported a band around 3.5 eV (FWHM $\sim 0.5\ eV$) as a feature of boron related defects. Here, since oxygen is added to the gaseous mixture during epi-layer growth, one can assume that such an oxygen or boron incorporation in extended defects can occur.

The CL spectrum of sample #3 mainly exhibited both the band A and another band at 3.7 eV. The CL intensity of these band in sample #1 were negligible compared to those of sample #3. This can be interpreted as a consequence of a higher density of extended defects responsible for these band emissions in sample #3. Moreover, such a high CL intensity of Si centers indicates a higher Si incorporation in p^- layer grown on sample #3 while sample #1 can be considered as non-containing any Si according to its negligible Si center peak intensity. Such a silicon incorporation is commonly explained by an interaction of active chemical species such as CH_x with the silica present in the growth chamber. This interaction was supposed to be more intense in the PLASSYS reactor (sample #3) where the growth was performed at high pressure and high methane concentration. Moreover, the excitonic region exhibited a lower BE^{TO} CL intensity of excitonic for sample #1 (Fig. 3.18). This indicates a lower boron incorporation in sample #1 compared to sample #3. The estimated boron concentration by using equation(3.1) is $1.8 \times 10^{15} cm^{-3}$ and $1.2 \times 10^{16}\ cm^{-3}$ for sample #1 and sample #3 respectively. The obtained doping level for all samples reported in this work are summarized in table 3.4. The p^- layers grown in NIRIM type reactor (samples #1 and #2) have a similar boron concentration which is an order of magnitude lower than in the epi-layer grown in the PLASSYS BJ 150 reactor (sample #3).

3.3.4.3 Summary

5K CL spectroscopy was performed on epi-layers grown with both NIRIM type and PLASSYS BJ150 reactors. The layers grown in PLASSYS BJ150 reactor exhibited high Si incorporation and furthermore broad bands around 2.9 eV and 3.7 eV, which are assumed to be related to extended defects. On the other hand, the CL spectrum of epi-layers grown in NIRIM type reactor yielded a relatively lower radiative recombination point defects (silicon center) and extended defects (band A) when compared to the layer grown with PLASSYS BJ 150 reactor. Layers grown in NIRIM type reactor (samples

#1 *and* #2) have a boron atomic concentration ($\sim 10^{15}$ cm^{-3}) one order of magnitude lower than the epi-layer grown in the PLASSYS BJ 150 reactor ($\sim 10^{16}$ cm^{-3}).

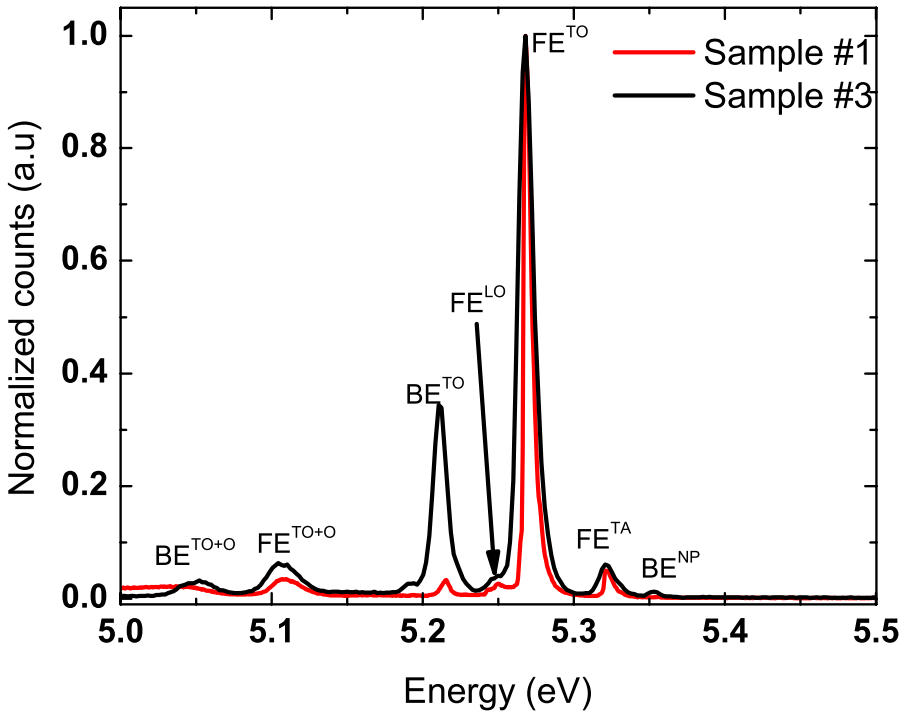

Figure 3.18: 5K CL spectrum in the excitonic region for samples #1 and #3.

3.4 Ohmic contact fabrication

Ohmic contacts are generally obtained by annealing carbide-forming metals deposited on diamond. Metal-diamond contact leads generally to a potential barrier because of the wide band gap of diamond. Thus, damaged diamond in contact region [Brandes 1999] by forming a carbide interfacial layer allows generating gap states which will lower the metal-diamond barrier height or enhance tunneling transport, or both [Tachibana 1992]. Apart from the carbide-forming metals requirement, ohmic contact will be selected according to the trade-off between various requirements such as a low contact resistivity, a good adhesion, a high thermal stability, and a bondable top-layer [Werner 2003]. The low contact resistivity $\rho_c = R_c \times S$ requirement is generally overcome by using a heavily doped diamond in the contact region. For boron doped diamond, the contact resistivity ρ_c can be approximated by a power-law [Werner 2003]: $\rho_C \sim N_A^{-n}$. For metallic contacts such as titanium (Ti) and molybdenum (Mo), n was found to be between 1.5 and 2.

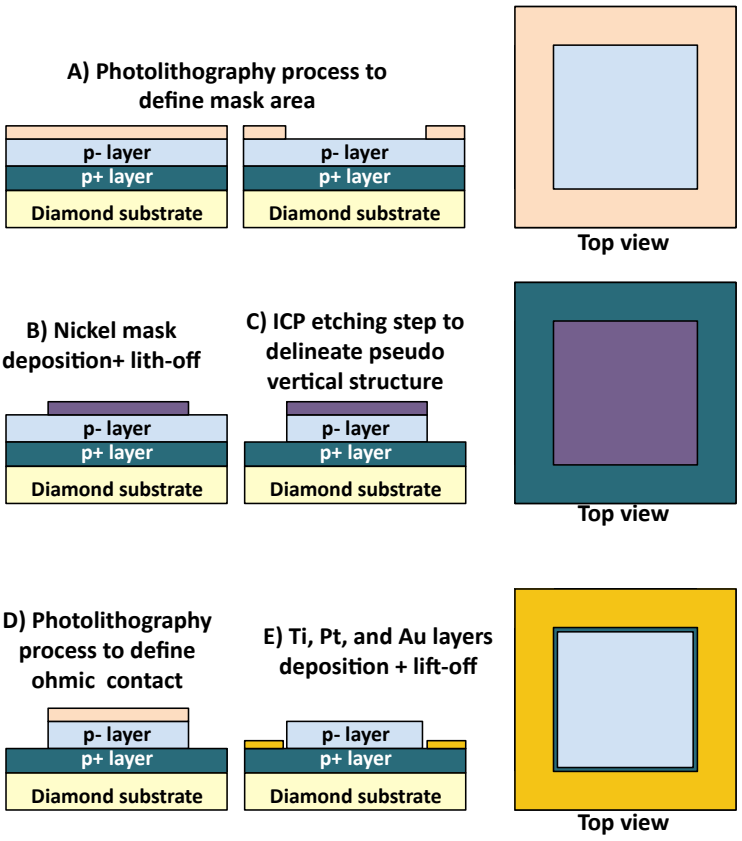

Figure 3.19: Schematic diagram of process flow towards pseudo-vertical structure fabrication.

Titanium (Ti) is one of the most commonly used metals to fabricate ohmic contacts on boron-doped diamond. Besides their relative good adhesion according to TiC interfacial layer formation, Ti ohmic contacts covered by stack comprising platinum (Pt) and gold (Au) cap layer have a good thermal stability (above 600 °C) and further a lower contact resistivity. For example, a ρ_C of 2×10^{-5} Ωcm^2 can be expected for a doping level N_A equal to 4.8×10^{20}cm^{-3}. This corresponds to a contact resistance of 20 mΩ for diode structure shown on Figure 3.1 where the ohmic contact surface is about 0.05 cm^2. Here, a (Ti/Pt/Au) metallic stack was deposited to obtain ohmic contact. Aiming to fabricate ohmic contacts on the heavily doped p^+ layer and thus delineate the pseudo-vertical structure, a selective Inductively Coupled Plasma (ICP) etching was undertaken.

ICP etching is a reactive ion etching process that allows an independent control of plasma density and reactive ion energy onto the etched surface. Accordingly, two radio frequency (RF) sources are therefore used in such etching reactors. The first RF source powers a coil generally wrapped around the etching chamber which, by an inductive coupling though a dielectric wall, allows plasma ignition and its control. The second RF source was used to power the substrate holder by capacitive coupling. Thus, it appears a

negative self bias on the holder that attracts the positive ion towards the etched surface and furthermore defines their kinetic energy. This second RF source defines both the etching rate and its anisotropy. The key parameters in such etching process are both the coil power (CP) and the substrate holder power (SHP). A CP power promotes a high density of reactive species. Conversely, a low SH power favours smooth etching by chemical reaction while a high SH power promotes a high etching rate and anisotropic etching by sputtering mechanism. Pure oxygen plasma etching was performed to delineate the pseudo-vertical structure with a 1000 W coil power, a 40 W platen power, a 100 sccm gas flow, and a 10 mTorr pressure. The CP and SH powers were selected to favour a smooth etching in order to preserve the selectivity of nickel etching mask used.

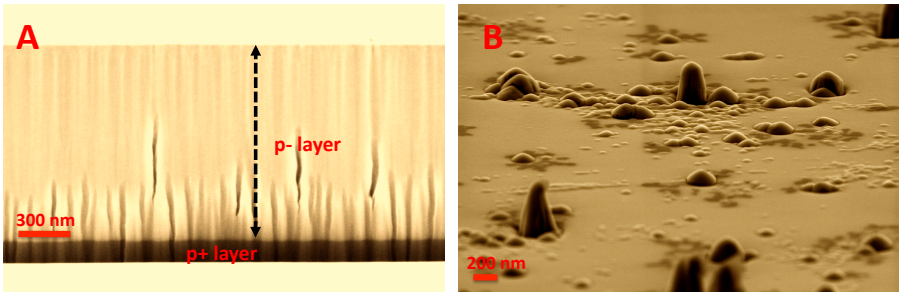

Figure 3.20: SEM images of etched diamond. A: an etching wall illustrating the epi-layers deposited, B : the surface state of etched parts where etches peaks appeared.

The process performed prior to this etching to define the etching area and thus the ohmic contact surface was briefly described on Figure 3.20. A photolithography process was first performed to delineate a square shaped masking area centered at the middle of the p^- layer (Fig. 3.20 step A). An electron beam evaporator was then used to deposit a 100 nm thick nickel mask followed by a lift-off process to define a square shape Ni mask (Fig. 3.20 step B). An ICP etching was then performed to completely etch the p^- layer down to the p^+ layer. Moreover, a 100 nm thick was etched in p^+ layer as shown the SEM image on Figure 3.20 to ensure the ohmic contact deposition on this heavily doped layer. The Ni mask was removed by chemical cleaning in hot aqua regia solution (150 °C). Ti (30 nm), Pt (50 nm), and Au (40 nm) layers were then successively deposited on p^+ layer by electron beam evaporator and was annealed at 750 °C to ensure titanium carbide interfacial layer formation (Fig. 3.20 step E).

3.5 Conclusion

A stack comprising an heavily doped layer and a slightly doped layer was grown on Ib (100) HPHT diamond samples in order to fabricate pseudo-vertical diamond Schottky diodes. The heavily doped layer was grown in a NIRIM type reactor and its growth conditions were set to get a doping level above the metallic transition level. This was expected to minimize its contribution to the diode serial resistance and obtain a negligible ohmic contact resistance. The slightly doped layers (diode active layers) were grown with NIRIM type reactor or a commercial reactor PLASSYS BJ150. Due to its high power microwave cavity, PLASSYS BJ150 was used to grow thick layer and therefore minimize defects generation on epi-layer surface. Active layers were non-intentionally doped in order to get a boron incorporation below 10^{17} cm^{-3}. The epi-layers (sample #1 and #2) grown on NIRIM type reactor were contaminated by unepitaxial crystals, which are known to lead to a high leakage current in the reverse regime. The CL spectrum of epi-layers grown in NIRIM type reactor point out their relatively lower radiative point defects (Si center) and extended defects (band-A) contents when compared to the layer grown with the PLASSYS BJ 150 reactor. Conversely, the epi-layers (sample #3) grown on the PLASSYS BJ150 were free of unepitaxial crystals. Accordingly, sample #3 was mainly used to fabricate large area devices. The active layer was etched back in order to fabricate the ohmic contact on highly doped layer thus delineating the pseudo vertical structure as shown on Figure 3.1. Ti (30 nm), Pt (50 nm), and Au (40 nm) layers were then successively deposited on heavily doped layer by electron beam evaporator and annealed at 750 °C to ensure titanium carbide interfacial layer formation (Fig. 3.20). Table 3.4 summarizes the main specifications (size, epi-layer growth, thickness, expected doping level estimated by CL and ohmic contact resistance) of the set of samples reported in this thesis. The final step that of Schottky metal deposition, will be introduced in the next chapter.

Table 3.4: Experimental details of growths described in this chapter. Epi-layers growth conditions, their thicknesses (deduced from Ellipsometry), and their expected acceptor concentrations (estimated by CL spectroscopy) are reported. The theoretical Ohmic contact resistance on the p^+ layer is also mentioned. **(1)** *growth performed with NIRIM type reactor,* **(2)** *growth performed with PLASSYS BJ150 reactor*

Sample	Substrate	Layer	Growth conditions					Thickness	[B]	R_C
			CH_4/H_2	O_2/H_2	[B]/[C]	T	P		(cm^{-3})	
#1	Ib (100) HPHT	p^+ (1)	4%	-	1200 ppm	830 °C	33 Torr	400 nm	$> 5\times10^{20}$	20 mΩ
	3×3 mm^2	p^- (1)	0.75%	0.25%	Residual	910 °C	50 Torr	1.3 μm	$\sim 10^{15}$	-
#2	Ib (100) HPHT	p^+ (1)	4%	-	1200 ppm	830 °C	33 Torr	400 nm	$> 5\times10^{20}$	20 mΩ
	3×3 mm^2	p^- (1)	0.75%	0.25%	Residual	910 °C	50 Torr	1.3 μm	$\sim 10^{15}$	-
#3	Ib (100) HPHT	p^+ (1)	4%	-	1200 ppm	830 °C	33 Torr	400 nm	$> 5\times10^{20}$	0.05 mΩ
	4.5×4.5 mm^2	p^- (2)	4%	0.75%	Residual	940 °C	150 Torr	2.5 μm	$\sim 10^{16}$	-

Chapter 4

Rectification behavior of Zirconium (Zr) electrodes on diamond

Contents

4.1 Introduction

This chapter introduces the final fabrication step of pseudo vertical diamond Schottky diodes. The Schottky metal deposition process and the electrical characteristics of the fabricated devices will be discussed. Besides the defects minimization in the diodes active layer as discussed in chapter 3, the electrical performances of diamond-based rectifiers will be correlated to the selected Schottky metal and the interface with diamond. Schottky metal must be selected to ensure good adhesion, thermally and chemically stable interface, and a potential barrier leading to an optimum forward losses (a low forward voltage drop) and minimal reverse current even at high temperatures. Conversely to an ohmic contact where a high density of gap states (or interface states) is promoted by forming a carbide interface layer, the main issue towards high performance diodes, fully exploiting the diamond's electrical and thermal properties, is to prevent the carbide formation while minimizing the interface states.

In this respect, diamond surface oxygenation, known to be an efficient way to minimize electronic states on diamond surface [Teraji 2009a], was adopted by several research groups as being the first step of the Schottky contacts deposition process [Muret 2011, Umezawa 2012, Ueda 2014]. Unfortunately, the Schottky barrier height on oxygen-terminated surface was generally larger than 2 eV (high forward losses). On the other hand, according to the Schottky electrodes selected, the rectifiers can be thermally unstable (alteration of the rectification behaviors) due to dissociation of oxygen bonds. Such thermal dissociations of the oxygen bonds was observed for inert metals such as gold [Teraji 2009b, Teraji 2014] (above 500 K) as well as for easily oxidizable metals like aluminum due to the thermal instability of the interface layer formed with diamond. An alternative solution to diamond surface oxygenation is reported in references [Teraji 2014, Fiori 2014]. It was established that carbide-preformed metals such as tungsten carbide (WC) have a better thermal stability up to 600 K. WC Schottky are annealed in the range of 560 K and 600 K in order to allow interfacial bonding between WC and diamond [Teraji 2014, Fiori 2014]. However, an operating temperature higher than 600 K induced a degradation of WC based diamond rectifiers [Fiori 2014].

In this thesis, a different approach was adopted. Conversely to the radical solution of the carbide-preformed metals, the Schottky metal was selected in such a way to favor a thin oxide interface. Aiming to fulfill this requirement, easily oxidizable refractory metals such as zirconium (Zr) was envisaged as potential candidate. This chapter will be

focused on the fabrication and the electrical characterization of pseudo-vertical architecture based on an oxygen-terminated diamond surface covered by Zr metal. Zr Schottky contact deposition process together with its interface investigation by High-Resolution Transmission Electron Microscopy (HRTEM) and Electron Energy Loss Spectroscopy (EELS) will be firstly introduced. The room temperature electrical characteristics followed by their thermal stability will be presented and discussed. Finally, the electrical characteristics of annealed Zr/oxygen-terminated diamond junction will be investigated.

4.2 Schottky contact

According to the difference of work functions, a Metal - Semiconductor (MS) junction will be a ohmic contact or a rectifier (Schottky contact). In our case where a p-type semiconductor is used, an ohmic contact is formed when the metal work function (ϕ_m) is higher than that of the semiconductor (ϕ_s) whereas a rectifier (Schottky contact) is obtained when $\phi_m < \phi_s$. This is well explained by the Schottky-Mott theory stating that the band alignment of a MS junction is related to a charges transfer from one side to other aiming to force the Fermis levels to coincide.

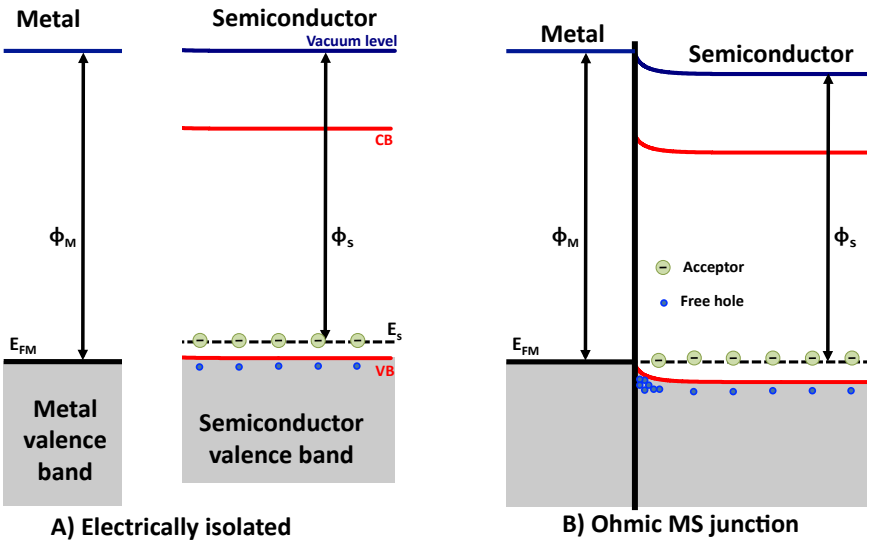

Figure 4.1: Band structure of ohmic metal/p-type semiconductor junction at thermal equilibrium: A) Electrically isolated metal and p-type semiconductor, B) band alignment at thermal equilibrium.

4.2.1 Ohmic contact

The band structure of an ohmic MS junction is shown on Figure 4.1. For a p-type semiconductor, when $\phi_m > \phi_s$, the band alignment at thermal equilibrium leads to an upward semiconductor band bending at the interface related to a hole accumulation (Fig. 4.1 B)). If such a junction is biased (V) so that holes flow from the semiconductor to the metal, they encounter no barrier. Moreover, in reverse direction, the upward band bending related to hole accumulation at the interface, behaves like an anode (holes source), which will provides a copious supply of holes [Rhoderick 1978]. The resistance (R) of the semiconductor will therefore determine the electrical current (I) via the ohmic law $V = R \times I$.

4.2.2 Schottky contact

When the metal work function is lower than that of the semiconductor (Fig. 4.2 A)), the band alignment gives rise to a built-in potential barrier the so-called Schottky barrier ϕ_b at the interface (Fig. 4.2 B)) and a downward semiconductor band bending.

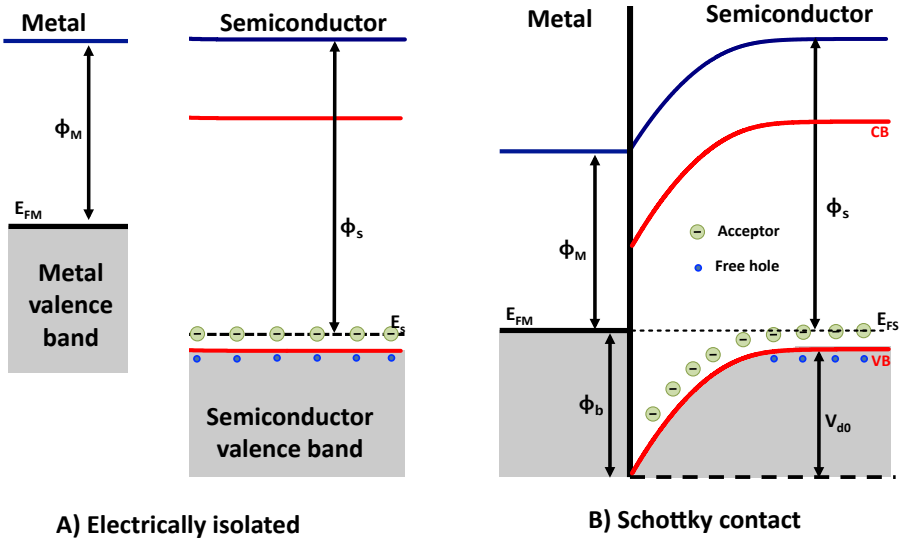

Figure 4.2: Band structure of metal/p-type semiconductor Schottky junction at thermal equilibrium: A) Electrically isolated metal and p-type semiconductor, B) band alignment at thermal equilibrium.

As stated by the Schottky-Mott theory, the potential barrier arises because of a charges transfer from the semiconductor (higher Fermi level) to the metal. The charges transferred, here holes, leave behind uncompensated acceptor atoms and furthermore a positive charges accumulation on the surface of the metal (extra conduction carrier contained

within a Thomas-Fermi screening distance ~ 0.5 Å [Rhoderick 1978]). At thermal equilibrium as shown on Figure 4.2 B), the band alignment involves a downward semiconductor band bending (diffusion potential V_{d0}) related to the negatively charged acceptor atoms the depletion region and an abrupt barrier in the metal side (ϕ_b). V_{d0} is the potential barrier that encounters free carrier diffusing towards the metal whereas ϕ_b inhibits carrier injection from the metal to the semiconductor. The ideal Schottky Barrier Height (SBH) is defined by the Mott equation:

$$\phi_b = E_g/q - (\phi_m - X_s) \tag{4.1}$$

where X_s is the Electron Affinity (EA) of semiconductor and q the elementary charge. Under zeros bias and for a slightly doped semiconductor (Fermi level close to acceptor level), V_{d0} can be approximated as followed $qV_{d0} \simeq q\phi_b - E_a$, where and E_a is the acceptor ionization energy. Under applied bias V, this potential becomes $qV_d = qV_{d0} + qV$. Accordingly, the barrier V_d is lower under forward bias (Fig. 4.2 A)) thus favoring a carrier injection from the semiconductor to the metal (J_{sm}). Figure 4.2 B) shows the reverse situation where the diffusion potential increases versus reverse bias V_r. The electrical current (J_{ms}) in this latter case is induced by a carrier injection from the metal to the semiconductor.

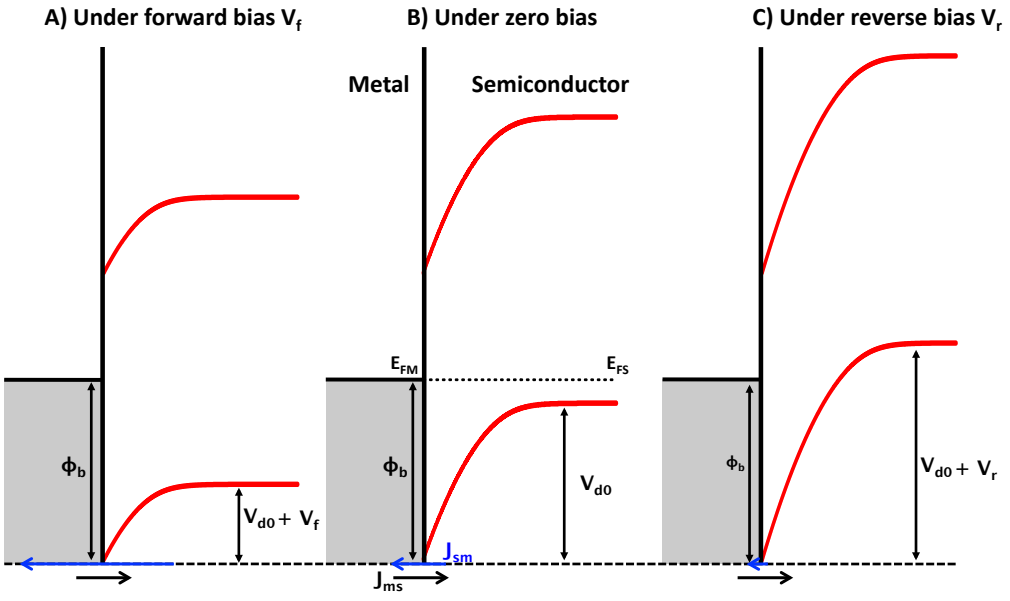

Figure 4.3: Band structure of metal/p-type semiconductor Schottky junction at thermal equilibrium (middle), under forward bias (left), and under reverse bias (right).

4.2.3 Real MS contacts

Before introducing the carrier transport mechanisms over a Schottky contact, it has to be noticed that the ideal junctions discussed in subsection 4.2 are rarely encountered in practice. For most of semiconductors, a metallic electrode generally leads to a rectifier. As discussed in Chapter 3, an ohmic contact is generally obtained by annealing a MS junction in order to damage the semiconductor in the contact region thus generating gap states and so, the lowering of the potential barrier at the interface or an enhancement of tunneling transport, or both [Tachibana 1992]. Moreover, experimental SBHs are generally less sensitive function of the metal work function [Rhoderick 1978] contrary to the Mott equation. This discrepancy is explained by interface states present in the junction area as suggested by Bardeen in 1947. Interfaces states are commonly ascribed to the imperfections in the junction area (dangling bonds, surfaces defects, etc). In practice, MS junctions can be defined by the Bardeen model shown on Figure 4.4. This model assumes the presence of a thin interface layer separating the metal and the semiconductor and a continuous distribution of interface states at the semiconductor surface.

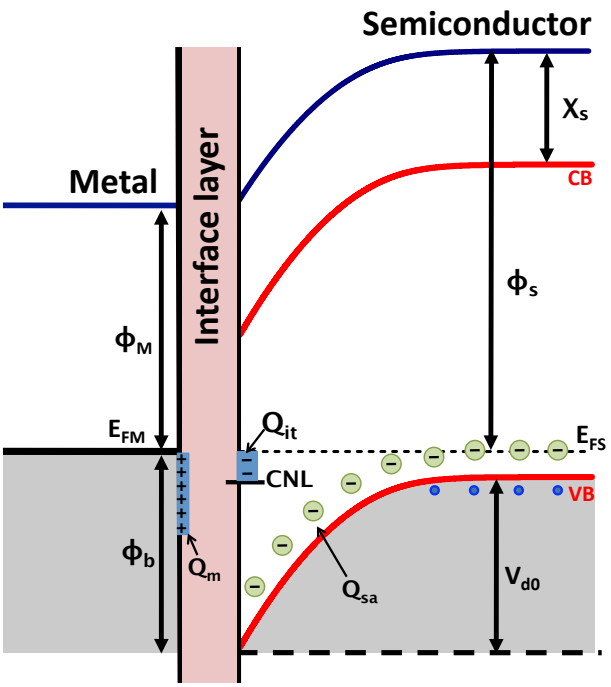

Figure 4.4: Band diagram of metal-semiconductor junction with an interface layer.

Bardeen's model is in good agreement with diamond rectifiers since diamond surface is passivated (hydrogen or oxygen termination) prior Schottky electrodes deposition thus leading to an interface layer. For conventional semiconductor such as Si or SiC, an intimate (abrupt) junction can be obtained by performing a silicidation of a portion of semiconductor to form a metal (Schottky electrodes). On the other hand, a continuous distribution of interface states always exists even for ideal MS junction (abrupt, without imperfections like dangling bonds or atoms vacancies for example) as stated by Heine's MIGS (Metal Induced Gap States) concept. Heine's MIGS concept defines a continuum virtual gap states at the junction interface originated from the metal's electron wave functions tailing in the semiconductor. The interface states are defined by their neutral level ϕ_0 (Charge-neutrality level CNL). Depending on whether the CNL

level is above or below the Fermi level, the surface states will contain a net negative or positive charge Q_{it} thus leading to the modification of the neutrality condition at the interface $Q_m = -(Q_{sa} + Q_{it})$ [Rhoderick 1978], where Q_m is the positive charge on the surface of the metal, Q_{sa} the negative charge associated to the depletion layer. The depletion layer and so the SBH will be adjust according to the amount Q_{it}. For a high density of interface states, the barrier defined by the Bardeen limit, is said to be 'pinned':

$$\phi_b \approx \phi_0 \tag{4.2}$$

SBH is then expected to vary between the limits define by the Mott equation and the Bardeen limit. The CNL level is generally about one third of band gap E_g for classical semiconductors such as Si where the experimental Bardeen limits for electron and hole SBH are respectively 0.75 eV ($E_g - \phi_0$) and 0.37 eV ($\phi_0 \approx E_g/3$) [Cowley 1965].
For diamond, CNL level related to Heine's concept was found to be 1.4 eV [Mönch 1994]. However, the surface termination (hydrogen or oxygen-terminated diamond) induces an additional dipoles layer in the junction region and highly affects this neutrality level.

4.3 Transport mechanisms

A basic schematic view of the non-linear current transport feature of a Schottky contact under an applied bias voltage was introduced in the previous section. Here, the transport mechanisms and the theoretical laws quantifying the electrical current across a Schottky contact will be presented with the emphasis on a p-type diamond.

4.3.1 Bias dependence of Schottky barrier height

The SBH expressions defined previously are only valid for a zero-bias voltage. Once a bias voltage is applied, the SBH changes even for ideal junction because of intrinsic mechanisms such as the image-force (the Schottky effect) and furthermore due to the influence of imperfections in junction area.

4.3.1.1 Schottky effect

The Schottky effect is a consequence of the requirement that the electric field at MS interface must be perpendicular to the metal (Schottky electrode) since its surface is an equipotential (no parallel current on its surface). Thus, as for metal-vacuum system,

this condition is satisfied by considering the Coulomb interaction (force of attraction) between a charge carrier located at a distance x in semiconductor and its mirror image charge (an electron if holes are majority carrier in semiconductor) at $-x$ in the metal[Rhoderick 1978, Sze 2007].

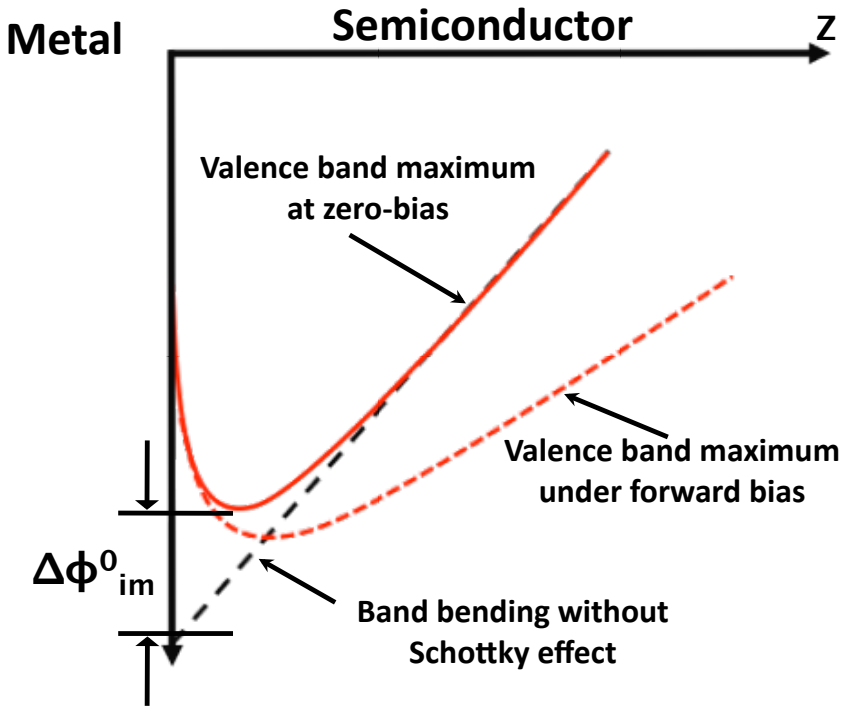

Figure 4.5: Schematic diagram of metal/p-type semiconductor junction illustrating the Schottky effect.

This consideration affects the carrier injection from one side to the other by inducing a barrier variation $\Delta\phi_{im}$ near the interface expressed as followed:

$$\Delta\phi_{im} = \sqrt{\frac{qE_m}{4\pi\epsilon_s}} \tag{4.3}$$

Accordingly, the Schottky barrier ϕ_b taking into account only the image force, is defined as followed (V_j is the voltage drop across MS junction):

$$\phi_b = \phi_{b0} - \sqrt{\frac{qE_m}{4\pi\epsilon_s}} \tag{4.4}$$

ϕ_{b0} is the zero-bias SBH without the image force lowering and E_m is the maximum field in the depletion region:

$$E_m = \sqrt{\frac{2qN_A(V_{d0} + V_j)}{\epsilon_0\epsilon_s}} \tag{4.5}$$

The following expressions point out the fact that the SBH is reduced even at zero-bias

due to the Schottky effect as illustrated on Figure 4.5. The zero-bias SBH ϕ_b^0 is then given by:

$$\phi_b^0 = \phi_{b0} - \Delta\phi_{im}^0 \approx \phi_{b0} - \left(\frac{2q^3 N_A}{(4\pi)^2 \epsilon_s^3} V_{d0}\right)^{1/4} \tag{4.6}$$

Moreover, when the electric field increase in the junction area i.e. under a reverse bias, the built-in potential barrier is reduced thus favoring the carrier injection from the metal to the semiconductor. Note that in this situation, the carrier injection from the semiconductor to the metal is inhibited by a high potential barrier (diffusion potential).

Under forward bias V_f, the SBH is still bias-dependent and conversely to reverse case, it is higher than ϕ_b^0 (confer Fig. 4.5) and the electrical current is defined by a carrier emission from the semiconductor to the metal. The bias dependence of SBH in the forward state is generally expressed as [Mönch 2004]:

$$\phi_b(V_f) = \phi_b^0 + (1 - 1/n_{if})\, V_f \tag{4.7}$$

where V_f is the voltage drop across the depletion layer and n_{if} is a bias-independent parameter called the ideality factor related to the Schottky effect only [Mönch 2004]:

$$n_{if} = \left(1 - \frac{\Delta\phi_{im}^0}{4qV_{d0}}\right)^{-1} \approx \left[1 - \frac{1}{4q}\left(\frac{2q^3 N_A}{(4\pi)^2 \epsilon_s^3}\right)^{1/4} (V_{d0})^{-3/4}\right]^{-1} \tag{4.8}$$

From equation 4.8, n_{if} tends towards unity for a high zero-bias diffusion potential V_{d0} and so for a high SBH. It has to be noticed that even for a low SBH, n_{if} is generally close to 1 for most of semiconductors. As example, for a p-type diamond doped at 10^{16} cm^{-3}, n_{if} is expected to be 1.005, 1.008, and 1.009 for respectively 2 eV, 1 eV, and 0.9 eV zero-bias barrier height. Thus, the SBH should be less sensible (quasi constant barrier) to forward applied bias voltage if the image force is only considered.

4.3.1.2 Real Schottky contact

The image force effect is generally not enough to explain the bias dependence of SBH. Indeed, the static dipoles and the states linked to the imperfections at MS interface also contribute to lower the SBH. The forward state is still described by the linear bias dependence mentioned above but the ideality factor is no longer related to the Schottky effect only. Under reverse bias, the SBH lowering is generally defined using the empirical

expression established by Andrews and Lepselter [Andrews 1970, Tung 1992]:

$$\begin{aligned} \phi_b(V_r) &= \phi_b^0 - \Delta\phi_{im} - \alpha E_m \\ &= \phi_b^0 - \left(\frac{2q^3 N_A}{(4\pi)^2 \epsilon_s^3}\left[V_{d0} + Vr\right]\right)^{1/4} - \alpha\left(\frac{2qN_A}{\epsilon_s}\left[V_{d0} + Vr\right]\right)^{1/2} \end{aligned} \tag{4.9}$$

α is a constant supposed to be related to the density and depth of interface states [Tung 1992, Parker 1968]. The bias dependence of the SBH mainly alters the reverse state since it increases the reverse current by continuously reducing the Schottky barrier height. However, a high reverse electric field in junction area induces carrier tunneling in the semiconductor, which can be the limiting transport mechanism and then define the electrical current.

4.3.2 Forward currrent

The carrier transport across a Schottky barrier under forward bias can contain the contribution of several mechanisms such as the thermionic emission, the recombination in depletion region, the diffusion mechanism, ...
The thermionic emission and the diffusion mechanism are generally the limiting mechanisms in the forward state. Thermionic mechanism is the thermally excited carrier emission over the top of Schottky barrier whereas the diffusion current depends on drift and diffusion phenomena in the junction region. For most of reported diamond rectifiers, the forward current is generally ascribed to a thermionic emission mechanism without any justification. Aiming to confirm this assumption theoretically for devices operating at room temperature and at high temperatures such as 500 K (the full boron ionization temperature range for slightly doped diamond), both diffusion and thermionic mechanisms will be introduced and the Bethe's criterion will be evaluated for each temperature.

4.3.2.1 Theoretical background

Let's first consider the general expression of the electric current taking into account both the thermionic mechanism and the diffusion mechanism (the thermionic-emission-diffusion model [Sze 2007]):

$$J_{TED} = \frac{qN_v v_R}{1 + v_R/v_D} \exp\left(-\frac{q\phi_b}{k_B T}\right)\left[\exp\left(\frac{qV_j}{k_B T}\right) - 1\right] \tag{4.10}$$

N_v is the effective density of states in the valence band, T is the temperature, k_B is the Boltzmann constant, and V_j is the forward bias voltage. v_R is the thermionic recombination velocity defining the carrier recombination velocity near the metal-semiconductor interface. The maximum value of v_R depends on the average thermal velocity [Mönch 2004] as followed:

$$v_R^{max} = \frac{< v_{th} >}{4} = \frac{1}{4}\left(\frac{8k_B T}{\pi m^*}\right)^{1/2} \tag{4.11}$$

On the other hand, v_D is defined as an effective carrier diffusion velocity from the edge of depletion layer (bulk region) to the potential energy maximum in the junction region [Sze 2007, Mönch 2004]. This velocity is approximated as followed [Mönch 2004]:

$$v_D \approx \frac{qD_p}{k_B T} E_i = \mu_p E_i, \quad E_i = \sqrt{\frac{2q\left(V_{d0} - V_j\right) N_a}{\epsilon_0 \epsilon_s}} \tag{4.12}$$

μ_p and D_p are the hole mobility and the diffusion constant, respectively. N_a is the doping level, ϵ_0 vacuum permittivity, and ϵ_s the relative permittivity of the semiconductor. v_D is dependent on the forward bias V_j and tends to decrease versus V_j. On the other hand, since the carrier mobility μ_p decreases versus T because of the scattering phenomenon (the optical phonon scattering in case of diamond [Pernot 2010] occurring when T is higher than 400 K for slightly doped material), v_D will be lower at high temperature whereas the thermal velocity which increases versus the square root of T. Thus, according to the ratio v_R/v_D, the diffusion or thermionic emission will be the limiting mechanism:

Diffusion current (J_D) $v_D << v_R$:

The forward current can be ascribed to the diffusion mechanism if v_D is much lower than v_R ($v_D << v_R$). The current-voltage relationship is then defined as followed:

$$J_D = {J_0}^{diff}\left[\exp\left(\frac{qV_j}{k_B T}\right) - 1\right] \tag{4.13}$$

where ${J_0}^{diff}$ is the saturation current and defined as :

$$\begin{aligned} {J_0}^{diff} &= qN_v v_D \exp\left(-\frac{q\phi_b}{k_B T}\right) \\ &= qN_v \mu_p E_i \exp\left(-\frac{q\phi_b}{k_B T}\right) \end{aligned} \tag{4.14}$$

Thermionic emission current (J_{TE}) $v_D >> v_R$:

If v_D is greater than v_R ($v_D >> v_R$), the electrical current over a Schottky contact will be related to the thermionic emission. The thermionic current is defined as followed:

$$J_{TED} = J_{TE} = {J_0}^{thermo}\left[\exp\left(\frac{qV_j}{k_B T}\right) - 1\right] \tag{4.15}$$

The saturation current for a thermionic model is given by :

$$\begin{aligned} {J_0}^{thermo} &= qN_v v_{coll} \exp\left(-\frac{q\phi_b}{k_B T}\right) \\ &= A^* T^2 \exp\left(-\frac{q\phi_b}{k_B T}\right) \end{aligned} \tag{4.16}$$

A^* is the effective Richardson constant related to the isotropic current flow from both light and heavy holes in case of p-type materials. This constant is expressed as $A^* = (m^*_{lh} + m^*_{hh})A/m^0$, where m^*_{lh} is the effective mass of light hole, m^*_{hh} that of heavy hole, and m^0 the effective mass of free electron. $A = 4q\pi m^0 k_B^2/h^3$ is the Richardson constant for free electron ($A = 120$ Acm^{-2}K^{-2}). For diamond where three uppermost valence bands have their maximum located at Γ the point of Brillouin zone (heavy and light holes bands degenerated at Γ and the spin-orbit band positioned at 13 meV below), only light and heavy holes are still considered. Indeed, for (100)-oriented boron doped diamond used in this thesis ($m^*_{hh} = 0.427$, $m^*_{lh} = 0.366$, $m^*_{hh} + m^*_{lh} = 0.793$ [Willatzen 1994, Pernot 2010]), the Richardson constant commonly used is 90 Acm^{-2}K^{-2} suggesting that the spin-orbit band must be unoccupied or its contribution is negligible.

4.3.2.2 Bethe's criterion

According to the condition defined above ($v_D >> v_R$), Bethe put forward a criterion stating that the thermionic emission theory applies if at the top of the depletion layer,

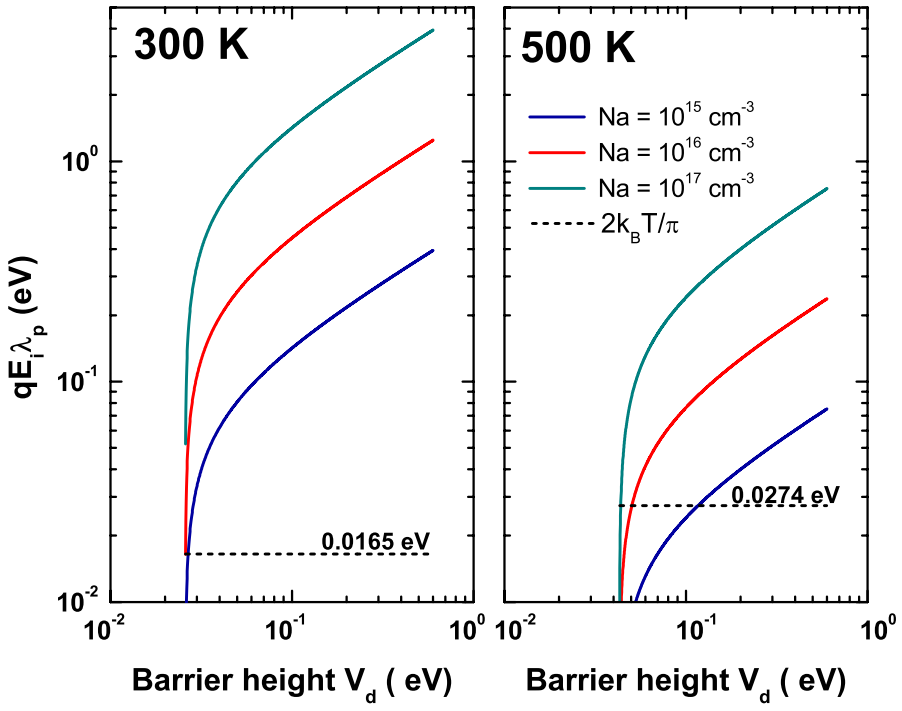

Figure 4.6: Bethe's criterion for p-type diamond Schottky diodes operating at 300 K and 500 K. The criterion was illustrated for different acceptor concentration.

the potential energy changes by more than k_BT within a distance of one mean free path λ_p [Mönch 2004] :

$$qE_i\lambda_p >> \frac{2k_BT}{\pi} \tag{4.17}$$

Since the electric field E_i right at the interface depends on the doping level and the barrier height (the diffusion potential $qV_d = q(V_{d0} - V_j)$) that encountered the carrier injected from the semiconductor in the metal, Mönch [Mönch 2004] reported that the Bethe's criterion is satisfied for n-type Si within a donor density above 10^{16} cm^{-3} and $qV_d > 0.4$eV.

Figure 4.17 shows the Bethe's criterion for p-type diamond Schottky diodes operating at 300 K and 500 K. The mean free path was calculated using the relaxation-time approximation and the maximum mobility at 300 K (2000 cm^2/Vs) and 500 K (300 cm^2/Vs) [Pernot 2010]. For diamond Schottky diodes, Bethe's criterion is satisfied at 300 K if the diffusion potential qV_d is higher than 0.05 eV. This low limit which can be assigned to the flat band situation where semiconductor serial resistance is the limiting parameter (ohmic regime), demonstrates that the electrical current over diamond Schottky diodes (at room temperature) will be a thermionic emission current. This is still true even for devices operating at 500 K if the doping level (acceptor concentration) is higher than 10^{15} cm^{-3} and qV_d higher than 0.1 eV.

4.3.2.3 Forward current

It has been established that the TE mechanism is appropriated to define the electrical current across diamond rectifiers even at high temperature when the doping level is higher than 10^{15} cm^{-3}. Taking into account the bias dependence of the SBH and the bulk resistance Rs, the TE model introduces above, is commonly rewrites as followed:

$$I = I_S \exp\left(\frac{q(V - R \times I)}{n k_B T}\right)\left[1 - \exp\left(-\frac{q(V - R \times I)}{k_B T}\right)\right] \tag{4.18}$$

where I_S is the saturation current:

$$I_S = A^* S T^2 \exp\left(-\frac{q\phi_b^0}{k_B T}\right) \tag{4.19}$$

S is the diode area and n the ideality factor defined as :

$$\frac{1}{n} = 1 - \beta = 1 - \left(\frac{\partial \phi_b}{\partial V_j}\right) \tag{4.20}$$

The ideality factor is a key indicator of rectifiers. If n close to 1 ($\beta \to 0$), the rectifier can be considered as ideal (abrupt and free of defects).

4.3.3 Reverse current

The reverse current of diamond rectifiers should be then explained by a thermionic emission mechanism. Such a reverse current is bias dependent because of the Schottky effect and expressed as:

$$J(V_j) = A^* T^2 \exp\left(-\frac{q(\phi_b^0 - \Delta\phi_{im}(V_j) - \alpha E_m(V_j))}{k_B T}\right) \tag{4.21}$$

However, the TE mechanism is enhanced by the tunneling of thermally excited carrier occurring in the thinner extension part of the potential barrier (Thermionic-Field Emission TFE) when a high electric field is applied. The general expression describing the TFE current was established by Padovani and Stratton [Sze 2007]. Moreover, Honeisen and Mead's expression is an alternative simple way to estimate the TFE current [Rhoderick 1978]. This latter expression will be preferentially used in this work. Anyway, Honeisen and Mead's expression is commonly rewritten in order to include the Schottky effect. The TFE reverse current is then defined as followed ($V = Vr + V_{d0}$,

$E_{00} = 18.5 \times 10^{-15}(N_a/(5.7m^*))^{0.5}$) [Umezawa 2007]:

$$J = \frac{2A^*(q\pi TV)^{1/2}qE_{00}}{k_B^{3/2}} \exp\left(-\frac{q(\phi_b^0 - \Delta\phi_{im} - \alpha E_m)}{k_B T} + \frac{q^3 V E_{00}^2}{3(k_B T)^3}\right) \tag{4.22}$$

4.4 Summary

In conclusion, the electrical properties of Schottky contact were introduced. For such a metal/semiconductor junction, the current transport depends on the built-in potential barrier (the Schottky barrier) and the depletion layer induced in the semiconductor side. The modulation of this layer (and so the potential barrier encountered by carrier flowing from the semiconductor to the metal) i.e. its increase or decrease by applying an external bias (V) gives rise to a non-linear current transport feature as shown on Figure 4.7:

On-state: Under forward bias (on-state), the depletion region decreases. The diffusion potential limiting the carrier injection from the semiconductor bulk (electrically neutral part) to the Schottky electrode, is attenuated. The electrical current increases exponentially versus the forward bias due to a thermionic emission mechanism. When the flat-band situation corresponding to the disappearance of the depletion region (diffusion potential close to zero) is reached, the on-state is characterized by a linear current-voltage (I-V) relationship $\Delta I = \Delta V/Rs$ (ohmic regime), where Rs is the semiconductor resistance (diode serial resistance). The on-state is then defined by:

- **The forward voltage drop ascribed to the threshold voltage (the extrapolation of the linear current part as shown on Figure 4.7) related to the SBH**
- **The serial resistance *Rs* defined by the semiconductor resistivity and the rectifier design (shape, area, ...)**

The voltage forward drop has to be as low as possible (lower SBH) in order to minimize the forward losses ($P = V \times I$). For silicon and silicon carbide Schottky diodes, the typical forward voltage drop is ranging between 0.15 V and 0.8 V whereas for most of the reported diamond rectifiers, this voltage drop was higher due to a high SBH (above 2 eV). Moreover, for diamond devices, the serial resistance decreases for a high operating temperature contrary to Si and SiC-based devices.

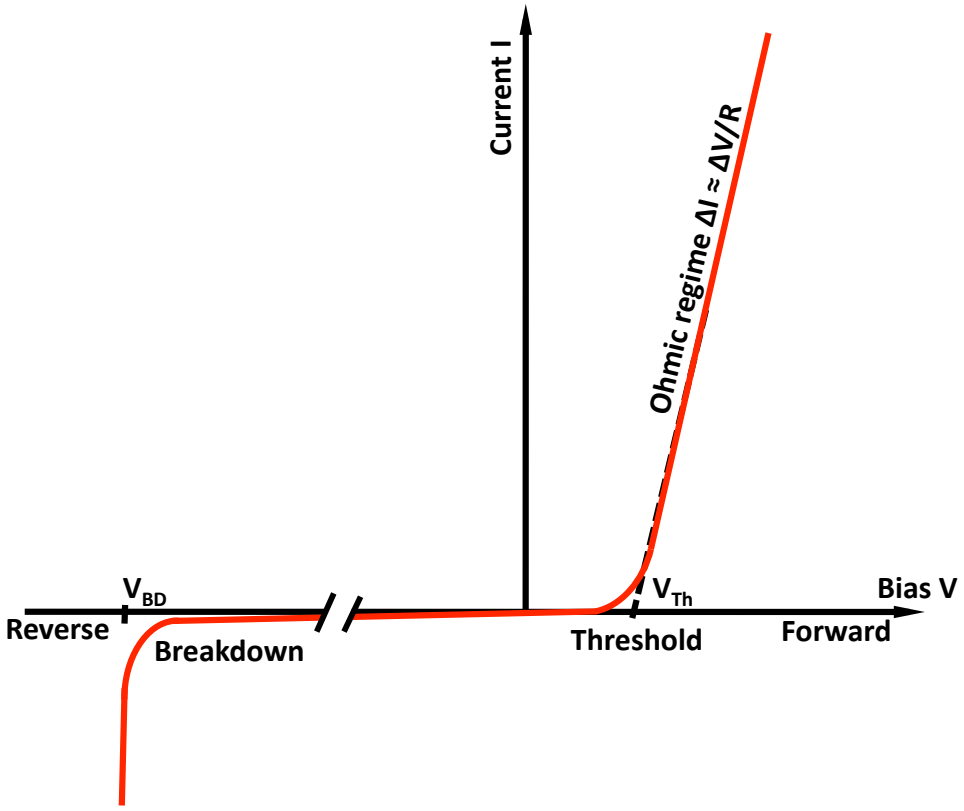

Figure 4.7: Current-voltage (I-V) characteristic of Schottky diode.

Off-state: Under reverse bias (off-state), the depletion region increases versus bias thus leading to a higher diffusion potential and so the inhibition of free carrier injection from the semiconductor to the Schottky electrode. The electrical current in this off-state (the leakage current) is ascribed to carrier injection from the metal to the semiconductor through Schottky barrier. The reverse current of an ideal Schottky contact (defects free junction) is several orders of magnitude lower than the forward current and increases (slowly for ideal diode) versus reverse bias because of barrier lowering mechanisms together with the thermionic-field emission mechanism. When the electrical field related to the diffusion potential in the junction region reaches the semiconductor critical field, the devices undergoes avalanche breakdown. The reverse performances of Schottky diode will be defined by:

- **The maximum blocking voltage**
- **The reverse current**

For vertical diamond Schottky diode or the pseudo-vertical structure adopted for our devices, defects such as dislocations [Umezawa 2012, Ohmagari 2011] propagates from the heavily doped substrate (highly conductive substrate) in the diode active layer during

epitaxial growth. As consequence, the obtained critical field (2.1 MV/cm [Umezawa 2013], 2.7 MV/cm [Kumaresan 2010]) even with a field plate structure used to avoid the edge field enhancement [Ikeda 2009], is much lower compared to those found for lateral diamond Schottky diodes (7.7 MV/cm [Volpe 2010]) and to the very first value reported for diamond (higher than 10 MV/cm) [Landstrass 1993].

For pseudo-vertical devices fabricated in this thesis, a thin highly conductive layer (p^+ layer) was grown in order to minimize defects generation and then improve the quality of diode active layer (p^- layer) by reducing defects propagation from the p^+ layer in the p^- layer. On the other hand, zirconium was identified as the best candidate to form a thermally and chemically stable interface without alter the oxygen passivation layer. The following parts will introduce the deposition process of Zr Schottky electrodes and discuss their electrical feature using the theoretical laws described in this background section.

4.5 Zr Schottky deposition process

4.5.1 Experimental setup

Figure 4.8 shows a schematic diagram illustrating the Schottky contact deposition process. First, diamond sample surface was oxygenated by ozone treatment [Teraji 2009a] prior the Schottky electrodes delineation by a photolithography process (Fig. 4.8 a)). This surface oxygenation technique proposed by Teraji et *al* [Teraji 2009a] consists to expose the diamond surface to a vacuum deep ultraviolet (VUV) light irradiation in an oxygen atmosphere. The VUV light source is a xenon Excimer lamp center at 172 nm. The ozone treatment was performed using a 500 mbar of pressure and the duration was 90 min. Second, Schottky electrodes were then defined by a photolithography process followed by an oxygen plasma etching (30 sec) to remove the residual resist and contaminations in the electrodes area (Fig. 4.8 b)). Third, a second ozone treatment using the conditions defined previously was performed to ensure diamond surface passivation (Fig. 4.8 c)).

Finally (Fig. 4.8 d)), Zirconium (Zr) Schottky contacts were therefore deposited by electron beam evaporator under high vacuum (10^{-7} Torr). This first metallic layer was

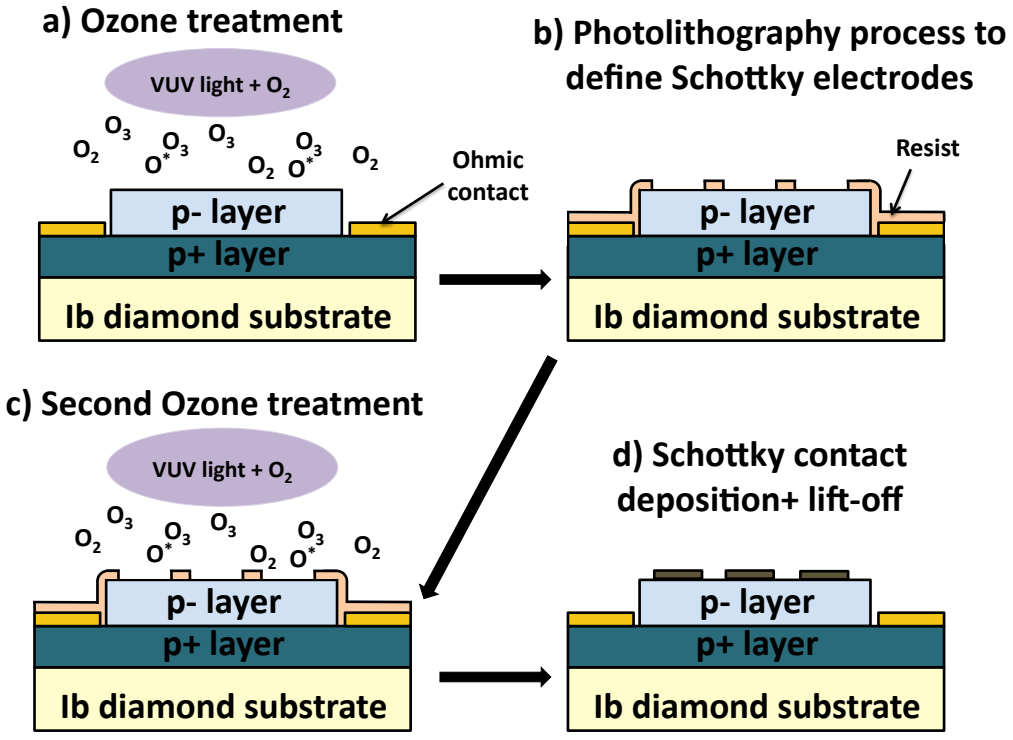

Figure 4.8: Schematic diagram of Schottky contact deposition process.

subsequently covered to prevent its oxidization. Different electrodes shape and metallic stacks were fabricated on samples reported in this thesis:

- For sample #1, 100 μm diameter circular shaped electrodes were fabricated. The Zr layer was covered with cap layers in order to obtain distinct metallic stacks on the same sample, defined as follows:
  - Stack 1 : Zr(20 nm)/Au(20 nm),
  - Stack 2 : Zr(20 nm)/Pt(30 nm)/Au(10 nm).

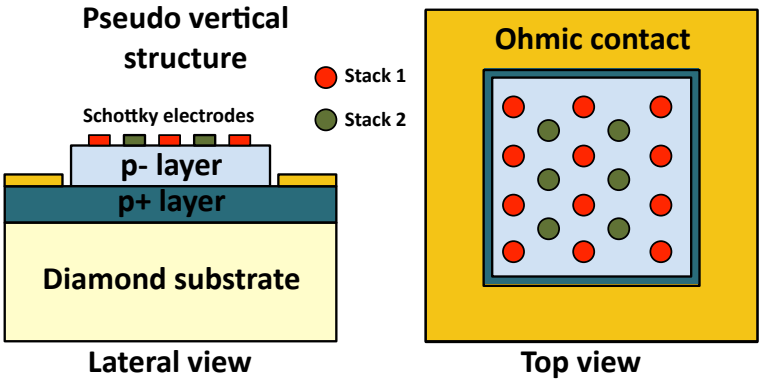

Figure 4.9: Schematic diagram of sample #1.

- For sample #2, the Schottky electrodes were metallic stack comprising a Zr (20 nm) layer, a Pt (30 nm) layer, and an Au (10 nm) top layer. These electrodes were 100 μm diameter circular shaped.

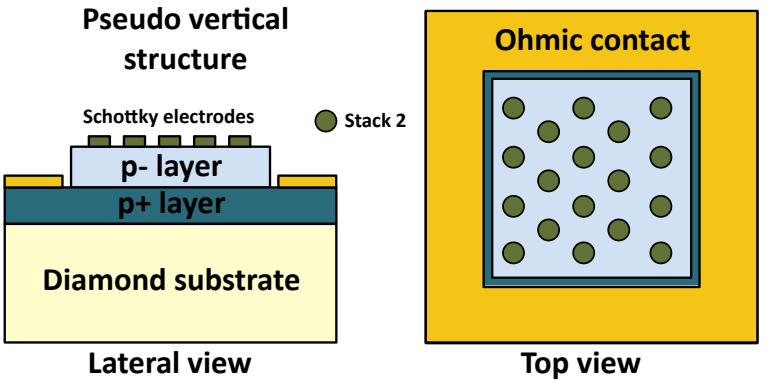

Figure 4.10: Schematic diagram of sample #2.

- For sample #3, circular and square shapes electrodes were fabricated as shown on Figure 4.11. Zr(20 nm)/Pt(30 nm)/Au(10 nm) stack was adopted for Schottky electrodes. Circular electrodes were 100 nm in diameter. On the sample sample, Schottky contact with various electrodes were fabricated: 500×500 μm^2, 300×300 μm^2, 200×200 μm^2.

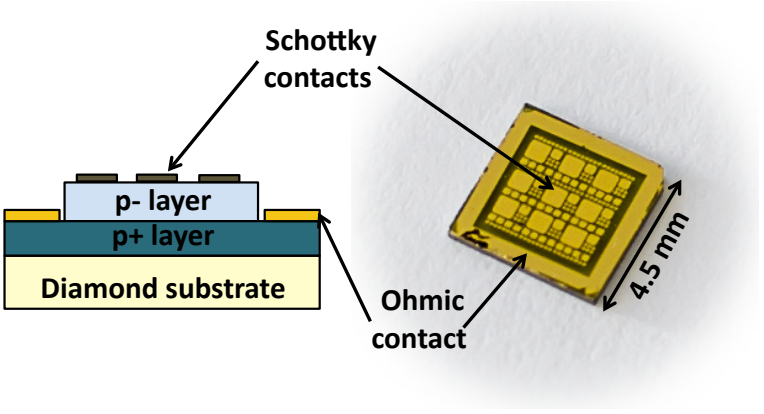

Figure 4.11: Picture of sample #3.

4.5.2 Zr/oxidized diamond interface

After Schottky electrodes deposition, microscopy techniques were used to check the structural properties of the interface. The interface formed between the as-deposited Zr contact and the oxidized diamond surface was then investigated by high-resolution transmission electron microscopy (HRTEM) and electron energy loss spectroscopy (EELS) to

get the characteristic of interface at sub-nanometer scale. This study was performed in collaboration with university of Cadiz, Spain (J.C. Piñero and D. Araujo). The samples preparations and experimental details are described in ref [Piñero 2014].

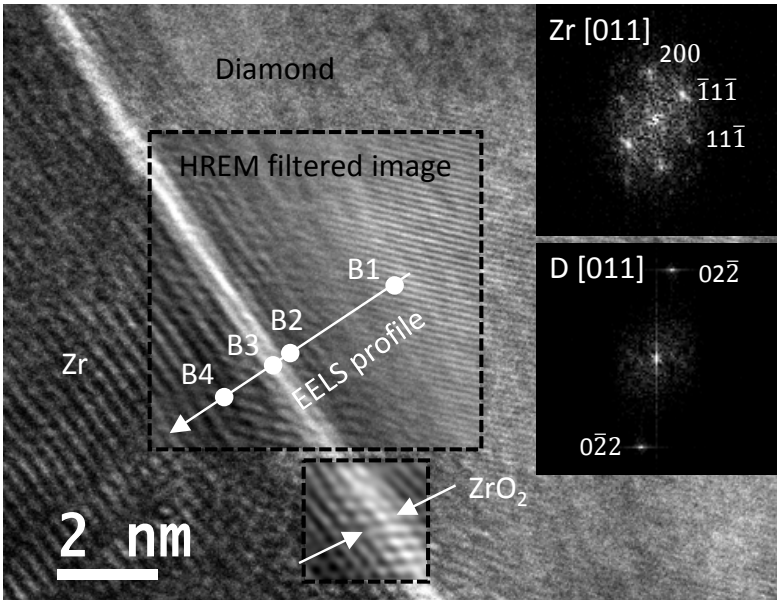

Figure 4.12: Filtered HREM micrograph of Zr/oxidized diamond interface. The white contrast is ZrO_2 type oxide layer which remains constant along the interface [Piñero 2014].

Figure 4.12 shows a HREM micrograph of Zr/oxidized diamond interface reported in ref [Piñero 2014]. EELS profiling recorded along the white line (B1, B2, B3, B4) indicated on Figure 4.12 allows identifying the white contrast (interface layer) as ZrO_2 (Zirconia) type oxide layer. Moreover, the thickness of this interface layer about 5 Å was found to be homogeneous along the studied interface. These investigations demonstrated the good chemical reactivity of Zr with oxygen present on diamond surface thus ensuring a good adhesion of Zr electrodes and forming a carbide free interface. Zr/ZrO_2/diamond type contact known as MIS (Metal Insulator Semiconductor) structure is evidenced.

4.6 Electrical properties of as-deposited Zr contacts

4.6.1 Experimental setup

Electrical characterizations of fabricated devices were performed with homemade probe station using several source measurement units (SMU) for static and dynamic acquisitions. A single channel Keithley SMU 2601A and a Keithley electrometer 6517B were

used for current- voltage (I-V) measurement.

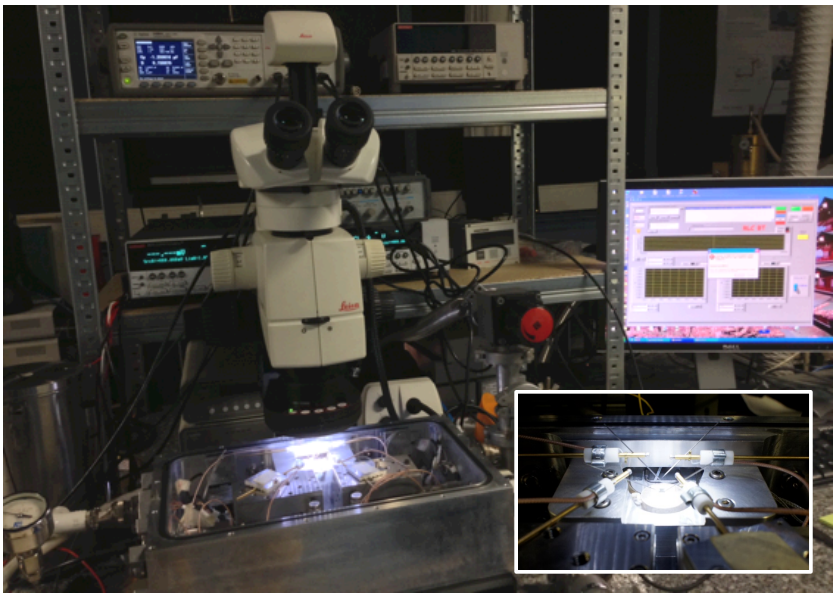

Figure 4.13: Picture of the probe station used for devices characterization.

The SMU 2601A is characterized a DC measurement mode (bias voltage ranging from -40 V to 40 V) and a Pulse mode for transient I-V tests. This SMU was preferentially used to investigate the forward state of fabricated diodes due to the fact it can source high currents up to 1 A in DC mode and 3 A in Pulse mode. Conversely, the Keithley electrometer 6517B (maximum current restricted at 10^{-2} A) was used to investigate the electrical performances of rectifiers in reverse state because of its maximum bias voltage of 1000 V and its detection limit of 10^{-15} A (10^{-12} A in DC mode for SMU 2601A). Thus, the complete I-V characteristic was obtained by combining the SMU 2601A (Forward regime) and electrometer 6517B (reverse regime) acquisitions. On the other hand, the capacitance measurements were performed using an Agilent E4980A LCR Meter with a AC signal frequency ranging from 100 Hz to 2MHz and a typical AC voltage amplitude of 50 mV. a DC bias can be also applied from -10 to 10 V. For all measurements, a Linkam cooling system (sample holder) with a liquid nitrogen feed, was used to set samples temperature (ranging from $-196\,^{\circ}\mathrm{C}$ to $600\,^{\circ}\mathrm{C}$).

4.6.2 Room temperature (RT) I-V Characteristics

Figure 4.14 shows the RT I-V characteristics of Zr electrodes with 100 μm diameter fabricated on sample #1. Zr contacts exhibited an good rectification behavior characterized by a rectification ratio larger than 12 orders of magnitude, a reverse current below the detection limit (10^{-13} A). The forward current of Zr/p-diamond rectifiers is

well fitted (bias ranging from 0 to 3 V) by a thermionic law (Fig. 4.14) thus demonstrating an unique conduction mechanism over the Schottky barrier. Moreover, this electrical current profile was found to be reproducible from one contact to the other on the same sample (Fig. 4.14) even in the ohmic regime where the current was limited by the serial resistance (about 50 Ω). This weak dispersion of electrical characteristics of rectifiers fabricated on sample #1 as illustrated for 27 diodes (Fig. 4.14) was ascribed to an identical Zr/p-diamond interface for all and furthermore a quasi-uniform doping profile over the sample #1.

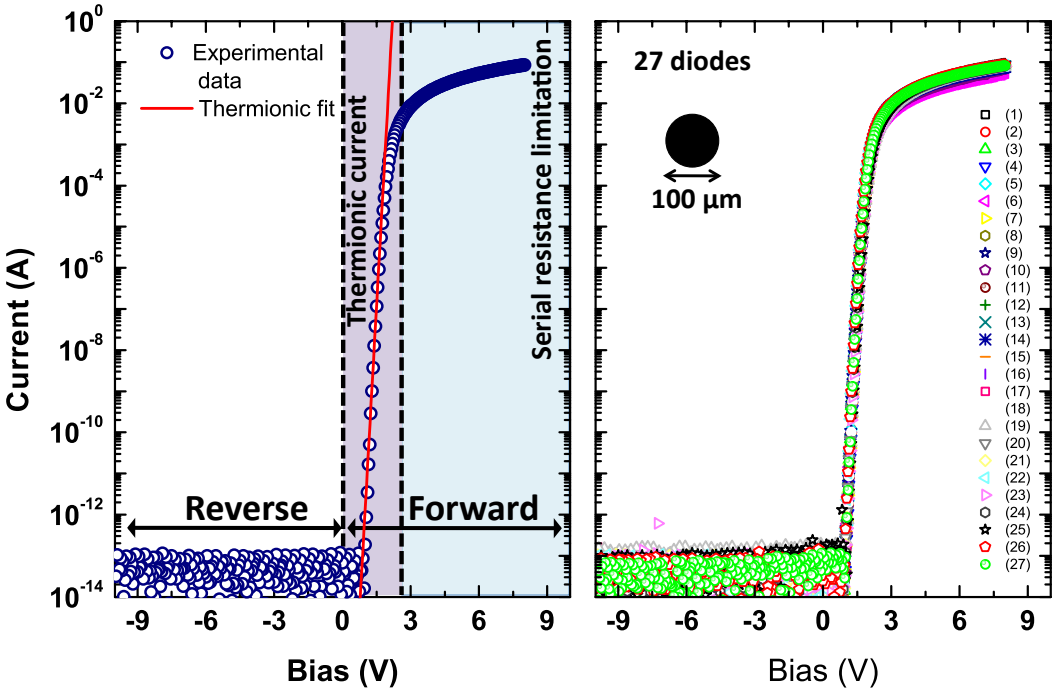

Figure 4.14: I-V characteristics of Zr/oxidized Schottky contacts fabricated on sample #1 illustrating the thermionic current and the serial resistance limitation (left) together with the electrical currents of 27 diodes (right) demonstrating the good reproducibility.

A similar behavior was observed for rectifiers fabricated on sample #2 and sample #3. Figure 4.15 illustrates the I-V curves of different Zr contacts sizes deposited on sample #3. The good rectification behavior and reproducibility of large area diodes fabricated on sample #3 close to those of small devices (sample #1 and #2), demonstrated the uniformity of Zr/oxidized diamond interface over large scales. According to these results and taking in account the HRTEM measurement previously performed (confer section 4.5.2), it can be assumed that the Zr metallic electrodes deposited on oxygen-terminated diamond surface always form a ZrO_2 interface type regardless of samples or devices size.

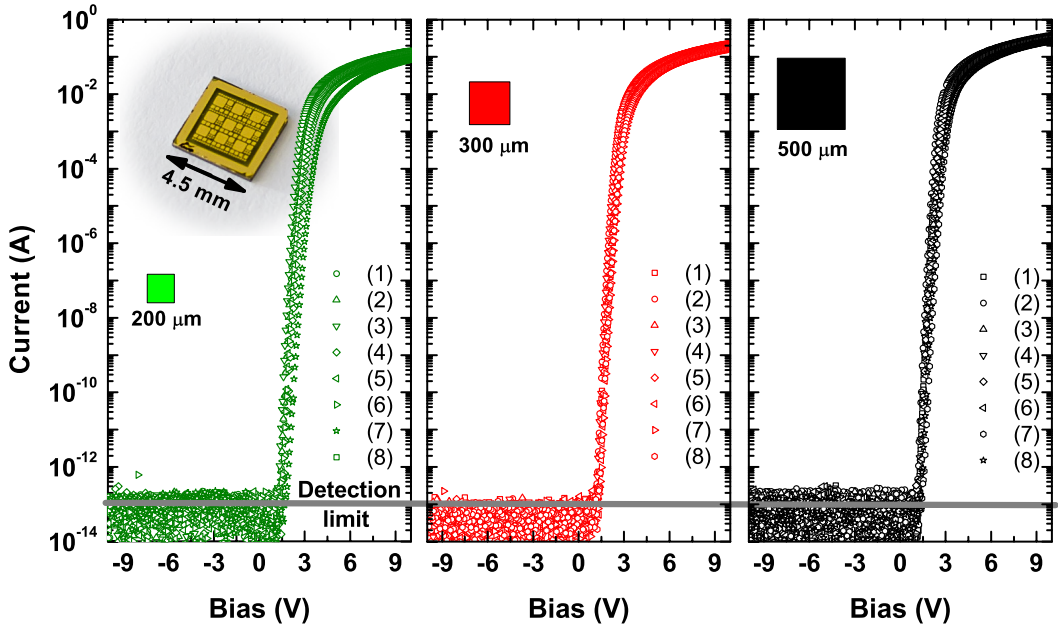

Figure 4.15: I-V characteristics reproducibility for large area Zr Schottky contacts fabricated on sample #3: 200 × 200 μm^2 diodes (left), 300 × 300μ m^2 diodes (middle), 500 × 500 μm^2 diodes (right).

4.6.3 Effective barrier height and ideality factor

The good reproducibility of electrical properties of Zr/p-diamond rectifiers was qualitatively demonstrated previously. This part attempts to highlight this reproducibility quantitatively by investigating the electrical characteristics dispersion of Zr/p-diamond rectifiers fabricated on a given sample and from one sample to the other. The forward characteristics reproducibility of a rectifier depends on the zero-bias Schottky Barrier Height (SBH) ϕ_b^0 and its ideality factor n if the thermionic emission is the limiting mechanism. Accordingly, the RT I-V characteristics previously reported were fitted by a thermionic law to assess to ϕ_b^0 and n. Noting that ϕ_b^0 was calculated using the theoretical value of the Richardson's constant 90 $Acm^{-2}K^{-2}$. Figure 4.16 shows the zero-bias barrier as function of ideality factor for devices fabricated on sample #1 (left), sample #2 (middle), and sample #3 (right). Sample #1 exhibited a unique family of diodes (IA) characterized by an ideality factor about 1.5 and a barrier height ranging from 1.5 to 1.6 eV. Moreover, a linear dependence was observed between ϕ_b^0 and n. Such a linear dependence as reported by W. Monch [Mönch 2004] for most of MS junctions (Ag/n-Si [Schmitsdorf 1995], Ag/n-GaN [Sawada 2000], Ti/n-SiC [Suezaki 2001],), was considered as an evidence of the existence of more than one physical mechanism that determining the barrier height. The barrier dependence on ideality factor is therefore

written as [Mönch 2004]:

$$\phi_b^0 = \phi_b^{nif} - \varphi_p\,(n - n_{if}) \tag{4.23}$$

where n_{if} is the ideality factor determined by the image force effect only ($n_{if} \approx 1.005$ for a barrier height of 2 eV). Conversely, ϕ_b^{nif} is the extrapolation of the ϕ_b^0 versus n to n_{if} and represents the zero-bias barrier height if the image force effect is only considered. Accordingly, the zero-bias barrier heights ϕ_b^0 of rectifiers fabricated on sample #1 were fitted using the equation 4.23 as shown on Figure 4.16.

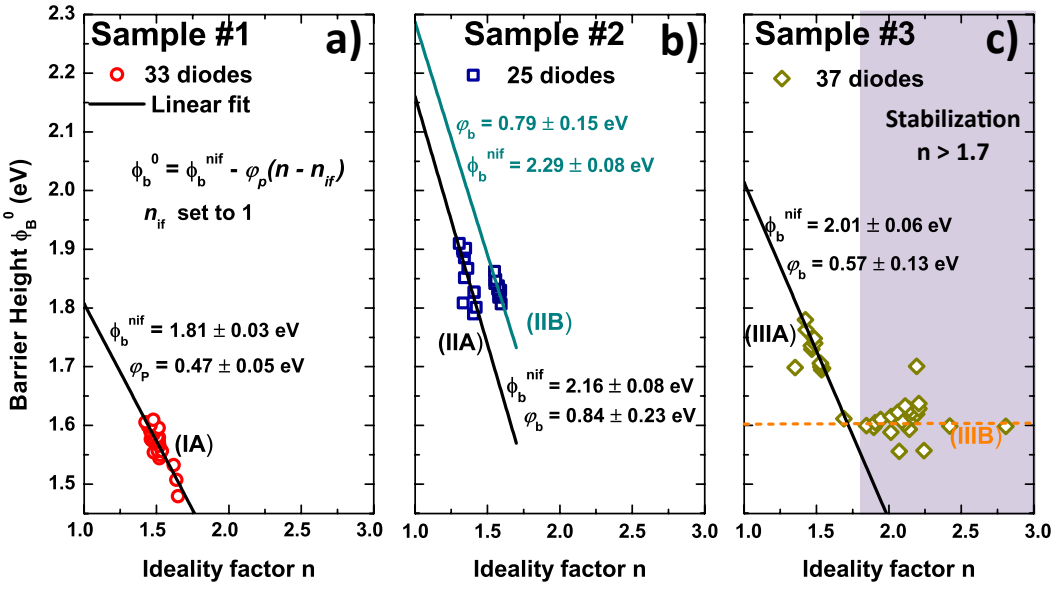

Figure 4.16: Effective barrier heights versus ideality factors determined from Zr/p-diamond diodes RT I-V characteristics fabricated on : a) sample #1, b) sample #2, c) sample #3. The solid lines are the linear fits.

Since n_{if} can be approximated to 1 (confer 4.3.3), the zero-bias SBH taking in account the image force effect only ϕ_b^{nif} was then calculated. Table 4.1 summarized the obtained results together with those calculated for rectifiers fabricated on sample #2 and #3 on which the same linear correlation was established. Conversely to sample #1, the rectifiers fabricated on sample #2 give rise to two distinct groups (IIA, IIB) of ϕ_b^0 with a separate linear dependence with ideality factor. Thus, two different ϕ_b^{nif} 2.16 eV and 2.29 eV were obtained for sample #2 for the family IIA and IIB respectively. An identical situation was observed for sample #3 (groups IIIA and IIIB). Moreover, a linear relationship was established for group IIIA only. For group IIIB, apart the high ideality factor calculated (n higher than 1.7), the zero-bias SBH was around 1.6 eV. Such a stabilization is generally encountered for other semiconductors when n is higher than 1.4 as reported in ref [Mönch 2004] without any explication. For group IIIB rectifiers

in our case, the higher ideality factor suggesting that they were far from an ideal junction, leaves one to believe they may be inhomogeneous and so the simplest thermionic emission model 4.20 was no more applicable. This could be ascribed to the surface of sample #3, which conversely to sample #1 and #2, was widely contaminated by surface defects such round hillocks and a mean roughness of several nanometers (confer Chapter 3). Another possibility could be a non-uniform oxygen-terminated surface leading to a non-uniform ZrO_2 interface layer or the influence of interface dipoles induced by this layer. Anyway, for groups IA, IIA, IIB, and IIIA rectifiers which allowed assessing to the SBH ϕ_b^{nif}, the different values determined, are ranging between 1.81 and 2.3 eV in disagreement with Mott equation ($\phi_b = Egq(\phi_m - X_s)$) if a electron affinity (X_s) of 1.7 eV [Maier 2001] is taken for diamond (Mott barrier is then about 3.15 eV). Moreover, if SBH was pinned at charge neutrality level as predicted by Bardeen model, these different groups of rectifiers should be the consequence of different neutrality level related to interface layer. For rectifiers fabricated on sample #1, the most likely explanation of the zero-bias SBH ϕ_b^{nif} which at least 200 meV lower than those of sample #2 and #3, could be the SBH lowering due to annealing (confer section 4.10). The fabricated rectifiers on sample #1 were unintentionally annealed because of self-heating effect during high forward bias voltages characterization electrical leading to a higher sample temperature above 600 K (confer section 4.8).

Table 4.1: Linear fitting parameter of Schottky barrier versus ideality factor obtained for distinct diodes groups observed on sample #1, #2, #3.

Sample	ϕ_b^{nif} (eV)	φ_p (eV)	Label
#1	1.81 ± 0.03	0.47 ± 0.05	IA
#2	2.16 ± 0.08	0.84 ± 0.23	IIA
	2.29 ± 0.08	0.79 ± 0.15	IIB
#3	2.01 ± 0.06	0.57 ± 0.13	IIIA
	Level off		IIIB

4.6.4 High field RT I-V characteristics

The RT current-voltage characteristic of Zr/p-diamond Schottky diodes fabricated on samples #1, #2, and #3, was measured for reverse bias ranging from 0 V to -1000 V. Figure 4.17 shows the typical reverse current observed for a large number of diodes. Besides these poor performances characterized by a high leakage and a low blocking voltage (below 300 V), at least 5% of Zr/p-diamond rectifiers exhibited a good reverse

performances. Figure 4.18 shows the diodes having the best characteristics. The electrical currents were divided by devices section which were 4×10^{-4} cm^{-2} for sample #3 (200×200 μm) and 7.85×10^{-5} cm^{-2} for sample #1 and sample #2 (circular electrodes with 100 μm in diameter). The I-V curves obtained reported for sample #3 are characterized by a current density of 110 A/cm^2 at 6 V and a maximum reverse bias of 100 V.

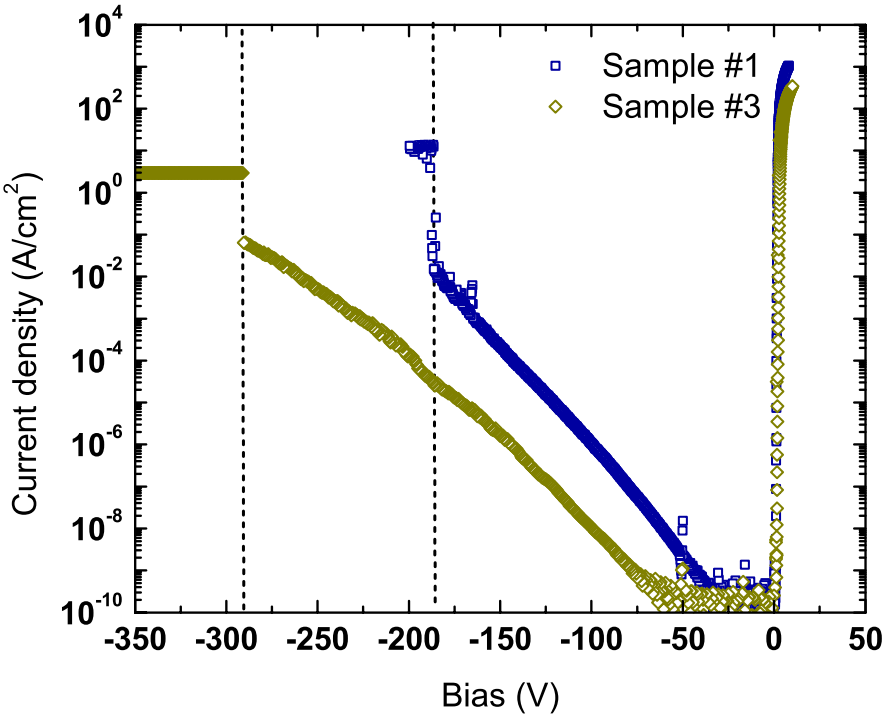

Figure 4.17: Typical high reverse bias characteristic of Zr/p-diamond diodes. The reported I-V curves were performed on samples #1 and #3.

Conversely, zirconium Schottky contacts fabricated on samples #1 and #2, exhibited an extremely good rectification behavior characterized by a high current density about 10^3 A/cm^2 at 6 V, a reverse current density less than 10^{-8} A/cm^2 up to the maximum voltage $\mid V_{max} \mid = 1000V$ available with our measurement setup. According to the drift layer thickness of 1.3 μm, a reverse field ($F = \mid V_{max} \mid /d$) at least 7.7 MV/cm has been reached for Zr/p-diamond diodes without any change in the reverse current level. It must be noticed that the equation used for the electrical field evaluation gives a lower boundary (assumption of an isolating diamond between Zr and p+ layer and so a constant field in the layer). Thus, a Baliga's Power Figure Of Merit $BFOM = (Vmax)^2 / = (RonS)$, where (Ron) is the specific on-resistance, of 244 MW/cm^2 at RT was obtained for Zr/p-diamond. The BFOM is a figure of merit for power semiconductor devices relating the power dissipation to the intrinsic materials parameters [Baliga 1989]. The calculated BFOM, 24 times larger than the Si BFOM limit (10 MW/cm^2) [Umezawa 2012], was

the largest value reported for diamond Schottky diodes and furthermore not so far from the theoretical one (1000MW/cm^2) [Umezawa 2012] for the same breakdown voltage and temperature which should be reached if the effective breakdown voltage was doubled.

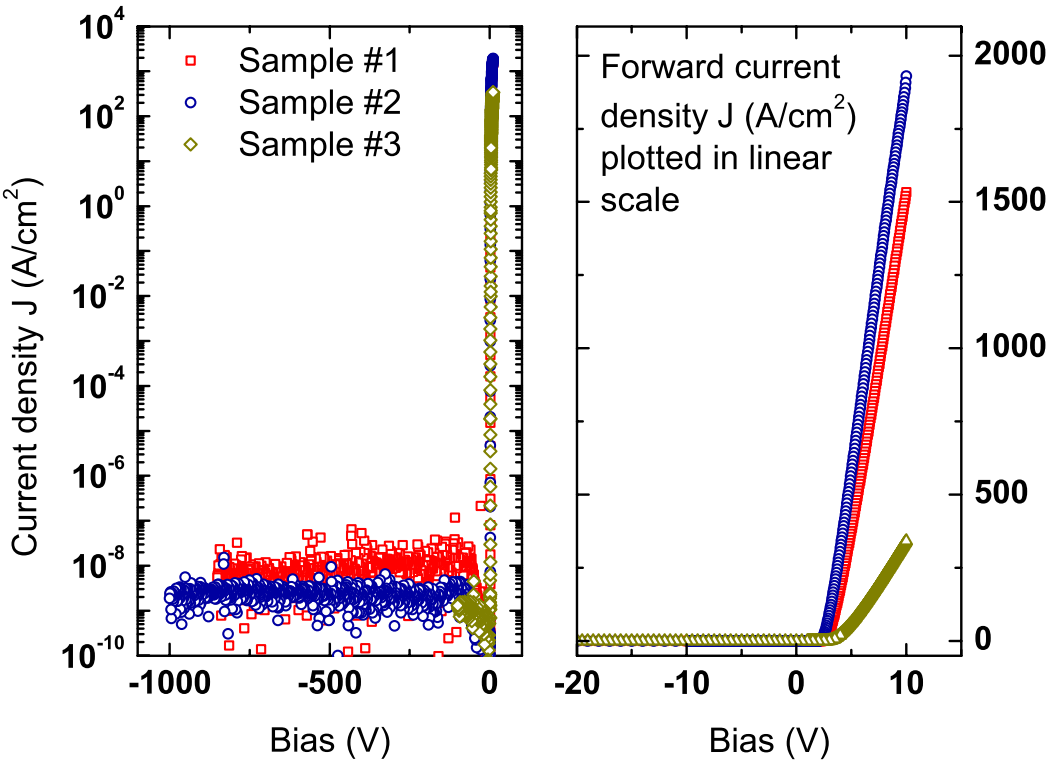

Figure 4.18: High blocking voltage Zr/p-diamond diodes obtained with samples #1, #2, and #3.

4.6.5 Summary

Besides their relatively good reproducibility, the as-deposited Zr Schottky electrodes exhibited high performances RT electrical properties. Indeed, the Zr/p-diamond rectifiers fabricated on sample #1 and sample #2 give rise to a high forward current density of 10^3 A/cm^2 (at 6 V) and a breakdown field larger than 7.7 MV/cm. The power figure of merit was above 244 MW/cm^2 and was the largest value reported for diamond Schottky diodes and furthermore not far from the theoretical one (1000MW/cm^2) [Umezawa 2012]. Unfortunately, this reverse performance was obtained for few rectifiers because of the surface and crystal quality of diode actives that must be more investigated in order to fabricate high performance large area Zr/p-diamond rectifiers.

4.7 Thermal stability of Zr/p-diamond rectifiers

A rectifier is characterized by a critical operating temperature limit (T_{max}) beyond which an alteration of its electrical properties may occur. The thermal stability is basically related to this upper limit T_{max} under which the rectifier can withstand a temperature fluctuation. For diamond rectifiers, it is well known that a transformation of rectifying junctions inducing by carbide interface layer formation or the surface passivation layer desorption (oxygen or hydrogen termination) are the main reasons for diodes electrical performances deterioration at high temperature. The critical limits T_{max} of diamond rectifiers are commonly defined by the temperatures at which such interface transformation arise. Aiming to identify the critical T_{max} for Zr/p-diamond junctions, their current voltage (I-V) characteristic was investigated at different temperatures (T) ranging from 300 K to 773 K.

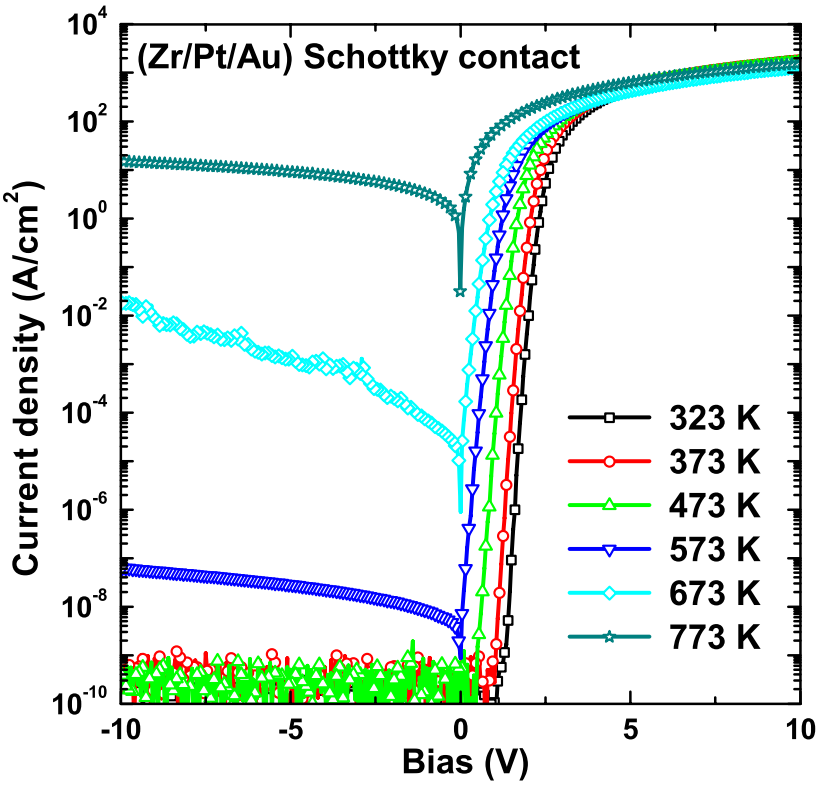

Figure 4.19: High temperature I-V characteristics of Zr/p-diamond rectifier.

4.7.1 High temperature I-V charactersitics

The electrical performances of Zr Schottky electrodes were investigated using sample #1 on which Zr layer was covered with two distinct cap layers: Au cap layer and (Pt/Au)

cap layer. Figure 4.19 shows the typical I-V characteristic measured at high temperatures. Zr/p-diamond junctions exhibited a good rectification behavior in the whole temperature range. On the other hand, all of these high temperature currents had a similar trend in the ohmic regime (high forward bias). Let's remind that this regime was related to the forward current limitation induced by the serial resistance Rs of diodes. A linear scale revealed that the electrical currents measured at high temperatures is lower than the RT current in ohmic regime (confer Fig. 4.19) thus indicating the serial resistance increases versus temperature.

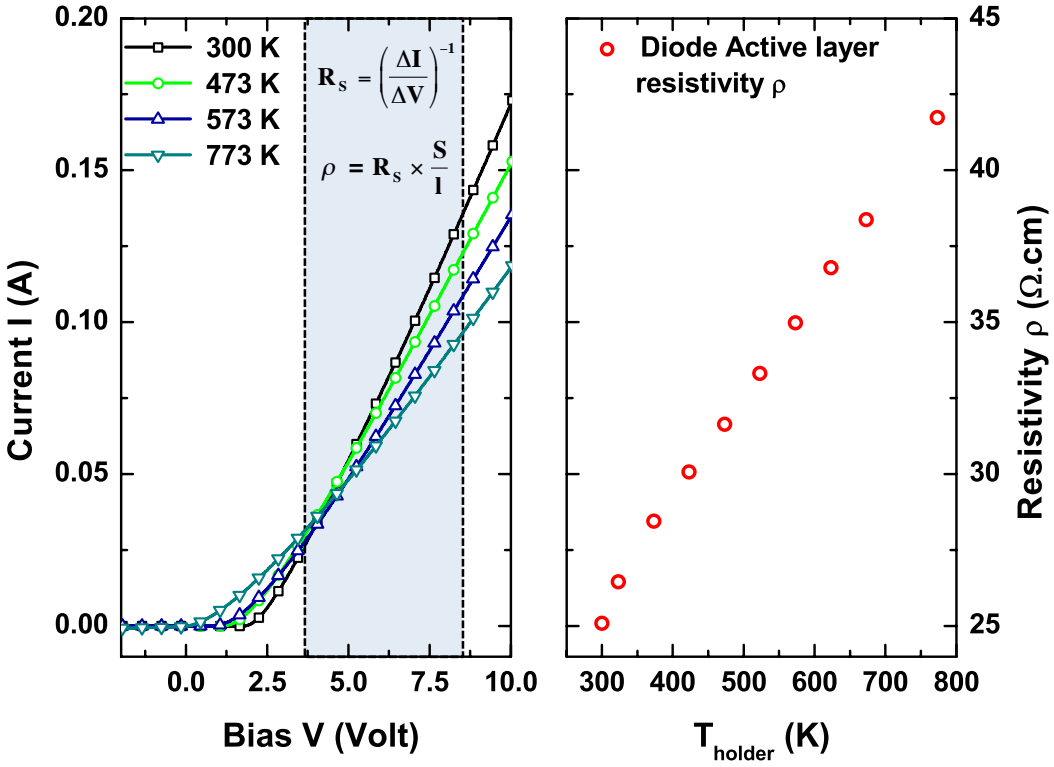

Figure 4.20: High temperature I-V characteristics of Zr/p-diamond rectifier (left) and the temperature dependence of calculated active layer resistivity (right).

Assuming that the resistance induced by the highly conducting diamond layer (metallic layer) in pseudo-vertical diode structure is negligible compared to that of the active layer, the serial resistance can be ascribed to the diode active layer (p^- layer). Diode active layer resistivity is therefore defined as $\rho = Rs \times S/l$, where S is diode area and l the thickness of diode active layer. Accordingly, the temperature dependence of the active layer resistivity was established. Figure 4.20 spotlights on a linear scale the forward bias range where the serial resistance of Zr/p-diamond rectifiers were calculated together with the resistivity profile. A monotonic increase of diode active layer resistivity with increasing of T was observed in disagreement with the expected resistivity

profile for diamond devices. Indeed, as discussed in Chapter 2, the resistivity of boron doped diamond decreases versus T because of the thermal ionization of boron until to the exhaustion regime. When the full ionization is reached, the resistivity increases versus T due to carrier mobility diminution versus T (confer Chapter 2). For a slightly boron doped layer ($N_a < 10^{17}$ cm^{-3}), the full ionization occurs in a temperature range starting from 500K to 800 K.

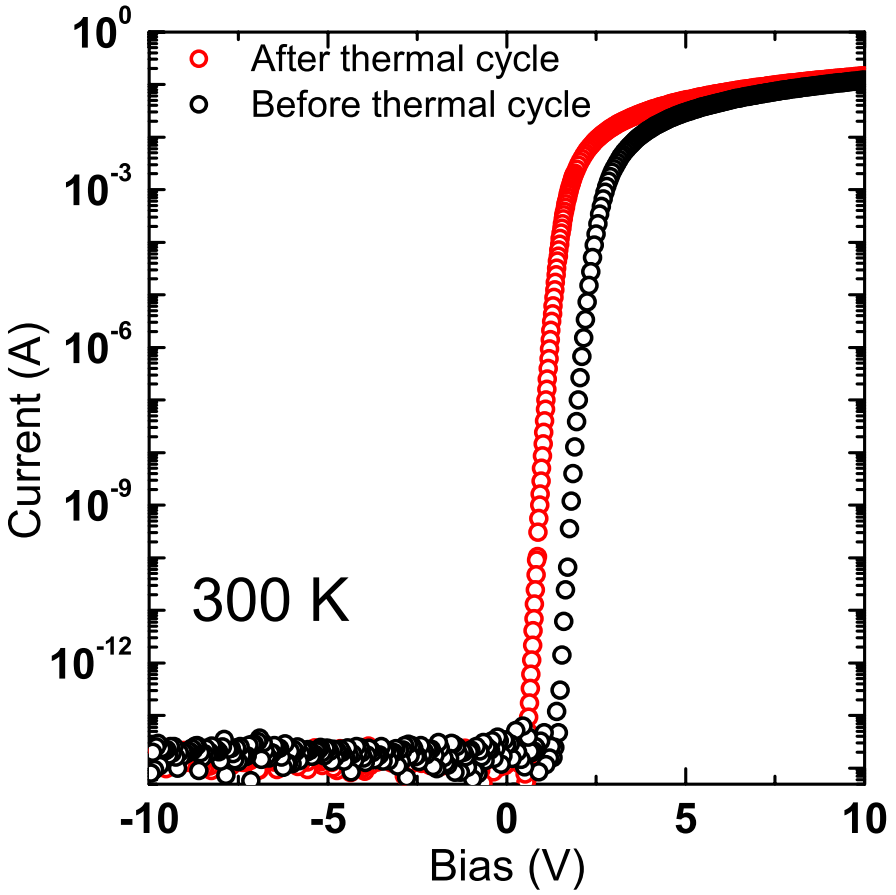

Figure 4.21: Current-Voltage characteristics before and after the thermal cycling measurments (from 300 K to 773 K). The threshold is lower after thermal cycling leading to higher current at low forward bias.

The experimental resistivity reported on Figure 4.20 demonstrated that the Zr/p-diamond rectifiers investigated here, behaves like semiconductors such as silicon where the full dopants ionization arises below RT (shallow dopants) and the resistivity only increases with T. The exhaustion regime must be reached for Zr/p-diamond rectifier thus suggesting that the temperature set point (sample holder T_{holder}) may not correspond to the diode active layer temperature (T_{sample}). This assumed temperature discrepancy can be a consequence of a self-heating which can provide a sufficient thermal energy to switch in a full ionization regime without a thermal runaway. Zr Schottky electrodes

deposited on sample #1 behaves like silicon or silicon carbides rectifiers for which the exhaustion regime (full dopant ionization regime) occurring at low temperature (below RT), the serial resistance increase versus temperature.

To end this temperature dependence study, the I-V characteristic was measured after the thermal cycling measurement. Apart the fact that they are still exhibiting a good rectification features attesting their thermal stability up to 773 K, the electrical characteristic of Zr/p-diamond rectifier was improved as shown on Figure 4.21. By comparing the I-V curves before and after the thermal cycling measurement, the latter was found to be shifted leading then to a higher current at low forward bias (lower Schottky Barrier Height SBH) than for as-deposited Zr electrodes. This work brought out the possibility to lower the forward losses (lower SBH) by performing an annealing stage.

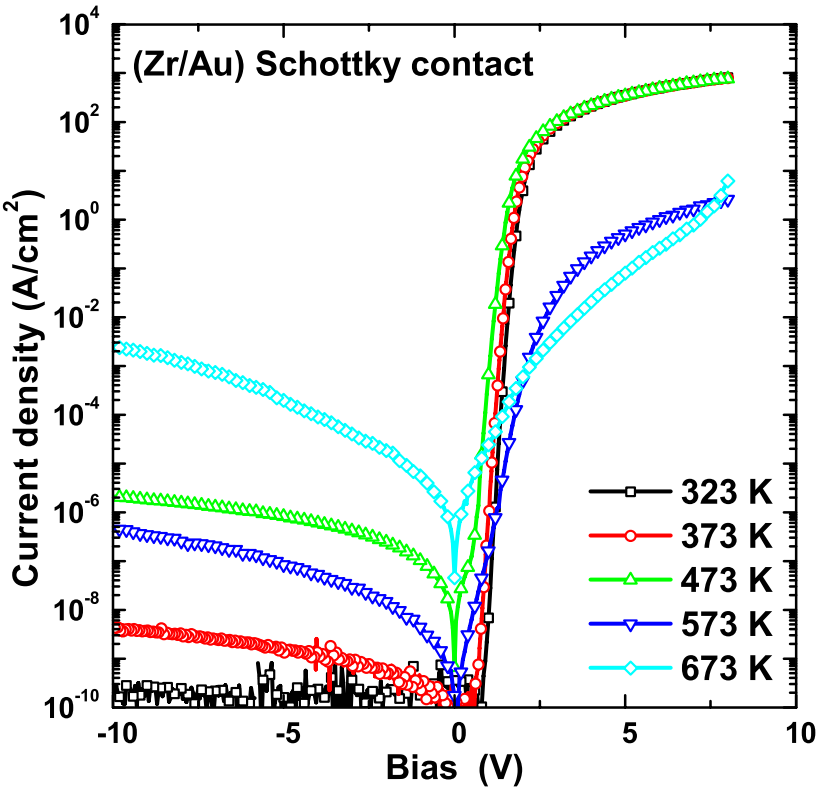

Figure 4.22: High temperature I-V characteristics using a (Au/Zr)/p-diamond rectifier.

4.7.2 Cap layer influence

The thermal cycling measurements discussed above was performed using a Zr Schottky electrodes covered by a stack (Pt/Au) cap layer. The high temperature measurements revealed the influence of the selected cap layer on the thermal stability of Zr/p-diamond

junctions. Indeed, conversely to (Zr/Pt/Au) Schottky metallic stack, it was seen that the electrical characteristics of Zr contacts covered directly with Au layer were altered for a operating temperature of at least 523 K. This deterioration shown on Figure 4.22, partly display the role of the platinum layer used as diffusion barrier avoiding oxygen migration through the Au layer leading to Zr oxidation, and/or metals intermixing.

4.7.3 Summary

The high temperature measurements demonstrated the good thermal stability of Zr/p-diamond rectifiers. For Zr Schottky electrodes covered with a (Pt/Au) cap layer, an operating temperature range starting from RT up to 733 K was established. Moreover, for the rectifiers fabricated on sample #1, the current in the ohmic regime was almost temperature independent because of a self-heating effect thus leading to a higher temperature than the set point values and a full boron ionization in diodes active layer. On the other hand, this study highlighted the possibility to lower the SBH and so the forward losses by performing annealing. The forthcoming sections will be focused on the investigation of the self-heating and the influence of the annealing Zr/p-diamond junctions.

4.8 Self heating of Zr/p-diamond rectifiers

Thermal management is a key step for high power devices. This section does not intend to address this topic, but merely demonstrate the heat generation in our devices and investigate its influence on their electrical performances. In the previous section, a discrepancy between the expected resistivity profile and those deduced from high temperature current-voltage characteristics was observed. Indeed, conversely to a resistivity diminution related to thermal ionization of boron atoms as discussed in Chapter 2, diode active layer resistivity tends to increase versus set temperature. This tendency was evidenced by a forward current diminution for a high operating temperature as previously illustrated on Figure 4.24. It must be noticed that such temperature dependence of electrical current was generally encountered for semiconductor as silicon where exhaustion regime (full dopant ionization) takes place below room temperature due to low ionization energy of dopants. Thus, the resistivity tends to decrease versus temperature because of the carrier mobility drop (confer Chapter 2). The fact that Zr/p-diamond rectifiers fabricated on sample #1 behave like classical semiconductors-based rectifiers, suggests

that the inner temperatures of the sample were higher than the one of the sample holder (T_h) and ranging in the exhaustion regime. It was then assumed that the devices were affected by a self-heating phenomenon providing sufficient thermal energy to increase diamond sample temperature (T_s) and so reach the full boron ionization regime.

This section attempts to demonstrate this assumption by establishing the self-heating evidences and its influence on the electrical properties of Zr/p-diamond rectifiers. Aiming to carry out these objectives, Zr/p-diamond diodes were measured at low temperature (ranging from 213 K to 300 K) in order to have high serial resistance and thus limited the forward current of the diode. Such low temperatures allow us to observe and investigate the self-heating effect.

4.8.1 Self-heating evidences at 213 K (T_h)

Self-heating is a consequence of heat generation related to the Joule effect losses and its storage in a device. The Joule losses represent the power dissipated P defined by $P = I \times V$, where I is the electrical current crossing the sample and V the applied bias voltage. Depending on whether the heat originating from this power dissipation is transferred in the surrounding environment with a high rate or not, and so on the thermal conductivity between sample and holder, the self-heating can arise or not. For power systems, heat sinks are used to enhance the heat dissipation ability of elementary devices such as rectifiers. The heat management was out of this thesis, which is focused on the investigation of diamond electronic properties of rectifying metal/diamond junction. During the electrical characterization of Zr/p-diamond rectifiers, the samples were directly put on a holder with a temperature controlled by a Linkam temperature regulation system. At low temperature, the probe station was kept under vacuum (below 10^{-3} Torr) in order to avoid water condensation on diamond sample and so to prevent a possible surface conduction. Figure 4.23 shows

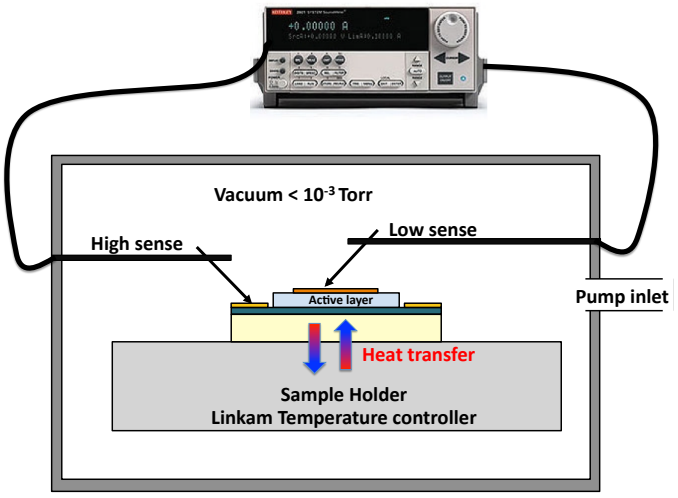

Figure 4.23: Schematic diagram of probe station illustrating the heat transfer between diamond and the sample holder.

a schematic diagram of the probe station illustrating the heat transfer between diamond and the sample holder cooled with a nitrogen feed. The heat exchange is assumed to exist between diamond and sample holder since the probe station is under vacuum. Thus, thermal resistance of diamond/holder contact should define the heat transfer from one side to the other and vise versa.

Before discussing the thermal resistance of this contact, let consider the I-V characteristic of Zr/p-diamond rectifier at 213 K shown on Figure 4.24. The rectifier was biased in a wide range of forward voltage in order to investigate the active layer resistivity in a large power dissipated scale. The electric current was plotted as function of the relative forward bias $V_{bias} - V_{th}$, where V_{th} is the threshold voltage and V_{bias} is the applied bias voltage. This relative bias allows an easier serial resistance determination and will preferentially adopted in this section as the forward bias. Figure 4.24 shows clear deviation of the measured electrical current in ohmic regime from that expected for constant serial resistance Rs (theoretical I-V curve). The current tends to stabilize towards a level that was at least 10 times higher than the expected value. This augmentation was correlated to the sample temperature increasing. Indeed, by focusing a pyrometer on diamond sample, its temperature variation was observed.

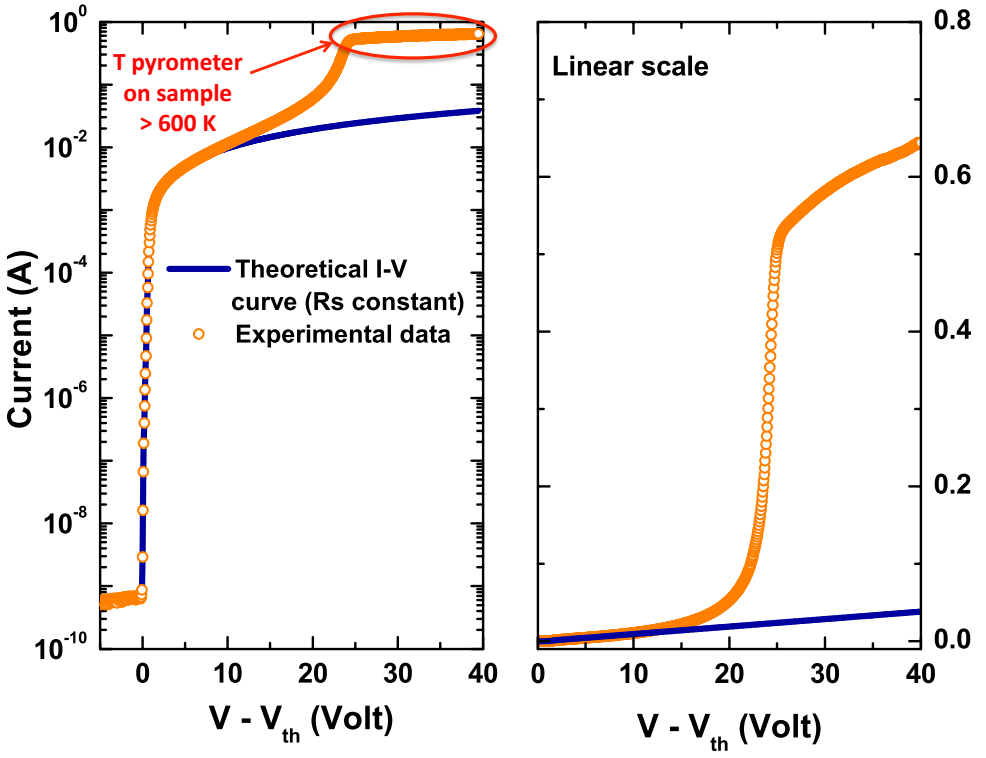

Figure 4.24: I-V characteristics of Zr/p-diamond rectifier operating at 213 K initially set via the holder (T_h).

Figure 4.25 shows an example of sample temperature profile as function of pyrometer measurement times. Unfortunately, the pyrometer was not synchronized with our source meter (Keithley 2601A) and so, a relation between the measured electrical current and the pyrometer temperature was not established. Anyway, it is observed that diamond temperature is higher than 600 K when the current tends to level off.

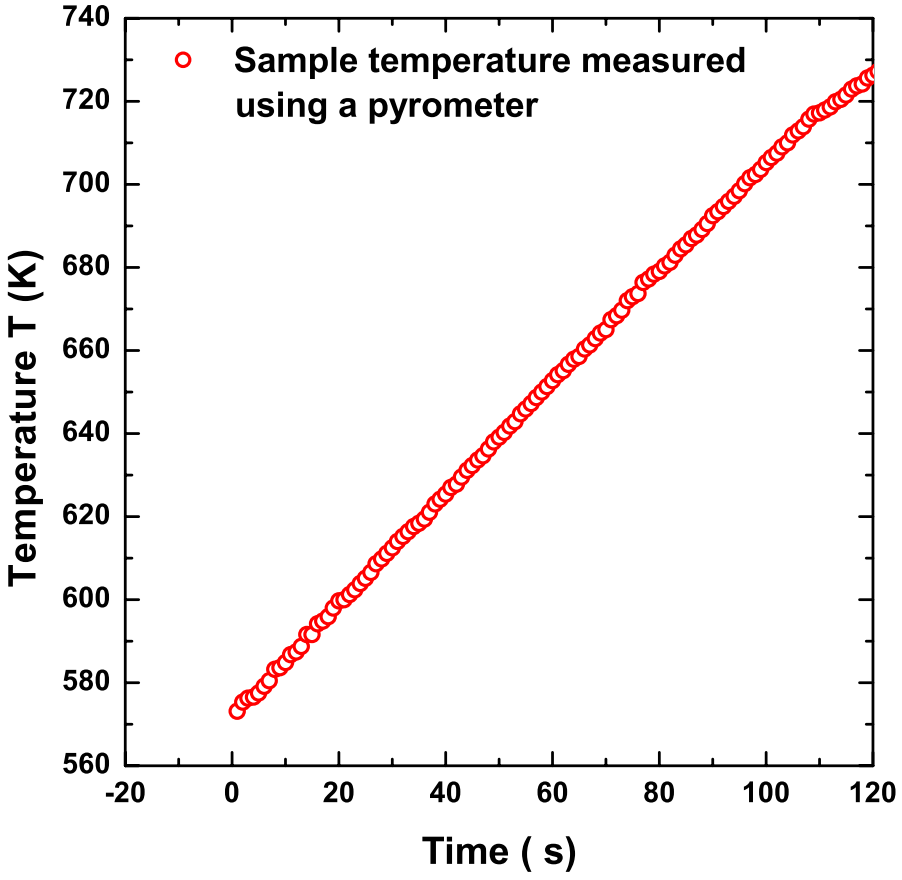

Figure 4.25: Example of Zr/p-diamond rectifier temperature increase due to self-heating.

These results demonstrate the presence of self-heating in Zr/p-diamond rectifier where temperature was initially set at 213 K (T_h). It must be mentioned that the electrical current feature shown on Figure 4.25 is independent of the measurement sweep duration and was even observed for fast measurements performed using the set conditions leading to the maximum single measurement rates of SMU (1800 operations per second). On the other hand, the sample holder was heated by the self heating of diamond rectifier and the system defined by diamond and sample holder, exhibited a transient temperature step which converged towards a high temperature. The electrical current increase related to the self-heating points out the diminution of the rectifier active layer resistivity ρ because of thermal ionization of boron atoms. Figure 4.26 shows the resistivity profile versus

power dissipated P. According to the power dissipation, three steps can be identified:

- A constant resistivity step for losses lower than 10^{-1} W. This resistivity corresponds to the active layer resistivity of a rectifier operating at 213 K without self-heating
- A resistivity decrease step due to the thermal ionization of boron atoms (P ranging from 10^{-1} to 10^{1} W)
- A weak resistivity increase step (P higher than 10^{1} W) where the full ionization regime is reached

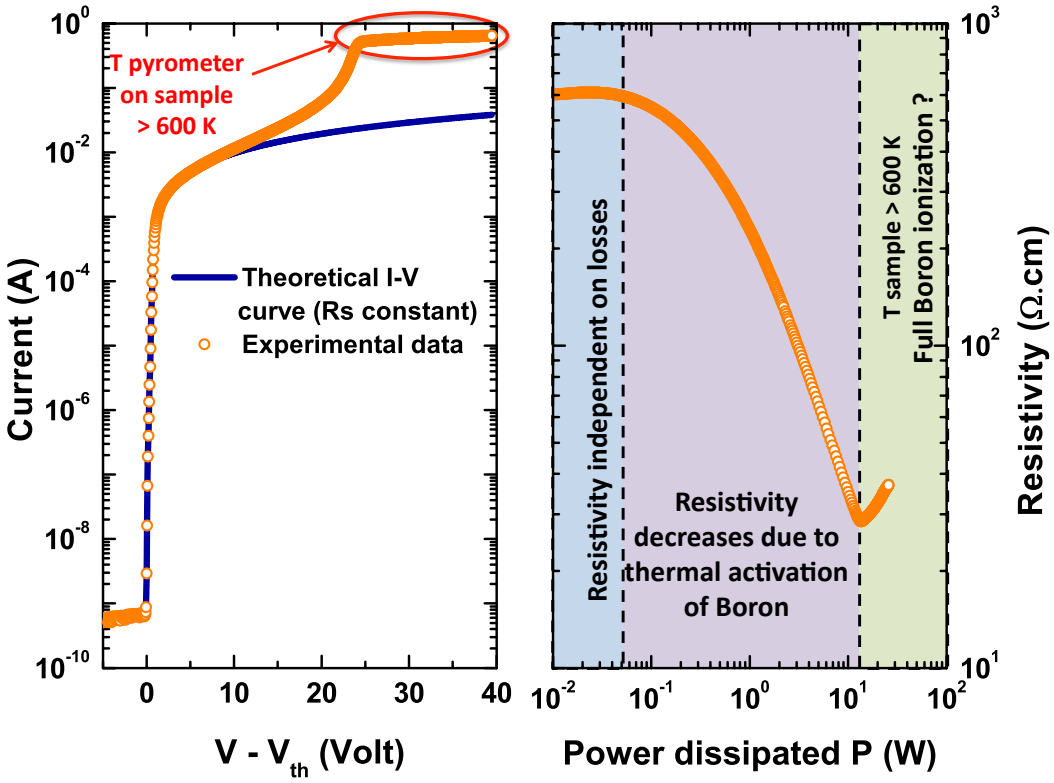

Figure 4.26: Electrical current measured at 213 K (left) and diode active layer resistivity (right) versus power dissipated.

Let's remind that the resistivity ρ is related to the carrier concentration p and carrier mobility μ as follows: $\rho(T_s) = 1/(q \times p(T_s) \times \mu(T_s))$. During the thermal ionization of boron atoms, the mobility diminution is counterbalanced by the carrier concentration increase until the full ionization regime (p independent of T) where the minimum resistivity is reached and its trend is inverted leading to a weak increase. The profile reported on Figure 4.26 is in good agreement with this statement. However, the electric field influence on carrier velocity must be considered since the field higher than 10^5 V/cm was reached. The best way to definitely ascribe such a resistivity variation to a temperature

variation only is the establishment of a relation between sample temperature and the dissipated power.

4.8.2 Self-heating at T_h higher than 213 K

The achievements reported above demonstrate the self-heating of Zr/p-diamond rectifier which temperature was initially set at 213 K. This rectifier temperature increase is observed when the Joule losses were higher than 10^{-1} W (forward bias higher than 7.5 V) and the active layer resistivity dropped from 600 Ωcm to 30 Ωcm due to the thermal ionization of boron atoms. For rectifier temperature initially set to a value higher than 213 K, the self-heating is expected to be observed at lower forward bias voltage since a high current level will be obtained at lower bias voltage (device active layer resistivity initially reduced).

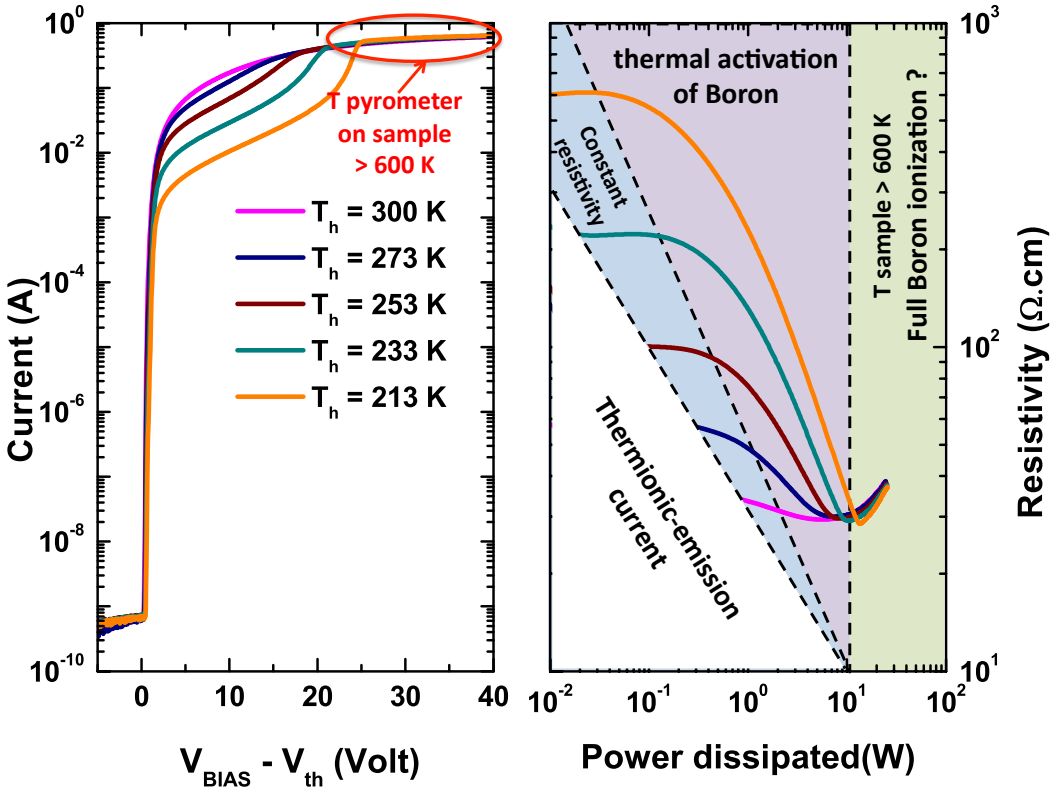

Figure 4.27: Electrical current measured at different operating temperatures (left) and diode active layer resistivity (right) versus power dissipated.

This is clearly illustrated on Figure 4.27 where the I-V characteristics of Zr/p-diamond measured at different T_h below 300 K are plotted together with their corresponding resistivity profile. The forward current enhancement related to diode active layer resistivity diminution is always observed. Moreover, this enhancement is no more clearly

perceptible for a T_h set at 300 K. Indeed, at RT, the current variation in the ohmic regime can be neglected since the maximum resistivity is only 1.17 times higher than the minimum value. For a rectifier operating at RT, the forward current in ohmic regime was therefore defined by a minimum resistivity of the diode active layer related to the self-heating. The power level from which this phenomenon started to appear at 213 K, was reached in the thermionic-emission regime for most of the measurements performed at T_h close to/or higher than room temperature, thus leaving one to believe that the self-heating ignition must occur in this regime. Thus, the current limitation related to rectifiers serial resistance for operating temperature higher than 300 K will be defined by losses-independent serial resistance which do not correspond to their real resistance because of the self-heating induced by a poor heat exchange between diamond sample and holder. On the other hand, the resistivity profiles exhibited an identical feature for losses higher than 10 W. This identical tendency characterized by a sample temperature above 600 K, was previously assumed to be a consequence of both the full dopant ionization and the carrier mobility diminution arising at high temperature.

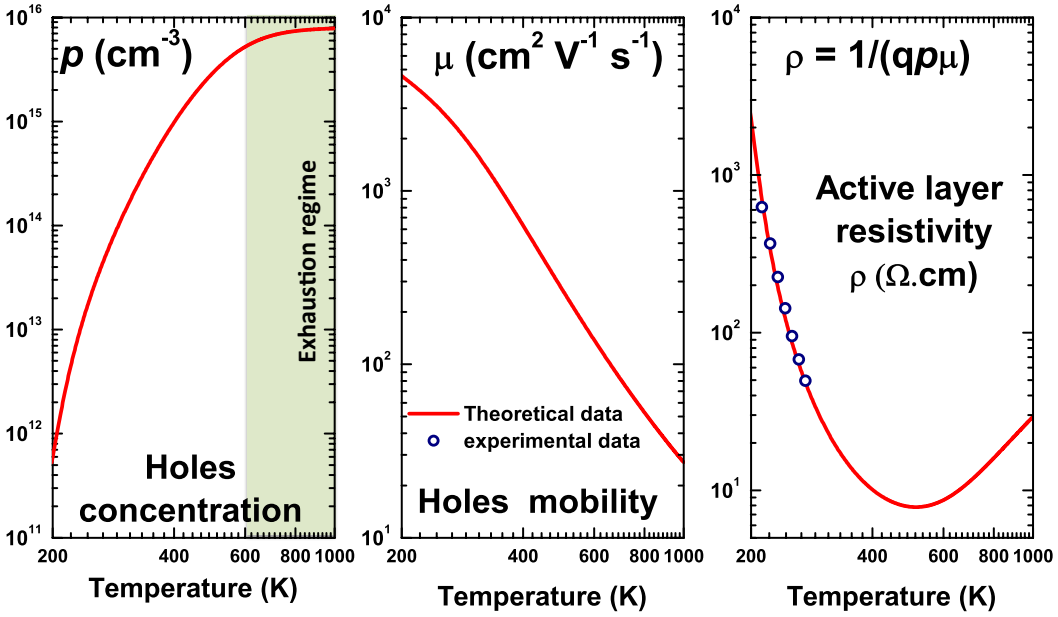

Figure 4.28: Theoretical carrier concentration (left), carrier mobility (center) versus temperature. The corresponding resistivity versus temperature was plotted together with the experimental data.

Before investigating this feature, let us consider the constant resistivity steps prior to self-heating shown on Figure 4.27. These resistivity denoted as ρ_{real} corresponds to the active layer resistivity when there is no self-heating. So, by calculating ρ_{real} at different temperatures below RT, the temperature dependence of Zr/p-diamond rectifier has been established. Figure 4.28 shows ρ_{real} as function of T_h. These experimental

data are fitted using the theoretical model introduced in Chapter 2 in order to establish the theoretical resistivity temperature dependence. For an acceptor concentration N_a of 8×10^{15} cm^{-3} and a compensation of 10^{13} cm^{-3}, a good agreement with the experimental data is obtained (Fig. 4.28). Moreover, this fitting allowed to evaluate the theoretical temperature dependence of carrier concentration and their mobility. Thus, a high hole mobility of 1750 $cm^2V^{-1}s^{-1}$ should be reached at RT in good agreement with the experimental hole mobility reported by Volpe et *al* [Volpe 2009b] (1870 $cm^2V^{-1}s^{-1}$ at 292 K) for epi-layer grown using the same reactor (homemade NIRIM type reactor) and quasi identical growth conditions. Unfortunately, such a Hall measurement can not be performed for diodes active layers due to the pseudo vertical structure adopted since the buried highly conductive layer (p^+ layer) should act as a bypass of the active layer. Anyway, the theoretical temperature dependence of resistivity established from experimental data, shows that the minimum resistivity is reached for temperature (T_s) ranging between 400 K and 600 K. For T_s higher than 500 K (full boron ionization), the resistivity increases monotonically because of mobility $T^{-\alpha}$ dependence.

4.8.3 Diamond sample temperature T_s versus Joule losses P

The theoretical resistivity offers the possibility to estimate diamond temperature for a given Joule losses. The heat exchange between diamond sample and its surrounding environment was assumed to occur with the sample holder in our experimental setup (confer Fig. 4.23). In this simplest configuration, the basic heat equation 4.24 can be used to model the heat transferred from diamond side in sample holder:

$$T_s = T_h + R_{th} \times P \tag{4.24}$$

T_s, T_h, P, and R_{th} are the sample temperature, the holder temperature, the Joule losses, and the thermal resistance of diamond/holder contact respectively. From equation 4.24 and taking the set value of sample holder temperature, the rectifier temperature was calculated in the power dissipation range where thermal ionization of boron atoms happens. This calculation was made for low temperature measurements where thermal ionization of dopants is clearly observable. Thus, by adjusting the thermal resistance, a good agreement with the theoretical temperature dependence of active layer resistivity is obtained for a R_{th} of 7.5 K/W. Figure 4.29 shows the experimental resistivity versus the sample temperature T_s calculated using equation 4.24 for three measurements performed with a holder temperature T_s initially set at 213 K, 223 K, and 233 K. Besides the fact that

they were perfectly overlapped, the comparison with the theoretical resistivity confirmed that the rectifier temperature variation due to self-heating can be adequately explained using the basic heat equation defined above.

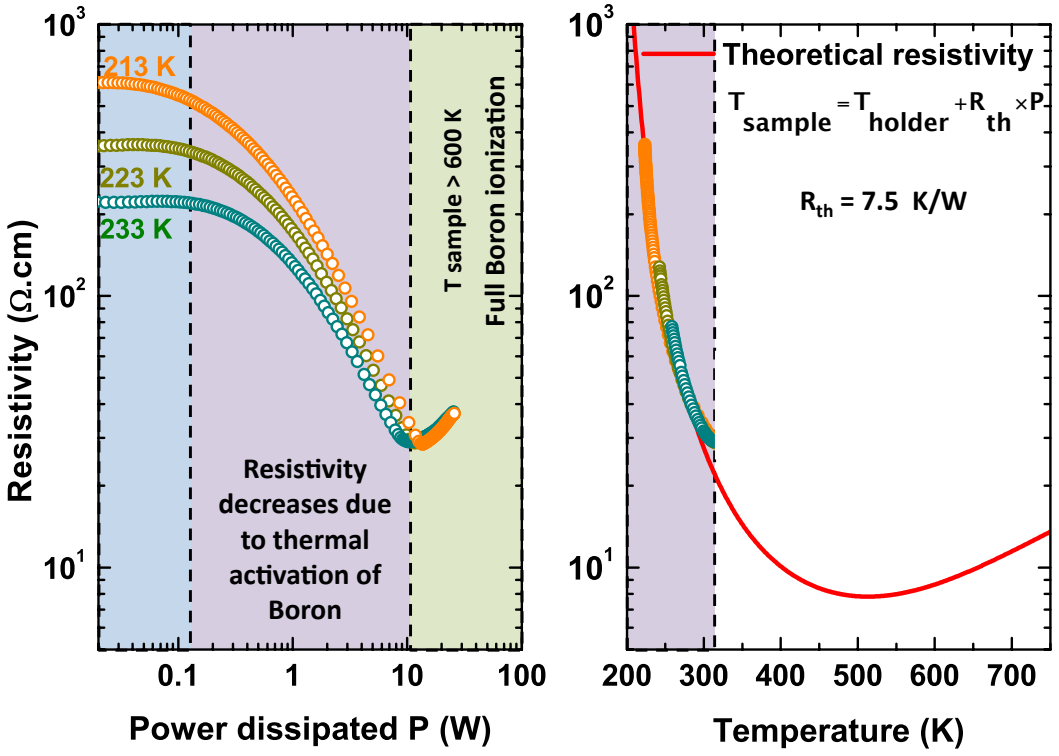

Figure 4.29: Diode active layer resistivity versus power dissipated (left) and its temperature dependence (right) established using equation 4.24 which was compared to the theoretical curve.

Unfortunately, this simple law is no longer sufficient to describe the identical resistivity feature observed when the dissipated power is higher than 10 W. Indeed, the temperature dependence of experiment resistivity established using this latter, started to deviate from the theoretical curve when the losses is above 10 W. Since the sample temperature reach the exhaustion regime for this high losses, the discrepancy with theoretical resistivity demonstrates that identical resistivity tendency for losses higher than 10 W cannot be ascribed to a carrier mobility decreasing only. This discrepancy could be a consequence of the invalidity of the main assumption made to estimate the experimental resistivity of the diode active layer. It was earlier assumed that the resistance induced by the highly conductive layer in pseudo-vertical diode structure was negligible and the serial resistance was ascribed the slightly doped active layer only. In the exhaustion regime, where the active resistivity is the minimum value, this latter assumption is no more obvious and can be inaccurate. However, this inaccuracy is not the main cause of the forward current limitation when the losses were higher than 10 W. It might be noted

that such a power level is obtained at high forward bias voltage (higher than 10 V). Thus, the influence of the carrier velocity saturation due to high electrical field related to the high forward bias must be taken in account to describe the observed resistivity profile.

4.8.4 High field influence on forward current

The electrical current in a semiconductor is non-ohmic under high electric fields. This is the consequence of hot-carrier phenomenon leading to a non linear relationship between carrier velocity v_d and electric field E:

$$v_d(T,E) = \frac{\mu_0(T)}{1+\mu_0(T)E/v_{sat}}E \tag{4.25}$$

μ_0 depends on temperature T and corresponds to the carrier mobility defined by the relaxation time approximation ($\mu_0 = q\tau_{rel}/m^*$), where τ_{rel} is the relaxation time of lattice scattering. Conversely, v_{sat} is the saturation velocity linked to optical phonon energy and carrier effective mass ($v_d = (\hbar\omega_0/m^*)^{0.5}$).

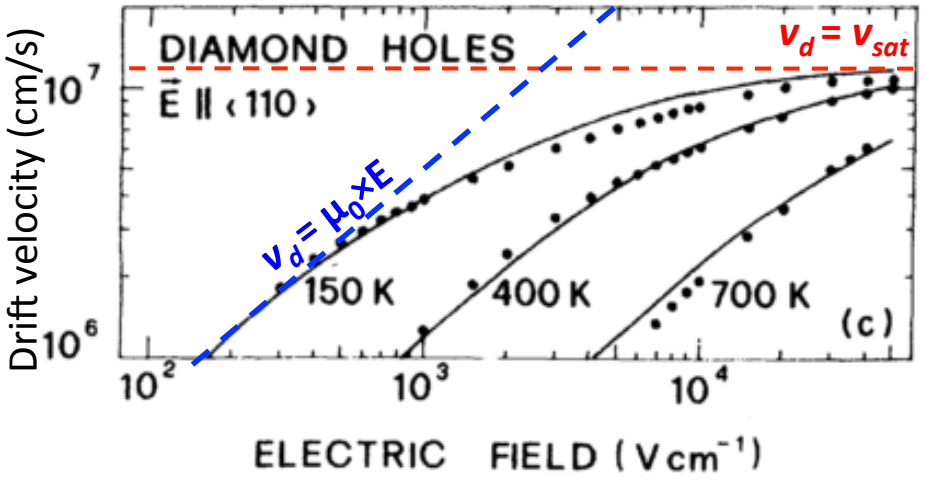

Figure 4.30: Hole-drift velocity versus electric field reported by Reggiani et al [Reggiani 1981] illustrating the linear correlation filed regime and the saturation velocity.

Figure 4.30 [Reggiani 1981] shows the typical temperature and field dependence of hole velocity. The ohmic regime "$V_d = \mu_0 E$" (field lower than 10^3 V/cm) and hole velocity saturation at 1.1×10^7 cm/s [Reggiani 1981] (field higher than 10^3 V/cm) are highlighted for a sample temperature of 150 K. Moreover, for an electric field higher than 10^5 V/cm (E_{lim}), it can be assumed that the holes velocity saturation occurred for a

diamond temperature lower/or equal to 700 K. Thus, if the electric field E is higher than E_{lim}, the electrical current density J (A.cm^{-2}) must be $J \approx qpv_{sat}$ and the resistivity ρ therefore defined as $\rho(E) \approx E/(qpv_{sat})$. A linear relationship must exist between the calculated resistivity and the electric field if the carrier velocity saturation occurs. For the current-voltage measurements previously discussed, the diode active layer is 1.3 μm thick and the E_{lim} should be reached at around 13 V.

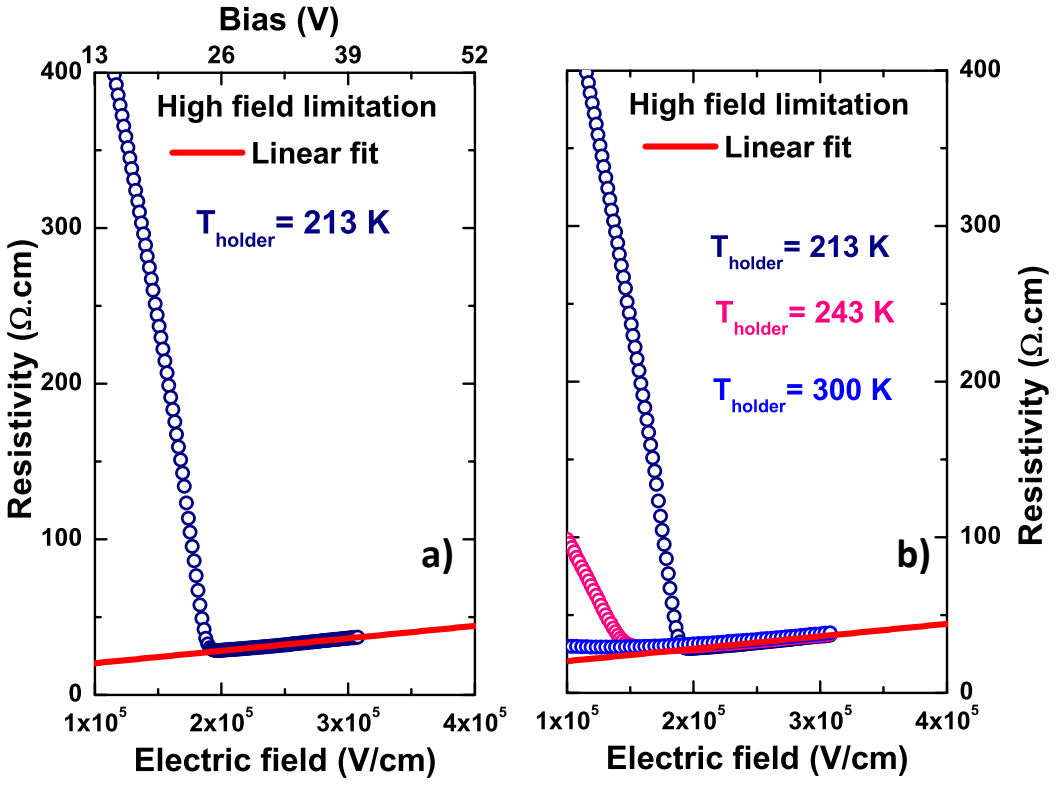

Figure 4.31: Field dependence of experimental resistivity calculated using: a) the I-V characteristic measured for a holder temperature initially set at 213 K, b) I-V characteristics measured for a holder temperature initially set at 213 K, 243 K, and 300 K. The linear field dependence is highlighted.

Figure 4.31 a) shows the field dependence of experimental resistivity calculated using the I-V characteristic measured at 213 K (initial temperature prior to the self-heating). The calculated resistivity is linearly correlated to the electric field when $E \geq 2 \times 10^5$ V/cm (get at 26 V). This linear feature demonstrates that the electrical current is limited by hole velocity saturation when the forward bias is higher than 26 V. Below this bias voltage, the calculated resistivity is driven by the thermal activation of boron acceptors (resistivity drop) due to diode self-heating. The linear field dependence of resistivity allows assessing to carrier concentration which was 8×10^{15} cm^{-3} in good agreement with full boron ionization regime. Indeed, for a forward bias above 26 V (losses higher than 10 W), the sample temperature is higher than 500 K. The theoretical

temperature dependence of resistivity established using the experimental data (confer subsection 4.8.2) demonstrates that the exhaustion regime (full boron ionization) occurs in this temperature range ($T \geq 500$ K). In sum, the weak resistivity increase observed for all I-V characteristics (Fig. 4.31 b)) is related to the carrier drift velocity saturation due to high forward field ($E \geq 2 \times 10^5$ V/cm). This field influence is predominant after the thermal activation of boron acceptors (for T higher than 500 K) due to self-heating.

4.8.5 Summary

The thermal cycling measurement demonstrates the heat generation in Zr/p-diamond rectifier due to joule effect losses. These losses induced the self-heating of the diode because of the poor heat transfer from diamond with its surrounding environment.

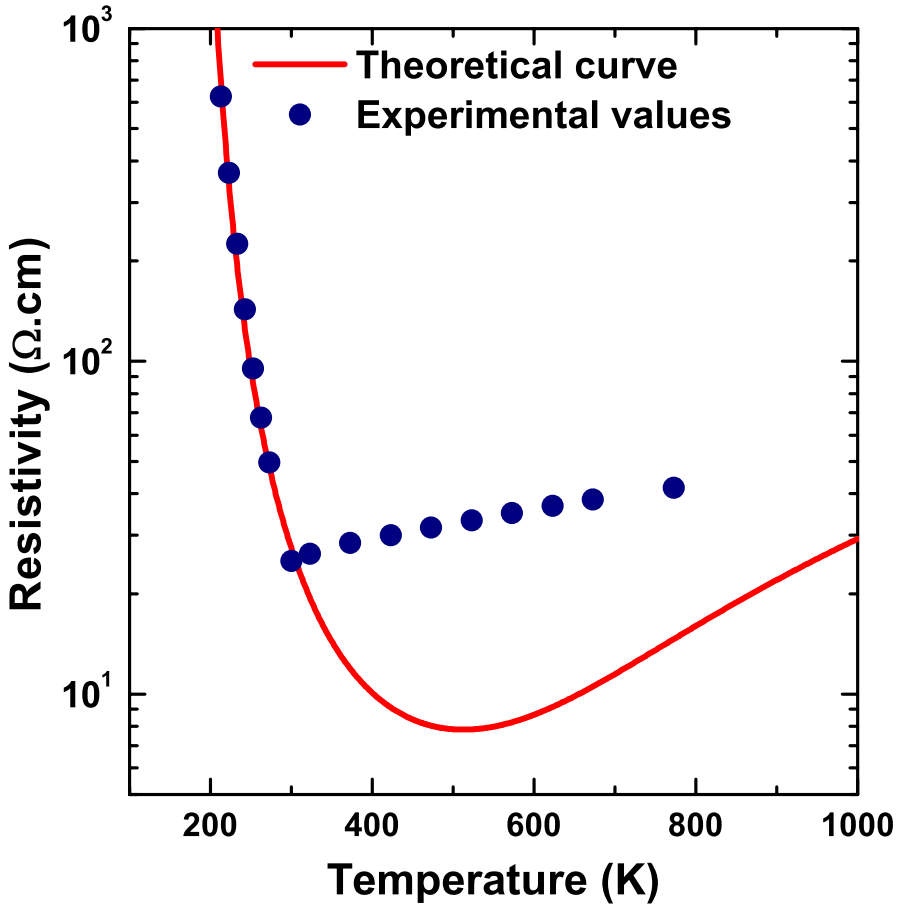

Figure 4.32: Temperature dependence of Zr/p-diamond rectifier active layer resistivity together with the theoretical profile deduced from low temperature data.

The self-heating leading to a sample temperature higher than 600 K, demonstrates again the thermal stability of Zr Schottky electrodes and furthermore the full ionization of boron atoms in diode active layer. As a result, the current in ohmic regime (bias > 3

V) and its corresponding active layer resistivity are almost temperature independent for a device operating above 300 K (confer Fig. 4.32) in disagreement with the theoretical serial resistance profile deduced low temperature I-V characteristics. Thus, the electrical current of Zr/p-diamond rectifier operating at high temperature is limited by a minimum serial resistance ($\sim 50\ \Omega$) partly related to full boron ionization. Indeed, the resistance of highly conducting layer of pseudo-vertical structure must be not negligible anymore when the full ionization occurs in diode active layer. This assumption is motivated by the expected resistance of active layer only ranging from 10 to 35 Ω when the exhaustion regime is reached ($T_s > 400$ K) and the maximum operating temperature is 800 K. Anyway, the results coming from this investigation suggests the possibility to thermally ionized boron atoms using the losses in diamond devices. The cooling of diamond power devices could be imagined so that it allows keeping a sufficient amount of heat generated to reach the full boron ionization regime.

4.9 Electrical properties of annealed Zr Schottky electrodes

The previous section highlighted the possibility to lower the SBH of Zr/p-diamond rectifiers by performing annealing. This section will focus on the investigation of electrical performances of Zr/p-diamond Schottky diodes. The rectifiers fabricated on samples #2 and #3 were successively annealed at 350 °C and 450 °C. For each annealing performed, the Schottky diodes are characterized in a wide temperature range.

4.9.1 Forward characteristics

RT electrical properties: Figure 4.34 shows the current-voltage characteristics of as-deposited and annealed Zr/p-diamond rectifiers fabricated on sample #2. As expected, the annealed Zr/p-diamond rectifiers exhibited a better electrical properties than as-deposited electrodes as reflected by the current density about 150 A.cm^{-2} for 450 °C annealing, 19 A.cm^{-2} for 350 °C annealing, and 0.61 A.cm^{-2} for as-deposited electrodes at 2 V. For each annealing, the effective SBH and the ideality factor (ϕ_B^{eff}, n) estimated from a thermionic model and the theoretical Richardson constant 90 A.cm^{-2}K^{-2}, were (1.97 eV, 1.58) for as-deposited electrodes, (1.4 eV, 1.28) for 350 °C annealed contacts, and (1 eV, 1.16) for 450 °C annealed contacts. Zr Schottky electrodes annealed at 450 °C exhibit a barrier height about 1 eV whereas the as-deposited electrodes have a SBH of 1.97 eV. Besides the diminution of SBH, the annealing leads to a decrease of the ideality

factor thus suggesting an improvement of Zr/p-diamond interface.

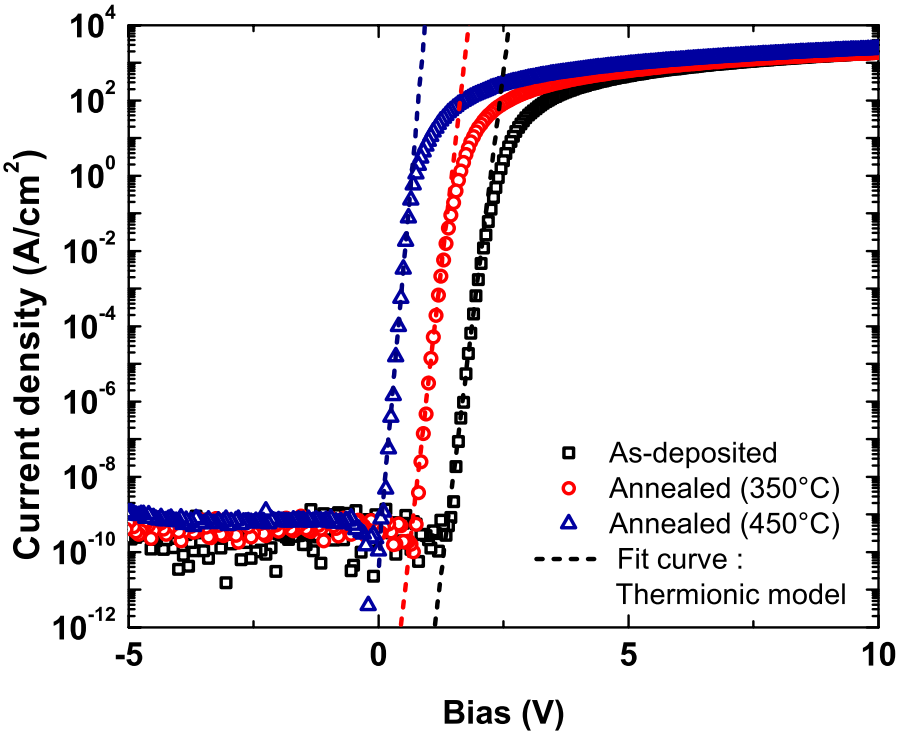

Figure 4.33: Room temperature current-voltage characteristics for as-deposited and annealed (Zr/Pt/Au) Schottky contacts.

Moreover, the rectifiers annealed at 450 °C are reproducible regardless of samples as shown on Figure 4.34 where the I-V characteristics of 18 diodes fabricated on sample #3 (100 μm in diameter diodes randomly selected). The reported I-V curves are perfectly overlapped in thermionic-emission current range. The calculated zero-bias SBH and ideality factor are then weakly dispersed as evidenced by the right graph shown on Figure 4.34. It must be noticed that the ohmic regime (serial resistance) together with the reverse current are spread. The dispersion in ohmic regime can be ascribed to serial resistance fluctuation due to inhomogeneous doping. At the opposite, the dispersion of reverse current is mainly linked to Schottky barrier fluctuation as shown on Figure 4.34.

Thermal stability: The thermal stability of each annealing is defined by the temperature range in which its barrier height can be considered as constant. A Richardson's plot appeared to be the best way to estimate this T range for each annealing performed. Indeed, from the expression of the saturation current (Is), as defined by the thermionic emission theory, a linear correlation may exist between $ln(Is/(ST^2))$ and $1/T$ as followed:

$$ln(Is/(ST^2)) = -\frac{\phi_b^0}{k_B}\left(\frac{1}{T}\right) + ln(A^*) \tag{4.26}$$

where S, k_B, and A^* are respectively the diode area, the Boltzmann's constant, and the Richardson's constant. This linear correlation called Richardson's plot, allows us to assess to the zero-bias barrier height ϕ_b^0 from the slope parameter and furthermore the Richardson's constant (intercept with $1/T = 0$).

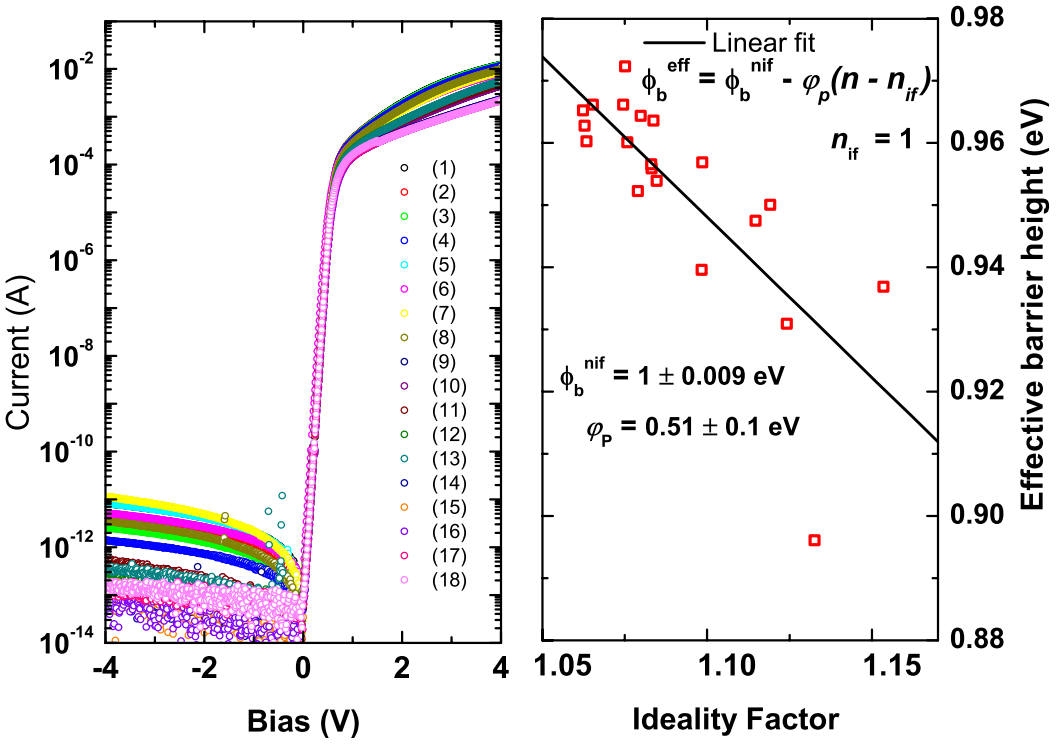

Figure 4.34: Current-voltage characteristics for annealed (450 °C) Zr Schottky contacts (sample #3) together with effective Schottky barrier versus ideality factor.

Figure 4.35 shows the Richardson's plot for each case. For as-deposited and annealed electrodes, the experimental values of $ln(Is/(ST^2))$ increased linearly versus $1/T$ in the whole operating temperature range (Fig. 4.35) thus attesting a constant slope and so a constant zero-bias SBH. The as-deposited electrodes remain stable up to 250 °C (473 K) while the electrical characteristics of electrodes annealed at 350 °C exhibit a modification for an operating temperature higher than 350 °C (623 K). On the other hand, Zr/p-diamond rectifiers annealed at 450 °C remain stable (no change on I-V characteristics) after a thermal cycling measurement ranging from room temperature to 500 °C (773 K). Its corresponding Richardson's plot is limited to 573 K because of a weak rectification factor (2 to 3 decades are needed to fit the thermionic regime) for a device operating above this limit. The zero-bias SBH for rectifiers annealed at 450 °C is about 0.88 eV which is at least 1eV lower than the as-deposited electrodes. This confirms again the diminution of SBH versus annealing and furthermore the possibility to get a barrier height below 1eV. On the other hand, the calculated Richardson's constants for

each annealing are at least three times lower than the theoretical value. This discrepancy presumed that the ZrO_2 interface layer should exist after annealing. Indeed, for rectifying MS junction with an insulating interface layer, the saturation current related to the thermionic current current must be corrected by a transmission coefficient corresponding to the carrier tunneling probability over this interfacial oxide layer. The transmission coefficient Tr is expressed [Card 1971, Altndal 2007] as $Tr = \exp(-\alpha\chi^{0.5}\delta)$, where $\alpha = (4\pi/h)(2m^*)^{0.5}$ is a constant that depends on the tunneling effective mass m^*, χ the mean tunneling barrier height, and δ the thickness of the insulating layer. The equation 4.26 then rewrites:

$$ln(Is/(ST^2)) = -\frac{\phi_b^0}{k_B}\left(\frac{1}{T}\right) + ln(A^*Tr) \tag{4.27}$$

Using the equation 4.27, one can estimate the transmission coefficient form intercept $ln(A^*Tr)$ and using the theoretical Richardson's constant.

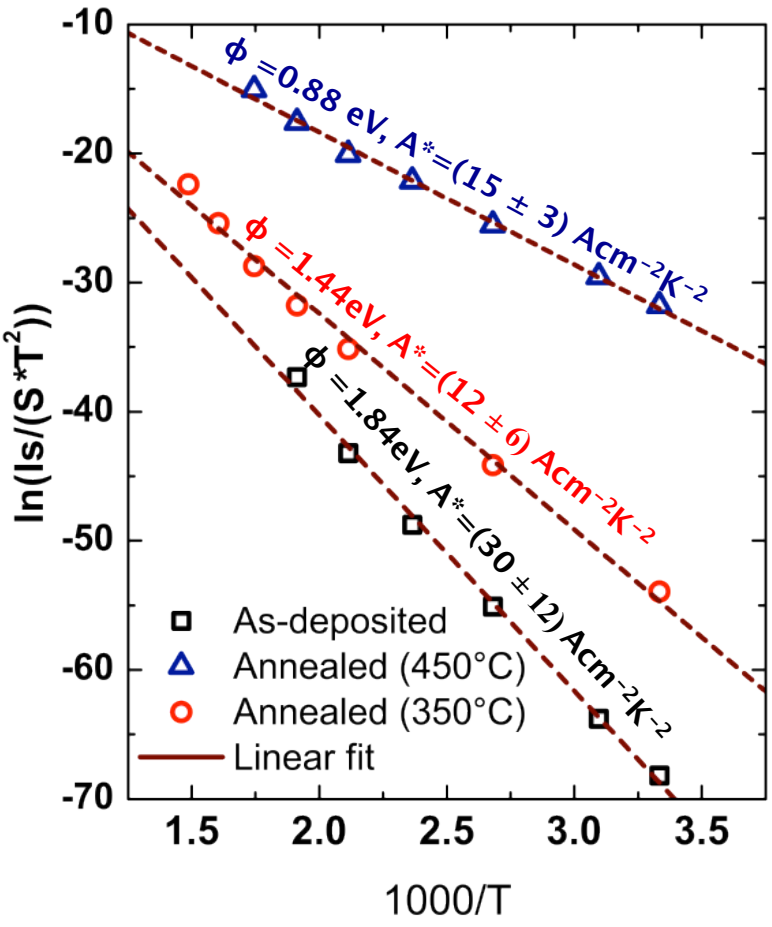

Figure 4.35: Richardson's plot for as-deposited and annealed (at 350 °C and 450 °C) Schottky contacts.

The calculated transmission coefficients were then around 0.33, 0.13, and 0.17 for respectively as-deposited and annealed electrodes (350 °C and 450 °C). In sum, according to the annealing temperatures, different barrier height can be obtained from Zr Schottky electrodes deposited of oxygen-terminated diamond. For rectifier annealed at 450 °C, apart the good reproducibility, the thermal stability up 450 °C, and the ideality relatively close to 1, the zero-bias SBH is about 0.88 eV which is 1 eV lower than in case of as-deposited electrodes.

4.9.2 Reverse characteristics

The reverse current of Zr/p-diamond rectifier annealed at 450 °C was measured under high applied bias voltage. Let's remind that for as-deposited Schottky electrodes, a maximum field of 7.7 MV/cm within a current level below the detection limit of our measurement set up (10^{-9} Acm^{-2}) was demonstrated. Figure 4.36 shows the typical reverse current profile measured for 500×500 μm^2 square shape Schottky diodes (sample #3) operating at 283 K.

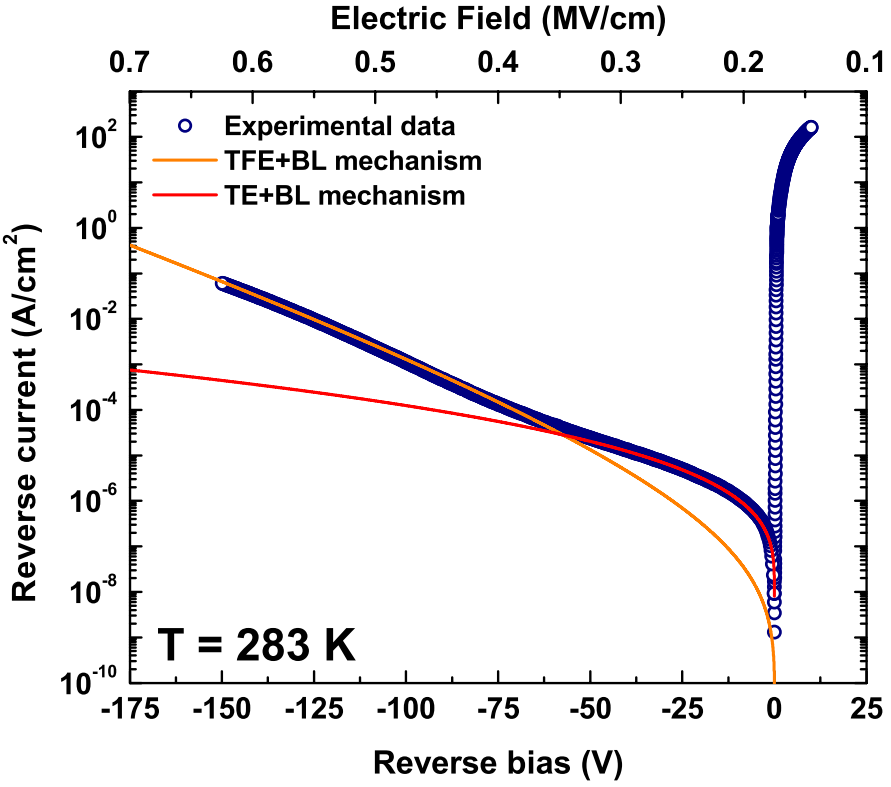

Figure 4.36: Current-voltage characteristic of annealed (450 °C) Zr Schottky contacts (sample #3) operating at 283 K. The current related to the TE+BL mechanism only and the tunneling current TFE+BL mechanism were highlighted.

The reverse current density is higher for annealed rectifier since their SBH is lower. Using the theoretical models defined in section 4.3, namely, the thermionic-emission (TE) and the thermionic-field emission (TFE) taking in account the barrier lowering (BL) due to Schottky effect, it is observed that this reverse current feature can be adequately explained. At low temperature, the contribution of the TE+BL mechanism and the TFE+BL can be clearly distinguished as shown on Figure 4.36. The electrical current related to the (TE+BL) mechanism only allows estimating the effective acceptor concentration Na and the parameter α related to density and depth of interface states as defined by the empirical expression of Andrews and Lepselter [Andrews 1970, Tung 1992] introduced in the section 4.3. Na and α are respectively 2.9×10^{16} cm^{-3} and 0.37 nm, which are in good agreement with the doping level estimated by CL spectroscopy (1.2×10^{16} cm^{-3}) and the thickness of interface layer measured by HRTEM (0.4 nm). The tunneling parameter E_{00} (eV) of 1.5×10^{-3} eV is furthermore deduced from TFE+BL fitting model. E_{00} depends on the doping level N_a and the carrier effective mass. For diamond devices, this parameter is given by $E_{00} = 18.5 \times 10^{-15}(N_a/(5.7 \times m^*))^{0.5}$.

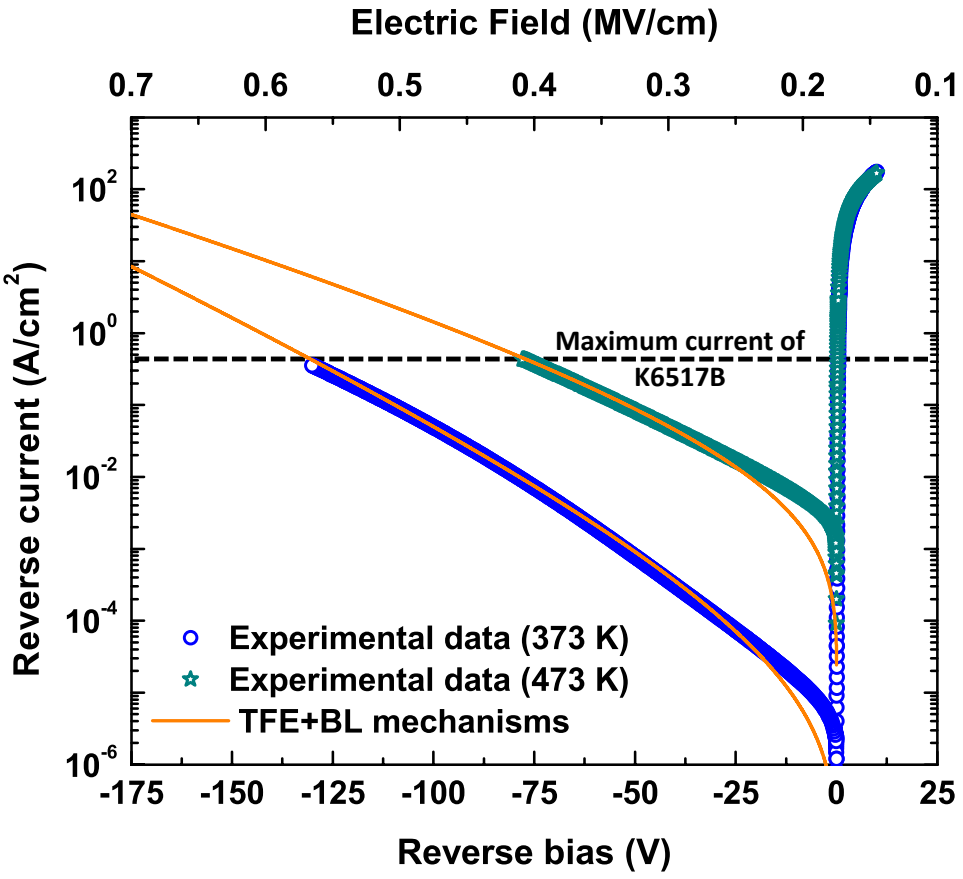

Figure 4.37: Current-voltage characteristic of annealed (450 °C) Zr Schottky contacts (sample #3) illustrating the TFE+BL current at 373 K and 473 K.

Thus, taking this expression and the acceptor concentration N_a estimated using the (TE+BL) model, the effective mass can be calculated. The theoretical effective mass is defined as $m^* = m^*_{hh} + m^*_{lh}$ [Mönch 2004] (m^*_{hh} is the effective mass of heavy hole and m^*_{lh} is the effective mass of light hole). For diamond sample oriented in (100) direction, $m^*_{hh} = 0.427$ and $m^*_{lh} = 0.366$ [Willatzen 1994] thus leading to a theoretical m^* of 0.793. The fitting performed gives rise to a N_a of 2.9×10^{16} cm^{-3} and a E_{00} (eV) of 1.5×10^{-3} eV. An effective mass $m^* = 0.77$ close to the theoretical value (0.793) was obtained using these values. This good agreement confirms that the models used were appropriated to describe the experimental electrical current. Thus, at low temperature as well as at high temperature as shown on Figure 4.37 (373 K and 473K), the electrical current under high reverse bias is related to the (TFE+BL) mechanism. Noting that both low temperature and high temperature measurements point out a substantial problem, which is the impossibility to reach the critical field of diamond keeping several orders of magnitude as rectification factor. As example, for a diode operating at 373 K, only a rectification ratio of 3 decades exists when a reverse field of 1.25 MV/cm (fig. 4.38) is reached.

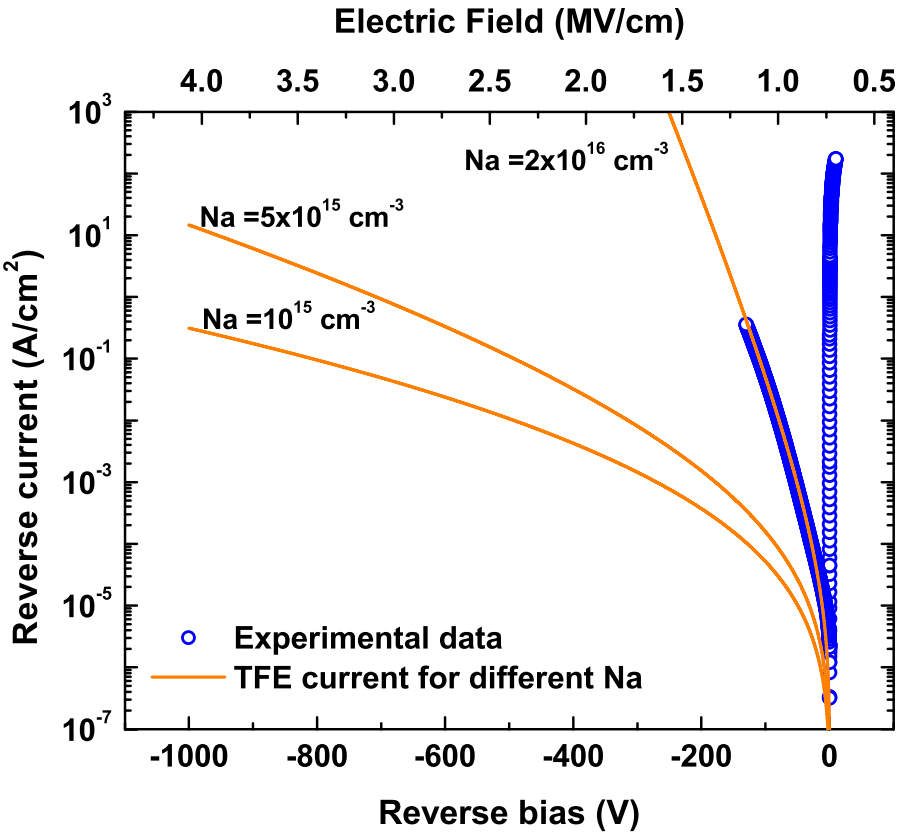

Figure 4.38: Current-voltage characteristic of annealed (450 °C) Zr Schottky contacts (sample #3) operating at 373 K. The TFE+BL current was calculated for different acceptor concentration to bring out its variation versus N_a.

4.9.2.1 Doping effect

One the most evident solution to enhance the reverse state (i.e. lower the reverse current) could be the diminution of the doping level N_a. Figure 4.38 shows theoretical reverse currents calculated using the (TFE+BL) mechanism together with the experimental current for a device operating at 373 K. A doping level below 10^{16} cm^{-3} involves a significant change on the current level. For a N_a of 5×10^{15} cm^{-3} and 10^{15} cm^{-3}, the TFE+BL reverse current at 373 K of annealed (450 °C) Zr/p-diamond diodes will be approximately about $\times 10^{-1}$ Acm^{-1} for a maximum field of 4 MV/cm. It must be noticed that the diminution of acceptor concentration will involve a reduction of forward current. For the example mentioned above, the forward current will divide by a factor less than ten. A minimum rectification factor of two order of magnitude may be expected for a devices switching from forward state to a reverse field of 4 MV/cm (-1000 V blocking voltage for devices fabricated on sample #3).

4.9.2.2 Barrier height effect

Another possibility to minimize the reverse current could be a higher barrier height. An annealing below 450 °C for example at 400 °C should allow getting a higher barrier ranging between 0.9 eV and 1.4 eV. Such an intermediate annealing will cause alone a limited diminution of the reverse current level. It must be combined with a low doping level aiming to get high critical fields in a wide operating temperature range. However, the thermal stability limit will be then defined by the annealing temperature since it was demonstrated that the Zr/p-diamond junction stayed relatively stable below their annealing temperature. Additionally, a higher SBH will give rise to a higher threshold voltage and so a higher forward losses.

Anyway, it is possible to explain the discrepancy between as-deposited and annealed Zr Schottky contact. Since, the reverse current is mainly originated from the thermionic-field emission taking in account Schottky barrier lowering related to image force and static dipoles at the interface, the theoretical current of as-deposited Zr electrical can then be calculated using a zero-bias barrier of 1.84 eV, a Richardson's constant of 33 A.cm^{-2}K^{-2}, an acceptor concentration of 2×10^{16} cm^{-3}, and a temperature of 300 K. The experimental and theoretical reverse current for as-deposited Zr electrodes are illustrated on Figure 4.39. The (TFE+BL) current is at least 3 orders of magnitude lower than the detection limit of measurement set up (10^{-9} Acm^{-2}).

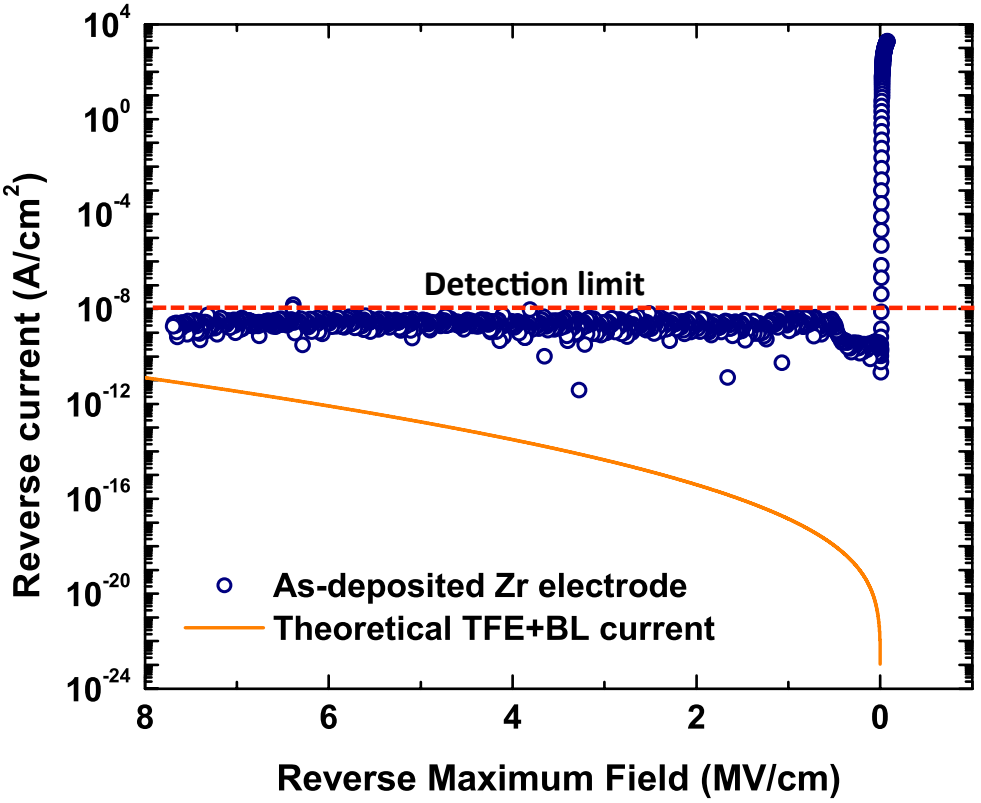

Figure 4.39: RT current-voltage characteristics of as-deposited Zr Schottky contacts (sample #2) together with the expected theoretical (TFE+BL) current.

4.9.3 Summary

In summary, the annealed Zr/p-diamond junction exhibited a lower SBH than as-deposited Zr electrodes. The 450 °C annealing allowed a significant reduction of SBH to a value lower than 1 eV. The Zr/p-diamond junctions annealed at 450 °C are thermally stable even for a operating temperature of 500 °C. Moreover, the annealed Zr electrodes are characterized by a reproducibility of their electrical properties regardless of samples and furthermore a reverse current mainly determined by a thermionic-field emission mechanism. The SBH diminution versus annealing reported here, is a general tendency suggesting a structural change of annealed Zr/oxygen-terminated diamond interfaces towards an identical configuration. According to the experimental Richardson's constants, which are at least one third lower the theoretical value, seems to be the consequence of ZrO_2 interface layer which is thermally stable.

4.10 Origin of Schottky barrier decrease: attempt to explain

Metal - oxygen terminated diamond junctions are known to be highly sensitive to annealing. This sensibility may be reflected in the thermal stability of the interface existing between the metallic electrodes and oxygen terminated diamond. When the Schottky electrode does not react sufficiently with the oxygen passivation layer (as for noble metals such as Au), apart the poor adhesion of this latter on diamond sample, the oxygen initially present on diamond surface may desorbed if a heat treatment (above 600 K) is performed as demonstrated by Teraji et *al* [Teraji 2009b]. The authors reported the main consequences of this desorption namely, the ideality factor increasing because of the apparition of spatial inhomogeneity and furthermore Schottky barrier height decreasing (SBH dropped from 2.2 eV to 0.9 eV after 870 K heat treatment). The SBH diminution due to annealing is a typical feature of diamond rectifiers based on oxygen terminating surface [Ikeda 2009, Liao 2005, Umezawa 2012]. The explanation given in reference [Teraji 2009b], is particularly appropriated for rectifiers where the Schottky electrodes do not react sufficiently with oxygen layer such as Au or Mo, Ru, Ir [Umezawa 2012]. However, the same barrier lowering was generally observed for easily oxidizable metal like Al (SBH of 2 eV for as-deposited electrodes [Koné 2010] and 0.4 eV after 673 K annealing [Umezawa 2012]). This last-mentioned case suggests the requirement of thermally stable interface layer to prevent the oxygen layer desorption when easily oxydizable metals are used.

For zirconium Schottky electrodes deposited on O-terminated diamond investigated here, the existence of thin ZrO_2 interface layer was demonstrated for as-deposited contact. Conversely, the electrical properties reproducibility of annealed (723 K) devices regardless of diodes or samples, seems to show that the oxygen layer desorption is no longer true to explain the SBH diminution observed. Aiming to confirm this and to investigate the origin of the barrier decrease occurring for Zr Schottky electrodes, the spatially inhomogeneous potential model established by Werner [Werner 1991] will be first used to inspect the homogeneity of as-deposited and annealed electrodes. On the other hand, HRTEM study results will be introduced and discussed. Finally, the MIGS-and-Electronegativity theory developed by Mönch[Mönch 2004] will be used in order to compare Zr electrodes SBH decrease to those reported in literature.

4.10.1 Homogeneity of Zr/O-terminated junction

4.10.1.1 Zero-bias SBH and ideality factor as function of temperature

In the situation where the Zr/O-terminated diamond rectifier interface is modified because of the oxygen desorption, the spatially inhomogeneous interface resulting should involve a SBH fluctuation in the junction area. For spatially inhomogeneous rectifier, the classical thermionic-emission theory is no longer adequate to explain the electrical current and furthermore the Schottky barrier [Werner 1991, Tung 1992]. One the main features of a spatially inhomogeneous rectifying junction commonly observed is a temperature dependent zero-bias SBH ϕ_b^0 on one hand, and on the other hand, a temperature dependent ideality factor n deduced from thermionic-emission theory [Werner 1991, Tung 1992]. Let's remind (confer section 4.3) ϕ_b^0 and n must be temperature independent in case of ideal junction.

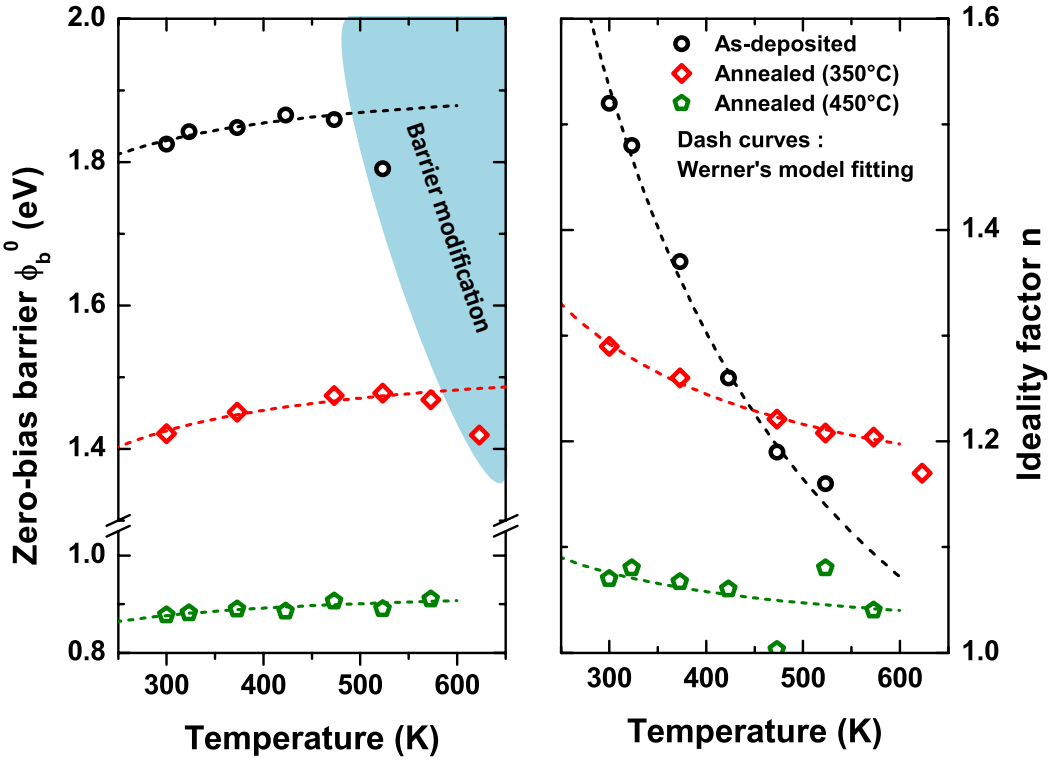

Figure 4.40: Effective barrier height (left) and ideality factor (right) versus temperature for as-deposited and annealed Schottky contacts.

Accordingly, the electrical characteristics of as-deposited Zr electrodes measured at different temperatures and those of electrodes annealed at 623 K (350 °C) and 723 K (450 °C) were fitted with the thermionic model in order to establish their zero-bias SBH and ideality factor profiles versus temperature.

Figure 4.40 shows, for each annealing, the zero-bias barrier height and ideality factor versus temperature. The as-deposited electrodes exhibit a weak ϕ_b^0 increase until to 473 K. Above this temperature limit, the SBH diminution due to heat treatment start to occur. As-deposited electrodes are then assumed to be thermally stable for an operating temperature lower than 473 K. A same feature was observed for rectifier annealed at 623 K for which thermal stability was ensured for a temperature lower than the annealed one. Additionally to the zero-bias SBH augmentation versus T observed in their thermal stability range, the calculated ideality factors for each of these two annealed electrodes are highly dependent versus temperature. For as-deposited electrodes, n dropped from 1.5 (RT value) to 1.15 (523 K). This variation is less visible when 623 K annealing is performed since n decreased from 1.3 (RT) to 1.2. Concerning Zr electrodes annealed at 723 K, both ϕ_b^0 (about 0.9 eV) and n (1.05) are relatively constant as shown on Figure 4.40 and may be considered as temperature independent. This latter annealing gives rise to features that might be expected only for ideal rectifier where the electrical current is defined by a thermionic-emission only.

Thus, the as-deposited Zr/O-terminated diamond electrodes are apparently spatially inhomogeneous. However, apart the SBH diminution falling from 1.94 eV to 0.9 eV, the spatial inhomogeneity of these rectifiers seems to disappear when an annealing is performed. Aiming to confirm this apparent disappearance of the spatial inhomogeneity correlated to the SBH lowering, the analytical potential fluctuation model developed by Werner and Guttler in 1991 [Werner 1991] (Werner's Model) has been applied to our case.

4.10.1.2 Werner's model

Several analytical models explaining the current transport over inhomogeneous MS junctions were reported in literature. The main idea behind most of theoretical modeling of electrical current across inhomogeneous junctions is to take into account the MS interface influences. Tung [Tung 2014] points out the complexity of this attempt and furthermore the difficulty to get a simplest theoretical model.

Werner model is one of the simplest theoretical models which is used here. This model explains the temperature dependence of ϕ_b^0 and n using the thermionic emission. In Werner's model, the SBH fluctuations due to the spatial inhomogeneities are modeled by a Gaussian distribution characterized by a mean value $\bar{\phi}$ and standard deviation σ_s.

From this empirical approach, a quantitative expression of SBH is established:

$$\phi_b(V_j,T) = \bar{\phi_b}(V_j) - \frac{\sigma_s^2(V_j)}{(2k_BT/q)} \tag{4.28}$$

SBH in case of spatially inhomogeneous junction is both bias and temperature dependent. At zero-bias, the SBH is therefore expressed as:

$$\phi_b^0(T) = \bar{\phi_b^0} - \frac{\sigma_{s0}^2}{(2k_BT/q)} \tag{4.29}$$

Thus, the T-dependence linked to standard deviation σ_{so} may not occur if the standard deviation tends towards zero, i.e. if sharp potential distribution (quasi uniform or uniform barrier height) exists in junction area.

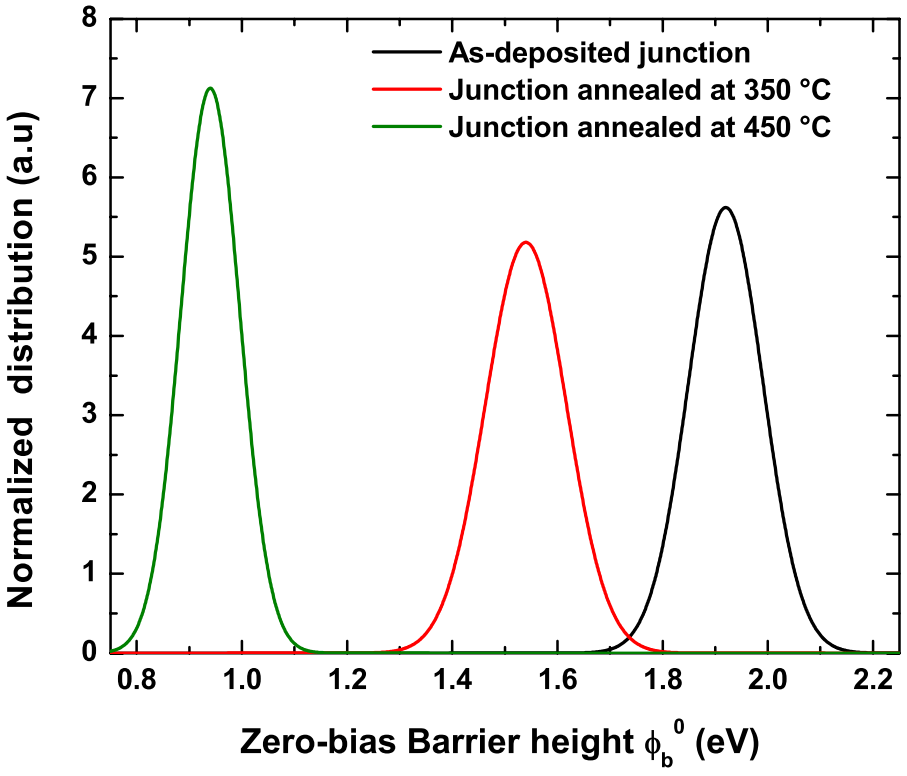

Figure 4.41: Zero-bias SBH distribution for as-deposited and annealed Zr/O-terminated diamond rectifier.

Accordingly, the SBH versus T established for each annealing are fitted with the equation 4.29 in order to model the potential distribution in each. The fit results illustrate on Figure 4.40 , shown a good agreement of Werner's model with experimental data in thermal stability range. The calculated mean barrier and standard deviation were summarized in Table 4.2. Figure 4.41 shows the theoretical SBH distribution for each

annealing performed. The rectifier annealed at 450 °C exhibit the sharpest SBH distribution characterized by a standard deviation of 0.056 eV. Unfortunately, this latter is relatively close to those of as-deposited electrodes making difficult to confirm the qualitative observation stating that the spatial inhomogeneity seems disappear if an annealing is performed.

Anyway, the theoretical analysis of the deformation of SBH distributions under applied bias reveals a relatively constant distribution for electrodes annealed at 450 °C. Noting that the ideality factor in Werner's model is defined as the result of the deformation of the spatial barrier distribution when a bias voltage is applied. The ideality factor is temperature dependent and expressed as [Werner 1991]:

$$n(T) = 1 + \rho_2 - \frac{\rho_3}{(2k_BT/q)} \tag{4.30}$$

ρ_2 and ρ_3 quantify the voltage deformation of Schottky barrier distribution and are originated from the requirement that the ideality factor must be bias-independent which is satisfied by assuming both $\bar{\phi_b}$ and σ_s may vary linearly with bias V_j:

$$\Delta\phi_b(V_j) = \bar{\phi_b}(V_j) - \bar{\phi_b^0} = \rho_2 V_j \tag{4.31}$$

$$\Delta\sigma_s(V_j) = \sigma_s^2(V_j) - \sigma_{s0}^2 = \rho_3 V_j \tag{4.32}$$

The fit results of ideality profiles obtained for each annealing are previously shown on Figure 4.40. A good agreement with the expression 4.30 is obtained and the calculated ρ_2 and ρ_3 are summarized in Table 4.2. The 450 °C annealing led to a coefficient ρ_2 of 0.004 and ρ_3 of -0.003 which are respectively 92 and 6 lower than those of as-deposited electrodes.

Table 4.2: Mean barrier, standard deviation, and voltage coefficients calculated for as-deposited and annealed Zr/O-terminated diamond rectifiers.

Zr electrodes	$\bar{\phi_b^0}$(eV)	σ_{s0} (eV)	ρ_2	ρ_3 (mV)
As-deposited	1.93	0.071	-0.37	-20
Annealed (350 °C)	1.54	0.077	0.1	-10
Annealed (450 °C)	0.93	0.056	0.004	-3

The parameter ρ_3 describes the narrowing of the gaussian distribution of SBH upon bias voltage [Werner 1991] whereas the coefficient ρ_2 reflects the bias-dependence of the

mean SBH. The lowest values of ρ_2 and ρ_3 explain the temperature independent feature of annealed Zr electrodes and furthermore a relatively weak bias dependent on SBH distribution under applied voltage. Indeed, under applied bias, the narrowing of barrier distribution is enhanced for annealed electrodes and the mean barrier is similar to the zero-bias value as shown on Figure 4.42. This figure illustrates the bias dependence of SBH distribution at zero-bias and 0.5 V calculated for as deposited and Zr electrodes annealed at 450 °C (723 K). The SBH distribution stays relatively constant compared to the as-deposited electrodes where the distribution is spread over a large range. The annealing allows then minimizing the influence of SBH fluctuation related to the spatial inhomogeneities. As consequence, the electrical current of Zr/O-terminated diamond rectifiers are adequately explained using a thermionic emission theory assuming a constant barrier and a constant ideality factor.

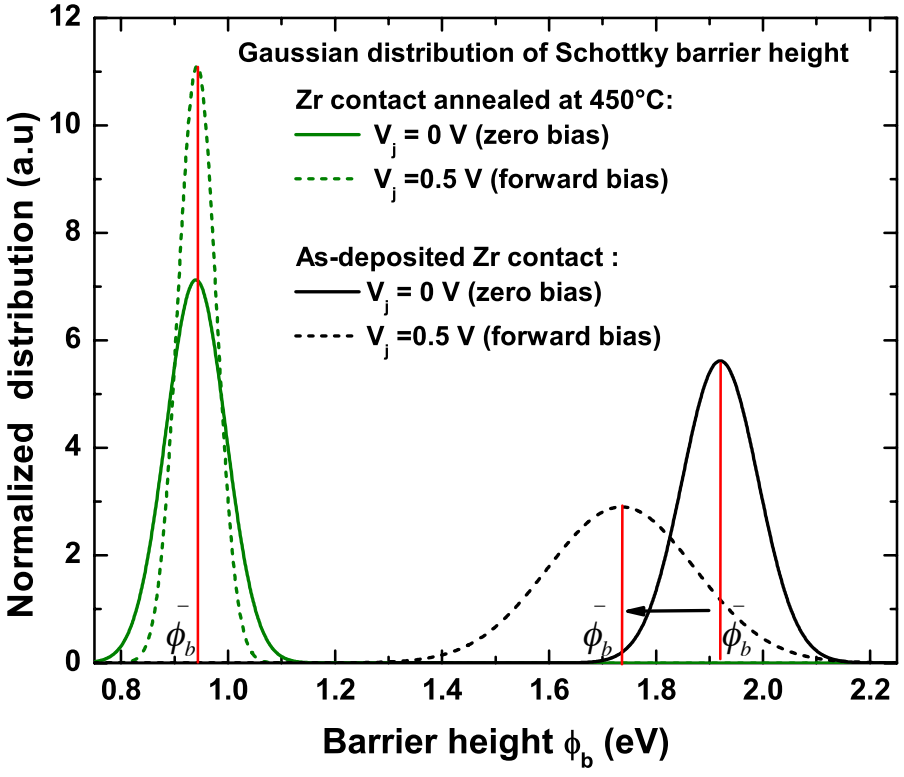

Figure 4.42: SBH distribution at zero-bias and 0.5 V calculated for as deposited and Zr electrodes annealed at 450 °C.

4.10.1.3 Summary

The analytical model developed by Werner and Guttler is used to investigate the homogeneity of as-deposited and annealed Zr/O-terminated diamond rectifiers. In the

simple model presented above, the barrier fluctuations related to the spatial inhomogeneities and assumed to be gaussian distribution, are characterized by their average and standard deviation. Although this model suffers from arbitrary assumptions not supported by any physical model, it allows to quantify bias and temperature dependence of SBH and ideality factor without considering in details the electrical properties of the interface. The temperature dependence of I-V characteristics demonstrate that the as-deposited Zr/O-terminated diamond rectifiers are spatially inhomogeneous. This spatially inhomogeneous seems to disappear when an annealing is performed. Unfortunately, the Werner's model do not allows confirming this observation. However, this model indicated that SBH distribution in case of annealed electrodes is relatively bias independent and temperature independent. As consequence, the electrical current of annealed (723 K) Zr/O-terminated diamond rectifiers were adequately explained using a thermionic emission theory assuming a constant barrier and a constant ideality factor. Thus, the annealing allowed minimizing the influence of spatial inhomogeneities on rectifiers properties in opposition to the junction deterioration reported in reference [Teraji 2009b, Teraji 2014] due to oxygen desorption.

4.10.2 Annealed Zr/O-terminated diamond interface

The theoretical model previously discussed, demonstrates the fact that Zr electrodes annealed at 450 °C behaves like a rectifier with a homogeneous barrier conversely to as-deposited electrodes. This feature suggests that the oxygen layer initially present on diamond surface still exists after annealing otherwise the resulting electrical properties should be deteriorated. Thus, the interface of Zr/O-terminated diamond rectifier annealed at 450 °C was then investigated by HRTEM and EELS at university of Cadiz, Spain (J. C. Pinero and D. Araujo) as previously made for as-deposited electrodes. HRTEM investigation demonstrates the existence and the thermal stability of the thin zirconia (ZrO_2) interface layer (0.4 nm thick) between as-deposited Zr electrodes and p-type diamond. Figure 4.43 shows the typical HRTEM image of annealed (450 °C) Zr/oxidized diamond interface performed in the same conditions as those used for as-deposited electrodes [Piñero 2014].

The white contrast between diamond and Zr layer still represents the ZrO_2 interface layer and no significant change is observed on its thickness which is always about two atomic layers as established previously after the 450 °C annealing. This result together with the

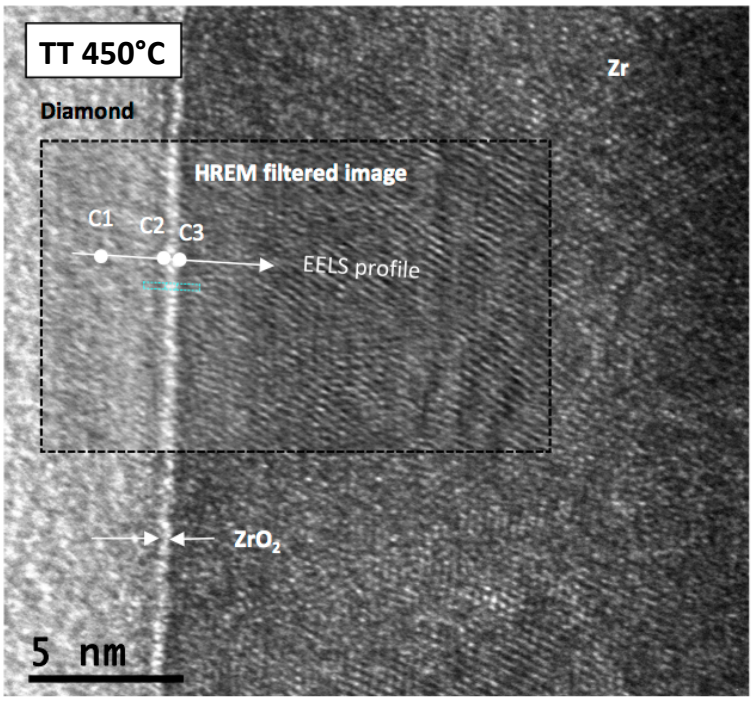

Figure 4.43: Filtered HRTEM micrograph of annealed (450 °C) Zr/p-diamond contact. The white contrast is ZrO_2 interface layer.

electrical properties reproducibility of Zr rectifiers annealed at 450 °C, definitely confirm the thermal stability of ZrO_2 interface layer, a typical feature for all devices annealed. Since the oxygen desorption not occur for annealed Zr/p-diamond diodes, the observed SBH decrease seems to be due to from a change in junction region which does not affect its interface nature.

4.10.3 MIGS-and-Electronegativity theory

Adsorbed atoms at diamond surface induce a dipole layer as demonstrated by Maier et *al*. [Maier 2001]. This dipole layer can affect the diamond Electron Affinity (EA) as illustrated for hydrogen and oxygen terminated diamond for which negative (-1.3 eV) and positive (1.7 eV) EA were respectively demonstrated. Thus, a high SBH (above 2 eV) is commonly reported for most of Schottky contacts on oxygen-terminated diamond whereas for diamond surface with hydrogen termination (H-terminated) the barrier height are generally below 1 eV. In 1994, W. Mönch [Mönch 1994] demonstrated the correlation between the low barrier height observed for metals/H-terminated diamond rectifier and C-H dipoles using MIGS-and-Electronegativity concept (Mönch's model). Let's remind that Heine's MIGS concept defines a continuum virtual gap states in junction area due to the metal's electron wave functions tailing in semiconductor. These

virtual states are defined by their neutral level ϕ_0 (Charge-neutraly level CNL) inducing a Fermi level pinned even for ideal junction.

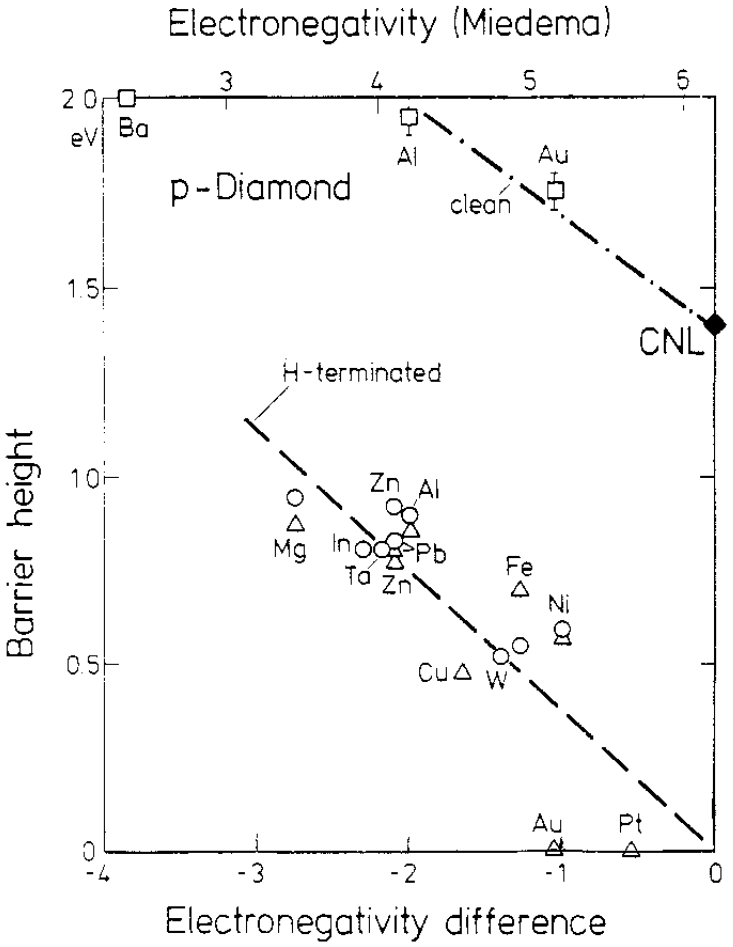

Figure 4.44: Barrier heights of metals/p-diamond contacts versus the difference of metals and carbon electronegativities reported by W. Mönch [Mönch 1994] for clean diamond surface and hydrogen terminating surface.

Mönch's model deals with Heine's MIGS theory and Pauling's electronegativity concept to describe the charge transfer across rectifying MS junction. This model predicts a linear correlation between SBH and the difference $X_m - X_s$ of the metal and the semiconductor electronegativities:

$$\phi_b^0 = \phi_0^* - S_x \left(X_m - X_s\right) \tag{4.33}$$

ϕ_0^* is the Charge Neutrality Level (CNL) at MS interface defined by Heine's MIGS theory. The slope parameter S_x is calculated from the expression $A_x/S_x - 1 = 0.1\,(\epsilon_r - 1)^2$, where ϵ_r is the electronic part of the static dielectric constant of semiconductor and $A_x = 0.86$ when the Miedema's electronegativity scale is used [Mönch 1994]. Miedema's

electronegativity scale is preferentially used within Monch's model to describe interfaces formed by solid materials. The author explained this choice by the fact that Pauling's scale should be applied when a local and molecule-like bond picture is more adequate [Mönch 1994, Mönch 2004]. For metals and clean surface diamond junctions, the zero-bias SBH ϕ_b^0 should be related to the difference of electronegativities as $\phi_b^0 = 1.4 - 0.3\,(X_m - X_s)$. This theoretical linear correlation is in good agreement with the experimental data as reported by Mönch [Mönch 1994] on Figure 4.44. In case of Metals/hydrogen terminated diamond junctions, a similar linear trend was demonstrated ($\phi_b^0 = 0.017 - 0.37\,(X_m - X_s)$). The slope parameter was identical to the theoretical value whereas the ϕ_0^* is found to be smaller than the CNL of MIGS theory (1.4 eV) by approximately 1 eV thus leading to a shift down of SBH of Metals contacts on hydrogen terminated diamond Figure 4.44. This deviation from the CNL defined by MIGS theory [Mönch 1994] only was ascribed to C-H bonds inducing negatively charges on diamond side since carbon atoms have a larger electronegativity than hydrogen ($H^{+0.06} - C^{-0.06}$).

The situation is inverted for oxygen terminated diamond surface where the positively charge part is on diamond side [Maier 2001]. Indeed, the electronegativity of carbon and oxygen are respectively 2.54 eV and 3.44 eV (Pauling's scale). On the other hand, the Schottky electrodes can react with oxygen (covalent bond) and then affect the initial charge repartition of dipoles induced by oxygen-carbon bonds. Easily oxidizable metals such as zirconium (Zr) illustrates this scenario since this metal always formed with oxygen -terminated diamond surface a thin zirconia interface layer (about two atomic layers). Thus, aiming to compare diamond rectifiers based on oxygen termination to those investigated by Mönch [Mönch 1994], the SBH reported in literature authors for different metallic electrodes were collected and plotted as function of the difference of metals and carbon electronegativity, as shown Figure 4.45. This plot is performed for as-deposited and annealed Schottky contacts (673 K to 723 K) reported by several groups. Conversely to H-terminated and clean p-type diamond surface, the generally linear tendency described by the SBH in case of oxygen termination as shown Figure 4.45, is characterized by a positive slope for both as-deposited ($\phi_b = 2.33 + 0.21\,(X_m - X_s)$) and annealed electrodes ($\phi_b = 1.45 + 0.23\,(X_m - X_s)$). Noting that such a positive slope must be expected for n-type semiconductor [Mönch 2004]. The MIGS-and-Electronegativities is apparently not appropriated for O-terminated diamond surface.

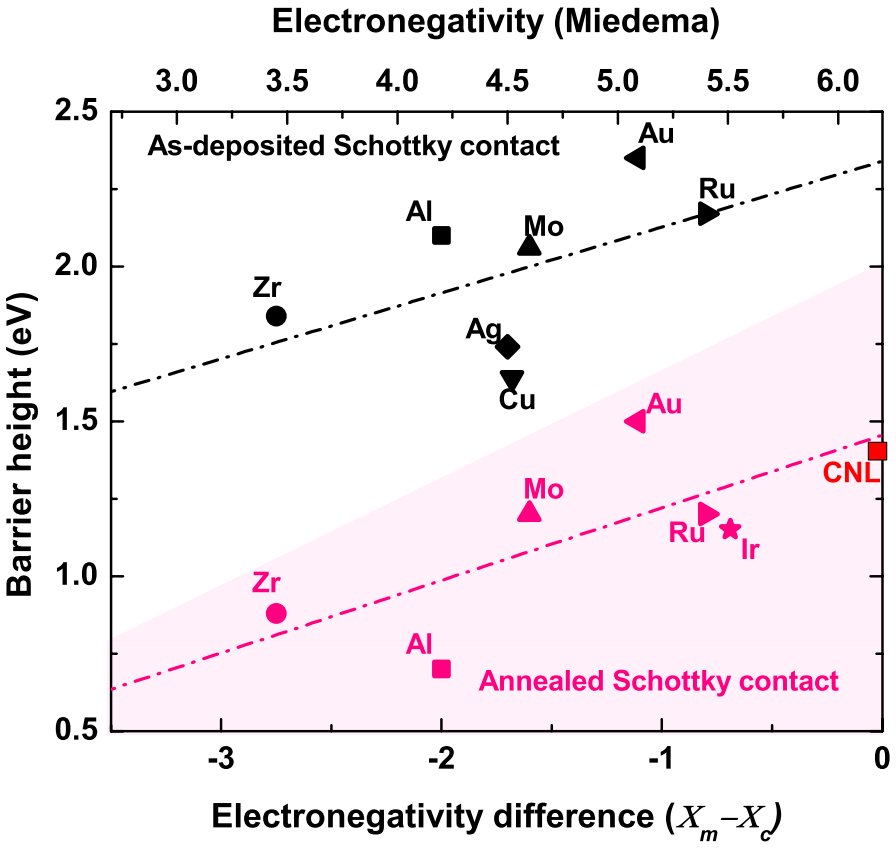

Figure 4.45: Metal/oxidized diamond SBH versus the difference of metals and carbon electronegativites performed for electrodes as-deposited and annealed at temperature ranging from 673 K and 723 K. The square symbols are as-deposited electrodes : Zr this work, Al reported by Koné et al [Koné 2010], Cu and Ag reported by Ueda et al[Ueda 2014], Mo and Ru reported by Ikeda etal [Ikeda 2009], Au reported by Teraji et al [Teraji 2009b]. the round symbols represents annealed MS junctions: Zr this work, Al Mo Ru Ir are reported by Umezawa et al [Umezawa 2012], Au reported by Teraji et al [Teraji 2009b].

4.10.4 Summary & Discussion

The analytical models discussed namely the potential fluctuation model developed by Werner and Guttler [Werner 1991] and the MIGS-and-Electronegativity concept established by Mönch [Mönch 1994], are not enough or are not appropriate to address the origin of Schottky barrier diminution due to annealing as observed for zirconium electrodes and for most metals reported in literature (Figure 4.45). Moreover, the SBH diminution due to annealing is a common feature of easily oxidizable metals (Zr, Al) as well as for noble metals (Ir, Au, Ru). Such a SBH diminution seems not happens for Ag and Cu electrodes since it was reported there were thermally stable up to 873 K at least [Ueda 2014]. For Zr, Mo, Ru and Ir Schottky electrodes, besides their thermal stability, it was reported that their exhibited a good electrical properties reproducibility

even after 673 K annealing [Ikeda 2009, Umezawa 2012]. On the other hand, their SBH dropped by approximated 1 eV. Taking in account the different oxidation features of these metallic electrodes, it could be assumed that the oxygen desorption is not the major cause of the SBH diminution. Annealing could favor the establishment of chemical bonds between Schottky metals and O-terminated diamond thus probably lead to oxide-type interface as for Zr electrodes. This might affect the positive charges on diamond side due to oxygen bonds in such a way that the SBH decreases. An effective diminution of O-terminated diamond EA due to these positive charges attenuation can be considered. However, Zr electrodes seems counterbalanced this assumption since an oxide interface layer always existed for as-deposited and annealed electrodes.

In this regard, Muret et *al.* (confer annex A for the submitted paper), improved the dipole-layer approach established by Tung [Tung 1992] to give analytical expressions of Schottky barrier height and ideality factor in case of inhomogeneous junctions. In Tung's model, the barrier inhomogeneity is treated as a perturbation induced by dipole layer with a varying dipole moment per area [Tung 1992]. Inhomogeneities are then ascribed to small regions (patches) with a low SBH embedded in an interface with an uniform high SBH. Using this concept, Muret et *al.* (confer annex A) demonstrates that the disappearance of interface dipoles initially present at Zr/oxygen-terminated diamond interface due to annealing, explain the SBH diminution observed here. The authors showed that:

- (i) As-deposited Zr Schottky electrodes interfaces have moderated density (few 10^6 cm^{-2}) of lowered barrier patches with sizes larger than the Debye length. Their barrier heights inhomogeneities are assumed to be a consequence of distinct oxygen terminations, which generate a strong sensitivity to the shrinkage of the current channels inside the lightly doped layer close to the interface. Indeed, apart the fact that diamond surface could be not entirely covered by oxygen layer, it is well established that oxygen adsorption on diamond surface give rise to several terminations such as carbonyl (C=O), hydroxyl (COH), carboxyl (O=COH) group [Klauser 2010, Notsu 2000] and eventually epoxide (COC) [Fink 2009]. It was demonstrated through theoretical calculations that these different terminations may induced different electron affinities as reported in references [Sque 2006, Robertson 1998]. Thus, according to the geometrical distribution of these different bonds, the SBH of a metal/O-terminated diamond junction could be spatially inhomogeneous.

- (ii) Zr Schottky electrodes annealed at 350 °C are an intermediate state characterized by a much larger density (few 10^9 cm^{-2}) of lowered barrier patches with sizes smaller than the Debye length. This different feature compared to as-deposited electrodes, is related to a probable partial cancellation of interface dipoles due to initial oxygen terminations at a nanometer scale.

- (iii) Zr electrodes annealed at 450 °C reach a final state where the complete cancellation of interface dipoles occur, resulting in almost homogeneous interfaces with an ideal behavior and a barrier height as low as 0.96 V. Several mechanisms linked to the presence of an oxide layer, can produce this effect: (a) the effective disappearance of the oxygen- carbon dipole layer due to a new bonding arrangement at the diamond interface after annealing; (b) the compensation of the initial dipole layer by positive charges in the oxide, as usually due to extrinsic deep levels, often related to oxygen vacancies; (c) intrinsic gap states within the oxide layer resulting in a new dipole induced by the alignment of the charge neutrality levels in the oxide and diamond; (d) a combination of these mechanisms or a change in the oxide properties which eventually promoted one of them after annealing.

4.11 Conclusion

Pseudo vertical diamond Schottky diodes based on zirconium contacts have been developed. The fabricated rectifiers highlighted the possibility to reach high forward current density (10^3 A/cm^2 at 6 V) and very low leakage current (under 10^{-9} A/cm^2) up to 1000 V corresponding to an electric field larger than 7.7 MV/cm in diode active layer. An unprecedented BFOM larger than 244 MW/cm^2 is then obtained due to self-heating leading to full dopants ionization. Moreover, the dispersion of zirconium Schottky electrodes electrical characteristics is extremely weak even for large diode area and regardless on samples because of an identical interface for all of the fabricated devices. Noting that zirconium Schottky electrodes were deposited on oxygen terminated diamond surface in order to favor oxide interface layer formation. The high-resolution transmission electron microscopy and the electron energy loss spectroscopy performed in collaboration with Cadiz university (Spain), demonstrates the existence of a thin oxide interface layer about two atomic layers. This layer, assumed to be zirconia (ZrO_2), is thermally stable and still exists even for Zr/diamond rectifier annealed at 450 °C, thus preventing from the oxygen passivation desorption required to reduce as much as possible the interface states. On the other hand, a thermal cycling measurement up to 500 °C points out the self-heating and our rectifiers inducing the full boron ionization in active layer. It was also observed that the SBH could be lower by performing an annealing. A 450 °C annealing allows to reduce the Schottky barrier height down to 1 eV. The SBH diminution due annealing is presumed to be a consequence of a structural change of ZrO_2 interface layer (about 0.4 nm) existing between Zr and oxygen terminated p-type diamond interfaces for as-deposited electrodes as well as for annealed electrodes.

Zr/p-diamond rectifiers annealed at 450 °C are thermally stable up to 500 °C. The reproducibility of forward characteristics whatever of samples and their reverse current are satisfactory explained by both thermionic-emission and thermionic-field emission mechanisms taken in the image force effect. The analytical potential fluctuation model developed by Werner and Guttler [Werner 1991] demonstrates that annealing minimizes the influence of spatial inhomogeneities of Zr/O-terminated diamond rectifiers in such a way that the rectifiers annealed at 450 °C behave like an ideal junction (abrupt and homogenous) characterized by a temperature independent ideality factor ($n = 1.05$) and Schottky barrier heights ($\phi_b = 0.9$ eV). Unfortunately, the empirical models discussed (Werner and Guttler [Werner 1991] model and the MIGS-and-Electronegativity concept established by Mönch [Mönch 1994]), are not enough to address the origin of Schottky

barrier diminution due to annealing observed for zirconium electrodes. Muret et *al* (confer annex A for the submitted paper), improved the dipole-layer approach established by Tung [Tung 1992] to evidence the origin of barrier lowering after annealing. It was then demonstrated that Zr electrodes annealing at 450 °C induces the complete cancellation of interface dipoles initially present at as-deposited Zr/oxidized diamond interface thus resulting in almost homogeneous interfaces with ideal behavior and barrier height as low as 0.96 V.

Zirconium Schottky electrodes demonstrate the superior performances and the advantage to form a thermally oxide interface layer between diamond and Schottky metals. In this regard, the conductive oxides could be considered as potential candidates for diamond rectifier fabrication. This was demonstrated for Indium Tin Oxide (ITO) electrodes deposited on oxygen terminated diamond by sputtering and annealed at 250 °C (confer Annex B). The electrical characteristics of ITO contacts were reproducible and thermally stability up 600 °C. However, the electrical performances (high barrier height (above 2 eV and a lower blocking voltage 300 V) were less interesting than those Zr electrodes.

General conclusion and outlook

This thesis is focused on the fabrication of high power diamond Schottky diodes and on the investigation of their electrical properties. Diamond growth and its doping are today well mastered. The diamond surface passivation which is required to reduce as much as possible the interface states, more specifically the oxygen-terminated diamond surface, is also well mastered. The advent of vertical architectures (diode active layer grown on heavily doped diamond substrate) and pseudo-vertical (stack of diode active layer and heavily doped layer grown on insulating substrate) allowed minimizing the high serial resistance related to the high ionization energy of acceptor-type dopants (boron doped diamond) preferably used for diamond-based rectifiers fabrication. Besides these geometrical configurations favoring high forward currents, diamond Schottky diodes (pseudo-vertical or vertical) were limited by i) the quality of the active layer altered by defects propagation from heavily doped layer thus leading to lower blocking voltage (maximum critical field of 3 MV/cm reported) than the theoretical values (theoretical values of critical field of 10 MV/cm), ii) the quality of metal/diamond interface together with its thermal and chemical stability. Schottky metal selection and surface pretreatment are crucial to get low enough barrier heights (low forward voltage drop and so low losses), low defects density at interfaces (low leakage current), and a thermally stable interface (high operating temperature).

In this thesis, we demonstrated that a pseudo vertical diamond Schottky diode based on an oxygen-terminated surface covered by an easily oxidizable metal such as zirconium (Zr) combined with a heavily doped layer with optimal thickness allow overcoming these limitations. We first found a trade-off between the thickness of heavily doped layer and its doping level in order to minimize defects generations and thus improve the quality of the active layer to be epitaxially grown on top of it (Less defect propagation). We then showed that the selected Zr metallic electrodes gave rise to a thermally stable thin zirconia interface layer. Zr/oxidized diamond rectifiers (pseudo-vertical structures) exhibited

better performance than the current state of art: a high forward current density (1000 A/cm^2 at 6 V), a critical field above 7 MV/cm (1000 V blocking voltage with a leakage current less than 1 pA), a Baliga's power figure of merit above 244 MW/cm^2 (the highest value reported to date), a good reproducibility regardless of diodes and samples, the possibility to get barrier heights below 1 eV by annealing, and a thermal stability up to at least 500 °C. Moreover, the reverse current of annealed Schottky electrodes, must be investigated in order to defined the best annealing temperature (Schottky barrier height) and doping level (previously introduced as a way to minimize the reverse current). Optimal values must be established in order to fully exploit diamond's outstanding properties whilst getting the best trade-off between the forward current, forward voltage drop, and reverse current.

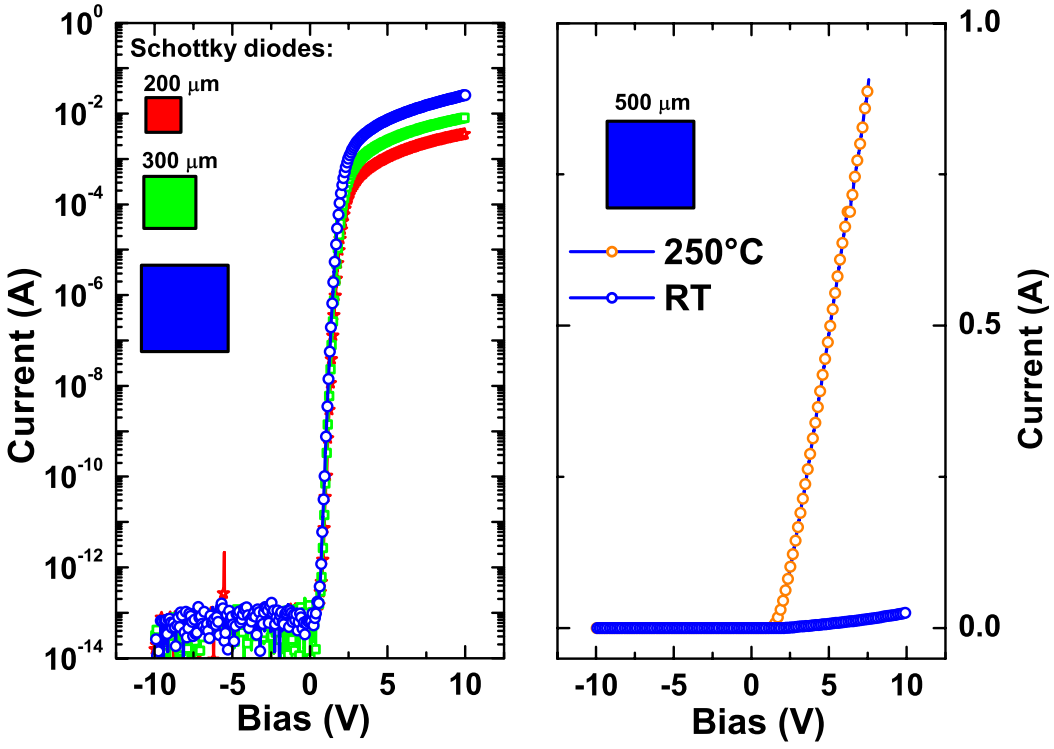

Figure 4.46: Vertical diamond rectifier based on Zr contact and fabricated in the framework on DIAMONIX II project

Along with the study of pseudo vertical diamond Schottky diodes using Zr electrodes, vertical diodes are addressed in the framework of French national project DIAMONIX2. Zirconium electrodes were deposited on epi-layers grown on highly doped diamond substrates ($Na \sim 10^{19}$ cm^{-3}) provided by the French lab "Laboratoire des Sciences des Procédés et des Matériaux" (LSPM). Figure 4.46 shows the first results obtained for different contact sizes which demonstrates again the high performance of Zr electrodes. The electrical current was lower at RT because of the high resistance of both active layer

and heavily doped substrates. At high temperature (250 °C), an electrical current of 1 A was measured for 500×500 μm^2 rectifier. Further work is needed. A particular attention must be paid to the rectifier design. Since the boron concentration in diamond substrate used in vertical configuration is still below the metal transition level, its contribution the serial resistance is not negligible and a high temperature will be required to enhance boron ionization rate and so the forward current. The results presented in this thesis demonstrate the possibility to fully ionize boron using self-heating. Accordingly, the devices could be designed in such a way that their self-heating (if any) serves as a heat source to minimize the serial resistance and optimize the forward current.

Appendix A

Potential barrier heights at metal on oxygen-terminated diamond interfaces

Potential barrier heights at metal on oxygen-terminated diamond interfaces

P. Muret,* A. Traoré, A. Maréchal, J. Pernot, and D. Eon

Univ. Grenoble Alpes, Inst. NEEL, F-38042 Grenoble, France

CNRS, Inst NEEL, F-38042 Grenoble, France

D. Araujo† and J. Pinẽro

Cadix University, E-xxxxx Cadix, Spain

(Dated: December 2, 2014)

Abstract

Electrical properties of metal-semiconductor (M/SC) and metal/oxide/SC structures built with Zr or ZrO_2 deposited on oxygen-terminated surfaces of (001)-oriented diamond films, comprising a stack of lightly p-doped diamond on a heavily doped layer itself homoepitaxially grown on a Ib substrate, are investigated experimentally and compared to different models. The interfacial oxide layer evidenced by high resolution transmission electron microscopy and electron energy losses spectroscopy before and after annealing, and barrier height inhomogeneities accounts for the measured electrical characteristics until flat bands are reached, in accordance with a model which generalizes that of R.T. Tung [Phys. Rev. **B 45**, 13509 (1992)] and permits to extract physically meaningful parameters of the three kinds of interface:(a) unannealed ones; (b) annealed at 350℃; (c) annealed at 450℃ with characteristic barrier heights of 2.2-2.5 V in case (a) while as low as 0.96 V in case (c). Possible models of potential barriers for several metals deposited on well defined oxygen-terminated diamond surfaces are discussed and compared to experimental data. It is concluded that interface dipoles of several kinds present at these compound interfaces and their chemical evolution due to annealing are the suitable ingredients able to justify the reverted slope observed regarding metal work function, in contrast to the trend always reported for all other metal-semiconductor interfaces.

PACS numbers: 73.20.r, 73.30.+y, 73.40.Qv, 73.40.Ns, 85.30.De

I. INTRODUCTION

Metal-semiconductor interfaces are necessary to implement sensors and electronic devices, and diamond does not escape to this need. Building well defined interfaces at nanometer scale is specially necessary for electrical rectifiers, which can gain high benefits from the bulk properties of boron doped diamond like its very high thermal conductivity, hole mobility and electrical breakdown field[1,2] if specific properties of the interface are also fulfilled. These are mainly good adhesion, thermal and chemical stability at elevated temperatures, compatible with the superior possibilities of diamond, and potential barriers ensuring both low electrical losses under forward voltage and minimal reverse currents even at high temperatures. Several attempts have been proposed, relying either on materials which react with the bare surface of diamond to form carbides, like silicon[3] or refractory metals and compounds[4–6], even hetero-epitaxially grown on diamond[7], or metals on either the oxygenated or hydrogenated surface of diamond[8–12]. In the first case, potential barriers near or higher than 2 eV, stable at temperatures higher than 500℃ have been obtained but reverse current densities and ideality factors were much greater than expected from the thermionic mechanism alone at least at room and moderate temperatures, and some of these contacts were ohmic. These poor rectifying current-voltage characteristics has been assigned to inhomogeneous and defective interfaces, specially with carbide forming metals[8,13]. Lower potential barriers are implemented on the hydrogen-terminated diamond surfaces due to the dipole $H^{+\vartheta}-C^{-\vartheta}$ responsible for the negative electron affinity of these surfaces, where ϑ is the averaged fraction of the elementary charge per atom. But the chemical stability is not guaranteed at temperatures as high as in the first case, and reverse current densities turn out to be hardly weaker than 10^{-7} A/cm^2 at room temperature, still higher than the thermionic limit. Because of an inverted electric dipole at the oxygenated surface of diamond, the largest potential barriers are generally obtained with either noble (Au) or transition metals deposited on this type of surface[9], but some authors have shown that thermal treatments up to 500 or 600℃ are able to decrease the barrier height down to 1.2 eV[14,15], probably because of the cancellation of the electric dipole $O^{-\vartheta'}-C^{+\vartheta'}$, still preserving a good adhesion of the metallic layer. More recently, we have shown that a less electronegative and more easily oxidizable metal like Zr was able to reach even more beneficial properties for the Schottky contact, namely an even lower potential barrier height while maintaining the reverse current density after an anneal

at 450 ℃ close to 3×10^{-10} A/cm^2 at room temperature[16] and an ideal current-voltage behavior for most diodes. However, a comprehensive picture of metal oxygenated-diamond interfaces did not emerge clearly in the last fifteen years, neither for the transport properties of carriers through interfaces, nor for the question of how the potential barrier height is determined, contrary to the case of hydrogen-terminated diamond surfaces[17]. In the present paper, mechanisms of carrier flow and significance of barrier heights are investigated on the one hand with more details and analysed with the help of several models.

On the other hand, the set of works quoted above demonstrates that both chemistry and physics must be both considered when dealing with Schottky barriers. This is specially true in the case of diamond where a large dispersion of barrier heights occurred for any metal[8] in literature. Much works were devoted in the past to general models able to explain and predict band misalignments at interfaces compounded of various materials, and a recent review of the various approaches, including a mixed physical-chemical point of view, has been published by R. T. Tung[18]. But, as often the case for more than one decade in the literature excepted in ref.[17], no experimental data regarding diamond interfaces has been brought and discussed. The present study aims at filling this gap, giving evidences of an oxide interfacial layer and discussing the relevance of various models of barrier height regarding data presented in this article and others available in literature for oxygenated diamond interfaces. In the second section, a brief study by high resolution transmission electron microscopy (HRTEM) and electron energy loss spectroscopy (EELS) is developed to show the characteristics of the interfacial layer at a sub-nanometer scale, the more noticeable being the systematic presence of oxygen at interface before and after annealing. In the third section, a first level analysis of the current-voltage characteristics relevant to the depleted semiconductor interface is presented and representative parameters of the junction are derived, confirming the presence of an interfacial layer in between Zr and diamond and the large decrease of the barrier height after annealing. In the fourth section, potential barrier inhomogeneities at different scales are analyzed and evidence of positively charged centers in the interfacial oxide is given. The consequences upon current-voltage characteristics are discussed and it is demonstrated that the junctions experience a change from depletion to accumulation regime at sufficient forward bias. Two models able to take into account the influence of the barrier height inhomogeneities are developed and matched to experimental data, allowing to derive meaningful parameters of each interface which indicate that large

barrier inhomogeneities prevail before annealing while they almost completely vanish after sufficient annealing. The previous results are used in the fifth section to address the problem of whether such an accurate control of the interface and metal choice can allow to tailor and predict the potential barrier heights of Schottky junctions on diamond. Gathering all the data available for well characterized interfaces of various metals on oxygen-terminated diamond permits to unveil a completely unusual relationship between potential barrier heights and metal work functions. Modeling this new result needs to consider the contribution of all electrical dipoles which may be present at these compound interfaces. Conclusions are drawn in the sixth section.

II. HIGH RESOLUTION IMAGING AND PROPERTIES OF THE DIAMOND LAYERS

Schottky junctions are implemented by deposition in ultra high vacuum of Zr on a stack comprising a lightly boron doped homoepitaxial diamond layer grown on a heavily doped one, itself grown on a Ib substrate. The surface of the lightly doped layer is submitted to a photo-chemical UV-ozone treatment for two hours at room temperature, so that oxygen terminations prevail on the diamond surface. Other details of the diamond growth and interface preparation are given in reference[16]. Three types of sample are elaborated, the first one being annealed at temperatures not exceeding 300℃, while the second and third ones are annealed respectively at 350℃ and 450℃; and the respective interfaces are labeled (a), (b) and (c). From the study of interfaces of kind (a) and (c) with the high resolution transmission electronic microscopy technique (HRTEM) as presented in Fig. (1) and electronic energy loss spectroscopy (EELS) technique, whose results are described in detail elsewhere, a ZrO_2 interlayer of 0.5 nm is detected, in both cases. Such a thickness is equivalent to two atomic monolayers.

III. CURRENT-VOLTAGE CHARACTERISTICS OF THE ZIRCONIUM-OXYGEN-TERMINATED DIAMOND INTERFACES

Current-voltage characteristics and mechanisms of carrier transport through the potential barrier present in metal-semiconductor junctions have been discussed extensively in review

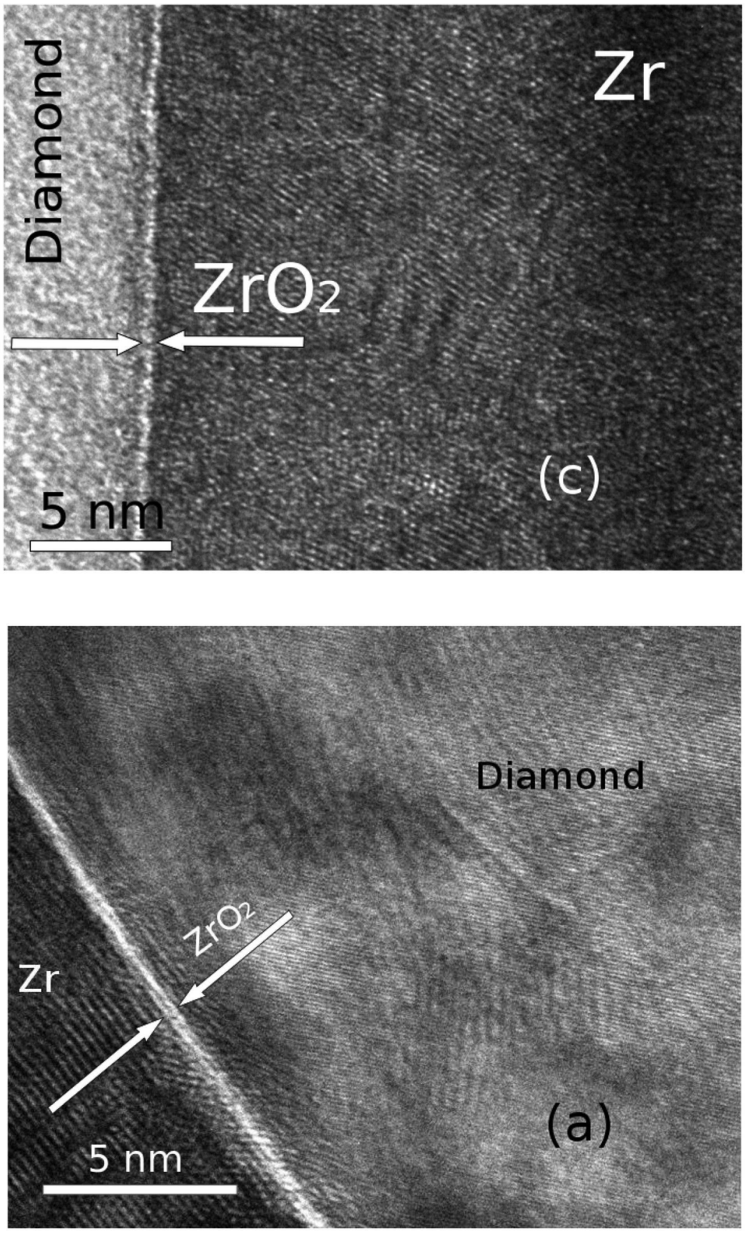

FIG. 1. HRTEM of interfaces (a) non intentionally annealed and (c) annealed at 450℃.

articles and textbooks[18–21]. The z direction being perpendicular to the $x-y$ plane of the interface, the current can be calculated in the semi-classical framework of the Maxwell-Boltzmann distribution of majority carrier velocities, by :

$$I_z = \iiint e_0\, v_z(E)\, D(E)\, dE\, dx\, dy \tag{1}$$

e_0 being the elementary charge, $v_z(E)$ the carrier velocity in the z direction and $D(E)$ the majority carrier distribution just at energies E above the point where the potential barrier

culminates. If the barrier is homogeneous, at a constant potential Φ_B throughout the x-y plane, the current density can be written from the previous expression, in the case of a voltage V_j applied to the junction[19,22]:

$$J_{z,2} = \frac{e_0 N_M v_{coll}}{1 + v_{coll}/v_{diff}} \exp\left(-e_0\Phi_B/k_BT\right)\left[\exp(e_0V_j/k_BT) - 1\right] \quad (2)$$

with N_M being the effective density of states at the majority carrier band edge, k_B the Boltzmann constant, T the absolute temperature, v_{coll} the collection velocity at interface $\sqrt{\frac{k_BT}{2\pi m^*}}$, due to the thermionic effect and equal to one quarter of the thermal velocity, m^* the conduction effective mass of majority carriers, and v_{diff} their diffusion velocity. The previous expression takes into account the two transport mechanisms of majority carriers which work in series, due respectively to the thermoionic velocity at interface and diffusion velocity inside the depletion zone, whereas it neglects bulk recombination. The diffusion velocity simplifies into the product of the majority carrier mobility by the electric field at interface if the band bending exceeds some k_BT/e_0 units and is generally not the limiting factor for the direct current, as confirmed in the samples under study from the comparison of the two velocities. The numerator of the first factor in Eq. (2) can be rewritten A^*T^2 where $A^* = (4\pi e_0 k_B^2 m_0/h^3) \times (m^*/m_0)$, the first quantity inside the parenthesis being the Richardson constant for emission of electrons into vacuum with a mass m_0 at rest, $A_R = 120$ A cm^{-2} K^{-2}. Because v_{diff} decreases with the increase of the forward bias voltage V_j, the pre-exponential factor of Eq. (2) becomes voltage dependent. Other reasons for such an effect involving also the factor $\exp\left(-e_0\Phi_B/k_BT\right)$, are (i) the image force lowering of the barrier, (ii) tunneling through the top of the barrier eventually assisted by the electric field, (iii) voltage drop inside an interfacial layer between the metal and semiconductor, (iv) charging interface states in equilibrium with the semiconductor and (v) a spatially inhomogeneous barrier as discussed further. However, the second effect is noticeable only in heavily doped semiconductors, a case which is not achieved in this study since the boron concentration of the lightly doped layer is close to $N_A = 5 \times 10^{15}$cm^{-3}. As one almost always wants to characterize the Schottky contact with a single potential barrier, the more common approximation consists in keeping only the zero bias voltage barrier height Φ_B^0 in the first exponential factor of Eq. (2) and gathering all the voltage dependent effects into the last factor. Since all these effects contribute to a slope of the logarithm of the current which is smaller than e_0/k_BT, an ideality factor n larger than one is introduced in the denominator

of the exponent of $\exp(e_0 V_j/k_B T)$ and often considered as a constant at least for a given temperature. Such an hypothesis is strictly valid in the case of an interfacial layer where the voltage drop is a constant fraction $1-1/n$ of the band bending $U = \Phi_B^0 - V_j - V_{dop}$ (with $e_0 V_{dop}$ being the energy difference between the Fermi level and majority carrier band edge in the bulk semiconductor) mainly determined by the oxide capacitance and density of interface states[23] when mechanisms (ii) and (iii) are combined. But it is not adequate if the interfacial layer either allows tunneling of carriers as the main transport mechanism or does not display any additional barrier for majority carriers because of band alignments similar to those occurring in type II heterostructures, or in the case of barrier inhomogeneities and even with image force lowering. Other effects, which are due to quantum reflexion, transmission and phonon scattering of carriers at the interface are voltage independent and generally very weakly temperature dependent so that it is convenient to lump them into an effective Richardson constant A^{**} which is weaker than A^* by some tens of percent in the case of intimate Schottky contacts[24], yielding the standard value of 90 A cm^{-2} K^{-2} usually considered for diamond. This effective Richardson constant can be further severely decreased because of the attenuation by a factor α of the collection velocity v_{coll} due to additional scattering of carriers by charged centers and roughness, and transport mechanisms through the interfacial layer when they exist. Finally, the non ideal current density is rewritten as :

$$J_{z,3} = \alpha A^{**} T^2 \exp\left(-\frac{e_0 \Phi_B^0}{k_B T}\right)\left[\exp\left(\frac{e_0 V_j}{n k_B T}\right) - 1\right] \tag{3}$$

Experimental current-voltage characteristics can then be accounted for by such an expression with the ideality factor n as an adjustable parameter, provided αA^{**} is known and the series resistance R_s is adjusted in order to fit the additional voltage drop $R_s I_z$ appearing in the total measured voltage $V = V_j + R_s I_z$. This is done in Fig. 2 for the three interfaces near room temperature. Two kinds of deviation between experimental data and the theoretical laws may appear as it can be seen on Fig. 2 ; the first one is due to a non constant ideality factor as long as the voltage drop in the series resistance is negligible (typically below 0.5 A/cm^2 in these diodes at room temperature) and the second one is due to less common transport mechanisms which are discussed in the following. It is worthwhile to notice that the rectification ratios are more than twelve decades and that no generation-recombination current is detected on these current-voltage characteristics, which would have involved a symmetrical behavior of the absolute value of the current around the origin at low voltages.

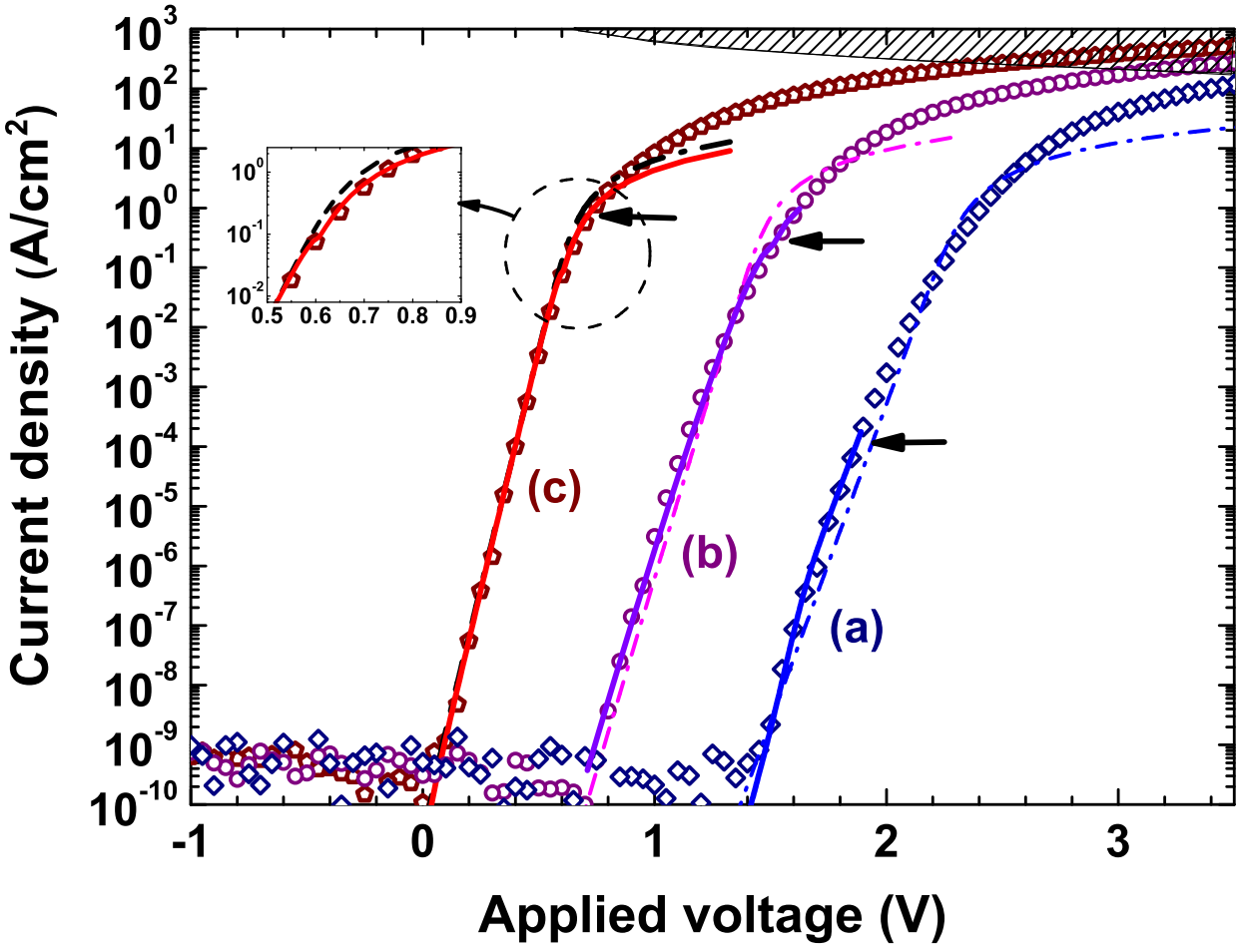

FIG. 2. Current density as a function of applied voltage at 300 K in the three interfaces made of Zr deposited on oxygen terminated diamond (a) with annealing temperature not exceeding 300 ℃; (b) annealed at 350 ℃; (c) annealed at 450 ℃. Dash-dot lines are calculated with the help of Eq. (3), αA^{**} values included in table I which are obtained from fits achieved in the two following figures, and adjusted constant values of the apparent barrier height and ideality factor in each case, that are respectively: (a) 1.83 V and 1.57 ; (b) 1.47 V and 1.29 ; (c) 0.97 V and 1.05. Voltage takes into account the voltage drop in a constant series resistance of 600 Ω in case (a) and 300 Ω in cases (b) and (c), in good agreement with the theoretical ones, but current densities above a few A/cm^2 turn out to be higher because of conductivity modulation due to hole injection from the heavily doped layer. Full lines rely on models which incorporate barrier height lowering and are described in section IV, with Eq. (7) for the cases (b) and (c), while Eq. (14) is used for the case (a). Horizontal arrows mark the flat band situation in each junction. The effect of image force lowering is displayed in the inset for the case (a). In the hatched area, self-heating becomes important.

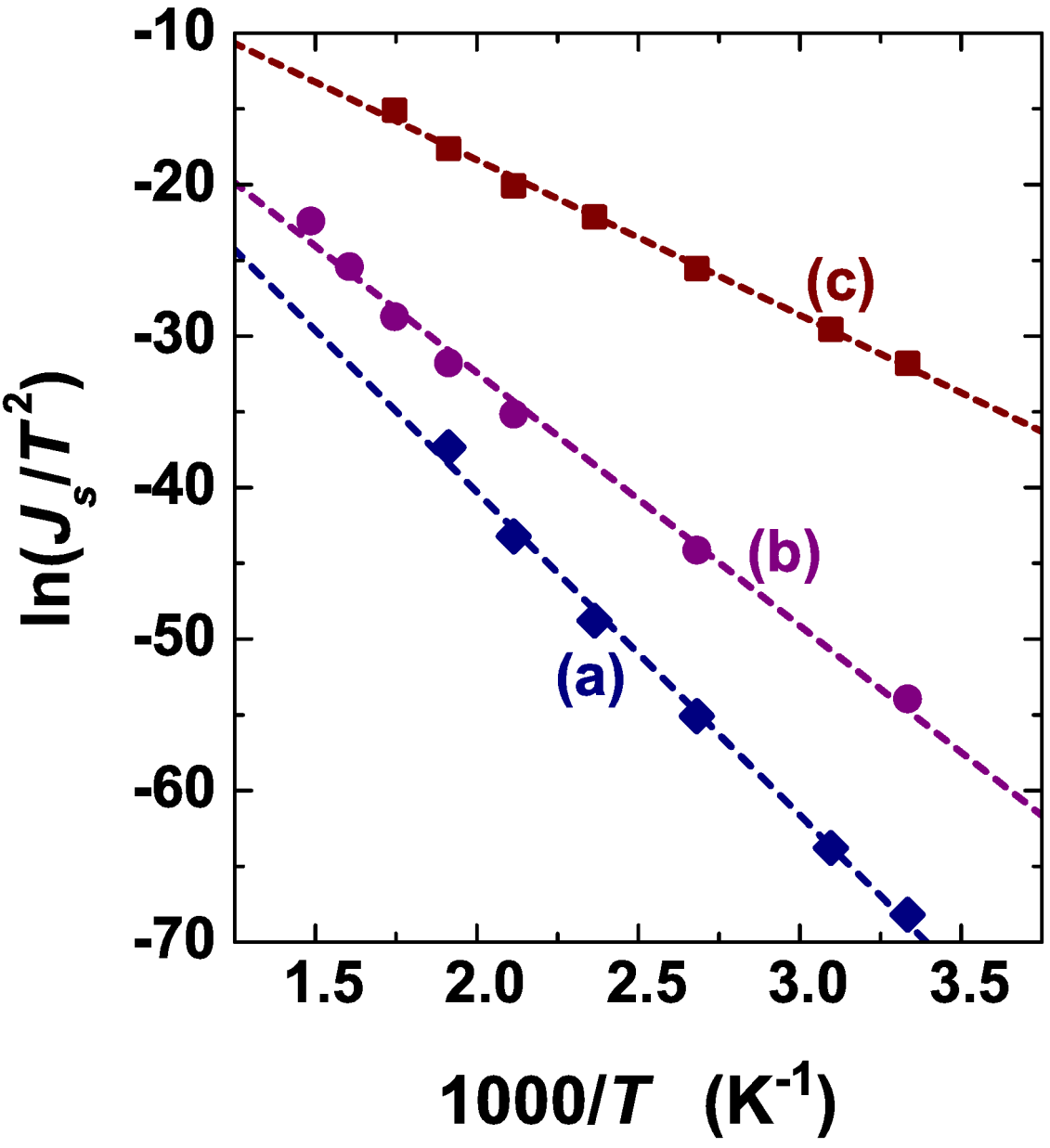

FIG. 3. Richardson plot for the three same interfaces as in Fig. 2. Averaged barrier heights deduced from the slope of each straight line are respectively: (a) 1.84 V; (b) 1.47 V; (c) 0.95 V; very close to that used in Fig. 2.

Such an almost ideal behavior strongly suggests that the oxygen terminated surface of diamond passivates very efficiently the interface defects able to develop leakage currents[25]. The determination of αA^{**} needs temperature variations in such a way that the saturation current density over T^2, namely $\alpha A^{**} \exp\left(-\frac{e_0 \Phi_B^0}{k_B T}\right)$, obtained from the extrapolated value of the current-voltage characteristic at $V_j = 0$, can be drawn. Such Richardson plots are

Sample type and	αA^{**}	n	$\overline{\Phi^0_{B,\infty}}$	σ^0_Φ
annealing temperature (℃)	A cm^{-2} K^{-2}	(at 300 K)	V	mV
(a) $<$ 300 ℃	11	1.52	1.93	71
(b) 350 ℃	2.8	1.29	1.57	87
(c) 450 ℃	8.5	1.00 to 1.07	0.93	54

TABLE I. Parameters of the Schottky barrier in the three interfaces according to the model of section III.

displayed in Fig. 3. The effective Richardson constants αA^{**}, ideality factors at room temperature and parameters described in the following are indicated in the Table I. It must be stress firstly that the αA^{**} values are at least ten times lower than the standard value A^{**} and secondly that a careful inspection of the Fig. 3 shows that the data points follow systematically a slight upward curvature, indicating a barrier height increase with temperature. The first result confirms indubitably the presence of an insulating interfacial layer. The second one is the preliminary indication of the presence of barrier inhomogeneities, a conclusion similar to that obtained in ref.[26] about silicides-silicon interfaces, also implying additional consequences which have to be analyzed more thoroughly.

Zero voltage barrier heights and averaged ideality factors are displayed in Fig. 4 as a function of temperature. On the first hand, the former quantities experience indeed an increase with temperature with generally an asymptotic behavior towards highest temperatures, while the latter ones are decreasing, starting from very different values at room temperature (which are reported in Table I) and displaying very different negative slopes. As noticed previously, such variable ideality factors cannot be ascribed to a voltage drop within an interfacial layer bearing an additional barrier to that built in the semiconductor, because they would not be coherent with oxide interfacial layers which still exist at the three interfaces. On the other hand, experimental data plotted in Fig. 2 deviate from the simulated curves drawn in dash-dot lines on the basis of a constant ideality factor when voltage drop in the series resistance and other effects remain negligible. A first attempt to fit more accurately experimental results uses an alternative definition of the current density, which is also more physically meaningful. It consists in using a temperature and voltage dependent

barrier height $\Phi_B(T, V_j)$, so that the current density can be rewritten more usefully for the homogeneous barrier case:

$$J_{z,4} = \alpha A^{**} T^2 \exp\left(-\frac{e_0 \Phi_B(T, V_j)}{k_B T}\right) \left[\exp\left(\frac{e_0 V_j}{k_B T}\right) - 1\right] \tag{4}$$

Introducing an inhomogeneous barrier which follows a Gaussian spatial distribution in the $x - y$ plane of the interface, characterized by an average value $\overline{\Phi_B}(T, V_j)$ and a standard deviation $\sigma_\Phi(V_j)$, permits to derive[21,26] a law similar either to Eq. (3) or (4), with an effective barrier given in the second case by :

$$\Phi_B(T, V_j) = \overline{\Phi_B}(T, V_j) - \frac{e_0 \sigma_\Phi^2(V_j)}{2 k_B T} \tag{5}$$

For each temperature, it is always possible to convert Eq. (4) into Eq. (3) through the definition of a voltage independent barrier height, conveniently taken at $V_j = 0$, and a voltage dependent ideality factor $n(T, V_j)$, valid in all situations, the inverse of which being evaluated from the derivative of the logarithm of the current density given by Eq. (3) and (4) when the reverse saturation current is neglected:

$$\frac{k_B T}{e_0} \frac{d(\ln J_z)}{dV_j} = \frac{1}{n(T, V_j)} = 1 - \frac{d\Phi_B(T, V_j)}{dV_j} = 1 + \frac{d\Phi_B(T, U)}{dU} \tag{6}$$

However, in this first level model, no explicit dependence of the parameters is given as a function of junction voltage V_j or band bending U. Some cases of potential barrier distributions have been analyzed analytically by R. T. Tung[27], who showed that the dependence of the parameters of Eq. (5) was not linear with the band bending and hence with the junction voltage, on the basis of a physical representation of the barrier lowering by a fictitious dipole located at interface. An additional source of non ideality may be present if a spreading resistance effect occurs, involving inhomogeneous current density inside the semiconductor because of current crowding near the pinch-off patches with a lowered barrier and located close to the interface[28,29]. This effect is normally expected to be relevant at current levels where the series resistance voltage becomes larger than some $k_B T/e_0$. But the combination of multiple barriers and incomplete ionization of doping impurities may induce deviation from the ideal current-voltage characteristic at much smaller currents because of severe weakening of the carrier concentration and narrowing of the current paths in the lowest barrier patches which cannot be assessed easily from the comparison to a voltage drop in an averaged series resistance. This kind of non ideality will be discussed in the next section.

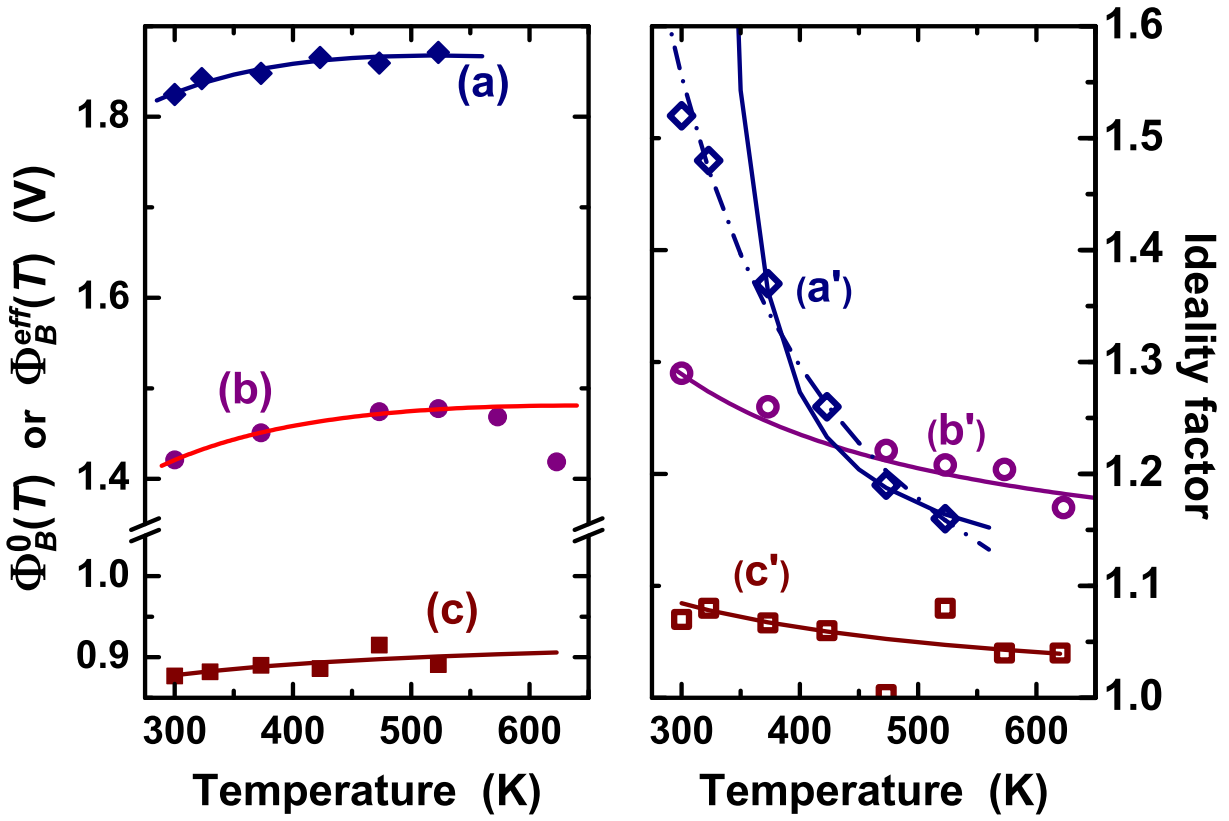

FIG. 4. At left, effective barrier heights as a function of temperature in (a) diodes not annealed at temperatures higher than 300 ℃; (b) annealed at 350 ℃; (c) annealed at 450 ℃; full curves are the best fits according respectively to Eq. (5) or Eq. (9) which results essentially in the same behavior for the effective barrier. The point at the highest temperature in data (b) must be discarded because it has been measured at the same temperature as the annealing one, involving an additional annealing time which has induced a further evolution of the interface towards its final state (c). At right, ideality factors for the same diodes after the same respective post-treatments in (a'), (b') and (c') ; the best fits to the ideality factor data obtained with the help of Eq. (11) are displayed in full curves for (b') and (c') and as a dash-dot curve for (a'), but using a non physical parameter in the last case. The full curve adjusted on (a') data exploits Eq. (17) and related ones with more meaningful parameters at the expense of a worse agreement with data (see text).

In the simple model presented above, the barrier fluctuations are characterized by their average and standard deviation but are not supported by any physical model. Such an approach prevents to work out the detailed electrical properties of the junction, specifically the behaviors of the barrier lowering and ideality factor with voltage and temperature, unless

arbitrary hypothesis are made. Therefore, the reasons for these barrier inhomogeneities have to be analyzed more accurately and an analytical model which will generalize that developed by R. Tung[27] will be implemented in the next section, concurrently with a realistic simulation of some potential fluctuations at interface. But within the framework of the simple approach developed in the present section, it is already possible to derive the two parameters $\overline{\Phi_B}(\infty, 0)$ and $\sigma_\Phi(0)$ at zero voltage from the fit of these quantities according to Eq. (5), which are renamed respectively $\overline{\Phi^0_{B,\infty}}$ and σ^0_Φ for sake of simplicity and displayed in the Table I, for the three types of interface. The average barrier height at infinite temperature $\overline{\Phi^0_{B,\infty}}$ decreases by about 0.5 V after each anneal while the standard deviation σ^0_Φ of the barrier fluctuations goes through a maximum after annealing the interface at 350 ℃. But the deficiency of the present model is confirmed by the different behaviors of the ideality factor with temperature plotted in Fig. 3 which cannot be explained. These discrepancies confirm the need for a more accurate model of the effect of potential fluctuations at interface upon current-voltage characteristics.

Meanwhile, an unusual result which ensues from the calculation of the current densities necessary to draw the fitting curves in Fig. 2 can be already pointed out. At some current threshold, flat bands are reached (see the arrows in the same figure) and it is necessary to consider that accumulation occurs at the interface to explain the continuous increase of the current densities beyond this threshold. Such a behavior matches Eq. (1) which states the proportionality of the current to a velocity and carrier concentration at interface. For example in the case (c), flat bands are reached at a voltage of 0.63 V, corresponding to an initial band bending of $0.97 - 0.38 = 0.59$V (here V_{dop}=0.38 V) plus the barrier increase of 0.04 V demonstrated in the next section, and the current density calculated directly with the hole concentration given by formula (1) in ref.[1], assuming a compensation of 20% (donor concentration $N_D = 10^{15}\text{cm}^{-3}$) and Eq. (1), with a collection velocity ten times smaller than that for an intimate contact, yields 0.4 A/cm^2, very close both to the experimental one and that calculated by Eq. (4). In cases (b) and (a), still at 300K, flats bands are reached respectively at lower current densities indicated in Fig. (2), which cannot be calculated with the help of the initial model because the apparent barrier heights deduced presently are largely underestimated and would produce irrelevant band bending. Therefore, assessing these values needs to wait for more accurate and physically relevant models which will be developed in the next section. In Eq. (2) and subsequent ones, the barrier height has been

introduced for convenience and it was often believed as an impassable limit in Schottky diodes. Such a statement is not true as everyone can be convinced if he realizes that Eq. (2) and subsequent ones all derive from Eq. (1) where the current is controlled by a carrier concentration. Band curvature reversal and occurrence of accumulation regime are possible and even necessary to reach high currents, up to more than thousand times that those got at flat bands, in these interfaces made on oxygen-terminated diamond, because firstly of the low values of the effective Richardson constant, secondly of the wide forbidden bandgap of diamond and thirdly of the large ionization energy of acceptors. In such a regime, diffusion flow is inverted close to the interface, the barrier seen by majority carriers is canceled and consequently, the models relying on Eq. (2) and following ones, and on the properties of barrier height inhomogeneities, specially their voltage dependence, become inappropriate. Conversely, current crowding near the pinch-off patches with a lowered barrier may become a major source of non ideality. If possible, these mechanisms have to be incorporated into the forthcoming models or else, at least kept in mind to assess the applicability of the following developments.

IV. POTENTIAL BARRIER INHOMOGENEITIES AND IDEALITY FACTOR

A. Potential fluctuations due to randomly distributed discrete charges and dipoles

The electrostatic potential experienced by mobile carriers originates from fixed charges scattered inside the space charge zone and interface. For modeling purposes, it is often derived from constant bulk charge concentration in the space charge zone and homogeneous charge density at interface. This view is correct for mechanisms characterized by lengths larger than the Debye length $\lambda_D = \sqrt{\varepsilon_{SC}\varepsilon_0 k_B T/(e_0^2 N_A)}$, where ε_{SC} and ε_0 are respectively the relative permittivity of the semiconductor and the vacuum permittivity, and when average laws are evaluated, but may fail if some physical property of carriers experiences microscopic fluctuations. Indeed, when the effects of potential inhomogeneities are at stake, the discrete nature of fixed charges accommodated within the metal/semiconductor or metal/oxide/semiconductor (MOS) structure must be taken into account and the average distance between these discrete charges have to be compared to λ_D. Here, λ_D amounts to 40 nm at 300 K and 52 nm at 500K. Three locations have to be considered: (i) inside

the depletion zone, the average distance between ionized acceptors is 58 nm, very close to λ_D. Only those which are at such comparable distances from the interface influence the potential barrier height, as clearly evidenced in a following subsection. (ii) The oxygen terminations bonded to the carbon atoms of the (001) diamond surface are making up the negative part of the interface dipole, really present at the interface up to some annealing temperature, an inverted situation in comparison to what happens on the hydrogenated diamond surface, due to the sign change of the electronegativity difference between carbon and oxygen or hydrogen respectively. The positive counterpart of this dipole lies within the first and second carbon layer just below the surface, resulting in a potential jump through the surface of $\Delta q\, d_{di}\, N_{di}/(\varepsilon_i\, \varepsilon_0)$ where Δq is the charge transfer, d_{di} the dipolar distance, N_{di} the site density and ε_i the relative interface permittivity[21]. This potential jump is directly reflected by the electron affinity change provided by oxygen terminations. In average, it can be estimated close to 1.7 V because the smaller difference between electron affinities of the free (2×1) reconstructed surface and the oxygenated surface[30] is probably due to already electron depleted bonds in the last carbon layer of the former one. Taking into account the 30 percent coverage measured by X-rays photo-electron spectroscopy[31] on our samples treated by UV-ozone, equivalent to 5×10^{14} sites per cm^2, a whole distance normal to the interface of roughly $d_{di} = 0.1 + 0.2 = 0.3$ nm and $\varepsilon_i = 2$, the estimated charge transfer turns out to be $2{\times}10^{-20}$ C, that is ϑ'=0.13 electronic charge. However, it is known firstly that there are several oxygen terminations, at least ether (C–O–C), carbonyl (C=O), hydroxyl (C–OH) and carboxyl (O=C–OH) groups[32–35] as individual adsorbates and eventually epoxide (bridged oxygen between two adjacent carbons)[36] in case of UV-ozone treatment as done on our samples. The electron affinities calculated theoretically for the three first terminations are different[34,37]. Secondly, all the sites are not occupied (in our case, about 30 percent, like when oxygen plasma treatment is applied to the diamond surface[31]) but when adjacent sites are provided with an oxygen termination, polymerization along chains may occur[32]. Therefore, the dipole strength resulting from these various adsorbates and able to modify the potential barrier height is far from being homogeneous at least over a scale length of few nanometers and also along a much larger scale if the various terminations are arranged in macroscopic domains, resulting in effective laterally non-uniform electronic affinity. An other reason which may lead to scattered patches with different barrier heights would be the chemical inhomogeneities like often present when carbide formation occurs[13], which might

also happen if the chemical composition of the interfacial oxide layer or its thickness were not homogeneous throughout the interface, although no evidence of such properties exists in the present case. And last but not least, extrinsic defects such as emerging dislocations cannot be excluded as sources of locally lowered barrier height like revealed at $CoSi_2/n$-Si(001) interfaces by ballistic electron energy microscopy[38]. On the contrary, the intrinsic dipole due to charge transfer across the interface because of an eventual misalignment of the charge neutrality levels in the two materials is supposed to be homogeneous because it results from the occupation of gap states which are delocalized in the plane of the interface and will not participate in potential fluctuations. (iii) As evidenced in the following, discrete charged centers exist inside the oxide of MIS structures and are expected to be also present in the thin interfacial oxide of the Schottky contacts. These cases are treated quantitatively in the next subsections and are brought face to face to experimental and simulation results.

B. Evidence of charged centers in oxide layers

To check quantitatively the presence of discrete charged centers inside the oxide, a MIS structure Al/ZrO_2/p-type (001) oriented diamond has been fabricated. The 25 nm oxide layer has been prepared by atomic layer deposition at 100 °C. The p-layer has a thickness of 2 μm, contains some 10^{17} B/cm^3 and has been epitaxially grown on top of a 200 nm p^{++} diamond layer itself in epitaxial relationship on a (001) oriented Ib substrate. After etching the p-layer and before the deposit of the last stack Al/ZrO_2, an ohmic contact is fabricated around the sample on the p^{++} layer, ensuring a series resistance close to a few kΩ. In this way, the proper time constant of the MIS structure is inferior to 1 μs. Such a property allows safe measurements of the static, pulsed and transient capacitances at a frequency of 1 MHz, as described in reference[39]. Results of the reciprocal square capacitance as a function of voltage and the isothermal spectra of projected interface states as a function of the hole emission time constant deduced from the first real Fourier coefficient of the capacitance transients at two time window durations are displayed respectively in Fig. 5(a) and Fig. 5(b) and (c). From the extrapolation of the linear part of the curve in Fig. 5(a) to zero ordinates, a flat band voltage V_{FB} of -4.1 V is deduced whereas a value equal to $\Phi_{MS} = \Phi_M - \chi_{SC} - E_G/2e_0 - (E_i - E_F)/e_0 = -2.4$ V would be calculated with the help of the electron affinity model and $\Phi_M = 4.28$ V for the Al work function[40], $\chi_{SC} = +1.6$eV

for the electron affinity of oxygen-terminated p-type diamond[30,41], $E_G = 5.45$ eV for the diamond band gap and $\phi_F = (E_i - E_F)/e_0 = 2.35$ V deduced from the difference between intrinsic and Fermi energy levels in bulk boron-doped diamond, assuming no charge in the oxide. The discrepancy comes from this last hypothesis which is not verified, implying that the real situation comprises a positive charge inside the parenthesis of the last term in $V_{FB} = \Phi_{MS} - \left(Q_{is}(0) + \overline{Q_{ox}}\right)/C_{ox}$, where C_{ox} is the oxide capacitance density, $Q_{is}(0)$ and $\overline{Q_{ox}}$ being respectively the charge per unit area in interface states at flat bands and the product of the total charge per unit area within the insulator by the ratio of the barycenter of this charge to the insulator thickness[39]. To reconcile the two values, a total number of positive charges per unit area must amount to 2×10^{13} cm^{-2} within the 25 nm thick oxide layer.

The centers which accommodate charge may experience change of their charge state if some mechanisms are occurring, like carrier emission from interface states lying in the common forbidden gap of the two materials, and also transport by hopping and tunneling across some thickness of the insulator. Such effects give rise to transient capacitances in the MIS structure because of the rearrangement of all the individual electric dipoles necessary to comply with the rule of a constant whole electric dipole if the MIS is submitted to a constant voltage[39]. Isothermal spectra are displayed in Fig. 5(b) and (c) as a function of the characteristic emission time. They are obtained from the Fourier transform of the transients which are recorded after two filling pulses lasting respectively 1 ms and 100 ms. They show a two peaks structure, the slower peak being higher for the longer filling pulse. This response can be viewed as the projected spectrum of states on the interface energy scale inasmuch both states located at interface and some oxide states as well may exchange holes with the valence band of diamond. Differential spectroscopy is here unnecessary just because emission from discrete interface states in the common bandgap largely dominates that from a hypothetical continuum since peaked structures clearly appear in Fig. 5, and an accurate calibration of the energy scale is not needed. The smaller filling pulse duration $t_p = 1$ ms has been chosen to ensure complete filling of interface states even with capture cross sections as low as 10^{-19} cm^2, whereas the larger $t_p = 100$ ms is able to involve additionally either injection or extraction of carriers trapped in discrete states localized within the insulator at some distance from the interface. The important point consists in the different behaviors followed by the two peaks as a function of t_p: the first occurring at the shorter emission

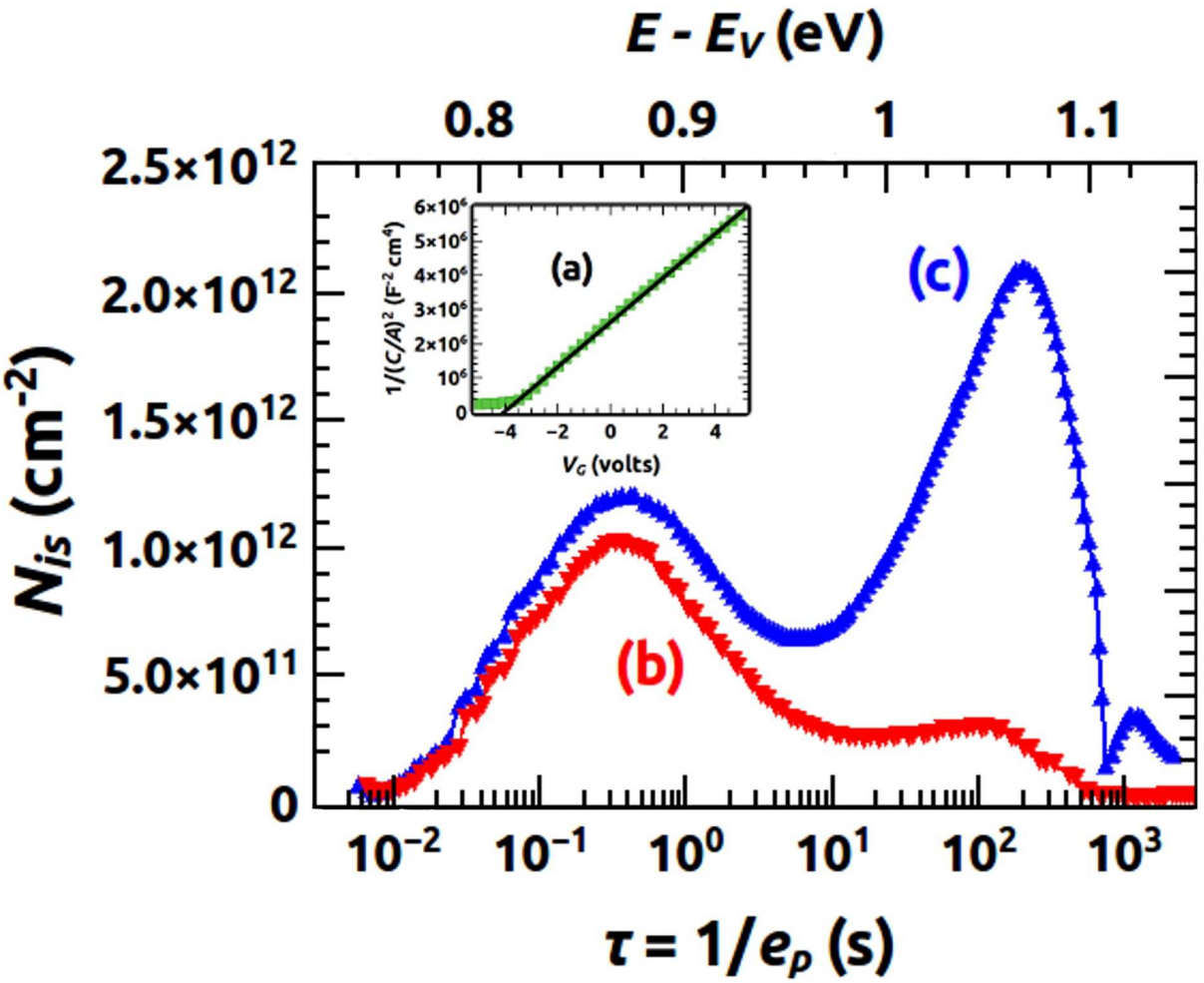

FIG. 5. (a) Square of the inverse capacitance density as a function of the gate voltage ; (b) and (c) curves are isothermal transient capacitance spectra respectively after a 1 ms and a 100 ms filling pulse, recorded at a gate voltage of 3 V and temperature of 362 K.

time is very weakly sensitive to t_p and consequently related to an interface state whereas the second one increases with t_p, involving carrier transport through some insulator slice. This is the demonstration that at least one discrete state exists inside the oxide. An order of magnitude of the distance d of these centers from the interface can be estimated from the inverse of the attempt-to-escape time checked by Jain and Dahlke for traps in Si/SiO_2 interfaces[42] and given by $\nu_0 \exp(-qd)$, with $\nu_0 \simeq 10^{16}$ s^{-1} and $\alpha \simeq 1.05 \mathring{A}^{-1}$, yielding roughly $d \simeq 3$ nm. The reciprocal attempt-to-escape time at zero insulator thickness ν_0 and the quantum transmission coefficient q are conditioned respectively by the quantum uncertainty about the potential well or barrier height, also close to $2\hbar/G$ where G is the line width

of the resonance[43], and tunneling transmission coefficient which depends on the square root of the previous quantities. Because the relevant energies are still about 1 eV, the order of magnitude of ν_0 and q are expected not to be largely different in the present case. The evaluated distance d is close to one tenth of the whole insulating layer thickness, a ratio similar to that of the center densities deduced by the transient and static capacitance methods in the MIS structure. Consequently, these point defects behaving as repulsive centers for holes and located inside the oxide layer at the Schottky interfaces under study might not be ignored unless other charged centers or dipoles prevail.

C. Effects of local barrier enhancement due to random elementary charges and dipoles close to the interface

Electrostatic potential along x and y directions, parallel to the interface, and z, normal to the interface, can be calculated by adding three terms as a function of normalized distances $\xi = x/\lambda_D$, $\nu = y/\lambda_D$ and $\zeta = z/\lambda_D$, and band curvature U in volt: the average potential of the depletion zone $\left(\sqrt{U - k_BT/e_0} - \zeta\sqrt{k_BT/(2e_0)}\right)^2$; the image force potential $-u_{im}/\zeta$ with $u_{im} = e_0/(16\pi\varepsilon_{SC}\varepsilon_0\lambda_D)$ and the potential due to either repulsive elementary charges positioned symmetrically at $\xi = \pm\xi_0$, $\nu = 0$, and beyond the interface plane by a distance ζ_0, that is

$$\frac{4u_{im}}{\sqrt{(\xi-\xi_0)^2+\nu^2+(\zeta+\zeta_0)^2}} + \frac{4u_{im}}{\sqrt{(\xi+\xi_0)^2+\nu^2+(\zeta+\zeta_0)^2}}$$

or replacing either one or two of the previous terms by

$$-\frac{4u_{im}}{\sqrt{(\xi\mp\xi_0)^2+\nu^2+(\zeta+\zeta_0)^2}} + \frac{4u_{im}}{\sqrt{(\xi\mp\xi_0)^2+\nu^2+(\zeta-\zeta_0)^2}}$$

at either one location $+\xi_0$ or both locations $\pm\xi_0$ to simulate either one or two elementary dipole due to negative oxygen termination beyond the interface and its positive counterpart on the diamond side. A 3-dimensional view of potential barriers in several cases is given in Fig. 6, the last one being obtained with an inverted sign before ζ_0 and four random locations of elementary charges within the depletion zone. The three first cases are respectively devised to mimic the mechanisms assumed to be at stake in the transport of carriers at interface, resulting from the repulsive effect of charges located just at interface or close to it inside diamond: (a) with negative oxygen terminations inducing interface dipoles which are supposed to dominate; (b) with a mixed influence of repulsive oxide charges and dipoles

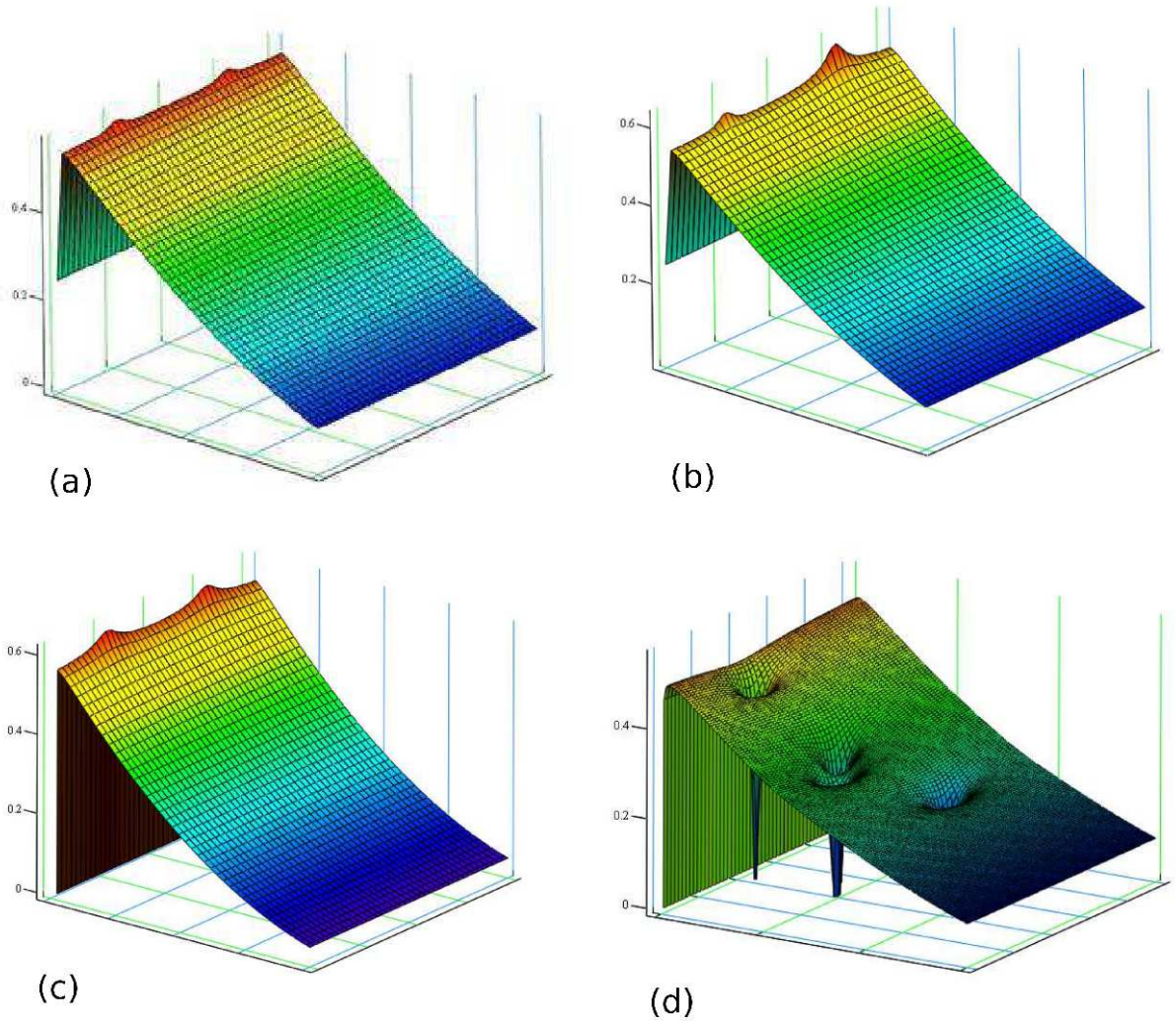

FIG. 6. Sketch of the potential barrier experienced by majority carriers with (a) two dipoles across the interface with a repulsive elementary charge on the semiconductor side; (b) one dipole of the same kind across the interface and one repulsive elementary charge beyond it; (c) two repulsive elementary charges beyond the interface; (d) randomly scattered attractive elementary charges inside the depletion zone.

similar to those of the previous case; (c) with only repulsive oxide charges. In these three cases, elementary charges or dipoles enhance the barrier locally. On the contrary, in the fourth case (d), barrier lowering $\delta\Phi_{B,1}^{sad}$ may occur with a saddle point at normalized distance ζ_{sad} from the interface which can be calculated exactly from the solutions of a quartic equation resulting from the cancellation of the potential derivative along the ζ direction. However, a rough estimate, easier to derive, relies on the geometric mean of the two extreme

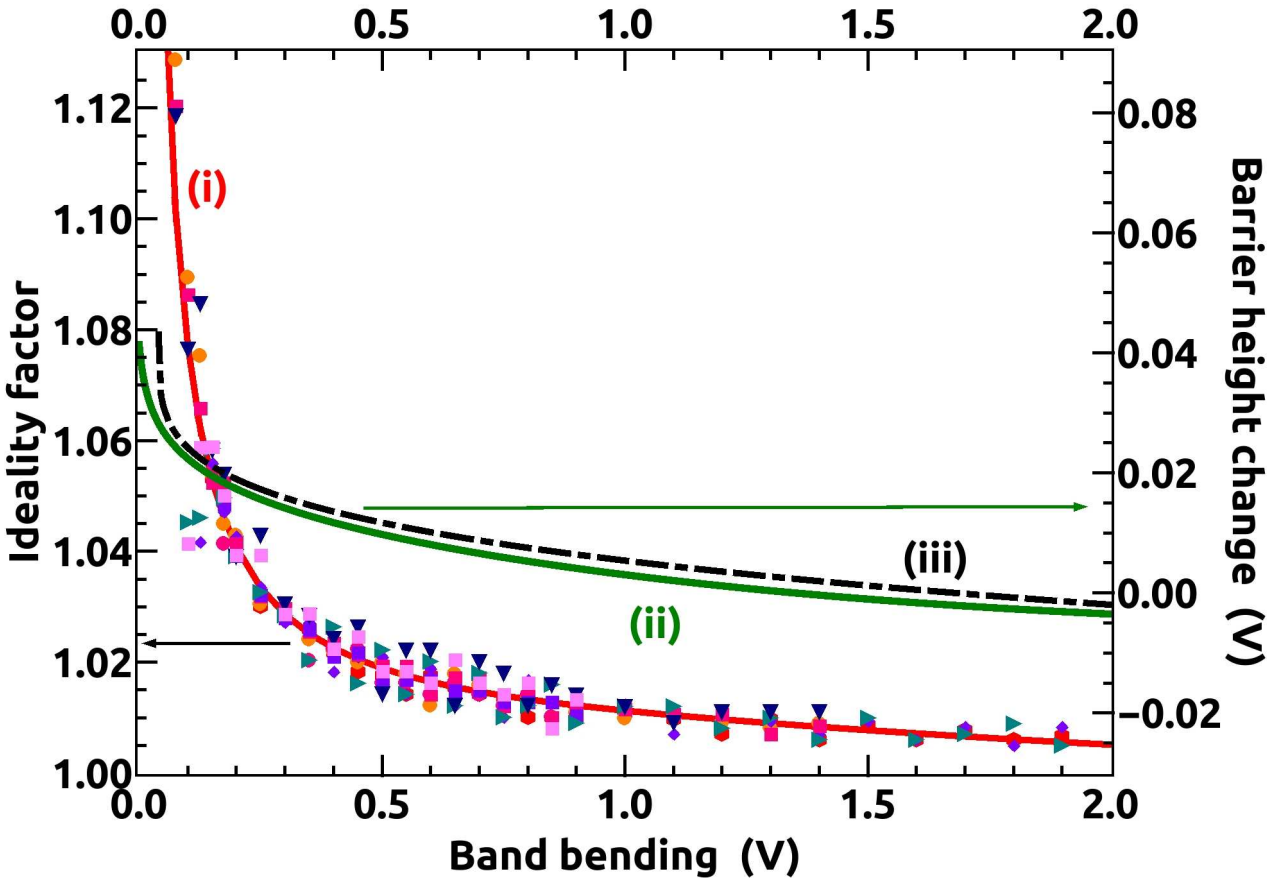

FIG. 7. Ideality factors deduced from the microscopic barrier inhomogeneities model for the three types of interface at 300 K (triangles), 400 K (squares) and 500 K (circles) as a function of the band bending U. Curve (i) is the best fit of data points by $1 + 1/P(U)$ with $P(U) = 136.8\,U - 76.4\,U^2 + 28.4\,U^3$. The curve (ii) displays the barrier height variation deduced from (i) with help of Eq. (6) which implies that $d\Phi_B\,/\,dU = -1/\,[1 + P(U)]$. Dash-dot curve (iii) shows the image force lowering variations.

solutions of the quartic equation, and can be expressed as $\zeta_{sad} \approx \sqrt{\chi(U)\,[\zeta_0 - 2\chi(U)]}$ with $\chi(U) = u_{im}^{1/2} \left(\frac{2k_BT}{e_0}\right)^{-1/4} \left(U - \frac{k_BT}{e_0}\right)^{-1/4}$, and results in $\delta\Phi_{B,1}^{sad} \approx 4\,u_{im}/\,(\zeta_0 - \zeta_{sad})$. The resulting effects of this barrier height lowering will not be treated in detail here. In the three first cases, the distribution function of potential barrier heights is then calculated with a fixed value of ζ_0 and random values of ξ_0 around a mean $\overline{\xi_0}$ according to a normal law with a standard deviation σ_ξ, to assess the possible values of $\overline{\Phi_B}(T, V_j)$ and $\sigma_\Phi(V_j)$, the characteristic parameters of the inhomogeneous barrier.

In a first step, the parameter $\sigma_\Phi(0)$ is adjusted to match the values displayed in Table I

at a medium temperature, typically 500 K with realistic values of ζ_0, $\overline{\xi_0}$ and σ_ξ. More specifically, $\zeta_0\lambda_D$ spans the range 0.2 to 0.46 nm and $(\overline{\xi_0}\lambda_D)^{-2}$ the range 1.5×10^{12} cm^{-2} to 3×10^{14} cm^{-2}, the two later limits featuring respectively a positive charge density inside the oxide layer and the dipole density at the oxygen terminated surface. Accordingly, the average distances $\overline{\xi_0}$ between point charges or dipoles span a range limited by 0.08 and 0.007 (in λ_D units) respectively. Therefore, the barrier height fluctuations are occurring along a microscopic scale, well below the Debye length. In a second step, the band bending is changed and the values of $\overline{\Phi_B}(T,U)$ and $\sigma_\Phi(U)$ are evaluated as a function of the band bending U. In all the cases and whatever the temperature, as suggested in[26], the increase of the average barrier height $\overline{\Phi_B}(T,V_j)$ and the decrease of the standard deviation $\sigma_\Phi(V_j)$ with increasing forward voltage and correlative decreasing band bending is fully confirmed, although the barrier height distribution is not symmetric and cannot be strictly depicted by a normal law. The trends followed by the two terms of Eq. (5) both contribute to an increase of the barrier height with forward voltage which can be also interpreted as an increase of the ideality factor, thus inducing a lower current density in comparison to that anticipated with the help of a constant ideality factor like sketched with dash-dot lines in Fig. 2. At variance with the hypothesis used in ref.[26], neither the variation of $\overline{\Phi_B}(T,V_j)$ nor that of $\sigma_\Phi(V_j)^2$ is linear with V_j or U, a law which would have resulted in a constant ideality factor, in contradiction both with experimental and simulation results. An other major feature is the relative insensitivity of the ideality factor to the density of point charges or dipoles $(\overline{\xi_0}\lambda_D)^{-2}$, the former starting from 1.01-1.02 for band bending corresponding to zero voltage bias and growing up to 1.05-1.15 when the band bending U becomes close to a few k_BT/e_0 like shown in Fig. 7, irrespective of the temperature. The barrier height variations which are deduced from the ideality factor match very well those of the image force lowering as clear in Fig. 7 too. This result coming from the simulated inhomogeneous barrier height with repulsive elementary charges or dipoles demonstrates that the image force lowering and its changes with the band bending is the main source of the variation of the average barrier height with the applied voltage, because barrier height enhancement does not contribute significantly to the whole barrier experienced by carriers responsible for the current, except for a reduced effective area. Such a result validates this hypothesis already done in ref.[27]. The whole variation amounts to about 40 mV like inferred in ref.[21] for the image force lowering alone. It is thus possible to derive a universal law featured by a solid line in Fig. 7 that may be

used to derive current density-voltage characteristics with the help of Eq. (4) and (6). The first important result coming out from this simulation turns out to be the better agreement of the simulated current density sketched in solid line in the inset of Fig. 2 in the case (c) where the barrier height correction has been taken into account. The second one is the insensitivity of the ideality factor to temperature, a property which matches rather well the behavior of the interface (c) in Fig. 4 (c'), in contrast to the absolute variations in data (a') and (b'), although the ideality factor (c') remains slightly higher than the values evaluated from the image force lowering alone. Taking all the arguments evidenced and discussed in the present subsection, one must conclude that microscopic barrier inhomogeneities resulting from repulsive elementary point charges or dipoles which have been however, experimentally evidenced, cannot account for most of the properties of the interfaces presently studied, and that an other type of barrier inhomogeneity must be present.

D. Barrier height and ideality factor of interfaces with lowered barrier patches of size either comparable to or smaller than the Debye length

The calculation of barrier height fluctuations due to barrier height lowering Δ_p at circular patches with radius R_0 or linear ones with width L_0 and their effect on the current-voltage characteristics relies on the same principle as previously, except for the weight of each dipole which has to be $2\pi\varepsilon_{SC}\varepsilon_0\Delta_p R_0^2$ to induce the desired barrier change at circular patches which will be only considered in the following because close to those happening naturally in inhomogeneous interfaces. Additionally, only patches with a lowered barrier are considered as demonstrated in the previous subsection. This method, known as the dipole-layer approach, has been implemented analytically by R. T. Tung[27] and summarized later by W. Mönch[21]. For a single circular patch with radius R_0 and barrier lowering Δ_p embedded into a homogeneous area characterized by a constant barrier height Φ_B^{hom}, a single parameter containing the two characteristic quantities R_0 and Δ_p, which is called the patch parameter $\gamma_p = 3(\Delta_p\ R_0^2/4)^{1/3}$ can be defined. Integrating Eq.(1) over the whole area A with the hypothesis of a parabolic shape of the potential around the saddle point restores the form of Eq. (3). But the new barrier height is Φ_B^{hom} minus an effective barrier lowering $\delta\Phi_p^{sad}$ at the potential saddle point, the ideality factor n is replaced by 1 and an effective area $A_{eff} = 4\pi\lambda_D^2\Gamma/3$ affects the current expression. The weight of the patch is proportional to

the dimensionless parameter $\Gamma = \frac{\gamma_p}{3}\frac{1}{\eta^{1/3}U^{2/3}}$ where $\eta = \varepsilon_{SC}\,\varepsilon_0\,/\,(e_0\,N_A)$. Both the effective barrier lowering $3\Gamma\,U = \gamma_p\,[U\,/\,\eta]^{1/3}$ and area $A_{eff} = \frac{4\pi\gamma_p k_B T}{9e_0}\,[\eta\,/\,U]^{2/3}$ are dependent on the band bending $U = \Phi_B^{hom} - V_j - V_{dop}$, while the ideality factor is approximately $1+\Gamma$, therefore increasing with the forward voltage. The final step consists in introducing a distribution of a variable patch parameter. In the Tung's original work[27], two cases were worked out : (i) a sharp distribution of lowered barrier patches approximated by a single patch parameter γ_0 and (ii) a broad distribution featured by half a Gaussian law which limited the γ_p range to the values pertaining to barrier height lowering alone, that are $\gamma_p \geqslant 0$. This choice was justified by the negligible contribution of patches characterized by a barrier height enhancement to the whole current as we checked in the previous subsection. In order to generalize such an approach, allowing to match continuously any intermediate behavior between the two previous cases, the patch parameter distribution function will be chosen as $N(\gamma_p) = \frac{D_p}{\sqrt{2\pi}\sigma_p}\exp\left(-\frac{(\gamma_p-\gamma_0)^2}{2\sigma_p^2}\right)$, characterized by a standard deviation σ_p of the patch parameter around the central value γ_0 and an areal density D_p. Depending on γ_0, the function $N(\gamma_p)$ depicts either a peaked distribution around the central patch parameter, or half a Gaussian law decreasing from its maximum at $\gamma_p = 0$ when $\gamma_0 = 0$ or even a decreasing Gaussian tail with a non zero initial slope if $\gamma_0 < 0$. After summation of all the currents dependent on any positive value of γ_p from zero to infinite, this procedure further allows to derive the following expression where only the last factor contains the effects of inhomogeneities while the others give the ideal thermionic current density of a homogeneous barrier height Φ_B^{hom}:

$$J_z^{patchy} = \alpha\,A^{**}\,T^2\,\exp\left(-\frac{e_0\Phi_B^{hom}}{k_BT}\right)\left[\exp\left(\frac{e_0V_j}{k_BT}\right)-1\right]$$
$$\times\left\{1+\frac{2\sqrt{2\pi}\,k_BT\,D_p\,\sigma_p\,\eta^{2/3}}{9\,e_0\,U^{2/3}}\exp\left(-\frac{\gamma_0^2}{2\sigma_p^2}\right)\left[1\,+\frac{\sqrt{2\pi}\,e_0\,<\delta\Phi_{p,0}^{sad}>}{k_BT}\exp\left(\frac{1}{2}\left(\frac{e_0}{k_BT}\,<\delta\Phi_{p,0}^{sad}>\right)^2\right)\right]\right\} \tag{7}$$

where the standard deviation $<\delta\Phi_{p,0}^{sad}>$ of the distribution of the saddle point of the barrier Φ_p^{sad} is:

$$<\delta\Phi_{p,0}^{sad}> = \sigma_p\left[\frac{U}{\eta}\right]^{1/3} + \frac{k_BT\,\gamma_0}{e_0\,\sigma_p} \tag{8}$$

But the current density deviates notably from the ideal thermionic law only if the factor inside the braces of Eq. (7) is larger than unity. As one is interested in this case, a reasonable

approximation consists in neglecting the unity terms inside the braces, so that the effective barrier height can be deduced from the exponent of the exponential factors, which turns out to be $\frac{1}{2}\left[\frac{e_0}{k_BT} < \delta\Phi_{p,0}^{sad} >^2 - \frac{\gamma_0^2}{\sigma_p^2}\right]$ inside the braces of Eq. (7) and logarithm of the pre-exponential factor :

$$\Phi_B^{eff}(T,U) = \Phi_B^{hom} - \left[\frac{e_0}{2k_BT}\sigma_p^2\left(\frac{U}{\eta}\right)^{2/3} + \gamma_0\left(\frac{U}{\eta}\right)^{1/3}\right] - \frac{k_BT}{e_0}\ln\left[\frac{4\pi\, D_p\, \sigma_p\, \eta^{2/3}}{9\, U^{2/3}} < \delta\Phi_{p,0}^{sad} >\right] \tag{9}$$

This last equation is similar to Eq. (5) with the new quadratic average $< \delta\Phi_B >$ of barrier fluctuations

$$< \delta\Phi_B >= \left[\sigma_p^2\left(\frac{U}{\eta}\right)^{2/3} + \frac{2k_BT}{e_0}\gamma_0\left(\frac{U}{\eta}\right)^{1/3}\right]^{1/2} \tag{10}$$

and an additional term which has a little influence due to the logarithm and a null value for D_p in the 10^{10} cm^{-2} range, but may give a non negligible contribution to the ideality factor appearing in next formula when the barrier inhomogeneity level is low. But the main issue is the dependence of $< \delta\Phi_B >$ on temperature which is different from that given by Eq. (5) and results in a shift of the high temperature asymptote of the effective barrier in comparison to Φ_B^{hom} by a quantity proportional to γ_0, leading to an apparent extrapolated barrier $\Phi_B^{app} = \Phi_B^{hom} - \gamma_0\left(\frac{U}{\eta}\right)^{1/3}$.

From Eq. (6), (8) and (9), the ideality factor can be calculated as:

$$\begin{aligned}\frac{n(T,U)-1}{n(T,U)} &= \frac{e_0}{3k_BT\,U}\left[\sigma_p^2\left(\frac{U}{\eta}\right)^{2/3} + \frac{k_BT}{e_0}\gamma_0\left(\frac{U}{\eta}\right)^{1/3}\right] - k_\Phi\frac{k_BT}{e_0\,U} \\ &= \frac{e_0}{3k_BT\,U} < \delta\Phi_B >^2 \; - \frac{\gamma_0}{3\eta^{1/3}U^{2/3}} \; - \; k_\Phi\frac{k_BT}{e_0\,U}\end{aligned} \tag{11}$$

where k_Φ is between 1/3 and 2/3 according to the respective dominance of either the first or the second term in $< \delta\Phi_B >$. This ideality factor increases with decreasing band bending and therefore with increasing applied voltage as long as flat bands are not reached, so that current-voltage characteristics plotted in a semilogarithmic diagram experience a downwards curvature, as in Fig. 2 (a) and (b). This model ceases to be valid neat flat bands and beyond because the current calculation relies only on the carrier flow at the saddle points of the potential barrier, neglecting the areas where the barrier is higher than Φ_B^{hom}. It must be also stressed that these ideality factor and effective barrier height must be evaluated around the same band bending $U = U_b$ if comparison at different temperatures or in different diodes are made. This is often done by assessing the corresponding ideality factor n_b at the same

current density although such a rule is almost true only at vanishing band bending. It is important to notice that various behaviors of the ideality factor as a function of temperature can result from Eq. (11), with a trend toward a constant value when the second term inside the brackets dominates at elevated temperatures as one can see in Fig. (3b'), the last term in Eq. (11) being negligible except near flat bands and for ideality factors below 1.1. Either neglecting the last term in Eq. (9) or lumping it into Φ_B^{hom}, a relationship between the effective barrier height and ideality factor n_b at the same band bending U_b for all the diodes investigated at a given temperature among a set of diodes belonging to a same sample, comes from Eq. (9), (10) and (11):

$$\Phi_B^{eff} \approx \Phi_B^{hom} \; - \; \frac{3U_b}{2}\frac{n_b - 1}{n_b} \; - \; \frac{\gamma_0}{2}\left(\frac{U_b}{\eta}\right)^{1/3} \; - \; k_\Phi \frac{k_B T}{e_0\, U_b} \tag{12}$$

Therefore, the difference between the effective barrier height Φ_B^{eff} and a quantity shifted from the homogeneous barrier Φ_B^{hom} mainly by a term proportional to the central patch parameter γ_0, follows a linear relationship regarding the ideality function $(n_b - 1)/n_b$. It does not depend on the standard deviation σ_p of the patch distribution, except for the last term including the factor k_Φ which is roughly constant for a given patch distribution. At constant temperature, this last term is indistinguishable from Φ_B^{hom} and adds a minor error to it. Conversely, the term proportional to γ_0 may contribute to an important shift of the apparent extrapolated barrier at unity ideality factor in comparison to Φ_B^{hom}, since this apparent barrier turns out to be $\Phi_B^{app} = \Phi_B^{hom} \; - \; \frac{\gamma_0}{2}\left(\frac{U}{\eta}\right)^{1/3}$ and this correction might not be ignored in general. It can also introduce some dispersion of the data when a family of diodes is studied. The effective barrier height Φ_B^{eff} is approximately linear with n_b only for typical values smaller than 1.4 like noticed in ref.[21], so that it is better to make plots of the apparent barriers as a function of $(n_b - 1)/n_b$ for sake of generality, as done in Fig. (8), which will be commented in the next subsection. However, it must be stressed that all the expressions derived for the effective barrier height and ideality factor within the framework of the present model, that are Eq.(9) to (12), assumed that the factor inside the braces of Eq. (7) is largely greater than one. Such a condition implies that the patch density D_p must be typically much larger than 10^7 cm^{-2}, so that one has to wonder whether the value deduced from adjustments has really a physical meaning in each situation.

In one diode alone, the fingerprint of the kind of barrier inhomogeneities breaks out in the behaviors of the ideality factor and to a smaller extent of the effective barrier height

Sample type and	Φ_B^{app}	σ_p	γ_0	$\Phi_{B,1}^{hom}$	D_p	$\Phi_{B,2}^{hom}$
annealing temp.	V	$V^{1/3}$ $cm^{2/3}$	$V^{1/3}$ $cm^{2/3}$	V	cm^{-2}	V
(a) $<$ 300 ℃	2.04±0.14	(9±3)×10^{-5}	(1.6±0.4)×10^{-4}	2.26±0.16	(3±1)× 10^6	2.38±0.02
(b) 350 ℃	1.68±0.1	(9.0±1)×10^{-5}	(1.85±0.3)×10^{-4}	1.87±0.1	(6±2)×10^9	1.90±0.02
(c) 450 ℃	0.93±0.04	(5.5±1.5)×10^{-5}	(1.3±1.2)×10^{-5}	0.94±0.04	$< 10^9$	0.99±0.01

TABLE II. Parameters of the Schottky barrier in the three interfaces according to the models detailed in section IV, with $\Phi_{B,1}^{app}$ and σ_p deduced from the adjustment of barrier height as a function of temperature according to Eq. (9). Then, γ_0, and $\Phi_{B,1}^{hom}$ are derived from ideality factors fitted as a function of temperature with respective help of Eq. (11) in the case of interfaces (b) and (c), and Eq. (16b) for interface of kind (a), while D_p and $\Phi_{B,2}^{hom}$ come from the direct adjustment of the current densities shown in Fig. (2) respectively to Eq. (7) for interfaces of kind (b) and (c) and Eq. (14) for interface of kind (a) as a function of voltage.

as a function of temperature, like shown in Fig. (4), where evolutions of the ideality factor are markedly different for the three interfaces in Fig. (4a'), (4b') and (4c'). All these features can be reproduced by the laws demonstrated above, specially the ideality factor variations with temperature which are strongly influenced by the central patch parameter γ_0 in Eq. (11). In the case (a), a good agreement with Eq. (11) can be obtained as depicted by the full curve in Fig. (4a') at the expense of a negative central patch parameter which would induce an apparent barrier Φ_B^{app} larger than the homogeneous one Φ_B^{hom}, obviously leading to an incoherent physical situation. Moreover, the direct adjustment of the current density according to Eq. (7) turns out to be impossible because this expression is unable to account for the curvature of the current density-voltage characteristic (a) in Fig. (2) below flat bands. An alternative model may be more appropriate to involve a better physical picture as discussed below for interfaces of kind (a). Data collected in 95 diodes prepared on three distinct diamond stacks which underwent the same pre-treatment before metal deposition and displayed in Fig. (8), give a first indication: if so different groups of data are possible for diodes whose diameter is 100 μm, specially the IB against IA and IIA, related to interfaces of kind (a), barrier heights extrapolated at unity ideality factor and averaged on such area must be different. Consequently, the scale of barrier inhomogeneities

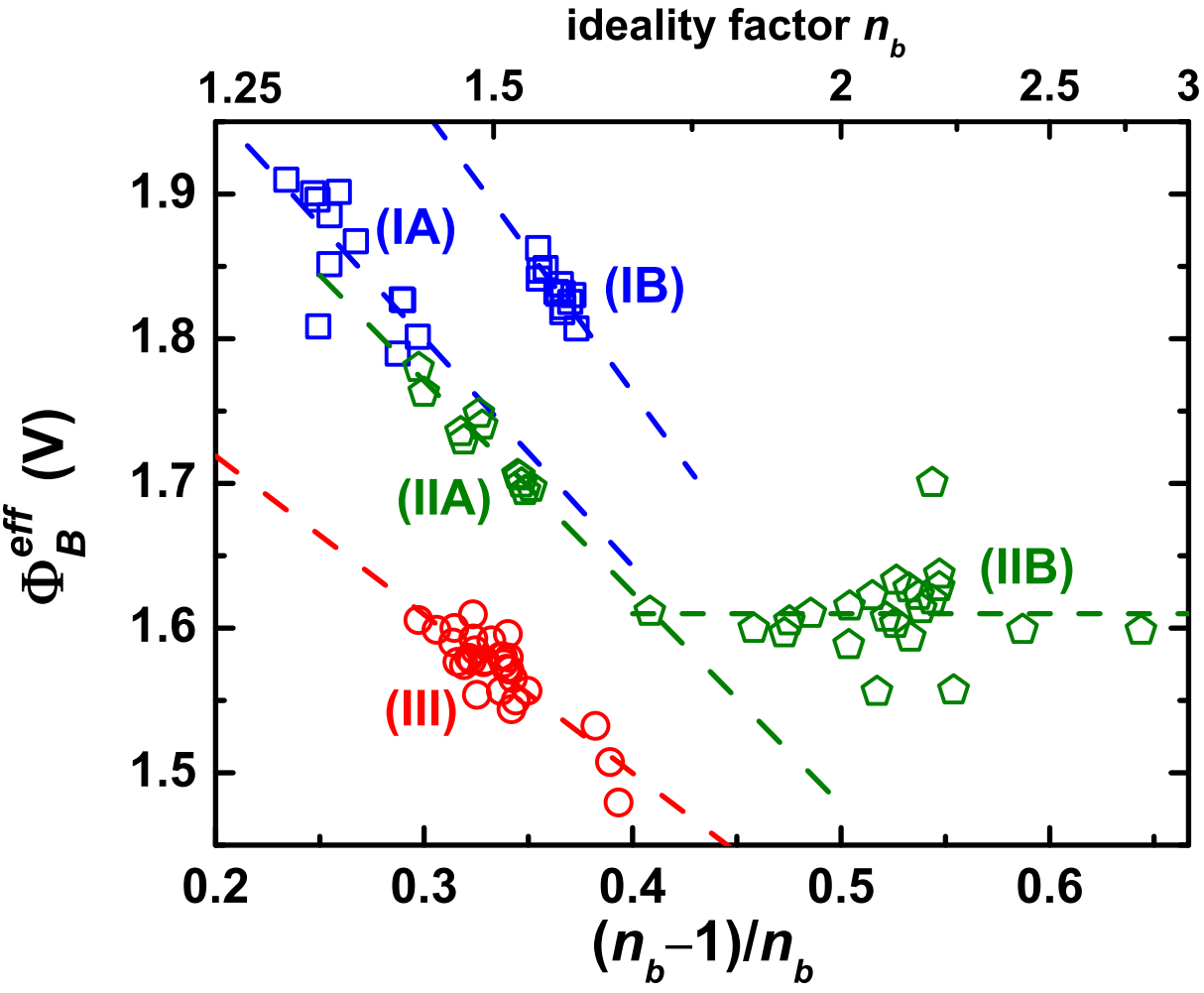

FIG. 8. Effective barrier height as a function of $(n_b-1)/n_b$, where n_b is the ideality factor at band bending U_b for 95 diodes fabricated on three distinct diamond stacks elaborated like described in section II, respectively identified by squares (I), pentagons (II) and circles (III). Samples I and II have not been intentionaly annealed while sample III has been annealed at 350 ℃. Dash lines are best linear fits of grouped data IA, IB, IIA, IIB and III according to Eq. (12).

may no longer be the Debye length but much more, and the approximations of a parabolic potential at the bottom of the lowered barrier patches depicted by the patch parameter γ_p would cease to be valid. Secondly, strong variations of the ideality factor with temperature like in Fig. (4a) suggests that diamond resistivity may play a role because acceptors are progressively ionizing in this temperature range.

E. Barrier domains with multiple sizes and inhomogeneities of the current density

When the lateral size of barrier inhomogeneities largely exceeds the Debye length, the previous model relying on a parabolic potential at the bottom of the patches with a lowered barrier is no longer relevant. These different areas with distinct barrier height can be treated as independent of the band curvature because the pinch-off of the channels where the current flows becomes negligible. Then, the total current is simply obtained by summation of all the currents like in a parallel circuit of the corresponding paths. But such a model is unable to fit the downward curvature experienced by the logarithm of the current density as a function of voltage in interfaces of kind (a) and yields merely an ideal behavior as soon as the lowest barrier is shifted below the others by some k_BT/e_0 because the corresponding current flow dominates the others. But this current inhomogeneity due to carrier crowding at the saddle points and lowest barrier domains remains when the z coordinate move away from the interface and therefore have a dramatic influence on the total voltage applied to the junction for a given current, specially when carrier freeze-in occurs, inducing large variations of the ideality factor with temperature. This effect is relevant both for barrier domains much larger than the Debye length where no pinch-off occurs and for pinched-off patches, and the voltage drops in these shrunk channels must be subtracted from the total applied voltage. In the pinched-off case, the diameter of patches is always much smaller than the lightly doped layer thickness t_l so that the spreading resistance can be approximated by $\frac{\rho(T)}{4\sqrt{\mathcal{A}^{p-o}_{eff,i}/\pi}}$ with a good accuracy[45], $\rho(T)$ being the resistivity of the lightly doped diamond layer. Therefore, the non pinched-off and pinched-off forward currents which flow respectively through individual areas $\mathcal{A}_i$ and $\mathcal{A}^{p-o}_{eff,i}$ under an applied voltage V_a read:

$$I_i^{non-p-o} \;=\; \mathcal{A}_i\,\alpha\,A^{**}\,T^2\,\exp\left[-\frac{e_0}{k_BT}\left(\Phi_B^{hom}\;-\;\Delta\Phi\;-\;V_a\;+\;I_i^{non-p-o}\rho(T)/\lambda_i\right)\right] \tag{13a}$$

$$I_i^{p-o} \;=\; \mathcal{A}^{p-o}_{eff,i}\,\alpha\,A^{**}\,T^2\,\exp\left[-\frac{e_0}{k_BT}\left(\Phi_B^{hom}\;-\;\gamma_p\left(\frac{U_i}{\eta}\right)^{1/3}\;-\;V_a\;+\;\frac{\rho(T)}{4\sqrt{\mathcal{A}^{p-o}_{eff,i}/\pi}}\,I_i^{p-o}\right)\right] \tag{13b}$$

with $\mathcal{A}^{p-o}_{eff,i} = \frac{4\,\pi\,k_B\,T\,\gamma_p}{9\,e_0}\left(\frac{\eta}{U_i}\right)^{2/3}$ and $U_i \;=\; \Phi_B^{hom} - \gamma_p\left(\frac{U_i}{\eta}\right)^{1/3} - V_a - V_{dop} + \frac{\rho(T)}{4\sqrt{\mathcal{A}^{p-o}_{eff,i}/\pi}}\,I_i^{p-o}$;

the lowest barrier spreading over the areas $\mathcal{A}_i$ with size much larger than the Debye length being $\Phi_B^{hom} - \Delta\Phi$. If the current inhomogeneity remains the same along the whole

depth of the lightly doped layer like assumed in ref.[28], the voltage drop along the i^{th} non pinched-off channel is simply proportional to a resistance $\rho(T)/\lambda_i$ where $\lambda_i = \mathcal{A}_i/t_l$. This hypothesis is true in the limit of a diameter of the area with a lowered barrier height well larger than t_l, a condition equivalent to $\sqrt{\mathcal{A}_i/\pi} \gg t_l/2$. But because this diameter can span a large range, from values well below t_l up to much wider ones, the corresponding spreading resistance should take the general form[45] $\frac{\rho(T)}{2\sqrt{\pi\mathcal{A}_i}} \arctan(2t_l/\sqrt{\mathcal{A}_i/\pi})$ and λ_i should become $2\sqrt{\pi\mathcal{A}_i}/\arctan(2t_l/\sqrt{\mathcal{A}_i/\pi})$. It must be noticed that the last term in the exponent of the expression of I_i^{p-o} and in U_i is added to Φ_B^{hom} and therefore plays the same role as a negative central patch parameter γ_0 in the effective barrier experienced by the whole current flowing through the pinched-off patches and given in Eq. (9). This fact explains why neglecting the confinement of current in channels which stretch out along some part of the lightly doped layer thickness had to be compensated by the occurrence of a negative figure for γ_0 in the simulation results of the previous subsection, leading to an incorrect value because of an inappropriate model applied to interfaces of kind (a).

Averaging all the currents over the whole diode area $\mathcal{A}_d$ is not tractable analytically. A reasonable approximation consists in calculating separately the total current and an estimate of the whole conductance within the shrunk channels from the integration of all the parallel conductances $\lambda_i/\rho(T)$ or $4\sqrt{\mathcal{A}_{eff,i}^{p-o}/\pi}/\rho(T)$ appearing in the last term of the exponent of each expression (13a) or (13b), weighted by the distribution $N(\gamma_p) = \frac{D_p}{\sqrt{2\pi}\sigma_p} \exp\left(-\frac{(\gamma_p-\gamma_0)^2}{2\sigma_p^2}\right)$ in the later case. It is also assumed like previously that only the lowest barrier for the current flow is efficient and that the barrier lowering is approximated by its quadratic average. For non pinched-off channels, the total conductance would result from the integral of $\lambda_i/\rho(T)$ weighted by an unknown distribution, so that it is more convenient to introduce a fictitious area $\mathcal{A}_{\Delta V}^{non-p-o}$ allowing to write the corresponding voltage drop $\Delta V^{non-p-o}$. In the case of the pinched-off currents, two integrals must be evaluated numerically as a function of $\gamma_0/(\sqrt{2}\sigma_p)$. Their ratio appears as a fraction in the next formula and gives the exact value within an error smaller than 10 % . With $\mathcal{A}^{non-p-o} = \sum_i \mathcal{A}_i$ representing the true area of the non pinched-off zones, the average current densities in the whole diode area become respectively for the non pinched-off and pinched-off channels:

$$J_z^{non-p-o} \approx \frac{\mathcal{A}^{non-p-o}}{\mathcal{A}_d}\ \alpha A^{**}T^2 \exp\left[-\frac{e_0}{k_B T}\left(\Phi_B^{hom} - \Delta\Phi - V_a + \Delta V^{non-p-o}\right)\right] \quad (14a)$$

with

$$\Delta V^{non-p-o} \approx \frac{\rho(T)\,\mathcal{A}^{non-p-o}}{(\mathcal{A}^{non-p-o}_{\Delta V})^{1/2}}\ \alpha A^{**}T^2 \exp\left[-\frac{e_0}{k_B T}\left(\Phi_B^{hom} - \Delta\Phi - V_a + \Delta V^{non-p-o}\right)\right] \tag{14b}$$

and $J^{p-o} = J_z^{patchy}$ from Eq. (7), with $V_j = V_a - \Delta V^{p-o}$ where

$$\Delta V^{p-o} \approx \frac{\pi}{6}\,\rho(T)\left(\frac{k_B T}{e_0}\right)^{1/2}\left(\frac{\eta}{U}\right)^{1/3}\ \frac{1.77\gamma_0 + \sigma_p^2/(\gamma_0 + \sqrt{2}\sigma_p)}{\sqrt{\pi\,\gamma_0 + \sqrt{2}\sigma_p/3}}$$
$$\times\,\alpha A^{**}T^2\,\exp\left[-\frac{e_0}{k_B T}\left(\Phi_B^{hom} - \frac{e_0}{2k_B T}<\delta\Phi_B>^2 - V_a + \Delta V^{p-o}\right)\right] \tag{14c}$$

and

$$U \approx \Phi_B^{hom} - \frac{e_0}{2k_B T}<\delta\Phi_B>^2 - V_a - V_{dop} \tag{14d}$$

It must be noticed that the patch density D_p does not appear in ΔV^{p-o} because both the conductance and current are proportional to it, so that it is canceled in the framework of the previous approximation. From these expressions, it is easy to guess that the lower the temperature, the higher the effect of the smallest barrier, like in previous models. If the non pinched-off current dominates, the apparent barrier lowering would be $\Delta\Phi - \frac{k_B T}{e_0}\ln(\mathcal{A}_d/\mathcal{A}^{non-p-o})$, inducing a linear decrease of the effective barrier as temperature is lowered, whereas alternatively Eq. (9) would be valid, at least when ΔV remains small regarding V_a. At sufficiently high temperature, the increase of the effective barrier would be linear with temperature when the non pinch-off current dominates, an effect which is not clearly detected in Fig. (4a), indicating that the pinch-off current might be the major one. Such a view is confirmed by the absence of any "S-shaped" current-voltage characteristic in Fig. (2a), which otherwise would reveal the existence of two parallel non pinched-off channels, each of ones having its own barrier height and series resistance with the corresponding condition $\sqrt{\mathcal{A}_i/\pi} \gg t_l/2$ indeed achieved.

From experimental data displayed in Fig. (8), it seems that the general trend involving a linear relationship between effective barrier height and ideality is still valid. Such a property can be checked from the integration of the central expression in Eq. (6) with V_a replacing V_j. It results in a linear relationship between the effective barrier and ideality factor function if the ideality factor does not depend on the band bending. Such a condition is only

approximately achieved, but better and better when higher and higher band bending are used, like those deduced from these data and reported in Table III. In such conditions, the voltage drop ΔV remains negligible and the ideality factor is close to a constant value when the band bending changes. In such an approximation, K and C being constants, one gets from the integration of Eq. (6) :

$$\frac{n(T,V_a)-1}{n(T,V_a)} = K\,\Phi_B^{eff}(T,V_a) + C \tag{15}$$

Therefore, the observed linear correlations in Fig. 8 can still be justified but the integration constant is not known and can be replaced by the term proportional to γ_0 in Eq. (12) only if the model relying on a patchy barrier height with a negligible voltage drop inside the lightly doped layer is relevant. In the opposite case, specially when non pinched-off zones dominate, the second member of the previous equation would be $K\,(\Phi_B^{hom} - \Delta\Phi)$ with an ideality factor close to unity if the previous condition applies, since the current would be essentially thermoionic in nature. In the general case, an uncertainty remains about the physical meaning of the extrapolated barrier and its eventual difference with Φ_B^{hom}. When the voltage drop inside the lightly doped layer is not negligible, approximate expressions of the ideality function can be drawn separately from the previous equations when either $I^{non\text{–}p\text{–}o} = \mathcal{A}_d J_z^{non\text{–}p\text{–}o}$ or $I^{p\text{–}o} = \mathcal{A}_d J_z^{p\text{–}o}$ dominates, which turns out to be respectively:

$$Y^{non\text{–}p\text{–}o} = \frac{n_a(T,V_a)-1}{n_a(T,V_a)} \approx \frac{e_0}{k_B T}\Delta V^{non\text{–}p\text{–}o} \tag{16a}$$

$$\text{or} \qquad Y^{p\text{–}o} = \frac{n_b(T,V_a)-1}{n_b(T,V_a)}$$
$$\approx \left[\frac{e_0}{3k_BT\,U}\sigma_p^2\left(\frac{U}{\eta}\right)^{2/3} + \frac{\gamma_0}{3\,U}\left(\frac{U}{\eta}\right)^{1/3}\right]\left(1 + \frac{e_0}{k_BT}\Delta V^{p\text{–}o}\right) + \frac{e_0}{k_BT}\Delta V^{p\text{–}o} \tag{16b}$$

When the ideality factor has to be studied as a function of temperature, measurements should be done at constant current density, because in such a case the product of $\alpha A^{**}T^2$ and exponential factors in Eq. (16a) and in the term $\Delta V^{p\text{–}o}$ of Eq. (16b) can be considered as almost invariant, making any parameter adjustment much easier. In each case, these expressions shows that the ideality factor may become very sensitive to temperature, specially because it follows the variations of the resistivity $\rho(T)$ which are very important in the range where freezing out of carrier occurs, typically from 300 K to 550 K in this study. Involvement of the voltage drop due to the flow of current through the narrow bottlenecks which lengthen

the lowered barrier regions inwards the lightly doped layer is able to explain qualitatively the strong negative slope of the ideality factor in Fig. (4a'). The general case relies on the combination of the two kinds of current with a proportion $P = I^{p-o}/(I^{p-o} + I^{non-p-o})$ and on Eq. (6), giving the global ideality function:

$$Y \;=\; \frac{n(T,V_a)-1}{n(T,V_a)} = P\;Y^{p-o} + (1-P)\;Y^{non-p-o} \tag{17}$$

The best match to the four data at highest temperatures is obtained with $P = 72\%$ and plotted as a full curve in Fig. (4a'), confirming the previous hypothesis about the dominance of the pinched-off current. The discrepancy at the lowest temperatures is commented in the following. But it must be stressed that the first term in Eq. (17) is unable to account for the ideality factor variation, which are mainly due to the second term despite its smaller weight. It is thus confirmed that the non pinched-off currents contribution is necessary to explain both the current density-voltage curvature and the ideality function shape with temperature in interfaces of kind (a). The more important voltage drop $\Delta V^{non-p-o}$ in these interfaces is also able to explain why flat bands are reached at a lower current density (see Fig. 2) in comparison to interfaces of kind (b) and (c) in which the patch and channel densities are so high (see Table II) so that the voltage drop remains negligible in this bias domain.

At sufficiently high forward bias, band curvature can be inverted in some areas or even in the whole diode, as the reader can realized from the comparison of Φ_B^{hom} (in Table II) minus $V_{dop} = 0.38$ V to the applied voltage in Fig. (2), so that the previous expressions can no longer be used. From Eq. (10), barrier lowering vanishes at flat bands for I^{p-o} while it stays constant for $I^{non-p-o}$ and one can think that the effective barrier height remains more or less at the value obtained at flat bands beyond this threshold. But previous models which rely only on barrier lowering are unable to take into account the progressive disappearance of current inhomogeneities in the lightly doped layer due to the general increase of the carrier concentration at the whole interface. Such a behavior would finally lead to a more homogeneous current density and a voltage drop within the lightly doped layer expected to be simply the product of a series resistance and the total current. But even this view fails because voltage drop turns out to be lower in Fig. (2) as if the resistivity were smaller than the predicted one. This discrepancy is neither an artifact of the adjustment procedure nor a self-heating effect which would hardly be justified because of the low dissipated power (typically

Interface type, sample and diodes set identifiers	Φ_B^{app} (V)	U_b (V)	Φ_B^{hom} (V) corrected for γ_0
(a) I A	2.27 ± 0.12	1.05 ± 0.28	
(a) I B	2.54 ± 0.14	1.30 ± 0.24	
(a) II A	2.21 ± 0.04	0.97 ± 0.04	
(a) II B	1.61 ± 0.06		
(b) III	1.94 ± 0.04	0.73 ± 0.08	2.04 ± 0.04

TABLE III. Schottky barriers extrapolated at unity ideality factor at band bending U_b in different sets of diodes fabricated on three distinct diamond stacks numbered I, II and III, according to best fits of Eq. (12) and Φ_B^{hom} after the γ_0 correction for the interface of kind (b).

one to some tens of mW in the range of interest), but is rather due to the injection of carrier by the heavily doped layer, involving a conductivity modulation due to the increase of carrier concentration above the equilibrium one and occurrence of a diffusion current starting from this heavily doped layer. This effect is evidenced from the comparison of the current-density data and curves simulated with a constant series resistance in Fig. (2) and can also be found in the lower value of the current-density derivative compared to the theoretical specific resistance (not shown) at sufficiently high current. It had been probably observed by other authors in Ni/SiC diodes[29], although they did not give such an interpretation. But this carrier injection which decreases the Fig. (2)resistivity is probably still efficient at lower current density, so that the hole concentration is underestimated even at the bias voltage where ideality factors are measured, at least when complete ionization of acceptors is not achieved. Correlatively, the effective resistivity is overestimated when its equilibrium value is taken into account as done in the present calculation, increasing thoughtlessly the simulated voltage drop and ideality factor in Fig. (4a') at the lowest temperatures. This injection effect probably occurs because the lightly doped layer is only 1.4 μm thick and would disappear for the larger thicknesses suited to higher voltage operation. In any cases, it must be noticed that all the previous models discussed and built in this work are applicable to a range of bias voltages and currents limited by the occurrence of flat bands in the junction.

F. Characteristics and origin of barrier height inhomogeneities in the three types of interface

The linear relationship between the effective barrier height as a function of the ideality factor function $(n_b - 1)/n_b$ is actually checked for diodes prepared with the same procedure on three different substrates either without intentional post-annealing or annealed near 350℃in Fig. (8). The correction of the constant term in Eq. (12) is done only in the case of indisputable relevance of the model of subsection IV D and as it is not certain for interfaces of kind (a), extrapolated barrier heights Φ_B^{app} and Φ_B^{hom} will be considered as the same in table III. It is noteworthy that the homogeneous barrier height Φ_B^{hom} can be different in two families of diodes (IA and IB; IIA and IIB) on the same diamond stack while it turns out to be very similar for two families of diodes (IA and IIA) belonging to two distinct diamond samples, whose the initial surfaces are all oxygen-terminated. Such results confirm that oxygen terminations, which are responsible for the enhanced electron affinity of the oxygen-terminated diamond surfaces and highest barrier at interfaces build on such surfaces, are expected to be organized in domains displaying distinct electron affinities[31–34,36,37], resulting in distinct barrier heights, and that the same kind of oxygen terminations can exist on different samples. This dispersion matches that of the various molecules and bonds presented in subsection IV A and probably also the lack of full coverage by oxygen related molecules. The linear relationship of Eq. (12) or (15) seems to apply irrespective of the scale of the barrier inhomogeneities in comparison to the Debye length provided ideality factor is measured at high enough band bending, typically two third of the barrier height, as justified in the previous subsection. But because the interface annealed at 350℃(Fig. (8, III)) is a matter of the lowered barrier patch model detailed in subsection IV D, the correction which gives the homogeneous barrier from the apparent one is only exerted in this case in table III where the parameters are collected and displayed for all the diodes families. It must be noticed that the coherence of the various Φ_B^{hom} values appearing in Tables II and III is reasonable and that an average value of 2.04±0.04 V can be inferred for the interface of kind (b), only about 0.2-0.5 V below the values at stake for the interfaces of kind (a). The relevance of the model relying for interfaces of kind (b) on lowered barrier patches with sizes comparable or smaller than the Debye length and depicted by a patch parameter distribution centered on a peculiar value $\gamma_0 > 0$, with a much higher patch density than for unannealed interfaces,

demonstrates that the main barrier inhomogeneities take place now along this microscopic scale, contrary to what happened in unannealed interfaces. One must remind that the patch parameters γ_p, σ_p and γ_0 depends on the one third power of the product of the square radius R_0 and initial barrier lowering Δ_p so that similar values of the two last quantities will not involve necessarily the same R_0 and Δ_p, which can move in opposite directions. From results given in Table II, such statements suggest that the 350℃anneal resulted in the partial and random cancellation of the dipoles $O^{-\nu'}-C^{+\nu'}$ whose stability is mainly governed by the enthalpy of the thermodynamical chemistry of these species and temperature, leaving the interface in an intermediate state and inducing new barrier lowering with a magnitude equal to the difference of the potential barrier in interfaces of kind (a) and (c), i.e. $\Delta_p \approx 1.4$ V at a microscopic scale, and increasing considerably the patch density. On the contrary, the initial inhomogeneities in unannealed interfaces of kind (a) likely resulted from the oxygen terminations dispersion over areas with larger size but smaller barrier lowering and much lighter density, with typical $\Delta_p \approx 0.3$ V, similar to the difference in potential barriers reported for various interfaces of type (a) in Table III. To comply with the similarity of σ_p and γ_0 for interfaces of kinds (a) and (b) in Table II, patches area has to be decreased by a factor of nearly five when going from case (a) to case (b), leading to a very good relevance of the model developed in subsection IV D. In the case of interfaces of kind (c) annealed at 450℃, these dipoles have completely disappeared, involving a barrier height as low as 0.96±0.04 V (average from Table II) and very low barrier fluctuations, as indicated by a central patch parameter γ_0 one decade smaller than that of other cases, inducing an almost ideal behavior of the current-voltage characteristics. In this last case, residual barrier inhomogeneities could be due to the random influence of the ionized acceptors close enough to the interface, as it can be evidenced according to the model sketched in Fig. (6d) and invoked in subsection IV C, but the calculation will not be developed further and the reader interested in this question may refer to ref.[18] and references therein. An other residual source of barrier inhomogeneities lies in the possible fluctuations of the oxide thickness, because of the link between these two quantities as discussed in the next section. However, as shown by HRTEM and EELS studies in section II, the interfacial layer thickness remains close to two oxide monolayers as an average before and after interface anneal, leading to the very probable hypothesis of a chemical mechanism involving only bonds change between the first oxygen layer and its neighbors. The main consequence of this bonds transformation shows

out through the very large change occurring in the averaged barrier heights of interfaces (a) and (c), with a difference near 1.4 V, resulting from the partial or complete cancellation of the dipoles $O^{-\nu'}-C^{+\nu'}$ and also other dipole changes as discussed in the next section. The case of the diodes set IIB in Fig. (8) does not comply with any previous models, a fact which suggests that the main part of the current in these diodes is not governed by an exponential law depending on the applied voltage, which was a common hypothesis of all the previous calculations. Therefore, leakage currents like those which might occur in threading dislocations or defects appearing as dark spots in cathodoluminescence images[25] could be responsible for a behavior characterized by rather higher ideality factors and constant apparent barrier height in Fig. (8 IIB). Finally, homogeneous barrier heights $\Phi_{B,2}^{hom}$ appearing in Table II can be considered as the most representative of the physical situation of each interface, except that unannealed interfaces of type (a) may experience two or three different values like mentioned in Table III, the lowest being about 0.2 V below that indicated in Table II. This local barrier lowering may agree the quantity $\Delta\Phi$ invoked in subsection IV E over areas with lateral size larger than the Debye length to built the last electrical model detailed in the previous subsection. It can be concluded that, despite some minor imperfect agreements between experimental data and models of inhomogeneous barriers detailed in this section and their limitations to the depletion regime of Schottky junctions, more informations and deeper physical insight into the situation of these metal-diamond interfaces have been gained and can be reinvested in barrier height models discussed in the next section. The most important quantity which can be extracted from the analysis of electrical characteristics of Schottky diodes is obviously the true potential barrier height at an interface free of inhomogeneities and it has been defined at the beginning of this study as Φ_B^{hom}. It is always underestimated if the barrier height is measured from the slope of a Richardson plot and a relevant value Φ_B^{hom} needs to be deduced either from adjustment of the measured barrier height as a function of temperature, or from the direct adjustment of the current-voltage density with the appropriate model chosen among those described in this section, or from the statistics of barrier heights as a function of ideality factors in a set of diodes, or preferably from several methods.

V. BARRIER HEIGHT MODELS AT METAL-OXYGENATED DIAMOND INTERFACES

The barrier heights issue at metal-diamond interfaces belongs to the long time debated topic of how the Fermi level position is determined at semiconductor surfaces and interfaces, discussed as early as in the thirties by Sir Nevill Mott[46] concerning the rectification theory and by Walter Schottky[47]. Because this first model, which stated the linear dependence of the barrier height upon the metal work function with a unity slope, did not comply with the huge amount of data gathered since its publication, other explanations have been proposed to justify the weaker dependence experimentally observed, known as Fermi level pinning. New barrier height models have been progressively introduced within the framework of the "metal induced gap states" principle[48] or its generalization to "interface induced gap states"[21] in order to link band alignment and either the work function or electronegativity of the metal at the broadest possible panel of metal-semiconductor interfaces. All rely on the existence of an interface state density localized in the first elementary cells of the semiconductor which is neutral when the Fermi level coincides with an energy level Φ_0 characteristic of the semiconductor and referred as to the neutral level, defined here as the energy difference between such a level and the valence band edge at interface. Deviations from this position and from neutrality occur if a metal having an electronegativity different from that of the semiconductor is put in intimate contact with the semiconductor surface, assuming that the interface states inside the semiconductor remain invariant. This last hypothesis leads to a negative feedback effect due to the reaction of the charge inside interface states onto the voltage jump due to the double layer of the areal dipole astride the interface, which induces a linear relationship between the barrier height and the difference of the metal and semiconductor electronegativities $X_m - X_s$, with either a positive slope S_X on a n-type semiconductor, or a negative one, $-S_X$, on a p-type semiconductor as here:

$$e_0\,\Phi_{Bp}^{hom} \;=\; \Phi_0 - S_X\,(X_m - X_s) \tag{18a}$$

where

$$S_X \;=\; \frac{A_X}{1 + (e_0^2\,/\,\varepsilon_i\,\varepsilon_0)\,D_{is}\,d_{di}} \tag{18b}$$

with D_{is} the interface state density and A_X a coefficient which depends on the electronegativity scale, equal to 0.86 if the Miedema scale is used[21]. This theory was rather successful

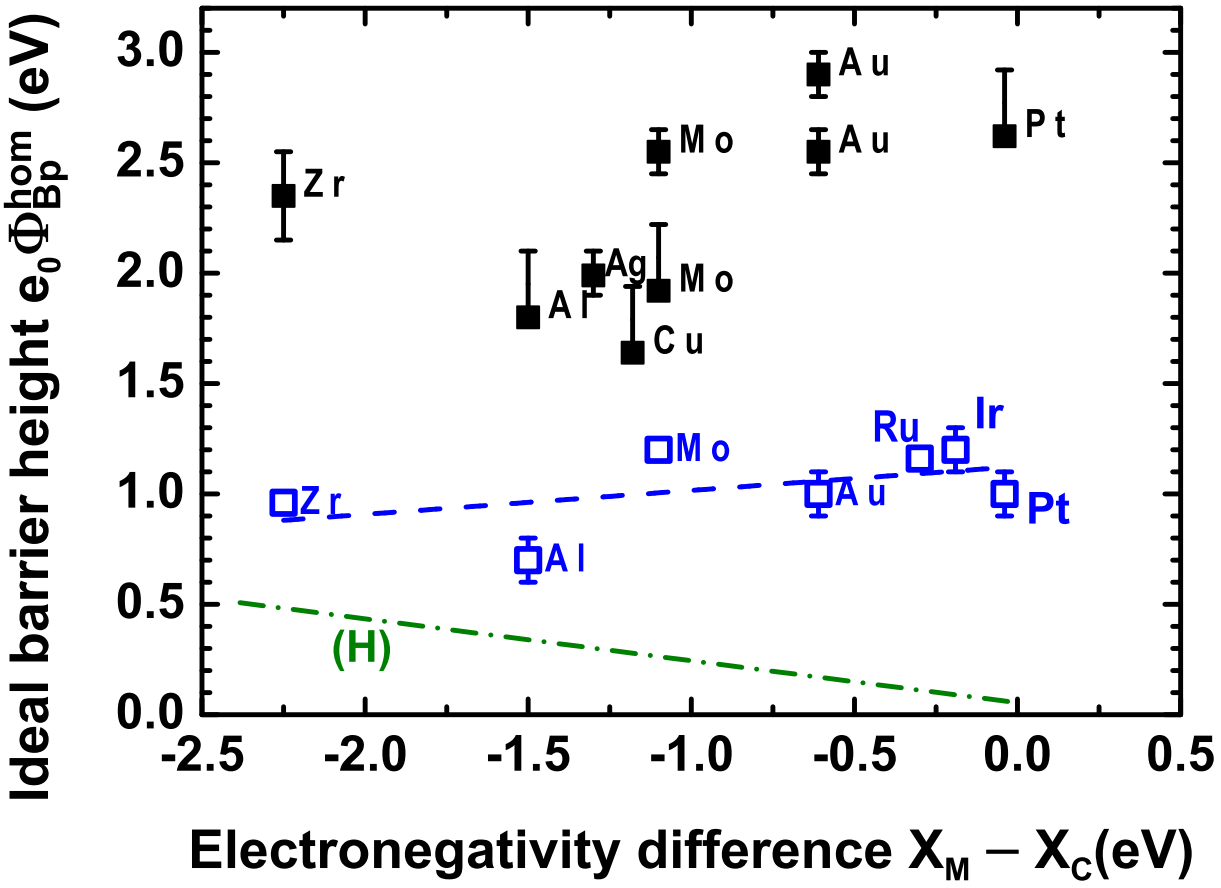

FIG. 9. Ideal barrier heights as a function of the Miedama electronegativity difference between metal and carbon (assumed to be 5.7 eV) for oxygenated interfaces annealed below 250 ℃ (full squares) and for those annealed in the range 400-650 ℃ (open squares), together with a linear fit in dotted line in the second case. The dash-dot line (H) is the best fit of barrier data on the hydrogenated surface by Tsugawa[17] *et al.* as a function of the same abscissa.

for intimate metal-semiconductor contacts, which have been better and better controlled at an atomic scale for the seventies, sometimes with an epitaxial metal layer. However, some dispersion still remained, which was not attributable to experimental uncertainties. This is specially true for diamond, which has not been the subject of extensive reports since the nineties, excepted to evidence the wide range of barrier heights existing for the same metal[8] and with the notable exception of the hydrogenated surface[17]. Such a dispersion has been ascribed to the various structures, terminations, ad-atoms and natures of bond which can exist at the diamond surfaces and interfaces, like already invoked in the case of oxygen termination. Recently, measurements of barrier heights have been published at carefully

prepared oxygenated and eventually post-annealed diamond surfaces[9,15,49–53]. Together with the present results for Zr-diamond interfaces, ideal barrier heights are plotted in Fig. (9) with error bars added according to the rules discussed in the previous section: either only above the published value when the method underestimated the ideal homogeneous barrier Φ_{Bp}^{hom}, or symmetrical when Φ_{Bp}^{hom} is directly indicated by authors or reassessed with the help of an appropriate method among those discussed in the preceding section. Despite some dispersion, illustrated sometimes in Fig. (9) and (10) with different barrier heights reported for the same metal in literature, two groups of data appear well separated, one for the contacts annealed at typical temperatures less than 250 ℃ or as-deposited and an other for contacts annealed at temperatures in the range 400-650 ℃, as a function of the Miedema electronegativity difference between metal and carbon, the last one being left constant at 5.7 eV. Electronegativity is a bulk property, so that it can hardly reflect the change in electron affinity of diamond due to oxygen terminations in the first group. Even if the diamond electronegativity were shifted by about -1.5 eV to take the oxygen terminations into account, although this is not a very sensible operation, the whole set of data does not show clearly any indisputable trend, testifying a first shortcoming. A second one appears if the search for a linear relationship is restricted to the second group of data, which shows a reasonable alignment depicted by the dotted line in Fig. (9), but characterized by a positive slope, in contradiction with Eq. (18a) and what is experimentally found for all other cases including that of a hydrogenated diamond surface[17]. This is the second shortcoming. Incidentally, it is difficult to believe that the energy distribution of "interface induced interface states" may remain the same when going from the hydrogenated then air-exposed diamond surfaces to oxygenated ones, as it is well known that the former is provided with adsorbates and conducting whereas the later is not[55]. An other approach, relying on physico-chemical quantities able to influence interface bonding, is necessary.

In the last twenty years, scientists performed modifications of the Schottky barrier heights by means of various ad-atoms and/or physical, chemical and thermal treatments applied to the surface generally before metal deposition excepted for annealing. They realized that these changes are dependent on bonding between interface atoms, and that chemical interactions cannot be ignored between atoms in the neighborhood of the interface. A first improvement of the theory has been brought by R.T. Tung who showed that potential energies in the solids and through the interface were more appropriate to describe band alignment[28]

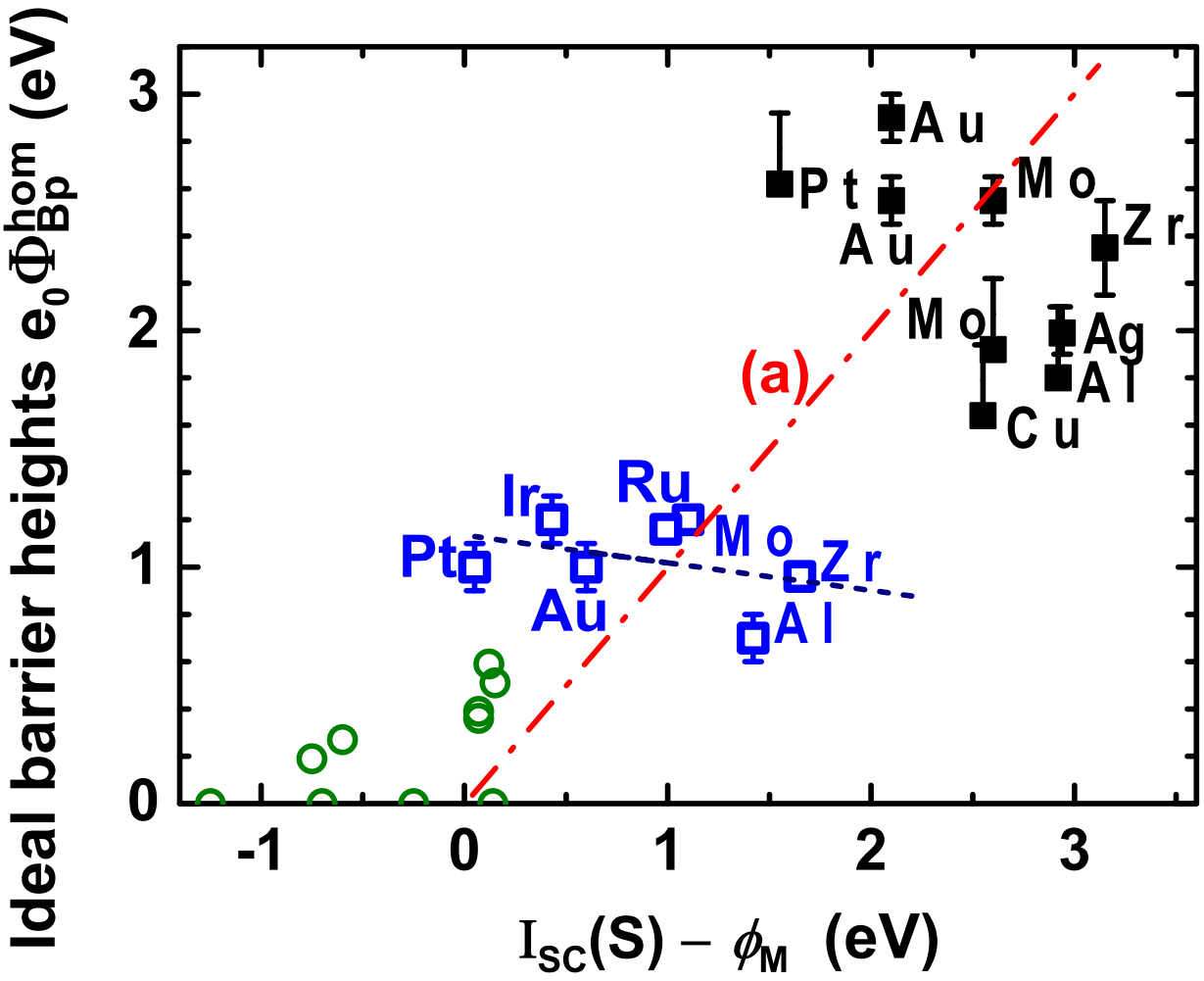

FIG. 10. Ideal barrier heights as a function of the difference between the ionization energy of diamond and the work function of metals for (i) as-deposited interfaces (full squares) on an oxygenated (100) surface, (ii) for contacts annealed in the range 400-650 ℃ (open squares) on an oxygenated (100) surface, together with a linear fit in dotted line, and (iii) for contacts on the hydrogenated (100) surface from ref.[17]. The ionization energy includes the electron affinity shift due to surface terminations, yielding (i) $\chi + \Delta\chi(S) = 1.7$ eV; (ii) $\chi + \Delta\chi(S) = 0.3$ eV and (iii) $\chi + \Delta\chi(S) = -1.1$ eV respectively for the oxygenated, bare and hydrogenated (100) surfaces from ref.[30]. The dash-dot line (a) displays Eq. (19a) where the last term is ignored, thus featuring the Mott-Schottky relationship.

in such a situation. Secondly, the dipole strength of the various double layers occurring at interface is the relevant quantity to take the possible interlayer atoms, the different bonds[54] and even the eventual new states due to transfer doping on the hydrogenated surface[17] into account. It is lumped into the last term in the following equation which makes use of the metal work function ϕ_M and electron affinity of the semiconductor as follows:

$$e_0\,\Phi_{Bp}^{hom} \;=\; (I_{SC}(S) \;-\; \phi_M) \;-\; e_0\,\Delta q\,d_{bd}\,N_{bd}/(\varepsilon_i\,\varepsilon_0) \tag{19a}$$

where the last term is the potential energy jump due to a surface dipole comprising a charge per bond Δq on the metal side and $-\Delta q$ on the diamond side separated by the distance d_{bd}, with an areal density of dipoles N_{bd}, while the ionization energy given by:

$$I_{SC}(S) \;=\; E_G \;+\; \chi \;+\; \Delta\chi(S) \tag{19b}$$

depends on the diamond band gap E_G, electron affinity χ of the bare surface and eventual change in electron affinity $\Delta\chi(S)$ due to foreign atoms termination or particular reconstruction on each surface S, the $\chi + \Delta\chi(S)$ values which are retained being indicated in the caption of Fig. 10.

When the last term is neglected in Eq. (19a), the Mott-Schottky relationship for contacts on p-type semiconductors is found, with a unity slope, sketched by a dash-dotted line in Fig. (10). If the dispersion of data is forgotten in a first approach and the clouds of points related to the three categories of interface in this graph are replaced by their respective barycenters, one can see that they align roughly on the Mott-Schottky line. This trend has been already evidenced in silicides on n-type silicon interfaces[56]. The influence of the cloud related to the hydrogenated surfaces should be minored because Pt, Au, Cu and Ag metals contacts are displayed with zero barrier heights although they should be negative but cannot be actually measured and reported. More accurately, if one observes the barrier heights of each metal (Pt, Au, Mo, Al, Zr) whose contact on diamond has been measured in the two groups of oxygenated interfaces, before and after annealing, the difference is very close to 1.4 ± 0.25 eV for all of them, corresponding to the same change in electron affinity. This common shift indicates that the barrier height for a given metal is primarily controlled by the electron affinity of diamond, with a little influence of the dipole due to interface bonding, reflected in the last term of Eq. (19a), and testifies the disappearance of

the oxygen terminations proper to initial oxygenated surfaces after annealing whatever the presence of an oxide or not as discussed further. But this statement does not mean that "interface induced gap states" have been suppressed or have never existed. They are just accommodating the electric charge which guarantees that the dipole layers, both necessary for setting the electron affinity and the bond dipole counterparts on the diamond side, can be present. Now, at a more subtle level, the general trend in each group of contacts made on the oxygenated surface has an inverted slope in comparison to the Mott-Schottky line, as already noticed in Fig. 9. The correlation coefficient is better in annealed interfaces, probably because the electron affinity dispersion due to various oxygen terminations has been suppressed, so that the origin of this linear relationship depicted by a dotted line in Fig. (10) can be discussed more thoroughly. First, it is useful to notice that neither the first term in Eq. (19a), which also scales the abscissa in this diagram, nor the second term can account for the observed trend if this later term is supposed to be proportional to the former one because the slope would be increased above one when the ionization energy is held constant. Therefore, one is forced to conclude that hidden physical parameters able to govern this second term might be involved. These are the nature of the bonds and interlayer, the charge transfer across them, their polarizability, and the interface structure with a special attention to the interlayer thickness and relative permittivity. In the case of metals like Pt, Ir and Au, oxide formation is very unlikely since the enthalpy of formation is either positive or close to zero, whereas an oxide is present when Zr, as shown at the beginning of this study, and most probably Al, are used. If the interlayer is supposed to be a dielectric consisting of a ionic solid, its thickness t_{ox} is added to the bond length d_{bl} so that the total dipolar distance is roughly $d_{bd} = t_{ox} + d_{bl}$. Then this distance determines the strength of the last term in Eq. (19a) since the charge counterpart of the dipole on the metal side is now located at a slightly larger length than t_{ox} from the last diamond atomic plane and if the charge inside the oxide layer is neglected at first approximation. Moreover, important effects are due to the charge transfer Δq which is governed by the nature of the bonds, electronegativity difference between the metal and semiconductor, the polarizability of bonds and interlayer thickness, as described in the bond polarization model proposed by R.T. Tung[28], and also screening which can mainly accounted for by the relative permittivity occurring at the denominator of the last term in Eq. (19a). To get a deeper insight in the problem at least at a first order level of approximation, let us define the abscissa $W_{SM} = (I_{SC}(S) - \phi_M)$ and take

the derivative of the barrier height $e_0\,\Phi_{Bp}^{hom}$ when the electron affinity, and hence ionization energy are constant:

$$\frac{d(e_0\,\Phi_{Bp}^{hom})}{dW_{SM}} \;=\; 1 \;+\; \frac{d(e_0\,\Delta q\,d_{bd}\,N_{bd}/(\varepsilon_i\,\varepsilon_0))}{d\phi_M} \tag{20}$$

This slope would stay close to one whenever the second term is negligible but can become negative as observed in Fig. (10) if both the second term is negative and its absolute value exceeds unity. Since the main trend occurring when the metal is changed to another one with an increased work function involves a decreased reactivity with oxygen and therefore a thickness reduction or disappearance of the oxide layer, one must wonder what are the resulting effects on the second term of Eq.(20), even if a continuous variation is more artificial than reality. The dipolar distance d_{bd} is obviously decreased while the interlayer permittivity ε_i initially near that of high-k dielectric materials is going down closer to unity, resulting in a smaller screening effect. But because theses two parameters are following the same direction of variation and influence the second term by their ratio, the resulting sign of the derivative turns out to be uncertain. Consequently, the fundamental issue relies mainly on the charge transfer Δq variation, which is dependent on the effective bonding at the metal-semiconductor interfaces[18,28], including not only orbitals of the two original materials but also atoms or molecules belonging to the interlayer. In such a molecular orbital scheme, metals with the lowest work functions (and also more electropositive) would make more ionic bonds, with a polarizability likely augmented by the presence of additional oxygen bonds inside the interlayer, thus inducing a stronger positive charge transfer Δq in the orbitals of the last metal atomic layer. Conversely, noble metals (and also more electronegative ones) are expected to share the electrons of their d states in a more equalized way with carbon orbitals, while carbide forming metals would follow a medium behavior. Such a general trend of the charge transfer Δq which would experience a decrease when the metal work function (and electronegativity) is increased, is able to justify the systematic negative sign of the derivative in the second member of Eq.(20). Consequently, the slope of barrier heights as a function of $W_{SM} = (I_{SC}(S) - \phi_M)$ can take values smaller than one, as often observed in many semiconductors, and in the case of a magnitude of the absolute value of the last term in the same equation greater than unity, it can become negative as shown in Fig. (10), in contrast to what is known in all other semiconductors. Such a model can also rely on the electronegativity difference between the semiconductor and metal, which mainly governs

the dipole strength induced by interface bonding, independent of the interface induced gap states at first order. At a second order level of approximation, the bonding nature of atoms inside the oxide and fixed charges in it will be also able to bring changes in Δq and these quantities probably contribute to the small deviations visible in Fig. (10) for annealed interfaces, together with the oxide interlayer thickness and permittivity, and changes in the atoms arrangement at interface and in the first diamond atomic layers. The same model also applies to unannealed interfaces, however with larger fluctuations in comparison to a linear behavior.

VI. CONCLUSION

In this work, interfaces of Zirconium with oxygenated diamond surfaces before and after two kinds of anneal has been characterized on the one hand by HRTEM imaging and EELS spectroscopy, and on the other hand by thorough electrical measurements made on the Schottky junctions. Evidence of an oxide interlayer comprising approximately two Zr and O atomic layers has been obtained. Current-voltage characteristics have been collected at several temperatures in some diodes and analyzed in order to investigate the detailed shape of the current density behavior with applied voltage, the Richardson constant, the apparent barrier height and the ideality factor. Models taking the barrier height and current density inhomogeneities have been implemented and brought face to face with experimental results. From these comparisons, several physical parameters have been estimated. The Richardson constant turned out to be close to one tenth of the standard value, and even one thirteenth when the barrier height disorder reached its maximum value. The effect of different shapes of barrier fluctuations has been studied either numerically in the case of local barrier enhancements or from two analytical models adapted to local barrier lowering and current crowding in the active layer of the diode. In the former case, which happens when fixed repulsive charges are close to the interface like evidenced in metal-ZrO_2 -diamond structures, the image force effect is the only relevant one as far as current-voltage characteristics are concerned. In the later case, it has been shown that barrier inhomogeneities can be characterized by three parameters related to their amplitude and density, and by the homogeneous barrier which is the truly representative physical quantity of the interface from the electrical point of view. It is free of the local and random lowered barrier patches

which are responsible for the non ideality of the diodes. Rules and uncertainties have been derived for a confident evaluation of this fundamental quantity. All these parameters have been extracted in turn from the comparison of these non idealities with the quantitative prediction of the models. Main conclusions were the strong reduction of both the barrier inhomogeneities and homogeneous barrier of 1.4 eV after annealing interfaces at 450 ℃. Because of the known inhomogeneity of the oxygen terminations and enhancement of the electron affinity by also 1.4 eV on the initial oxygenated diamond surface, these facts strongly suggested that these oxygen terminations vanished after such an annealing. Then, the more general issue of barrier height determination and Fermi level pinning has been addressed by means of an analysis of the experimental data collected in the present work and in recent literature, eventually reassessed with the help of the methods presented before. The same evolution of barrier heights for four other metals after annealing confirms the disappearance of oxygen terminations, irrespective of the presence of an oxide interlayer or not, and the electron affinity of the diamond surfaces as a relevant quantity for barrier height description. For the whole set of metals in contact with either unannealed or annealed oxygenated surfaces, or hydrogenated surfaces, a rough but clear alignment of barrier heights along the Mott-Schottky straight line, with a unity slope, really emerged regarding the difference between the ionization energy of diamond surfaces and metal work function. However, for each particular interface, the behavior at a smaller scale appeared different. In the case of annealed oxygenated interfaces, the slope turns out to be slightly negative, a result incompatible with the interface induced gap states model which assumes these states as invariant from one metal to another. On the contrary, the bond-polarization scheme, which relies on the interface dipole strength, itself dependent of the molecular orbitals involved in the bonds across the interface, may justify the slopes both at a global level and for a particular surface. All these concerns have been presented and discussed with the help of new experimental results, improved models and recent high quality experimental works in the purpose of fostering new advances in the old problem of potential barrier at metal-covalent semiconductor interfaces.

---

* pierre.muret@neel.cnrs.fr

† daniel.araujo@@uca.es

[1] P.-N. Volpe, J. Pernot, P. Muret, and F. Omnès, Appl. Phys. Letters **94**, 092102 (2009).

[2] P.-N. Volpe, P. Muret, J. Pernot, F. Omnès, T. Teraji, Y. Koide, F. Jomard, D. Planson, P. Brosselard, N. Dheilly, B. Vergne, and S. Scharnholz, Appl. Phys. Letters **97**, 223501 (2010).

[3] A. Vescan, I. Daumiller, P. Gluche, W. Ebert and E. Kohn, Diam. Related Mat. **7**, 581 (1998).

[4] P. Muret, F. Pruvost, C. Saby, E. Lucazeau, T.A. Nguyen Tan, E. Gheeraert, A. Deneuville, Diam. Related Mat. **8**, 961 (1999).

[5] M. Liao, J. Alvarez, and Y. Koide, Jpn. J. Appl. Phys. 44 (2005) 7832.

[6] A. Craciun, C. Saby, P. Muret, A. Deneuville, Diam. Related Mat. **13**, 292 (2004).

[7] C. Saby, P. Muret, F. Pruvost, G. Patrat, Diamond Related Mat. **11** 1332 (2002).

[8] D. A. Evans, O. R. Roberts, G. T. Williams, A. R. Vearey-Roberts, F. Bain, S. Evans, D. P. Langstaff and D. J. Twitchen, J. Phys.: Condens. Matter **21**, 364223 (2009).

[9] T. Teraji, Y. Garino, Y. Koide and T. Ito, J. Appl. Phys. **105**, 126109 (2009).

[10] P. K. Baumann and R. J. Nemanich, J. Appl. Phys. **83**, 2072f (1998).

[11] H. Kawarada, Surf. Sci. Rep. **26**, 205 (1996).

[12] E. H. Aoki and H. Kawarada, Jpn. J. Appl. Phys. **33**, L708 (1994).

[13] J. Alvarez, F. Houzé, J.P. Kleider, M.Y. Liao, Y. Koide, Superlattices and Microstructures **40**, 343 (2006).

[14] K. Ikeda, H. Umezawa, K. Ramanujam and S. Shikata, Appl. Phys. Express **2**, 011202 (2009).

[15] T. Teraji, Y. Koide, and T. Ito, Phys. Status Solidi RRL **3**, 211 (2009).

[16] A. Traoré, P. Muret, A. Fiori, D. Eon, E. Gheeraert, and J. Pernot, Appl. Phys. Letters **104**, 052105 (2014).

[17] K. Tsugawa, H. Noda, K. Hirose, and H. Kawarada, Phys. Rev. B **81**, 045303 (2010).

[18] R. T. Tung, Appl. Phys. Rev **1**, 011304 (2014).

[19] E. H. Rhoderick, J. Phys. D: Appl. Phys. **5**, 1920 (1972).

[20] E. H. Rhoderick, *Metal-Semiconductor Contacts*, ed. Oxford: Clarendon Press (1978).

[21] W. Mönch, *Electronic Properties of Semiconductor Interfaces*, ed. Springer-Verlag Berlin Heidelberg (2004).

[22] C. R. Crowell and M. Beguwala, Sol. St. Electron. **14**, 1149 (1971).

[23] H. C. Card and E. H. Rhoderick, J. Phys. D: Appl. Phys. **4**, 1589 (1971).

[24] J. M. Andrews, M. P. Lepselter, Sol. St. Electron. **13**, 1011 (1970).

[25] S. Ohmagari, T. Teraji and Y. Koide, J. Appl. Phys. **110**, 056105 (2011).

[26] J. H. Werner, H. H. Güttler, J. Appl. Phys. **69**, 1522 (1991).

[27] R. T. Tung, Phys. Rev. B **45**, 13509 (1992).

[28] R. T. Tung, Mater. Sci. Eng. **35**, 1 (2001).

[29] P. M. Gammon, A. Pérez-Tomás, V. A. Shah, O. Vavasour, E. Donchev, J. S. Pang, M. Myronov, C. A. Fisher, M. R. Jennings, D. R. Leadley, and P. A. Mawby, J. Appl. Phys. **114**, 223704 (2013).

[30] J. Ristein, M. Riedel,and L. Ley, J. Electrochem. Soc., **151** E315 (2004).

[31] J.-C. Arnault, private communication.

[32] F. Klauser, S. Ghodbane, R. Boukherroub, S. Szunerits, D. Steinmüller-Nethl, E. Bertel, N. Memmel, Diamond Related Mat. **19** 474 (2010).

[33] S. Ghodbane, D. Ballutaud, F. Omnès, C. Agnès, Diamond Related Mat. **19** 630 (2010).

[34] S. J. Sque, R. Jones, P. R. Briddon, Phys. Rev. B **54**, 085313 (2006).

[35] H. Notsu, I. Yagi, T. Tatsuma, D. A. Tryk, A. Fujishima, J. Electroanalytical Chem. **492**, 31 (2000).

[36] C. K. Fink and S. J. Jenkins, J. Phys.: Condens. Matter **21**, 264010 (2009).

[37] J. Robertson, M. J. Rutter, Diamond Related Mat. **7** 620 (1998).

[38] H. Sirringhaus, T. Meyer, E. Y. Lee, H. von Känel, Phys. Rev. B **53**, 15944 (1996).

[39] P. Muret, J. Vac. Sci. Technol. **B 32**, 03D114 (2014).

[40] H. Michaelson, J. Appl. Phys. **48**, 4729 (1977).

[41] P. Muret, C. Saby, Semicond. Sci. Technol. **19**, 1 (2004) ; a typographic error in table 2 must be corrected by changing the minus sign into plus sign in each of the three last columns at the last line which recapitulates the electron affinities, only that of the hydrogenated surface being really negative.

[42] S. Jain and W. Dahlke, Sol. St. Electron. **29**, 597 (1986).

[43] S. Collins, D. Lowe and J. R. Barker, J. Phys. C: Solid State Phys. **20**, 6233 (1987).

[44] T. Teraji, S. Koizumi, and Y. Koide, J. Appl. Phys. **104**, 016104 (2008).

[45] R. H. Cox and H. Strack, Sol. St. Electron. **10**, 1213 (1967).

[46] N. F. Mott, Proc.Roy. Soc. London **171**, 27 (1939).

[47] W. Schottky, Z. Physik **113**, 367 (1939).

[48] J. Tersoff, Phy. Rev. Lett. **52**, 465 (1984).

[49] S. Koné, G. Civrac, H. Schneider, K. Isoird, R. Issaoui, J. Achard, A. Gicquel, Diamond Related Mat. **19**, 792 (2010).

[50] H. Umezawa, M. Nagase, Y. Kato, S-i Shikata, Diamond Related Mat. **24**, 201 (2012).

[51] A. Nawawi, K.J. Tseng, Rusli, G. A. J. Amaratunga, H. Umezawa, and S. Shikata, Diam. Related Mat. **35**, 1 (2013).

[52] K. Ueda, K. Kawamoto, T. Soumiya, H. Asano, Diamond Related Mat. **38**, 41 (2013).

[53] K. Ueda, K. Kawamoto, H. Asano, Jpn. J. Appl. Phys. **53**, 04EP05 (2014).

[54] R. T. Tung, Phy. Rev. Lett. **84**, 6078 (2000).

[55] J. Ristein, F. Maier, M. Riedel, J. B. Cui and L. Ley, Phys. Status Solidi (a) **181**, 65 (2000).

[56] R. T. Tung, J. Vac. Sci. Technol. **B 11**, 1546 (1993).

Appendix B

Electrical properties of ITO Schottky electrodes on oxygen-terminated diamond

A transparent conductive oxide (Indium Tin Oxide: ITO), tested as a Schottky contact, resulted in a larger barrier height (above 2 eV) and a lower breakdown field (300 V). Tin doped Indium oxide (ITO) were deposited on sample #1 to fabricate Schottky contacts with a diameter of 100 μm corresponding to an area $S = 7.85 \times 10^{-5}$ cm^{-2}. ITO contacts were deposited by sputtering and annealed at 200 °C during 30 min allowing crystallization. A good reproducibility of I−V characteristics was observed for ITO Schottky electrodes (Fig. B.1). The BFOM in the case of ITO/p-diamond diode was about 8 MW/cm^2, due to the low breakdown field of 1.5 MV/cm (Fig. B.1). ITO/p-diamond diodes preserved their rectification behavior up to 723 K and were not affected by the thermal cycling study.

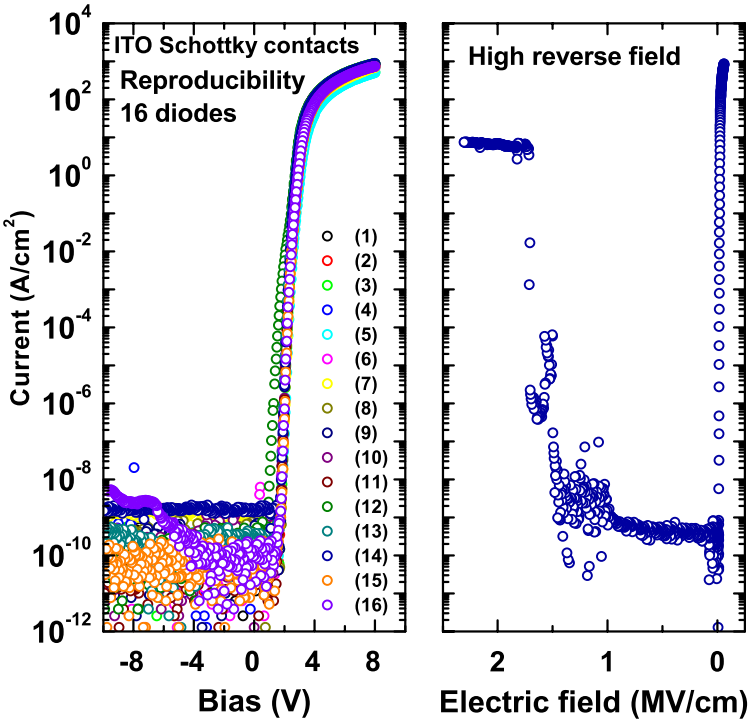

Figure B.1: Electrical properties of ITO/diamond junctions

Bibliography

[Achard 2005] J. Achard, Al. Tallaire, R. Sussmann, F. Silva and A. Gicquel. *The control of growth parameters in the synthesis of high-quality single crystalline diamond by CVD.* Journal of Crystal Growth, vol. 284, no. 3-4, pages 396–405, November 2005.

[Achard 2011] J. Achard, F. Silva, R. Issaoui, O. Brinza, a. Tallaire, H. Schneider, K. Isoird, H. Ding, S. Koné, M. A. Pinault, F. Jomard and A. Gicquel. *Thick boron doped diamond single crystals for high power electronics.* Diamond and Related Materials, vol. 20, no. 2, pages 145–152, February 2011.

[Altndal 2007] . Altndal, H. Kanbur, A. Tatarolu and M. M. Bülbül. *The barrier height distribution in identically prepared Al/p-Si Schottky diodes with the native interfacial insulator layer (SiO2).* Physica B: Condensed Matter, vol. 399, no. 2, pages 146–154, November 2007.

[Andrews 1970] J. M. Andrews and M. P. Lepselter. *REVERSE CURRENT-VOLTAGE CHARACTERISTICS DIODES OF.* Solid-State Electronics, vol. 13, pages 1011–1023, 1970.

[Anthony 1990] T. R. Anthony. *Metastable synthesis of diamond.* Vacuum, vol. 41, no. 4-6, pages 1356–1359, January 1990.

[Baliga 1982] B. J. Baliga. *Semiconductors for high-voltage, vertical channel field-effect transistors.* Journal of Applied Physics, vol. 53, no. 3, page 1759, March 1982.

[Baliga 1989] B. J. Baliga. *Power semiconductor device figure of merit for high-frequency applications.* Electron Device Letters, IEEE, vol. 10, no. 10, pages 455–457, October 1989.

[Balmer 2013] R. S. Balmer, I. Friel, S. Hepplestone, J. Isberg, M. J. Uren, M. L. Markham, N. L. Palmer, J. Pilkington, P. Huggett, S. Majdi and R. Lang. *Transport behavior of holes in boron delta-doped diamond structures.* J. Appl. Phys., vol. 113, no. 3, pages 033702–033702–10, January 2013.

[Bousquet 2014] J. Bousquet, G. Chicot, D. Eon and E. Bustarret. *Spectroscopic ellipsometry of homoepitaxial diamond multilayers and delta-doped structures.* Applied Physics Letters, vol. 104, no. 2, page 021905, January 2014.

[Brandes 1999] G. R. Brandes, C. P. Beetz, C. F. Feger, R. W. Wright and J. L. Davidson. *Ion implantation and anneal to produce low resistance metaldiamond contacts.* Diamond and Related Materials, vol. 8, no. 10, pages 1936–1943, October 1999.

[Bundy 1980] F. P. Bundy. *The P-T phase and the reaction diagram for elemental carbon.* Journal of Geophysical Research, vol. 85, page 6930, 1980.

[Butler 2003] J. E. Butler, M. W. Geis, K. E. Krohn, J. Lawless Jr, S. Deneault, T. M. Lyszczarz, D. Flechtner and R. Wright. *Exceptionally high voltage Schottky diamond diodes and low boron doping.* Semiconductor Science and Technology, vol. 18, no. 3, page S67, 2003.

[Card 1971] H. C. Card and E. H. Rhoderick. *Studies of tunnel MOS diodes I . Interface effects in silicon Schottky diodes.* Journal of Physics D, vol. 4, page 1589, 1971.

[Chicot 2012] G. Chicot, T. N. Tran Thi, A. Fiori, F. Jomard, E. Gheeraert, E. Bustarret and J. Pernot. *Hole transport in boron delta-doped diamond structures.* Appl. Phys. Lett., vol. 101, no. 16, pages 162101–162101–4, October 2012.

[Chicot 2013] G. Chicot, A. Maréchal, R. Motte, P. Muret, E. Gheeraert and J. Pernot. *Metal oxide semiconductor structure using oxygen-terminated diamond.* Applied Physics Letters, vol. 102, no. 24, page 242108, June 2013.

[Cowley 1965] A. M. Cowley and S. M. Sze. *Surface States and Barrier Height of Metal-Semiconductor Systems.* Journal of Applied Physics, vol. 36, no. 10, page 3212, 1965.

[Dean 1965] P. J Dean, E. C Lightowlers and D. R Wight. *Intrinsic and Extrinsic Recombination Radiation from Natural and Synthetic Aluminium-Doped Diamond.* Physical Review, vol. 140, page A352, 1965.

[Dorkel 1981] J. M. Dorkel and PH. Leturcq. *Carrier mobilities in silicon semi-empirically related to temperature, doping and injection level.* Solid-State Electronics, vol. 24, no. 9, page 821, 1981.

[Edgington 2012] R. Edgington, S. Sato, Y. Ishiyama, R. Morris, R. B. Jackman and H. Kawarada. *Growth and electrical characterisation of 6-doped boron layers on (111) diamond surfaces.* J. Appl. Phys., vol. 111, no. 3, February 2012. WOS:000301029800053.

[Elhajj 2008] H. Elhajj, A. Denisenko, A. Bergmaier, G. Dollinger, M. Kubovic and E. Kohn. *Characteristics of boron delta-doped diamond for electronic applications.* Diamond and Related Materials, vol. 17, no. 4-5, pages 409–414, April 2008.

[Ferro 2002] S. Ferro. *Synthesis of diamond.* Journal of Materials Chemistry, vol. 12, no. 10, pages 2843–2855, September 2002.

[Fink 2009] C. K. Fink and S. J. Jenkins. *Ozonolysis of diamond.* Journal of physics. Condensed matter : an Institute of Physics journal, vol. 21, no. 26, page 264010, July 2009.

[Fiori 2012] A. Fiori. *Nouvelles générations de structures en diamant dopé au bore par technique de delta-dopage pour l électronique de puissance : croissance par CVD et caractérisation.* PhD thesis, Université de Grenoble, 2012.

[Fiori 2014] A. Fiori, T. Teraji and Y. Koide. *hermal stabilization and deterioration of the WC/p-type diamond (100) Schottky-barrier interface.* Journal of Materials Chemistry, 2014.

[Frenklach 1991] M. Frenklach and H. Wang. *Detailed surface and gas-phase chemical kinetics of diamond deposition.* Physical Review B, vol. 43, no. 2, 1991.

[Gabrysch 2008] M. Gabrysch, S. Majdi, A. Hallén, M. Linnarsson, A. Schöner, D. Twitchen and J. Isberg. *Compensation in boron-doped CVD diamond.* Physica Status Solidi (a), vol. 205, no. 9, pages 2190–2194, September 2008.

[Goodwin 1997] D. G. Goodwin and J. E. Butler. Handbook of industrial diamonds and diamond films. Springer, 1997.

[Harris 1989] S. J. Harris and A. M. Weiner. *Effects of oxygen on diamond growth.* Applied Physics Letters, vol. 55, no. 21, page 2179, 1989.

[Hiraiwa 2012] A. Hiraiwa, A. Daicho, S. Kurihara, Y. Yokoyama and H. Kawarada. *Refractory two-dimensional hole gas on hydrogenated diamond surface.* J. Appl. Phys., vol. 112, no. 12, pages 124504–124504–6, December 2012.

[Hirama 2006] K. Hirama, S. Miyamoto, H. Matsudaira, K. Yamada, H. Kawarada, T. Chikyo, H. Koinuma, K. Hasegawa and H. Umezawa. *Characterization of diamond metal-insulator-semiconductor field-effect transistors with aluminum oxide gate insulator.* Appl. Phys. Lett., vol. 88, no. 11, page 112117, 2006.

[Hirama 2010] K. Hirama, K. Tsuge, S. Sato, T. A. Tsuno, Y. Jingu, S. Yamauchi and H. Kawarada. *High-Performance P-Channel Diamond Metal–Oxide–Semiconductor Field-Effect Transistors on H-Terminated (111) Surface.* Appl. Phys. Express, vol. 3, no. 4, page 044001, March 2010.

[Huang 2004] W. Huang, T. P. Chow, J. Yang and J. E. Butler. *HIGH-VOLTAGE DIAMOND SCHOTTKY RECTIFIERS.* International Journal of High Speed Electronics and Systems, vol. 14, no. 03, pages 872–878, 2004.

[Ikeda 2009] K. Ikeda, H. Umezawa, N. Tatsumi, K. Ramanujam and S. Shikata. *Fabrication of a field plate structure for diamond Schottky barrier diodes.* Diamond and Related Materials, vol. 18, no. 2-3, pages 292–295, February 2009.

[Johnson 1965] E. Johnson. *Physical limitations on frequency and power parameters of transistors.* In IRE International Convention Record, volume 13, pages 27–34, 1965.

[Kamo 1983] M. Kamo, Y. Sato, S. Matsumoto and N. Setaka. *Diamond synthesis from gas phase in microwave plasma.* Journal of Crystal Growth, vol. 62, pages 642–644, 1983.

[Kanaya 1972] K. Kanaya and S. Okayama. *Penetration and energy-loss theory of electrons in solid targets.* Journal of Physics D: Applied Physics, vol. 5, no. 1, page 43, 1972.

[Kasu 2006] M. Kasu, K. Ueda, H. Ye, Y. Yamauchi, S. Sasaki and T. Makimoto. *High RF output power for H-terminated diamond FETs.* Diamond and Related Materials, vol. 15, no. 4–8, pages 783–786, April 2006.

[Kasu 2012] M. Kasu, H. Sato and K. Hirama. *Thermal Stabilization of Hole Channel on H-Terminated Diamond Surface by Using Atomic-Layer-Deposited Al2O3*

Overlayer and its Electric Properties. Appl. Phys. Express, vol. 5, no. 2, page 025701, February 2012.

[Kato 2012] H. Kato, K. Oyama, T. Makino, M. Ogura, D. Takeuchi and S. Yamasaki. *Diamond bipolar junction transistor device with phosphorus-doped diamond base layer.* Diamond and Related Materials, vol. 27-28, pages 19–22, July 2012.

[Kato 2013] H. Kato, T. Makino, M. Ogura, D. Takeuchi and S. Yamasaki. *Fabrication of bipolar junction transistor on (001)-oriented diamond by utilizing phosphorus-doped n-type diamond base.* Diamond and Related Materials, vol. 34, pages 41–44, April 2013.

[Kawarada 1994] Hiroshi Kawarada, Makoto Aoki and Masahiro Ito. *Enhancement mode metal-semiconductor field effect transistors using homoepitaxial diamonds.* Applied Physics Letters, vol. 65, no. 12, page 1563, 1994.

[Kawarada 2014] H. Kawarada, H. Tsuboi, T. Naruo, T. Yamada, D. Xu, A. Daicho, T. Saito and A. Hiraiwa. Applied Physics Letters, vol. 105, no. 1, page 013510, July 2014.

[Keyes 1972] R. W. Keyes. *Figure of merit for semiconductors for high-speed switches.* Proceedings of the IEEE, vol. 60, no. 2, pages 225–225, 1972.

[Klauser 2010] F. Klauser, S. Ghodbane, R. Boukherroub, S. Szunerits, D. Steinmüller-Nethl, E. Bertel and N. Memmel. *Comparison of different oxidation techniques on single-crystal and nanocrystalline diamond surfaces.* Diamond and Related Materials, vol. 19, no. 5-6, pages 474–478, May 2010.

[Klein 2007] T. Klein, P. Achatz, J. Kacmarcik, C. Marcenat, F. Gustafsson, J. Marcus, E. Bustarret, J. Pernot, F. Omnès, Bo E. Sernelius, C. Persson, A. Ferreira da Silva and C. Cytermann. *Metal-insulator transition and superconductivity in boron-doped diamond.* Phys. Rev. B, vol. 75, page 165313, Apr 2007.

[Koizumi 2001] S. Koizumi, K. Watanabe, M. Hasegawa and H. Kanda. *Ultraviolet Emission from a Diamond pn Junction.* Science, vol. 292, no. 5523, pages 1899–1901, June 2001. PMID: 11397942.

[Koizumi 2006] S. Koizumi and M. Suzuki. *n-Type doping of diamond.* Physica Status Solidi A, vol. 203, page 3358, 2006.

[Koné 2010] S. Koné, G. Civrac, H. Schneider, K. Isoird, R. Issaoui, J. Achard and A. Gicquel. *CVD diamond Schottky barrier diode, carrying out and characterization.* Diamond and Related Materials, vol. 19, no. 7-9, pages 792–795, 2010.

[Kumaresan 2009] R. Kumaresan, H. Umezawa, N. Tatsumi, K. Ikeda and S. Shikata. *Device processing, fabrication and analysis of diamond pseudo-vertical Schottky barrier diodes with low leak current and high blocking voltage.* Diamond and Related Materials, vol. 18, no. 2-3, pages 299–302, February 2009.

[Kumaresan 2010] R. Kumaresan, H. Umezawa and S. Shikata. *Vertical structure Schottky barrier diode fabrication using insulating diamond substrate.* Diamond and Related Materials, vol. 19, no. 10, pages 1324–1329, 2010.

[Landstrass 1993] M. I. Landstrass, M. A. Plano, M.A. Moreno, S. McWilliams, L. S. Pan, D. R. Kania and S. Han. *Device properties of homoepitaxially grown diamond.* Diamond and Related Materials, vol. 2, no. 5-7, pages 1033–1037, April 1993.

[Lawson 1995] S. C. Lawson, H. Kanda, H. Kiyota, T. Tsutsumi and H. Kawarada. *Cathodoluminescence from high-pressure synthetic and chemical-vapor-deposited diamond.* Journal of Applied Physics, vol. 77, no. 4, page 1729, 1995.

[Liao 2005] J. Liao M.and Alvarez and Y. Koide. *Thermal Stability of Diamond Photodiodes Using Tungsten Carbide as Schottky Contact.* Japanese Journal of Applied Physics, vol. 44, no. 11, pages 7832–7838, November 2005.

[Liu 2014] J-W. Liu, M-Y. Liao, M. Imura, E. Watanabe, H. Oosato and Y. Koide. *Diamond field effect transistors with a high-dielectric constant Ta 2 O 5 as gate material.* Journal of Physics D: Applied Physics, vol. 47, no. 24, page 245102, June 2014.

[Maier 2001] F. Maier, J. Ristein and L. Ley. *Electron affinity of plasma-hydrogenated and chemically oxidized diamond (100) surfaces.* Physical Review B, vol. 64, no. 16, page 165411, October 2001.

[Makino 2008] T. Makino, N. Tokuda, H. Kato, S. Kanno, S. Yamasaki and H. Okushi. *Electrical and light-emitting properties of homoepitaxial diamond p–i–n junction.* phys. stat. sol. (a), vol. 205, no. 9, pages 2200–2206, 2008.

[Makino 2009] T. Makino, S. Tanimoto, Y. Hayashi, H. Kato, N. Tokuda, M. Ogura, D. Takeuchi, K. Oyama, H. Ohashi, H. Okushi and S. Yamasaki. *Diamond*

Schottky-pn diode with high forward current density and fast switching operation. Applied Physics Letters, vol. 94, no. 26, page 262101, 2009.

[Makino 2014] T. Makino, K. Oyama, H. Kato, D. Takeuchi, M. Ogura, H. Okushi and S. Yamasaki. *Diamond electronic devices fabricated using heavily doped hopping p + and n + layers.* Japanese Journal of Applied Physics, vol. 53, page 05FA12, 2014.

[Matsumoto 2014] T. Matsumoto, H. Kato, T. Makino and M. Ogura. *Carrier transport in homoepitaxial diamond films with heavy phosphorus doping.* Japanese Journal of Applied Physics, vol. 53, page 05FP05, 2014.

[Millán 2012] J. Millán, P. Godignon and A. Pérez-Tomás. *Wide Band Gap Semiconductor Devices for Power Electronics.* Automatika Journal for Control Measurement Electronics Computing and Communications, vol. 53, no. 2, pages 107–116, May 2012.

[Mönch 1994] W. Mönch. *Barrier Heights of Metal Contacts on H-Terminated Diamond : Explanation by Metal-Induced Gap States and Interface Dipoles .* Euphysics letters, vol. 27, no. 6, page 479, 1994.

[Mönch 2004] W. Mönch. Electronic Properties of Semiconductor Interfaces. Springer Series in Surface Sciences. Springer, 2004.

[Mori 1992] Y. Mori, N. Eimori, H. Kozuka, Y. Yokota, J. Moon, J. S. Ma, T. Ito and A. Hiraki. *Oxygen diffusion into diamond induced by hydrogen microwave plasma.* Applied Physics Letters, vol. 60, no. 1, pages 47–49, 1992.

[Muret 2011] P. Muret, P.-N. Volpe, T.-N. Tran-Thi, J. Pernot, C. Hoarau, F. Omnès and T. Teraji. *Schottky diode architectures on p-type diamond for fast switching, high forward current density and high breakdown field rectifiers.* Diamond and Related Materials, vol. 20, no. 3, pages 285–289, March 2011.

[Notsu 2000] H. Notsu, I. Yagi, T. Tatsuma, D. A. Tryk and A. Fujishima. *Surface carbonyl groups on oxidized diamond electrodes.* Journal of Electroanalytical Chemistry, vol. 492, no. 1, pages 31–37, September 2000.

[Ohmagari 2011] S. Ohmagari, T. Teraji and Y. Koide. *Non-destructive detection of killer defects of diamond Schottky barrier diodes.* Journal of Applied Physics, vol. 110, no. 5, page 056105, 2011.

[Omnès 2011] F. Omnès, P. Muret, P-N. Volpe, M. Wade, J. Pernot and F. Jomard. *Study of boron doping in MPCVD grown homoepitaxial diamond layers based on cathodoluminescence spectroscopy, secondary ion mass spectroscopy and capacitancevoltage measurements.* Diamond and Related Materials, vol. 20, no. 7, pages 912–916, July 2011.

[Ozpineci 2011] B. Ozpineci and L. Tolbert. *Power electronics for distributed energy systems and transmission and distribution applications.* IEEE Spectrum, 2011.

[Parker 1968] G. H. Parker, C. T. McGill and C. A. Mead. *ELECTRIC FIELD DEPENDENCE OF GaAs SCHOTTKY BARRIERS *.* Solid-State Electronics, vol. 11, pages 201–204, 1968.

[Pernot 2001] J. Pernot, W. Zawadzki, S. Contreras, J. L. Robert, E. Neyret and L. Di Cioccio. *Electrical transport in n-type 4H silicon carbide.* Journal of Applied Physics, vol. 90, no. 4, page 1869, 2001.

[Pernot 2005] J. Pernot, S. Contreras and J. Camassel. *Electrical transport properties of aluminum-implanted 4HSiC.* Journal of Applied Physics, vol. 98, no. 2, page 023706, 2005.

[Pernot 2006] J. Pernot, C. Tavares, E. Gheeraert, E. Bustarret, M. Katagiri and S. Koizumi. *Hall electron mobility in diamond.* Applied Physics Letters, vol. 89, no. 12, page 122111, 2006.

[Pernot 2008] J. Pernot and S. Koizumi. *Electron mobility in phosphorous doped {111} homoepitaxial diamond.* Applied Physics Letters, vol. 93, no. 5, page 052105, 2008.

[Pernot 2010] J. Pernot, P. N. Volpe, F. Omnès, P. Muret, V. Mortet, K. Haenen and T. Teraji. *Hall hole mobility in boron-doped homoepitaxial diamond.* Physical Review B, vol. 81, no. 20, page 205203, May 2010.

[Piñero 2014] J. C. Piñero, D. Araujo, A. Traoré, G Chicot, A. Maréchal, P. Muret, M. P. Alegre, M. P. Villar and J. Pernot. *Temperature and density dependence metaloxidediamond interface investigation by TEM: Toward MOS and Schottky power device behavior.* Physica Status Solidi (a), 2014.

[Reggiani 1981] L. Reggiani, S. Bosi, C. Canali and F. Nava. *Hole-drift velocity in natural diamond.* Physical Review B, vol. 23, no. 6, pages 3050–3057, 1981.

[Rhoderick 1978] E. H. Rhoderick. Metal semiconductor contacts. Oxford Unuversity Press, 1978.

[Robertson 1998] J. Robertson and M. J. Rutter. *Band diagram of diamond and diamond-like carbon surfaces.* Diamond and Related Materials, vol. 7, page 620, 1998.

[Sawada 2000] T. Sawada, Y. Ito, K. Imai, K. Suzuki, H. Tomozawa and S. Sakai. *Electrical properties of metal r GaN and SiO 2 r GaN interfaces and effects of thermal annealing.* Applied Surface Science, vol. 159-160, pages 449–455, 2000.

[Scharpf 2013] J. Scharpf, A. Denisenko, C. I. Pakes, S. Rubanov, A. Bergmaier, G. Dollinger, C. Pietzka and E. Kohn. *Transport behaviour of boron delta-doped diamond.* Phys. stat. sol. (a), vol. 210, no. 10, pages 2028–2034, 2013.

[Schmitsdorf 1995] R. F. Schmitsdorf, T. U. Kampen and W. Mönch. *Correlation between barrier height and interface structure of Ag / Si (111) Schottky diodes.* surface Science, vol. 324, page 249, 1995.

[Silva 2009] F. Silva, J. Achard, O. Brinza, X. Bonnin, K. Hassouni, a. Anthonis, K. De Corte and J. Barjon. *High quality, large surface area, homoepitaxial MPACVD diamond growth.* Diamond and Related Materials, vol. 18, no. 5-8, pages 683–697, May 2009.

[Sque 2006] S. Sque, R. Jones and P. Briddon. *Structure, electronics, and interaction of hydrogen and oxygen on diamond surfaces.* Physical Review B, vol. 73, no. 8, page 085313, February 2006.

[Suezaki 2001] T. Suezaki, K. Kawahito, T. Hatayama, Y. Uraoka and T. Fuyuki. *Electrical Properties and Thermal Stability of Cu / 6H-SiC Junctions.* Japanese Journal of Applied Physics, vol. 40, page L43, 2001.

[Suzuki 2013] M. Suzuki, T. Sakai, T. Makino, H. Kato, D. Takeuchi, M. Ogura, H. Okushi and S. Yamasaki. *Electrical characterization of diamond PiN diodes for high voltage applications.* Phys. Status Solidi A, vol. 210, pages 2035–2039, 2013.

[Sze 2007] S. M. Sze and Kwok K. NG. Physics of Semiconductor Devices, 3rd ed. Springer Series in Surface Sciences. Wiley, 2007.

[Tachibana 1992] T. Tachibana, B. E. Williams and J. T. Glass. *Correlation of the electrical properties of metal contacts on diamond films with the chemical nature*

of the metal-diamond interface. II. Titanium contacts: A carbide-forming metal. vol. 45, no. 20, page 11975, 1992.

[Takeuchi 2001] D. Takeuchi, H. Watanabe, S. Yamanaka, H. Okushi, H. Sawada, H. Ichinose, T. Sekiguchi and K. Kajimura. *Origin of band-A emission in diamond thin films.* Physical Review B, vol. 63, no. 24, page 245328, June 2001.

[Tallaire 2008] A. Tallaire, M. Kasu, K. Ueda and T. Makimoto. *Origin of growth defects in CVD diamond epitaxial films.* Diamond and Related Materials, vol. 17, no. 1, pages 60–65, January 2008.

[Tavares 2005] C. Tavares, A. Tajani, C. Baron, F. Jomard, S. Koizumi, E. Gheeraert and E. Bustarret. *{111}-oriented diamond films and p/n junctions grown on B-doped type Ib substrates.* Diamond and Related Materials, vol. 14, pages 522–525, 2005.

[Teraji 2009a] T. Teraji, Y. Garino, Y. Koide and T. Ito. *Low-leakage p-type diamond Schottky diodes prepared using vacuum ultraviolet light/ozone treatment.* Journal of Applied Physics, vol. 105, no. 12, page 126109, 2009.

[Teraji 2009b] T. Teraji, Y. Koide and T. Ito. *High-temperature stability of Au/p-type diamond Schottky diode.* physica status solidi (RRL) - Rapid Research Letters, vol. 3, no. 6, pages 211–213, September 2009.

[Teraji 2014] T. Teraji, Y. Koide and T. Ito. *Schottky barrier height and thermal stability of p-diamond (100) Schottky interfaces.* Thin Solid Films, vol. 557, pages 241–248, April 2014.

[Tolbert 2005] L. M Tolbert, T. J. King, B. Ozpineci, G. Muralidharan, D. T. Rizy, A. S. Sabau, H. Zhang, W. Zhang, X. Yu, H. F. Huq and H. Liu. *Power electronics for distributed energy systems and transmission and distribution applications.* OAK RIDGE NATIONAL LABORATORY UT-BATTERELLE US DEPARTEMENT OF ENERGY, 2005.

[Tsukioka 2006] K. Tsukioka and H. Okushi. *Hall Mobility and Scattering Mechanism of Holes in Boron-Doped Homoepitaxial Chemical Vapor Deposition Diamond Thin Films.* Japanese Journal of Applied Physics, vol. 45, no. 11, pages 8571–8577, November 2006.

[Tumilty 2009] N. Tumilty, J. Welch, R. Lang, C. Wort, R. Balmer and R. B. Jackman. *An impedance spectroscopic investigation of the electrical properties of*

delta-doped diamond structures. J. Appl. Phys., vol. 106, no. 10, November 2009. WOS:000272932300045.

[Tung 1992] R. T. Tung. *Tung_inhomogeneous_barrier_theory.* Physical Review B, vol. 45, page 15509, 1992.

[Tung 2014] R. T. Tung. *The physics and chemistry of the Schottky barrier height The physics and chemistry of the Schottky barrier height.* Appl. Phys. Rev, vol. 1, page 011304, 2014.

[Twitchen 2004] D. J. Twitchen, A. J. Whitehead, S. E. Coe, J. Isberg, J. Hammersberg, T. Wikstrom and E. Johansson. *High-voltage single-crystal diamond diodes.* Electron Devices, IEEE Transactions on, vol. 51, no. 5, pages 826–828, May 2004.

[Ueda 2014] K. Ueda, K. Kawamoto and H. Asano. *High-temperature characteristics and stability of Cu / diamond Schottky diodes.* Japanese Journal of Applied Physics, vol. 53, page 04EP05, 2014.

[Umezawa 2007] H. Umezawa, T. Saito, N. Tokuda, M. Ogura, S-G. Ri, H. Yoshikawa and S-I. Shikata. *Leakage current analysis of diamond Schottky barrier diode.* Applied Physics Letters, vol. 90, no. 7, page 073506, 2007.

[Umezawa 2012] H. Umezawa, M. Nagase, Y. Kato and S-I. Shikata. *High temperature application of diamond power device.* Diamond and Related Materials, vol. 24, pages 201–205, April 2012.

[Umezawa 2013] H. Umezawa and Y. Kato. *1\Omega On-Resistance Diamond Vertical-Schottky Barrier Diode Operated at 250.* Applied Physics Express, vol. 6, pages 3–6, 2013.

[Umezawa 2014] H. Umezawa, S-I. Shikata and T. Funaki. *Diamond Schottky barrier diode for high-temperature , high-power , and fast switching applications.* Japanese Journal of Applied Physics, vol. 53, page 05FP06, 2014.

[Volpe 2009a] P-N. Volpe. *Réalisation de composants unipolaires en diamant pour l électronique de puissance.* PhD thesis, Université Joseph Fourier - Grenoble, 2009.

[Volpe 2009b] P-N. Volpe, J. Pernot, P. Muret and F. Omnès. *High hole mobility in boron doped diamond for power device applications.* Applied Physics Letters, vol. 94, no. 9, page 092102, 2009.

[Volpe 2010] P-N. Volpe, P. Muret, J. Pernot, F. Omnès, T. Teraji, Y. Koide, F. Jomard, D. Planson, P. Brosselard, N. Dheilly, B. Vergne and S. Scharnholz. *Extreme dielectric strength in boron doped homoepitaxial diamond.* Applied Physics Letters, vol. 97, no. 22, page 223501, 2010.

[Warren 1966] J. E. Warren and J. L. Yarnell. *Lattice Dynamics of Diamond *.* Physical Review, vol. 158, page 805, 1966.

[Werner 1991] J. H. Werner and H. H. Gijttler. *Barrier inhomogeneities at Schottky contacts.* Journal of Applied Physics, vol. 69, page 1522, 1991.

[Werner 1997] M. Werner, R. Locher, W. Kohly, D. S. Holmes, S. Klose and H. J. Fecht. *The diamond Irvin curve.* Diamond and Related Materials, vol. 6, no. 2-4, pages 308–313, March 1997.

[Werner 2003] Matthias Werner. *Diamond metallization for device.* Semiconductor Science and Technology, vol. 18, page 41, 2003.

[Willatzen 1994] M. Willatzen and M Cardoua. *Linear mufBn-tin-orbital and k p calculations.* Physical Review B, vol. 50, no. 24, pages 54–59, 1994.

[Zaitsev 2010] A. M. Zaitsev. Opticacal properties of diamond. a data hanbook. Springer, 2010.